# Controlling the electrical properties of oxide heterointerfaces through their interface chemistry

Marc-André Rose

JÜLICH
Forschungszentrum

# Controlling the electrical properties of oxide heterointerfaces through their interface chemistry

Marc-André Rose

*This thesis is dedicated to my loving wife Katja.*
*Without her, I would not be the person I am today.*

# Kurzfassung

Zum heutigen Zeitpunkt werden mehrere Ansätze verfolgt, um die Leistung moderner Computer zu steigern. Neben Ansätzen in den Bereichen der Software und Elektrotechnik, werden große Bemühungen in die Verbesserung der fundamentalsten Einheit von Computern, den elektronischen Bauelementen, gesteckt. Um diese weiter und weiter zu verbessern, optimiert die Halbleiterindustrie elektronische Bauelemente durch einen Skalierungsansatz. Jedoch erreicht diese Methodik ihre physikalischen Grenzen, weshalb neue Konzepte und Materialien erforscht werden, welche eine weitere Verbesserung der rechnerischen Leistungskraft ermöglichen könnten. Aufgrund ihrer diversen und einstellbaren Eigenschaften, sind Oxide und ihre Grenzflächen vielversprechende Kandidaten für diese Anwendung. In diesem Kontext führte die Entdeckung eines 2-dimensionalen Elektronen Gases (2DEG) an der LaAlO$_3$/SrTiO$_3$ Grenzfläche zu einem hohem Interesse an diesem Materialsystem. Grund hierfür ist die zentrale Bedeutung von 2DEGs für moderne Transistoranwendungen wie z.B. in Transistoren mit hoher Elektronenbeweglichkeit. Allerdings konnte noch kein vollständiges Verständnis über das elektische Verhalten von LAO/STO etabliert werden, trotz über eines Jahrzehnts an Forschungsarbeit.

Diese Arbeit erforscht wie sich die Grenzflächenchemie der LAO/STO Heterostrukturen auf ihre elektrischen Eigenschaften auswirkt. Um dies zu erreichen, werden zwei Ansätze verfolgt. Zum einen wird das System in lateraler Richtung untersucht (entlang der Grenzfläche), wo die Präsenz unterschiedlicher Oberflächenterminierung des STO Substrats zu lokalen Inhomogenitäten des 2DEGs führen. Zum anderen, wird das System in vertikaler Richtung untersucht (über die Grenzfläche hinweg). In diesem Fall, lassen sich ionische Bewegungsprozesse durch thermodynamische Behandlungen anregen, was zu einer Veränderung der lokalen Defektstruktur führt. In beiden Fällen werden *in-situ* Methoden verwendet, welche eine direktere Beobachtung der Prozesse erlauben.

In der lateralen Richtung werden *in-situ* Rastersondenverfahren angewandt. Hierdurch wird eine Kartographierung des 2DEGs erreicht, welche es erlaubt die nanoskopische Verteilung des 2DEGs mit seinen makroskopischen Eigenschaften zu korellieren. Weiterhin wird gezeigt, wie die Verteilung des 2DEGs manipuliert werden kann. Dies wird zum einen durch die natürlich vorkommende Variabilität der Oberflächenterminierung des STO Substrats, und zum anderen durch die kontrollierte Abscheidung von SrO Sub-Monolagen auf Ti-terminiertem STO erreicht. Abhängig von der Anordnung der leitfähigen und isolierenden Regionen, verändern sich die makroskopischen elektrischen Eigenschaften der Heterostruktur bis in den Tieftemperatur Bereich.

Für die vertikale Richtung, wurde *in-situ* Nah-Umgebungsdruck-Röntgenphotoelektronenspektroskopie genutzt. Diese Methode ermöglicht es die Entstehung von Zweit-

phasen und Veränderungen in der Bandstruktur zu beobachten, während spezifische thermodynamische Glühungen angewandt werden. Durch die Oxidation von LAO/STO, wird eine Ausscheidung von Sr Ionen aus der Grenzfläche beobachtet, welche zu einer Verarmung des 2DEG führt. Die Sr Ionen weisen eine überraschend hohe Mobilität auf, da unter den relativ moderaten Temperaturen (470 °C) keine signifikante Kationendiffusion erwartet werden würde. Die eingebrachte Modifikation der Grenzflächenchemie verändert nicht nur die elektrischen, sondern auch die magnetischen Eigenschaften der Grenzfläche. Dies führt zu einer signifikanten Erhöhung des beobachten Tieftemperatur Magnetismus in oxidierten Heterostrukturen. Basierend auf spektroskopisch erlangten Wissen wurde ein Verfahren etabliert, welches erlaubt das magnetische Verhalten der oxidierten Grenzflächen zu kontrollieren. Dieses basiert auf einer Kombination von LAO Stoichiometrie und thermodynamischen Glühen. Zum Schluss der Arbeit werden die erlangten Resultate zusammengefasst und ein Defektchemisches Modell vorgestellt, welches konsistent das beobachtete Verhalten erklären kann. Durch die Resultate dieser Arbeit wurde ein wichtiger Schritt getan , um ein vollständiges Wissen über die Beziegung zwischen der ionischen Struktur und elektrischen Eigenschaften zu etablieren.

# Abstract

Multiple routes are taken today to improve the processing power of modern computers. Besides software and electrical engineering approaches, high effort is taken in improving the most fundamental building block of computers, namely their electronic devices. To enhance the performance of electronic devices, the semiconductor industry applied further and further optimization, driven by a down-scaling approach. The advent of the physical limitation of this approach has led to the search of alternative materials and concepts, which could allow even higher computational performance. Oxides and their interfaces are promising candidates due to their highly diverse and tunable properties. In this context, the $LaAlO_3$/$SrTiO_3$ (LAO/STO) interface sparked high interest, as it possesses an interfacial 2-dimensional electron gas (2DEG), which is a vital part of modern transistor technology (in particular for high-electron-mobility-transistors). However, even though the system has been researched for over a decade, the details of its electronic behavior are still not fully understood.

This thesis investigates how the interface chemistry of LAO/STO heterostructures influences the electronic properties of the 2DEG. A twofold approach is taken to elucidate this topic. For one, the lateral direction was analyzed (along the interface), where local inhomogeneities of the 2DEG due to the STO substrate termination appear. Second, the vertical direction was analyzed (across the interface), where local defect concentrations can be altered through thermodynamic annealing and trigger ionic motion across the interface. In both cases, *in-situ* methods are used, which allow investigation of the pristine process at the interface.

In the lateral direction, *in-situ* scanning probe techniques are applied. In this way, a mapping of the 2DEG is achieved, which allows to correlate the nanoscopic 2DEG distribution to macroscopic sample properties. It is shown how the 2DEG distribution can be manipulated, for one by the use of naturally occurring STO substrate termination variations and second, by the controlled growth of SrO sub-monolayers on single terminated STO. Depending on the arrangement of conducting and insulating regions, the electrical macroscopic behavior is changed down to the low-temperatures range.

In the vertical direction, *in-situ* near-ambient pressure X-ray photoelectron spectroscopy is applied. This enables the monitoring of evolving secondary phases and changing band alignment, while applying thermodynamic annealing. Upon oxidation, Sr ions precipitate out of the interfacial region, depleting the 2DEG. An unexpected high mobility of Sr ions is observed, as the applied moderate temperatures (470 °C) would not allow significant cation diffusion in the STO bulk. The induced change of interfacial defect chemistry alters not only electronic, but also the magnetic properties of the interface, leading to a significant increase of low-temperature magnetism

in oxidized heterostructures. Based on the acquired knowledge from spectroscopic analysis, a route to control the magnetic behavior upon oxidation is established, using a combination of LAO stoichiometry and thermodynamic annealing. At the end, the gained results are summarized and a defect chemical model is proposed, which can consistently explain the observed behavior. Through these results, an important step towards the full understanding of the relationship between ionic structure and electronic properties is taken.

# Contents

# Chapter 1

# Introduction

The progress of electronics has led to the development of ever faster computers and smaller devices, changing the lifestyle around the globe. The advance of computational power accelerated progress in industry and science, and the portability of devices brought smart-phones into the daily private as well as professional life. New ideas and concepts are based on future electronic devices being able to provide even more portability and computational power. Examples of these concept are the internet of things or artificial intelligence. The route to enhance the characteristics of electronic devices in the semiconductor industry is based on the downscaling of the devices, which enabled smaller and better transistors. This behavior was described by Gordon Moore, stating that the number of transistors in a circuit is doubled every two years. [1] However, this trend is approaching the physical limit and for further progress new concepts and materials, aside from the Si based transistor have to be developed. Here, oxide based electronics are a promising candidate to develop highly functional devices which bring the advantage of combining the properties of different materials into one device. With this approach, e.g. logical devices are made possible which also function as a memory. [2,3] Another example is the field of quantum computing, where the low temperatures permit the complex physics of oxides to be exploited. [4,5] Furthermore, the electrical tunability of oxide properties make them especially interesting for the development of neuromorphic computing. [6,7]

In the field of oxide electronics, the scientific interest in transition metal oxides and especially their interfaces has grown tremendously over the last decades. Their complex behavior and unique capability to change electronic properties depending on the highly correlated electronic structure of the system has led to a vast array of possible applications. Therefore, they pose an ideal candidate to build highly functional devices, introducing complex physics into the circuits of modern day electronics. [8–10] The electrical properties of oxides depend on their ionic constitution, of which a variety of states can be achieved at room temperature. This makes it possible to manipulate the state of an oxide over short time scales at elevated temperatures, while still being able to exploit the set state for a prolonged duration at room temperature. Their new functionalities in combination with the possibility to manipulate them, make oxide heterointerfaces an opportunity to overcome current problems in advancing electronic systems. Examples are the approaching limit of down-scaling or the challenges of the increasing power consumption by the ever increasing amount for electronic

devices. [11, 12]

One of the very promising candidates for the generation of oxide devices is the LaAlO$_3$/SrTiO$_3$ (LAO/STO) system, which holds a remarkable range of electronic properties. [13] Between the two band-gap insulators, a 2-dimensional electron gas (2DEG) is formed at the interface. The system's inherent structure makes it ideal to use in all oxide field effect transistors. [14–16] However, the properties of the LAO/STO system extend much further from being just a gate-tunable 2DEG. The presence of ferromagnetism could be observed [17] as well as superconductivity. [18] Most astonishingly, both of these usually exclusive properties were found in one and the same sample. [19, 20] Furthermore, both of these properties can be tuned by gating, making LAO/STO an example of the achievable enhanced functionality proposed for oxide electronics. [21, 22] The tuning capability of LAO/STO, makes it highly interesting for spintronics applications as well. [4, 23, 24]

The details on the origin of the LAO/STO conductivity as well as its properties are a highly debated topic since its discovery. After years of research, it is clear that a complex interplay of phenomena is present at this interface. The proposed models reach from the incorporation of oxygen vacancies [25–28] to the intermixing of cations across the interface, [29, 30] to the influence of oxygen octahedral rotations [31–33] to electron donating surface states. [34–36] All take part in shaping the exact properties of the LAO/STO heterostructure. Still, the general understanding of this system is lead by a purely electronic approach and if ionic defects are considered, they are assumed to be fixed after thin film fabrication. As the 2DEG in LAO/STO is residing on the STO side of the interface, the inherent properties of STO are essential for the understanding of the interface. [37] The defect chemistry of STO, is mostly neglected in the LAO/STO framework, especially the role of Strontium. In this context, typically only oxygen vacancies are considered which resemble the most important defect species. However, also cation vacancies, Sr in particular, play an important role for the electronic properties of the material. Only a few studies take them into consideration, [38–40] even though they play a major part in describing the defect chemistry of STO. [41] This comes from the fact that bulk derived diffusion coefficients seem too low to enable cation motion, but recent studies have shown that at surfaces this situation can be different with highly accelerated cation movement. [42]

The focus of this thesis, is the analysis of LAO/STO by *in-situ* methods to elucidate the impact of interface chemistry on the systems electronic and magnetic properties. This is approached in two ways as is sketched in Figure 1.1. In the first approach, the vertical direction is analyzed (left hand side of Figure 1.1), by the application of thermodynamic annealing to trigger ionic motion at the interface. Until now, experiments which consider Sr ions to play a role were mostly of indirect nature, monitoring LAO/STO conductivity in thermodynamic equilibria. The work done here will expand on the previous results and apply more direct measurement techniques. Through the analysis of LAO/STO heterostructures via X-ray photoelectron spectroscopy under applied thermodynamic equilibrium, the change of interface chemistry is elucidated. The second approach considers the lateral direction by analyzing the homogeneity of the 2DEG via scanning probe techniques (right hand side of Figure 1.1). One known factor for the interfacial conductivity of the 2DEG is the termination of the STO substrate. Only TiO$_2$-terminated STO surfaces are commonly observed to provide
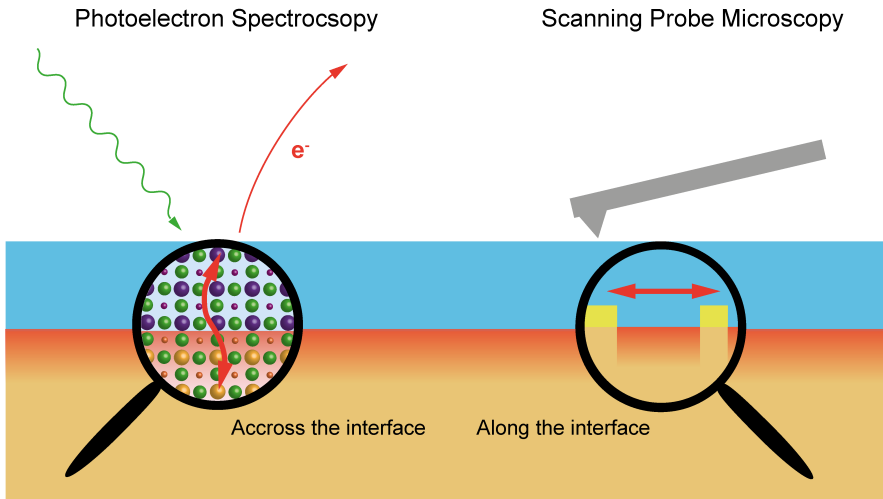
**Figure 1.1:** The twofold approach of the thesis to analyze influences on the electrical properties of LAO/STO are sketched. The respective main methods used for characterization are included in the sketch.

conducting LAO/STO interfaces. [13, 43–45] The role of local inhomogeneities in the form of SrO-terminated regions is going to be investigated to identify where SrO resides on STO surfaces, if a local 2DEG is achieved by the termination distribution and, if this interface chemistry can be used to manipulate 2DEG properties. In both of these approaches, the electrical and magnetic properties of the 2DEG are characterized to determine the macroscopic changes of functional interface properties induced by the alteration of the local interface chemistry.

**Outline of this thesis**

The two main materials used in this thesis (STO and LAO) are going to be shortly described in chapter 2.1 and 2.2 respectively. The scientific background of the LAO/STO system needed for the understanding of this work is going to be explained in detail in chapter 2.3. This will be followed in chapter 2.4, by an in depth discussion on the influence of STO defect chemistry on defect concentrations at its interfaces. The experimental methods that were used to gain insight into the systems properties will be introduced in chapter 3. Therein, also the most important aspects about the data analysis are discussed. The details of the growth process of LAO thin films are summarized in chapter 4.1. In this context, also the STO substrate treatment is discussed in chapter 4.2, as it impacts the stacking order of grown thin films and, therefore, the electronic properties of the system. To elucidate how LAO/STO properties can be manipulated by LAO growth parameters, the influence of growth pressure on the STO reduction behavior and laser fluence on LAO stoichiometry are discussed in chapter 4.3 and 4.4 respectively. To manipulate the STO termination, an SrO PLD growth process was used, which is discussed in chapter 4.5. Chapter 5 is going to address the lateral approach, looking along the interface, using scanning probe techniques. Here, the

local formation of the 2DEG in LAO/STO due to its interface chemistry is analyzed. A mapping of the LAO/STO 2DEG is achieved by using *in-situ* conductive atomic force microscopy and scattering-type scanning near-field optical microscopy. The different extends of inhomogeneity and their influence on low-temperature transport are going to addressed. Regarding the evolving defect structure upon thermodynamic annealing, high temperature conductivity measurements are used to analyze the defect chemical constitution of LAO/STO interfaces in chapter 6. These results form the basis and motivation for the more extensive experiments performed in near-ambient pressure photoelectron spectroscopy experiments, which are discussed in chapter 7. Therein, the interface chemistry of the LAO/STO system under thermodynamic equilibria is going to be unraveled. These changes of interface chemistry, also affect the magnitude of ferromagnetism at low temperatures. This behavior and the distinct changes through the combination of stoichiometry and thermodynamic annealing are discussed in chapter 8. The generalized understanding gained from experiments is going to be discussed and summarized in chapter 9. Following the presented twofold approach (along and across the interface), this includes an analysis on how the local distribution of the 2DEG is influenced by its interface chemistry (direction along the interface). Furthermore, a thermodynamic model of ionic motion across the interface is deduced that links the observed electrical changes to the interfaces defect structure (direction across the interface).

# Chapter 2

# Background

The material system studied in this thesis will be introduced in this chapter. First, $SrTiO_3$ and $LaAlO_3$ will be introduced in general. Second, the combined system $LaAlO_3/SrTiO_3$ and its properties will be discussed in more detail. At last, the defect chemistry of $SrTiO_3$ will be explained and its implications for the interface chemistry of $LaAlO_3/SrTiO_3$ will be discussed.

## 2.1   Strontium titanate

Strontium titanate belongs to the ternary transition metal oxides with the chemical formula of $SrTiO_3$ (STO). The crystal structure is of the perovskite type with a cubic lattice parameter of 3.905 Å. [46] A sketch the unit cell (uc) structure of STO is shown in Figure 2.1. STO is an ionic crystal, where oxygen is the anion with a charge of -2. The cations are Strontium and Titanium which are fully ionized with a charge of +2 and +4 respectively. Oxygen is placed on the face centered sites of the cube, forming an octahedral lattice. Titanium is located in the center of the cube, in the center of
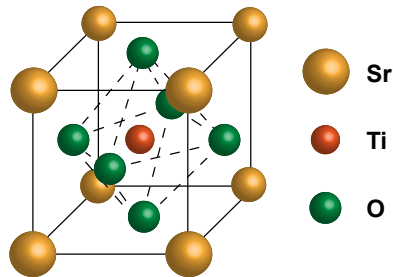


**Figure 2.1:** The crystal structure of a STO unit cell is shown.

the oxygen octahedra. Strontium sits on the corners of the cube. This leads to a coordination number of 8 for Ti and of 12 for Sr. A special property of STO is its mixed ionic and covalent bonding which influences its electronic structure. While the Sr-O bond is ionic, the Ti-O bonds shows covalent bonding. [47, 48] The valence bands of STO are mainly comprised of O $2p$ orbitals, with a contribution from the Ti $3d$ orbitals for energetically deeper states. [48] The conduction band is comprised of the empty Ti $3d$ states which due to their covalent bond to O is hybridized with the O $2p$. This bonding in combination with the fact that Ti is surrounded by eight O ions, leads to a crystal field effect that lifts the fivefold degenerate states of the Ti $3d$ orbitals into two bands, a high energy band ($e_g$) and a low energy band ($t_{2g}$).

The band structure further changes when the system is cooled down. STO undergoes a tetragonal transition at 105 K, which is caused by an antiferrodistortive rotation of the oxygen octahedra by 2.1° in STO. [49–52] However, in the particular case of STO also a ferroelectric type distortion of the lattice is possible. [53] The exact interplay of the two effects is complex and a topic of current research. [49] Another factor is the dielectric function of the STO, which is strongly temperature dependent. [54] As the band structure of STO depends on its crystal symmetry, these structural changes lead to a highly complex behavior of the STO band structure to low temperatures. When combined in an interface, the increasing dielectric constant adds to this complexity by widening interfacial confinement of charge. Furthermore, even though STO is a band gap insulator with a band gap energy $E_g$ of 3.2 eV, [55] conductivity can be induced by extrinsic doping as well as through self doping effects. [41, 56] The latter is enabled by the electronic compensation of intrinsic ionic defects, such as oxygen vacancies which act as donors in STO. The combination of highly changeable carrier concentration with its richness in electronic structure leads to a highly complex behavior making it interesting for a variety of fields. First, the mixed ionic and electronic conductivity makes it interesting for fuel cell applications, as well as for mixed ionic-electronic conductors. Second, the complex electronic behavior makes it suitable for certain fields in oxide electronics such as spintronics or for the study of highly correlated physics phenomena. As it is very well researched, has a wide variety of properties and is commercially available, STO is one of the most commonly used substrates for the growth of oxide heterostructures in the research field of oxide electronics. [10, 57, 58]

## 2.2    Lanthanum aluminate

Lanthanum aluminate belongs to the rare earth aluminates, having the chemical formula of LaAlO$_3$ (LAO). The crystal structure is rhombohedral but can be described by a distorted perovskite structure with a pseudocubic lattice parameter of 3.788 Å. As in STO, the oxygen anions are twofold ionized and form a octahedral lattice, occupying the face centers of the cube. Aluminum cations sit inside this octahedra in the center of the cube and have a charge of 3+. The corners are occupied by the Lanthanum cations with a charge of 3+. The material is used in context of the LAO/STO heterointerface
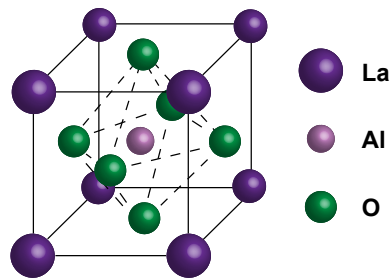


**Figure 2.2:** The crystal structure of a LAO unit cell is shown.

where it is grown on STO, but also as substrate material for epitaxial growth and was considered as a high-k dielectric for the replacement of SiO$_2$. Like STO, this material is a band gap insulator with an $E_g$ of 5.6 eV. [59]

## 2.3 The LaAlO$_3$/SrTiO$_3$ system

The two-dimensional electron gas (2DEG) in LaAlO$_3$/SrTiO$_3$ (LAO/STO) heterostructures was first discovered by Ohtomo and Hwang in 2004. [13] Both of the used materials are high band gap insulators, but through deposition of LAO on TiO$_2$-terminated STO (*n*-type interface), the heterostructures show metallic conductivity down to low temperatures. In the low-temperature regime, mobilities in the range of 1000-10000 cm$^2$/Vs are observed, [60] which is high compared to mobilities in doped STO with similarly high carrier densities. [61] Later it was discovered that during growth of the thin films, a significant amount of oxygen vacancies is introduced, which lead to additional conductivity but can be removed via annealing. [62] If such an annealing is applied, a sharp transition from insulating to conducting interfaces is achieved when the fourth unit cell of LAO is deposited. [63] In contrast, interfaces where LAO was deposited on SrO-terminated STO (*p*-type interface) turn out to be insulating.

This behavior can be explained by an electronic reconstruction process induced through the polarity mismatch between the two oxides. [13] A sketch of this process is shown in Figure 2.3 in analogy to Ref. [64]. Envisioning a stack of LAO/STO in (001) direction the atomic planes can be seen as SrO, TiO$_2$, LaO and AlO$_2$. The charges for the subsequent layers can be calculated as follows: Sr$^{2+}$ + O$^{2-}$ = 0, Ti$^{4+}$ + 2O$^{2-}$ = 0, La$^{3+}$ + O$^{2-}$ = +1 e, Al$^{3+}$ + 2O$^{2-}$ = -1 e. Therefore, LAO is seen as a polar oxide where charge alternates from plane to plane in the (001) direction and STO is seen as a non polar oxide where every plane holds the same amount of charge. For a *n*-type interface (Figure 2.3a), where an interfacial stacking of TiO$_2$/LaO is present, the integration of these charges ($\rho$) leads to a positive electrical field (*E*). A further integration leads to a positive potential (*V*), diverging for thicker LAO layers. To compensate this diverging potential, half an electron per areal unit cell is transferred to the interface. The transferred charge residing at the interface shifts the starting point of the resulting electrical field and ultimately leads to a non-diverging potential (Figure 2.3c).

The same line of thought can be carried out for the *p*-type interface, where the interfacial stacking of SrO/AlO$_2$ is present. In this case, a negative, diverging potential would theoretically induce the transfer of half an electron per areal unit cell to the surface of the LAO layer and the formation of a hole gas. A few experiments have shown that this theoretically proposed hole gas can be achieved in practice [65], however, the vast majority of *p*-type interfaces turn out insulating. [13, 43–45, 64] This behavior is commonly explained by a preferred ionic defect compensation of the diverging potential via oxygen vacancy formation. [66] The typical absence of hole conductivity shows how the polar discontinuity model is able to illustrate an important driving force of electronic charge transfer, but fails to describe the more complex reality. From the purely electronic model, also the LAO surface should show hole conduction, which is also not the case, as the positive surface charge is compensated by the incorporation of oxygen vacancies. [67–70] However, hole conduction could be achieved by capping the surface with an additional STO layer, preventing ionic compensation. [71] Therefore, the polar discontinuity model is an important aspect to understand charge transfer processes in LAO/STO, but oxides in general have the ability to compensate charge ionically, [41, 72] which has to be taken into account.
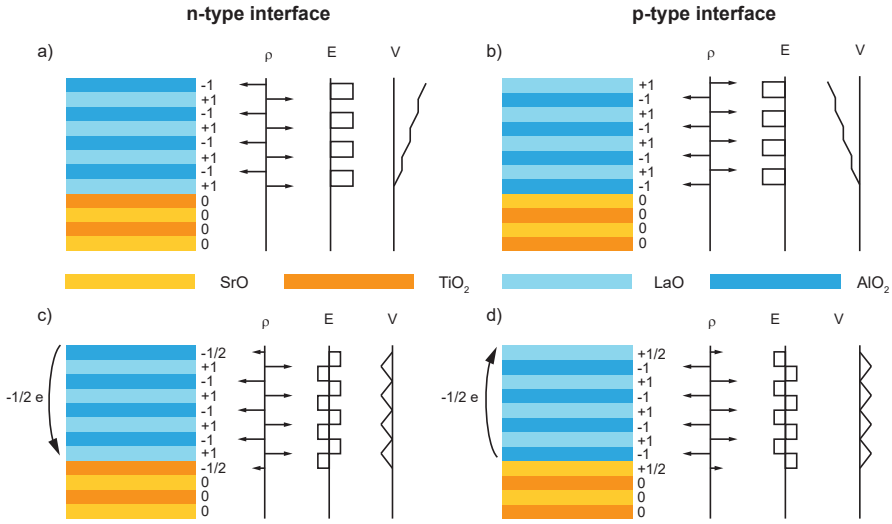
**Figure 2.3:** Sketches explaining the theory of polarity mismatch induced charge transfer are shown from charges to electrical field to resulting potential. a) Shows a stack of LAO on TiO$_2$ terminated STO (n-type). b) Shows a Stack of LAO on SrO terminated STO (p-type). c) Shows the electric charge transfer compensating the voltage for n-type LAO/STO. d) Shows the electric charge transfer compensating the voltage for p-type LAO/STO.

The LAO/STO interface holds more properties than charge transfer phenomena. For oxides, a remarkably high mobility (10.000 cm$^2$/Vs) can be achieved, [60] but especially at low temperatures more phenomena arise due to the unique properties of STO (see chapter 2.1). Here, the LAO/STO 2DEG becomes ferromagnetic, [17] or even superconducting (below $\approx$ 200 mK). [18] Most remarkably both properties were discovered in one and the same sample, [19] which is a rare observation only seen in a few other materials [73]. Superconductivity is usually explained by the pairing of two electrons to a Cooper pair [74], transitioning them from a fermion to a boson, which is not subjected to the local band structure. Magnetism is explained by localized spins aligning in the same direction [75]. Therefore they are treated as contradicting properties, which can only coexist under special circumstances. On top of these intriguing phenomena the conductance as well as the superconductivity of LAO/STO are gate-tunable, [22] which opens the possibility to study the interplay between charge carrier concentration and superconducting states. [76, 77] The gate-tunable properties of the LAO/STO system made it also especially interesting for the spintronics applications. [4, 8, 23, 24] For these purposes the heterostructure has to be patterned, which is possible by an array of methods. A common approach is to apply hard mask lithography by growth of AlO$_2$. [78] However, also the inherent properties of the metal to insulator transition of LAO/STO can be used as patterning technique in the nanometer range. Conductive atomic force microscopy has been used to locally transition LAO/STO heterostructures of 3 uc, which is just below the thickness of electronic reconstruction, to the conducting state. [79, 80] A similar effect

was achieved by using electron beam lithography. [81] The reverse process can also be used to pattern the 2DEG, where 4 uc LAO/STO are covered with a patterned photoresist and milled down, using an Ar ion beam. [82]

**Controversy about the true origin of conductivity**

As can be seen in the discussion above, the properties of LAO/STO are extremely diverse and its physical origins are debated since its discovery. The polar discontinuity model described above is not the only way to explain the conduction observed in LAO/STO. Because Lanthanum is a well known donor for STO, [56] the interfacial conductivity observed could also be a mere intermixing effect of a smeared interface. Multiple reports show the detection of intermixing at the LAO/STO interface and interpret resulting implications. [29, 30, 83] On one hand, this body of data shows that in reality intermixing plays a crucial part in understanding the details of the diverse properties of the LAO/STO interface. On the other hand, the very consistently observed insulator to metal transition at 4 uc LAO, [84] cannot be easily explained by this model. Another model is based on the role of oxygen vacancies for the system. The conductivity of samples grown in low oxygen pressure is dominated by the presence of oxygen vacancies. [85] This reduction of the STO crystal stems from the chemical reaction of the laser plume with the STO crystal and is specific to the ablated material as could be shown in room temperature deposition series with different materials. [86] However, while amorphous LAO/STO structures are dominated by oxygen vacancy creation and can be turned insulating by an anneal in oxygen, [87] this behavior is not observed for crystalline LAO. [88] In summary, the polarity of the LAO layer remains a key element for the understanding of the heterointerface, while oxygen vacancies and cation intermixing contribute important aspects to the electronic properties.

Another discrepancy of the polar discontinuity model is the predicted carrier density of interfaces. To compensate the electrical field to the point where the polarization of the LAO layer is completely screened, half an electron per areal unit cell has to be transferred into one STO unit cell. This leads to a carrier density of roughly $3.3 \times 10^{-14}$ cm$^{-2}$. In experiment, the reported carrier densities typically fall below this value up to one order of magnitude ($2.2 \times 10^{-13}$ – $2 \times 10^{-14}$ cm$^{-2}$). [13, 63, 89] Also the low-temperature mobility of samples can vary by one order of magnitude. [60] One model which can answer to these discrepancies is to apply the well-known defect chemistry of STO to interface of LAO/STO. Studies have shown that the interface of LAO/STO under applied thermodynamic equilibria behaves quite similar to that of donor doped STO. [39] Therefore, it is considered that the discrepancies of a lowered carrier density and mobility in some LAO/STO samples are caused by the incorporation of Sr vacancies in oxidizing conditions. [40] The role of these thermodynamic equilibria and the influence of Sr on the LAO/STO properties is going to be explored by this work.

**Ionic charge transfer at the interface**

As surfaces and interfaces of materials pose a sudden break of the crystal order, the consequence is often a compensation of charge by space charge regions (SCR), where the system internally compensates the electrostatic potential at its surface/interface. Such

effects are known from semiconductors in the form of *pn*- and Schottky-diodes. Also in oxides, SCR form for various reasons at their surfaces, [42, 90], interfaces [39, 91, 92] and grain boundaries. [93, 94] While in semiconductors, charges are mostly compensated by electrical reordering, oxides have the capability to ionically compensate excess charge. This principle is widely known from the sintering of oxide ceramics, where dopant atoms are often internally compensated by the oxide through this ionic charge transfer. [41, 72] In the context of LAO/STO the 2DEG itself can be considered as a SCR, where the polarity of the LAO thin film is compensated by electrons at the interface. However, the further implications of ionic charge transfer are mostly neglected, considering only oxygen vacancies for the electronic properties of the 2DEG. Only few studies try to encompass the whole picture of the defect chemical model and its implications for the 2DEG. This would include also the presence of cation defects which can compensate negative charge in an oxide. The full perspective of the defect chemistry on LAO/STO is going to be discussed in chapter 2.4.

Considerations of the exact ionic defect constitution are not only interesting from a fundamental point of view, as it is known that the concentration of point defects has a high impact on the electronic properties of the system. First, each ionic defect leads to an alteration of the charge balance of the system. Second, each ionic defect poses a scattering center for electron transport. These two aspects are the most direct influences, however, due to the altered strain field around a point defect, also the structure of the crystal lattice is affected, which in turn also affects the band structure of the system. The presence of cationic point defects, is considered to be also a vital point for the understanding of the highly debated source of magnetism of the LAO/STO interface. [67, 95, 96]

**Lateral (in)homogeneity**

In the commonly applied models, the LAO/STO 2DEG is assumed to be completely homogeneous along the heterostructure. The role of local inhomogeneities is mostly addressed at low temperatures, where the system undergoes a transition to the tetragonal lattice order, or magnetic moments emerge. In the context of resolving the lateral landscape of the heterostructure, scanning probe techniques have been proven to be suitable tools. It could be shown by scanning quantum interference device measurements, that the LAO/STO system is structured in a domain order at low temperatures, due to the tetragonal transition of the STO substrate. [97] Along this domain order, highly conducting pathways form, [98] and a strain tunable magnetic ordering aligns to the domain order as well. [99] At room temperature, anisotropic transport of LAO/STO samples could be induced by an ordered mixed termination of the STO substrate. [100] The surface termination was identified using phase contrast in atomic force microscopy (AFM) measurements. This identification was also applied in other works as well as the contact AFM counterpart, lateral force AFM. [101, 102] Scattering-type scanning near-field optical microscopy could be shown to be able to detect free charge carriers in STO ceramics [103] and also for LAO/STO it could be shown that this technique is able to detect the presence of the 2DEG. [104–106] Kelvin probe force microscopy revealed the influence of oxygen vacancies on the systems band alignment. [107] Magnetic force microscopy was used to show that magnetic moments of the system depend on thickness and carrier density. [108] Also conductive atomic

force microscopy (c-AFM) was applied to write conducting lines into LAO/STO of sub-critical LAO thickness, [79, 109, 110] enabling the use of c-AFM as patterning technique [111] and to study of one dimensional transport phenomena. [112] Even though c-AFM could be shown in these experiments to be able to resolve the conducting nano-wires, it was not used to resolve the homogeneity of the LAO/STO 2DEG. These works show, that a homogeneous interface is not guaranteed and further research in this area could be beneficial for the understanding of the system. In this way, often observed discrepancies like the above mentioned sample to sample variation of carrier density and mobility, could be elucidated. A destruction-free method, that resolves the homogeneity of the system, would be valuable tool in achieving this insight. Therefore, enabling a mapping of the 2DEG, using c-AFM is a further point of focus in this thesis.

## 2.4 The defect chemistry at charge-transfer interfaces

In the scientific field of electronics, one aim is the search for new electronic phenomena in material systems. In this context, charge transfer at oxide interfaces has led to the discovery of a wide range of phenomena which are not present in the bulk of the two components. [10, 113] The wide range of properties emerging in the LAO/STO system alone (see chapter 2.3) shows the richness of possible physical effects arising at such interfaces. The band alignment is changed in LAO/STO and also in other heterostructures like $LaTiO_3/SrTiO_3$ by the transfer of electrons to the STO side. [13, 114] In contrast to semiconductors, oxides can compensate electrical charge by a redistribution of ionic defects. At an interface or surface, the chemical potential is changed compared to the bulk of the material, leading to the formation of space charge regions (SCR), [115] as could be seen at grain boundaries in STO, [93, 94] as well as in donor doped STO. [103] This leads to the accumulation of free electrons at the grain boundaries, as the band alignment is changed close to such interfaces. From these considerations it becomes clear, that the local band alignment and local defect chemistry are closely related, where a change in one will affect the other. However, in the literature, this interplay is often not considered and purely electronic charge compensation models are frequently applied. To give an understanding of the defect chemical reaction of oxide interfaces, the defect chemistry of the bulk phase will be shortly explained in this chapter. A complete description of the STO defect chemistry can be found in the Appendix and in the literature. [41]

In this thesis, point defects will be described by the Kröger Vink notation [116], as is common in the literature. Here, elements denoted by their symbol in the periodic table. Vacancies are written as V. If a defect is negatively charged, a dot is placed in superscript (˙). A positive charge is marked by a ′, while charge neutral elements have a x in superscript (ˣ). The location of an element or vacancy is characterized by the element which occupies the crystal lattice site in a perfect crystal and is marked by the symbol of the respective element in subscript. Free carriers such as electrons and holes are described by an e and h respectively.

In the following, the focus will lie on the behavior of donor-doped STO as it encompasses the most relevant aspects for the later discussion of LAO/STO. The

implications from defect chemical considerations for the LAO/STO system is going to be addressed by first discussing the observed defect concentrations of STO in equilibrium. These considerations will be the basis for a discussion on the influence of interfaces on defect chemistry. At last, the defect chemical equilibria at LAO/STO interfaces and possible kinetic limitations are going to be discussed.

### 2.4.1   Equilibrium defect concentration

In an ionic crystal, each charge (electric or ionic) has to be compensated by a charge of opposite sign. This leads to the charge neutrality condition, which is fulfilled in an equilibrated ionic crystal to minimize electrical fields. As this condition is always fulfilled in a perfect crystal lattice, it is sufficient to only account for the charges of defects rather than all possible charges. In the case of donor-doped STO, the charge neutrality condition can be simplified. First, Ti vacancies are energetically less favorable than Sr vacancies and can therefore be neglected. [56, 117, 118] Second, as electrons are the majority free charge carrier in donor-doped STO, the concentration of holes is very low and their presence can also be neglected. This leads to the charge neutrality condition for donor-doped STO, which reads

$$n + 2[V_{Sr}''] = 2[V_O^{\bullet\bullet}] + [D^{\bullet}] \tag{2.1}$$

Here the denotations stand for the concentration of their respective species and follow the aforementioned Kröger Vink notation: $n$ for electrons, $[V_{Sr}'']$ for Sr vacancies, $[V_O^{\bullet\bullet}]$ for oxygen vacancies and $[D^{\bullet}]$ for donor dopants. When considering defect concentrations in equilibrium, the charge neutrality condition has to be fulfilled. Free charge carriers in donor doped STO are generated by the dopants, which contribute one free electron per atom. At room temperature it can be assumed that the dopants are completely ionized. To determine the minority carrier concentration the STO band gap excitation has to be considered. As STO is a band gap insulator ($E_g$ = 3.6 eV), electron-hole pairs can be generated by

$$e' + h^{\bullet} = 0 \tag{2.2}$$

The excitation process is temperature activated following a law of mass action

$$n \cdot p = N_e(T)N_p(T) \exp\left(-\frac{E_g(T)}{k_B T}\right) \tag{2.3}$$

Here $n$ denotes the concentration of electrons, $p$ the concentration of holes, $N_e$ the density of states (DOS) inside of the conduction band, $N_p$ the DOS inside of the valence band and $E_g$ the band gap. With equation 2.3, the concentrations of free charge carriers can be determined at room temperature. However, as defects inside the crystal lattice also contribute or eliminate free charge carriers, their generation has to be considered. Above 750 K, the oxygen sub lattice becomes active, meaning that the bulk crystal can achieve the equilibrium amount of oxygen vacancies. At lower temperatures, the surface exchange reaction with the surrounding atmosphere limits this equilibration process. [119] The incorporation of oxygen vacancies into the crystal is described by

$$O_O^x \rightleftharpoons \frac{1}{2}O_2(g) + V_O^{\bullet\bullet} + 2e' \tag{2.4}$$

Here $\frac{1}{2}O_2(g)$ denotes gaseous oxygen from the surrounding atmosphere. One oxygen vacancy releases two electrons into the crystal lattice, as they are double ionized. In principle also singly ionized or neutral oxygen vacancies can occur but due to their very small ionization energies, they are only relevant at low temperatures [120]. The change in concentration of oxygen occupying the oxygen lattice ($O_O^x$) is small, so it can be assumed to stay constant. With this assumption, a corresponding law of mass action for equation 2.4 can be written as

$$[p(O_2)]^{\frac{1}{2}}[V_O^{\cdot\cdot}]n^2 = K_0^{red}\exp\left(-\frac{\Delta H_{red}}{k_B T}\right) \tag{2.5}$$

Here, $p(O_2)$ describes the oxygen partial pressure, $K_0^{red}$ the reaction constant and $\Delta H_{red}$ the activation enthalpy of the reduction reaction. Equation 2.5 gives the means to describe how electron concentration and oxygen vacancy formation correlate under certain temperature and $pO_2$. In analogy the inverse process (oxidation reaction), can be derived in the same way to describe the interplay of the hole concentration with the oxygen vacancy concentration and oxygen partial pressure (see Appendix).

When the temperature is further increased above 1250 K, the cation lattice becomes active, enabling the formation of Schottky defects, which are defined as the complete removal of a unit cell. As mentioned above, the role of Ti vacancies is negligible, meaning that the formulation of a partial Schottky defect is sufficient to describe the cation reaction in STO. It can be written as
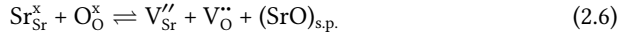
$$Sr_{Sr}^x + O_O^x \rightleftharpoons V_{Sr}'' + V_O^{\cdot\cdot} + (SrO)_{s.p.} \tag{2.6}$$

Assuming the amount of crystalline species, namely $Sr_{Sr}^x$, $O_O^x$ and SrO, to be constant the corresponding law of mass action reads

$$[V_{Sr}''][V_O^{\cdot\cdot}] = K_0^S\exp\left(-\frac{\Delta H_S}{k_B T}\right) \tag{2.7}$$

From equation 2.5, it can be seen that the oxygen vacancy concentration is $pO_2$ dependent in STO, influencing the concentration of free electrons in the system. As the concentration of Sr vacancies is connected to the oxygen vacancy concentration (see equation 2.7), their concentration also becomes $pO_2$ dependent and in turn also impacts the electron concentration. The complete behavior can be best summarized in a so called Brouwer-diagram, where the defect concentrations are plotted over $pO_2$ on a double logarithmic scale. The corresponding Brouwer-diagram for donor-doped STO with an active anion lattice is shown in Figure 2.4a.

In very reducing conditions the conductivity is dominated by oxygen vacancies, leading to the charge neutrality condition of

$$n \simeq 2[V_O^{\cdot\cdot}] \tag{2.8}$$

Inserting this condition into equation 2.5 leads to

$$n = (pO_2)^{-\frac{1}{6}}(2K_0^{red})^{\frac{1}{3}}\exp\left(-\frac{\Delta H_{red}}{3k_B T}\right) \propto (pO_2)^{-\frac{1}{6}} \tag{2.9}$$

Therefore, the electron concentration is proportional to the oxygen partial pressure to the power of -1/6, leading to the observed slope in the Brouwer-diagram in reducing conditions (Figure 2.4a). When the oxygen vacancies are being refilled to higher $p\mathrm{O}_2$, their concentration is decreased below the dopant concentration. This changes the charge neutrality condition to

$$n \simeq [D^{\bullet}] \tag{2.10}$$

This fixes the electron concentration, leading to no observable change in the conductivity for higher $p\mathrm{O}_2$. The oxygen vacancy concentration can be determined by inserting equation 2.10 into 2.5, which leads to

$$(p\mathrm{O}_2)^{\frac{1}{2}}[V_{\mathrm{O}}^{\bullet\bullet}][D^{\bullet}]^2 = K_0^{\mathrm{red}}\exp\left(-\frac{\Delta H_{\mathrm{red}}}{\mathrm{k_B}T}\right) \implies [V_{\mathrm{O}}^{\bullet\bullet}] \propto (p\mathrm{O}_2)^{-\frac{1}{2}} \tag{2.11}$$

The oxygen vacancy concentration therefore drops to the power of -1/2 without influencing the electron concentration. However, when the cation lattice is activated this changes due to equation 2.7. Under an active Schottky equilibrium, the dropping oxygen vacancy concentration leads to a rising Sr vacancy concentration to the power of 1/2. This behavior is shown in the Brouwer-diagram in Figure 2.4b. The Sr vacancy concentration rises until they start to compensate the dopants, leading to a new charge neutrality condition of

$$2[V_{\mathrm{Sr}}''] = [D^{\bullet}] \tag{2.12}$$

This fixes the Sr vacancy concentration and the oxygen vacancy concentration (see equation 2.7). A fixed oxygen vacancy concentration in equation 2.5 leads to an electron concentration that drops with $p\mathrm{O}_2$ to the power of -1/4. This leads to the behavior of the conductivity as it is sketched in Figure 2.4c. In reducing conditions the conductivity is dominated by oxygen vacancies and depends on $p\mathrm{O}_2$ to the power of -1/6. In intermediate pressure a plateau region is reached and to oxidizing conditions the conductivity drops to the power of -1/4 due to the compensation by Sr vacancies.

### 2.4.2   Influence of interfaces on defect chemistry

In the previous chapter, the defect chemistry of bulk STO crystals was explained at the example of donor-doped STO. Interfaces in the form of the crystal surface, [122] grain boundaries [93] or to another material [91] pose a disruption of the perfect crystal lattice leading to a changed chemical potential at such interfaces opposed to the bulk. [94] This inevitably changes the formation energy of defects close to such interfaces. The effect was first observed at grain boundaries in acceptor-doped STO by impedance spectroscopy, showing a depletion of holes due to the formation of oxygen vacancies and a negative space charge layer. [93] The driving force is a lowered Gibbs energy of the oxygen vacancies at grain boundaries [94] and surfaces. [115, 123] Due to this changed Gibbs energy, a similar effect is also observed in Nb doped STO thin films. [123] For these, it could be shown that the observed lowered conductivity with decreasing thin film thickness can be consistently interpreted as an increasing domination of the conductive behavior by the surface near SCR.

As the defect chemistry of donor-doped STO is different to the one of acceptor-doped STO (see Appendix), its interface reaction is also changed. This leads to the
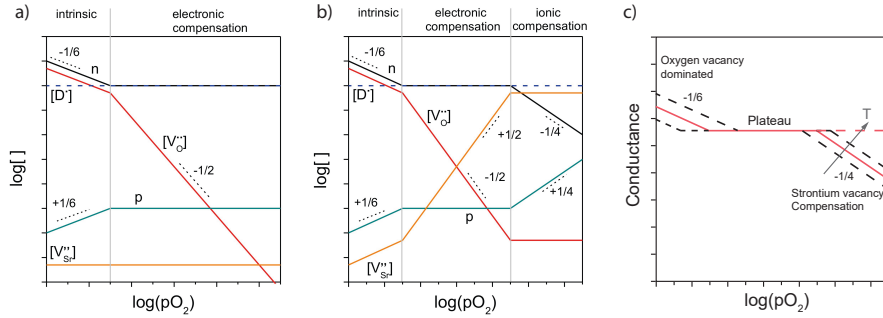
**Figure 2.4:** a) The concentration of defects and charge carriers is plotted over oxygen partial pressure in donor doped STO. b) The concentration of the same defects and charge carriers is shown as in a) but in an active Schottky equilibrium. c) The resulting conductance dependence on oxygen partial pressure of donor doped STO through the changes in carrier densities is sketched as red line. The conductance behavior without active Schottky equilibrium is shown as red dashed line. An indication of the temperature dependence is included as black dashed lines. By courtesy of Ref. [121].

depletion of electrons at interfaces instead of an accumulation (depletion of holes). [56, 103] In this case, the incorporation of Sr vacancies upon oxidation instead of oxygen vacancies is responsible. [118, 122] For the reaction of the Sr sub lattice with surrounding oxygen equation 2.6 can be expressed as

$$V''_{Sr} + (SrO)_{s.p.} \rightleftharpoons \frac{1}{2}O_2 + Sr^x_{Sr} + 2e' \tag{2.13}$$
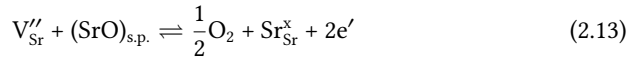
Therefore, the formation of Sr vacancies is an electron depleting effect, as can be also seen in the equilibrium of donor-doped STO (see Figure 2.4b). If the formation energy of Sr vacancies is lowered in respect to the bulk material, a positive space charge region of lower conductivity would develop. In the literature, this consideration is mostly disregarded due to the low diffusion coefficient of Sr vacancies. [124] For this reason, the Sr vacancy formation is usually only considered for high temperatures above 1250 K. [41, 125] However, simulations of the defect chemical behavior on Nb doped STO show that the oxidation induced depletion of electrons at high temperature can be rather fast in the near surface region. [126] The principle of this behavior is shown in Figure 2.5. In the initial state, the whole sample (surface and bulk) has the same concentration of dopants, defects and electrons (Figure 2.5a). As the precipitation of Sr is depending on the surrounding oxygen atmosphere (see equation 2.13), a precipitation of Sr under incorporation of Sr vacancies is facilitated through higher $p$O$_2$ (Figure 2.5b). Over time, the Sr vacancies diffuse into the bulk, extending the SCR (Figure 2.5c). Due to the electron depleting nature of Sr vacancy formation (see equation 2.13), electrons and Sr vacancies behave inverse to each other. This results in the formation an electron depleting negative SCR at the STO surface. Therefore, the SCR is an effect resulting from thermodynamic equilibria due to the preferred SrO phase of Sr. Using near ambient pressure X-ray photoelectron spectroscopy (NAP-XPS, for details of the method, see chapter 3.6), the reaction of the Sr lattice to the surrounding $p$O$_2$ could be
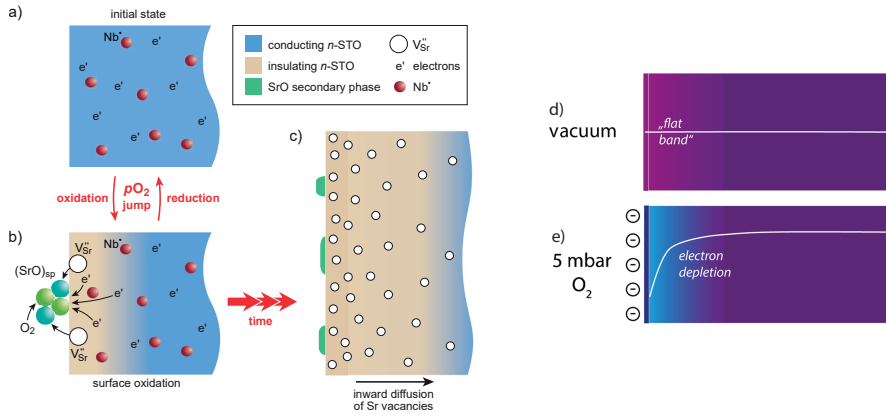
**Figure 2.5:** The formation of a SCR at the surface of Nb doped STO is shown. a) Shows the initial state (reducing atmosphere). b) Shows the oxidized state, where Sr precipitates on the STO surface (oxidizing atmosphere). c) Shows the inward diffusion of Sr vacancies over time. The SCR of a Nb:STO surface, deduced from NAP-XPS experiments is shown in d) in vacuum and in e) in oxygen pressures of 5 mbar. The sub-Figures a-c are by courtesy of Ref. [126]. The sub-Figures d-e are by courtesy of Ref. [42].

verified to be present already at temperatures of 670 K. [42, 90] The behavior of the surface band alignment as deduced from binding energy shifts in NAP-XPS is shown in Figure 2.5d and e. Here, the Sr ions leave the bulk crystal lattice under the formation of a positive SCR, as predicted by the literature. [126] In vacuum (Figure 2.5d), a flat band scenario is observed, where surface and bulk of the sample exhibit similar defect concentrations (Figure 2.5a). Upon introduction of oxygen, the predicted positive SCR (Figure 2.5a) forms under reconstruction of the Sr sublattice, leading to an electron depletion (Figure 2.5e). Furthermore, simulations based on these results showed that the shape of SCR can be effectively tuned by the anneal in varying $pO_2$. [127]

### 2.4.3   Kinetic limitations at the LAO/STO interface

The discussed results show that in principle the movement of Sr close to a surface can be much faster than expected from bulk experiments. Furthermore, it could be seen that defect structure and SCR show a distinct interplay, where charge is redistributed by defect formation leading to the formation of an SCR. Also at interfaces the formation of SCRs is used to apply defect engineering and manipulation of electronic properties. An example is the use of an SrO layer in $La_{2-x}Sr_xCuO_4$. [128] Here, the insertion of SrO leads to the formation of a negative SCR attracting holes which form a superconducting layer. At all of the mentioned interfaces (grain boundaries, surfaces, heterointerfaces), charge redistribution leads to the formation of intrinsic defects, which influence the electronic properties of the system. In the case of LAO/STO, the system already exhibits an SCR, due to the transferred electrons caused by the polarity of the LAO layer. Considering the thermodynamic equilibrium SCR present in donor doped STO, a $pO_2$ dependent SCR can be expected in LAO/STO. In other words, as the described SCR

in STO are a consequence of defect formation, an already present SCR should have an impact on the equilibrium concentration of defects in LAO/STO. This is due to the strong electrical fields present, which should enhance the formation of Sr vacancies at the interface.

The possibility of Sr vacancy formation at an LAO/STO interface is already considered in the literature. [39,40,92] The interplay between an SCR and defect concentration profiles can be described by using the electrochemical potential of a defect ($\eta_{\text{def}}$) and the local electrostatic potential ($\phi(x)$) stemming from the SCR. A formalism for this purpose is deduced in Ref. [40], where $\eta_{\text{def}}$ is first expressed in a general form as

$$\eta_{\text{def}} = g_{\text{def}} + k_B T \ln \left( \frac{c_{\text{def}}(x)}{N_{\text{def}} - c_{\text{def}}(x)} \right) + z_{\text{def}} e \phi(x) \tag{2.14}$$

Here $c_{\text{def}}(x)$ denotes the defect concentration at a distance $x$ from the interface, $g_{\text{def}}$ the standard defect formation energy, $N_{\text{def}}$ the number of available lattice sites per volume, $z_{\text{def}}$ the defects charge number and $e$ the elementary charge. Assuming $g_{\text{def}}$ to be independent from the distance to the interface and using the bulk equilibrium concentration of defects far away from the interface ($c_{\text{def}}(\infty) = c_{\text{def}}^{\text{b}}$), equation 2.14 can be solved for $c_{\text{def}}(x)$

$$c_{\text{def}}(x) = \frac{c_{\text{def}}^{\text{b}} \exp \left( \dfrac{- z_{\text{def}} e \phi(x)}{k_B T} \right)}{1 + \dfrac{c_{\text{def}}^{\text{b}}}{N_{\text{def}}} \left( \exp \left( \dfrac{- z_{\text{def}} e \phi(x)}{k_B T} \right) - 1 \right)} \tag{2.15}$$

Equation 2.15 shows the relation between SCR and equilibrium defect concentration and can be applied to the different defect species such as, electrons, holes, oxygen vacancies and strontium vacancies.

However, vacancy formation at a heterostructure might be kinetically limited, preventing the system to reach thermodynamic equilibrium. The interface exchange of Sr could be slow and effectively block Sr vacancy formation as is seen in the case for oxygen vacancy formation, when the temperature is not sufficiently high. [119] In turn, the region of interfacial conductivity is highly confined in LAO/STO. [37] Therefore, also kinetically limited scenarios already result in strongly changed electron concentrations at the interface. [40] The principle of these considerations as deduced from simulations using thermodynamic modeling is shown in Figure 2.6. Under an electrostatic potential (φ) shown in Figure 2.6a, the system reacts by accumulating negative charges and repelling positive charges. Therefore, close to the interface electrons are accumulated (Figure 2.6b), holes and oxygen vacancies are depleted (Figure 2.6c-d). For Sr vacancies, three cases are considered, an unhindered case (Figure 2.6e), a kinetically limited case (Figure 2.6f) and an immobile case (Figure 2.6g). While Sr vacancies can move into the bulk in the unhindered case, their formation is limited to the first unit cell of the STO crystal at the interface in the kinetically limited case. In the immobile case, no Sr vacancy formation is allowed at all. Only in the immobile case, no influence of the surrounding $p\text{O}_2$ on the electron concentration could be seen. In the kinetically limited case, the 2DEG is depleted by the presence of Sr vacancies, which is shown in Figure 2.6h. Even though Sr vacancies are only
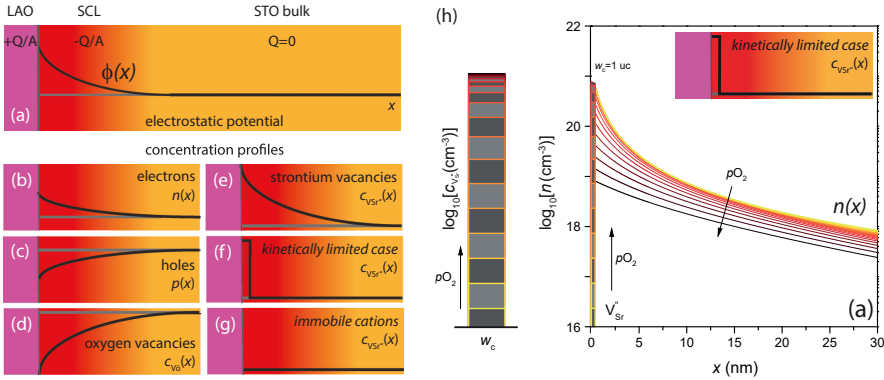
**Figure 2.6:** Simulations of the defect concentrations using a thermodynamic model are shown. (a) Shows the electrostatic potential at an LAO/STO interface. The resulting equilibrium concentrations of electrons (b), holes (c) and oxygen vacancies (d) are shown. For the Sr lattice, three cases are considered: Unhindered Sr vacancies (e), kinetically limited Sr vacancies (f) and immobile Sr vacancies (g). The electron concentration under varying $p$O$_2$ for the kinetically limited case is shown in (h). By courtesy of Ref.: [40].

present in the first unit cell, the electron profile is significantly changed. The electron concentration shows a distinct dependency on the surrounding atmosphere, where the curve is shifting to lower electron concentrations with increasing $p$O$_2$. At the same time, an increasing concentration of Sr vacancies is present in the first unit cell. The resulting electron profiles explain the observed $p$O$_2$ dependence in high temperature equilibrium conductance (HTEC) measurements, where the equilibrium conductivity is recorded under applied thermodynamic conditions. [39] In turn, if the Sr lattice would be completely inactive, no $p$O$_2$ dependence at all would be expected.

A comparison of simulated and experimentally determined conductances is shown in Figure 2.7. In Figure 2.7a, the sheet carrier density ($n^s$) is calculated under the influence of the rising equilibrium sheet concentration of Sr vacancies ($c^s_{V''_{Sr}}$). As discussed in chapter 2.4, $c^s_{V''_{Sr}}$ rises to the power of 1/2 in oxidizing atmosphere. When they reach a concentration close to the electron concentration, $n^s$ drops to the power of -1/4 (see also chapter 2.4.1). The resulting equilibrium $n^s$ under varying temperatures are shown in Figure 2.7b. As the formation of an Sr vacancy is an exothermic process, $n^s$ is less lowered for higher temperatures. The $p$O$_2$ dependency in oxidizing conditions from HTEC experiments is shown in Figure 2.7c. In oxidizing conditions, a depletion of electrons is observed, which follows the power of -1/4 when LAO/STO bilayers on LSAT are used. These samples are in very well agreement with the proposed mechanism. Also for pure LAO/STO heterostructures, a lowered $n^s$ in oxidizing is observed although to a much lower extend. This discrepancy can be explained by the increasing conductance of the STO substrate in these thermodynamic equilibria (see Appendix). In these thermodynamic conditions, the STO substrate becomes increasingly $p$-type conducting, which overshadows the 2DEG conductance.

In summary, the formation of Sr vacancies, driven by the electrostatic potential of the LAO/STO interface, can explain the observed $p$O$_2$ dependence of the LAO/STO
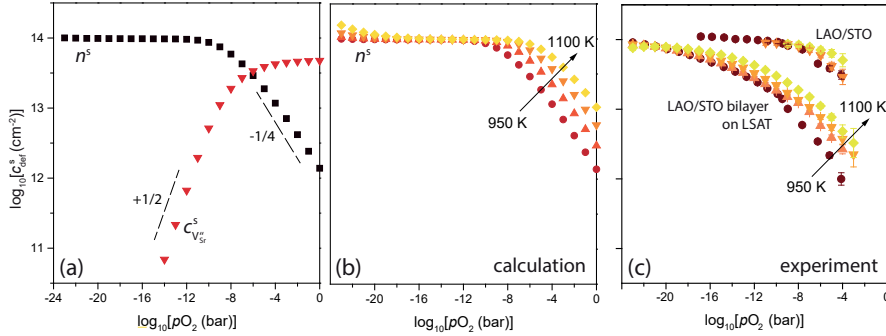
**Figure 2.7:** (a) Shows the equilibrium sheet carrier density ($n^s$) and sheet concentration of Sr vacancies ($c^s_{V''_{Sr}}$) over $pO_2$. (b) Shows the calculated sheet carrier densities over $pO_2$ under varied temperatures. (c) Shows HTEC experiments of conducted on LAO/STO bilayers on LSAT and LAO/STO heterostructures. By courtesy of Ref. [40].

conductance. Even considering a kinetically limited case due to the low $V_{Sr}$ diffusion coefficient, a strong reaction of the systems conductance is expected from simulations. This is due to the highly confined interface, where strong electrical fields are present, which influence the Sr vacancy formation due to equation 2.15. Still, Sr precipitation is disregarded in most of the current literature because the Sr lattice is considered to be inactive until high temperatures are applied. However, these considerations stem from bulk measurements, where the surface near regions do not have a high contribution to the overall conductance. In a highly confined system, such as LAO/STO, the situation might be different, as could be already shown for the case of Nb:STO surfaces. [42] The shown experiments are indirect in nature and direct evidence is still missing. For this purpose, LAO/STO would need to be analyzed by an *in-situ*-method, due to the high sensitivity of the systems conductivity to surface effects. Furthermore, a method would be needed which can identify different chemical phases and the band alignment, to identify a dependence of the SCR and $pO_2$.

Due to its more complex nature, LAO/STO holds more possibilities than doped STO thin films to compensate charge. Even though the results discussed in this chapter favor the scenario of Sr precipitation being the cause for the observed $pO_2$ dependency, alternative scenarios could also be responsible. For example, LAO/STO shows a high sensitivity to surface modifications which was shown in experiments, where different solvents were applied to the surface. [34, 129] Therefore, the question remains which scenario is truly responsible for the lowered conductivity in oxidizing atmosphere. To tackle this issue the LAO/STO system is going to be characterized electrically under different atmospheres *in-situ* and in quenching experiments to analyze the electronic property changes. However, most importantly near ambient pressure X-ray photoelectron spectroscopy is going to be used, which allows the identification of secondary phases and the characterization of the systems band structure *in-situ*. Using this approach, the attempt is made to prove, disprove or augment model presented in this chapter.

# Chapter 3

# Experimental methods

In the following chapter the experimental methods used in this thesis are explained. Their working principle and most important aspects in regard to the thematic of this thesis will be elucidated. The list of methods encompasses the following: Pulsed laser deposition, atomic force microscopy, local conductivity atomic force microscopy, Hall measurements, X-ray diffraction, X-ray photoelectron spectroscopy and near ambient pressure X-ray photoelectron spectroscopy.

## 3.1   Pulsed laser deposition

Pulsed laser deposition (PLD) belongs to the category of physical vapor deposition techniques and is the used fabrication method for ultrathin films in this thesis. The strength of PLD is the ability to transfer the stoichiometry of a target material into the deposited thin film, while being simple in comparison to other methods like molecular beam epitaxy. [130] However, the details of the deposition influence the exact stoichiometry of the grown thin film. [130–132] A sketch of the a PLD setup is shown in Figure 3.1. A target, consisting of the material to be deposited, is placed opposite to a substrate in a vacuum chamber. The vacuum conditions can range from UHV to a few millibars and typically oxygen atmosphere is used for oxide growth. The deposition process is achieved by shooting UV laser pulses (usual wavelength of 248 nm) on the target to ablate the material. As a high energy density is used, the material directly evaporates into a plasma plume. Due to the low pressures, material can travel over the short distance to the substrate (usually a few tens of millimeters) where it deposits as a thin film. The laser pulse length is kept to a few nanoseconds to prevent a melting of the target material. To further prevent the accumulation of heat over continuous shots at one spot and to keep the targets morphology constant during growth, the target is typically rotated. Through the direct phase transition from solid to plasma, the ablation of thicker, molten particles is avoided. Using these measures, the deposition of high quality thin films can be achieved, where the stoichiometry of the target can be transferred to the thin film, if the deposition parameters are set correctly. This makes PLD a widely used technique for the growth of epitaxial thin films of complex oxides. [130, 133] As only a target of the desired material is required, most materials can be deposited in this way. One has to keep in mind, however, that the thin film composition will highly depend on the used parameters during the ablation
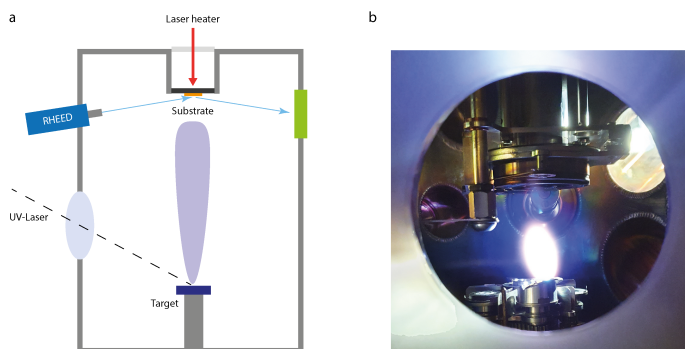
**Figure 3.1:** a) A sketch of the used PLD setup is shown; b) a photograph of a PLD process is shown.

process. [130]

The most important parameters for PLD processes are: Laser fluence, pressure, target to substrate distance and substrate temperature. The laser fluence is defined as the energy of the incoming laser beam divided by the area on which it is focused on the target. This energy density determines the initial kinetic energy of the ablated ions. On their way to the substrate surface they are scattered by the chamber gas and therefore loose some of their initial energy. The combination of laser fluence and chamber pressure determines the distance an ablated ion can travel without losing its momentum completely. In general, the distance between target and substrate has to be sufficiently small. Therefore, the kinetic energy of ions arriving at the substrate surface is determined by the combination of laser fluence, gas pressure and target to substrate distance. It is distinguished between a ballistic regime, where ions are almost not scattered by gas molecules, and a diffusive regime where the ions lost at least some their initial energy. [132, 134] These two regimes determine the growth mode of epitaxial thin films and in most cases the diffusive regime is preferred as in many materials it allows for a better control of the thin films stoichiometry and leads to sharper interfaces. Furthermore, when depositing materials containing multiple elements, for both to arrive at the substrate by the same amount, the combination of laser fluence, pressure and target to substrate distance has to be tuned to the specific element combination. This comes from the fact that, due to different masses, different elements will be scattered more or less by the gas molecules, influencing the angular distribution of elements throughout the plume. [135–137] By correct fine tuning of the above mentioned parameters, however, this can be avoided. On the other hand this inherent scattering preference can also be used to tune the stoichiometry of a thin film to a desired composition. At last, the substrate temperature determines the mobility of arriving species on the substrate surface. Depositions in room temperature leads to a "freeze in" of arriving ions and typically to amorphous thin films. For epitaxial thin films the substrate has to be heated to a certain degree, which is usually in the range of 600 to 1000°C. The key element for the correct growth temperature is setting it high

enough, which is necessary to form a crystalline thin film, while not going too high to prevent unwanted effects such as the evaporation of more volatile elements. [138] The substrate temperature influences the mobility of ionic species on the STO surface and therefore the growth mode. [44, 139] Since the growth of the thin films can be set to be rather slow, epitaxial thin films can be grown layer by layer. This enables monitoring the process by reflection high-energy electron diffraction, which will be discussed in the next chapter.

## 3.2 Reflection-High-Energy-Electron-Diffraction

Reflection high energy electron diffraction (RHEED) is a commonly used technique to monitor the growth of epitaxial thin films. The working principle is shown in Figure 3.1 a. An electron beam is targeted on the substrate surface during thin film growth under a small angle with respect to the surface. This way, a reflection of the electrons by the sample surface is achieved. The reflected electrons are made visible by collecting them on a phosphorous screen. Depending on the exact morphology of the substrate surface, different patterns (called RHEED patterns) arise. A crystalline sample typically creates spots to the right and to left of the specular spot, called diffracted spots. They correspond to electrons which are diffracted by the crystal lattice along the surface and hence contain information about the in-plane crystal lattice. RHEED patterns change according to the crystal surface properties and can be a powerful analytical tool. [140, 141]

To monitor the thin film growth, the intensity of the specular spot is monitored. When the material grows in a layer-by-layer growth mode, it follows distinct oscillations as is shown in Figure 3.2. At the beginning of the deposition process, the electron beam is reflected on a flat surface leading to a high intensity of the specular spot. During thin film growth the partially covered surface is essentially roughened, leading to scattering of electrons and a decrease of intensity. When roughly half a unit cell is deposited, a minimum is reached from which point the intensity recovers as the new surface is completed. Due to this mechanism the growth of a thin film can be monitored by counting the number of intensity oscillations, also called RHEED oscillations, where each oscillation corresponds to one unit cell of grown material. This is an idealized picture. In reality the shape of the RHEED intensity oscillations highly depends on the deposited material and its exact surface morphology during growth. [142–144] However, it is sufficient for a crystalline thin film growing in layer-by-layer growth mode, where the arriving ions form a coverage of islands that are only of unit cell height, as is the case for the growth of LAO thin films. When other growth modes occur as e.g. island growth mode where larger islands are formed this method to determine the thickness of the thin film fails. Still, valuable information can be extracted, as e.g. growth in regular islands leads to a distinct RHEED pattern. [145]
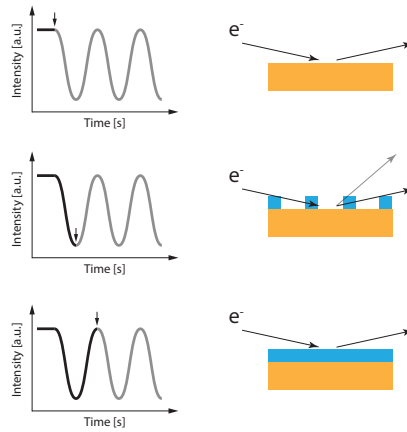
**Figure 3.2:** Sketches of the intensity evolution of the reflected RHEED spot during a growth process are shown over time (left) including sketches of the thin film surface during growth (right).

## 3.3   Atomic force microscopy

Atomic force microscopy (AFM) is a technique to resolve the topography of surfaces with a resolution that can be as low as a few nanometers or even Ångstroms. [146] Two kinds of AFM were used during the course of this thesis, so called tapping-mode AFM and local conductivity AFM (c-AFM). In both cases a probe is used, which is usually a sharp tip attached to rectangular bar made out of silicon. This so-called cantilever is scanned across the samples surface. Only the very end of the tip is in contact with (contact mode) or tapping over the sample surface (tapping mode).

To achieve the highest possible resolution, the movement of the cantilever in all directions is accomplished by the use of a piezoelectric elements. The tracking of the exact cantilever movement in the vertical direction is commonly achieved by the combination of a laser and a four quadrant photodiode. The laser is focused on the backside of the cantilever from which it reflects and hits the photodiode. By this setup the vertical position of the cantilever can be determined by the recorded deflection of the laser beam. To enable a continuous scanning over the sample surface the height information is coupled in a feedback loop, controlling the vertical axis. By scanning the height information over an investigated area, topography maps can be constructed.

For c-AFM the cantilever is scanned in constant contact over the sample surface and the topography is recorded. As current must be able to pass through the cantilever, a conductive coating is applied. A voltage is applied between tip and sample while the AFM scan is carried out, simultaneously recording the current passing through. Through this method, local conductivity can be monitored while recording the surface topography. The c-AFM measurements in this thesis were exclusively conducted under vacuum conditions of $1 \times 10^{-9}$ mbar using an Omicron VT-SPM system (Omicron Nano Technology GmbH) while using NANOSENSORS™ CDT-FMR cantilevers. The

measurement system is connected to the PLD deposition chamber via a pumped transfer tunnel. This was done to prevent artifacts through surface contaminations like adsorbates or the thin coverage of water on every surface in atmosphere. Ex-situ samples were baked out at 200 °C for 1 hour to remove surface adsorbates.

To record the surface topography of samples in ambient atmosphere, tapping AFM systems were used. In tapping AFM, the cantilever is oscillated at a frequency in the order of 100 kHz. The cantilever is brought close to the surface to the point were it is making physical contact. This results in a tapping motion of the cantilever, when its scanned across the surface. Tapping AFM has the advantage over contact AFM that the tip is not exposed to large lateral forces. This prevents difficulties which contact AFM can face due to friction or adhesion between tip and sample surface. Additionally the forces between tip and sample are weaker, leading to less influence of the cantilever on the sample. Furthermore, this enables the use of phase contrast to detect different surface chemistries of a sample. As the tip-to-surface interaction force depends on the chemistry of the surface, the repulsion force experienced by the AFM tip changes when it is tapping over two surfaces of different chemistry. This changes the energy of the oscillating cantilever, leading to a shift of its resonance frequency, which induces a shift of the phase between driver and cantilever. [146] The recorded phase at a constant frequency can, therefore, be used to identify surfaces of different chemistry. This measurement mode was used to identify the surface termination of STO crystals. Tapping AFM measurements were carried out using either a Cypher Atomic Force Microscope (Asylum Research) or a Nanosurf flex Axiom (Nanosurf AG).

## 3.4   Hall measurements

To determine the carrier density and mobility of charge carriers in LAO/STO samples, Hall measurements were conducted. A sketch of such a Hall measurement on a LAO/STO sample is shown in Figure 3.3. In this sketch a thickness (d) is given, even though the analyzed system can be effectively treated as two dimensional. [37] However, to also give a general definition of the Hall effect, a thickness is assigned here. The data obtained in Hall measurements contains information that is integrated
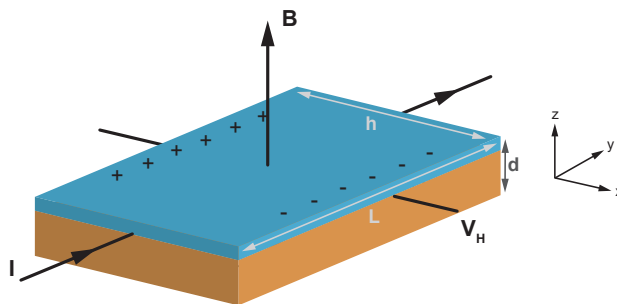


**Figure 3.3:** The principle of the Hall effect is sketched using a rectangular LAO/STO sample as example.

across the sample, which in this case is dominated by the 2DEG. Therefore, the two dimensional character of the system can be accounted for by directly using the integrated result, namely sheet resistance and sheet carrier density.

The Hall effect (named after its discoverer Edwin Hall [147]) is used to determine the carrier density and mobility for a given conductor in a so-called Hall measurement. The effect is based on the Lorentz force experienced by electrons with a drift velocity ($v$) in a magnetic field ($B$). It is assumed here, that the free charge carriers can be described by the Drude model. As a consequence a current driven through a material under a magnetic field leads to a carrier separation perpendicular to current and magnetic field. This in turn gives rise to an electrical voltage across the sample and leading to a steady state in which electrical Force ($F_e$) and Lorentz force ($F_L$) are canceling out. The build up of the counteracting voltage is almost instantaneous, meaning that in a Hall measurement, only the steady state is observed. A sketch of the principle is shown in Figure 3.3. Electrical and Lorentz force are equal to each other, which leads to the following equation

$$F_L = qvB; \quad F_e = qE; \quad F_e = F_L \Longleftrightarrow qvB = qE \tag{3.1}$$

Here $q$ denotes the charge of the carrier. The Hall voltage can be defined by $U_H = Eh$, where $h$ is the sample width (see Figure 3.3). Therefore, the Hall voltage can be directly deduced from equation 3.1 to be

$$U_H = vBh \tag{3.2}$$

It is possible to establish a direct relation to the sample geometry, which in turn enables the determination of carrier density from measuring the Hall voltage. For this purpose, the definition of the current density ($j$) with the sample geometry shown in Figure 3.3 is used $j = I/hd = qnv$. Here $h$ is the sample width and $d$ the sample thickness. Inserting this relation into equation 3.2 leads to

$$U_H = \frac{1}{nq}\frac{BI}{d} = \frac{BI}{n_s q} \tag{3.3}$$

From equation 3.3 it is possible to determine the carrier density and type ($p$ or $n$) under an applied current and magnetic field by only knowing the sample thickness. As a thickness is difficult to assign to a 2-dimensional system, the sheet carrier density is commonly used for LAO/STO, which is defined as $n_s = nd$ making the thickness obsolete. A Hall measurement can be also performed on non-rectangular sample shapes as was shown by van der Pauw [148] as long as the contacts are placed close to the edges of the sample. By simultaneously measuring the conductance ($G$) of the sample, the mobility ($\mu$) can be determined by the simple expression $G = n_s e\mu$ .

**Non-linear Hall effect**

For measurements conducted at room temperature, the above used description of the Hall effect, which behaves linear with increasing magnetic fields, is sufficient. However, at low temperatures the Hall effect becomes non-linear because the 2DEG of LAO/STO consists of two bands with different effective electron masses. [76] These are not distinguishable at room temperature because of the low mobility, which shifts the non-linearity to very large fields. However, below 100 K the non-linearity is also

visible for lower fields, so that it becomes necessary to apply a two carrier model to the Hall coefficient. [149] For this purpose a formalism will be derived in general to achieve a description of the Hall effect for an arbitrary number of carriers. From this point a two-carrier model can be easily derived (see also chapter 12 of Ref.: [150]). The forces an electrical charge carrier experiences in a Hall measurement are the electrical force from the applied voltage and the Lorentz force from the applied magnetic field. This can be summarized using the relaxation time approximation for electron transport and assigning a drift velocity ($\boldsymbol{v}$) to the electron (Drude model). The equation reads

$$m^* \left( \frac{d\boldsymbol{v}}{dt} + \frac{\boldsymbol{v}}{\tau} \right) = q\boldsymbol{E} + q\boldsymbol{v} \times \boldsymbol{B} \tag{3.4}$$

where $m^*$ is the effective mass of the charge carrier, $\boldsymbol{v}$ is the velocity vector, $\tau$ is the scattering time, $\boldsymbol{E}$ is the vector of the applied electrical field, $q$ is the carrier charge and $\boldsymbol{B}$ is the vector of the applied magnetic field. As it is needed to connect the velocity vector to the applied current density $\boldsymbol{J}$ later on, the drift velocity $\boldsymbol{v}_\mathrm{D}$ from the Drude model is inserted. Furthermore, because a steady state is investigated ($d\boldsymbol{v}/dt = 0$), equation 3.4 can be simplified to

$$m^* \frac{\boldsymbol{v}_D}{\tau} = q\boldsymbol{E} + q\boldsymbol{v}_D \times \boldsymbol{B} \tag{3.5}$$

As all forces only act in the plane perpendicular to $\boldsymbol{B}$ it is sufficient to split equation 3.5 into the $x$ and $y$ components and solve the vector product. Additionally, the electrical field is only applied in $x$ direction ($E = (E_x, 0, 0)$) and the magnetic field is only applied in z-direction ($B = (0, 0, B_z)$), which simplifies the relations. The resulting electrical field from carrier accumulation ($E_y$) can be handled separately. The resulting equations are

$$v_x = \frac{q\tau}{m^*}(E_x + v_y B_z) \tag{3.6}$$

$$v_y = -\frac{q\tau}{m^*} v_x B_z \tag{3.7}$$

The drift velocity can be linked to the current density and conductivity by the following expression

$$\boldsymbol{J} = nq\boldsymbol{v} = \sigma\boldsymbol{E} = \begin{pmatrix} \sigma_{xx} & \sigma_{xy} \\ \sigma_{yx} & \sigma_{yy} \end{pmatrix} \tag{3.8}$$

When the complete conductivity tensor is known, it becomes possible to determine the Hall coefficient. For this purpose, the left hand side of equation 3.8 is first determined by combining equations 3.6, 3.7 and 3.8. This leads to an expression for the current densities in $x$ and $y$ direction

$$J_x = \frac{q^2 n\tau}{m^*} \left( E_x + \frac{J_y B_z}{nq} \right) \tag{3.9}$$

$$J_y = -\frac{q\tau}{m^*} J_x B_z \tag{3.10}$$

Inserting 3.10 into 3.9 leads to an expression, where $J_x$ and $J_y$ are independent from each other. The cyclotron frequency $\omega_c = eB/m^*$ and the Drude conductivity $\sigma_0 = nq^2\tau/m^*$

are used here to simplify the expression. To derive the conductivity tensor, first only the electrical field in $x$ direction is going to be considered, using $\boldsymbol{E} = (E_x, 0, 0)$ the equations read

$$J_x = \frac{\sigma_0}{1 + \omega_c^2 \tau^2} E_x = \sigma_{xx} E_x \tag{3.11}$$

$$J_y = -\frac{\sigma_0 \omega_c \tau}{1 + \omega_c^2 \tau^2} E_x = \sigma_{yx} E_x \tag{3.12}$$

In analogy the two missing components of the conductivity tensor can be derived by considering the electrical field that results from carrier accumulation using $\boldsymbol{E} = (0, E_y, 0)$. The end result can be written as

$$J_x = \frac{\sigma_0 \omega_c \tau}{1 + \omega_c^2 \tau^2} E_y = \sigma_{xy} E_y \tag{3.13}$$

$$J_y = \frac{\sigma_0}{1 + \omega_c^2 \tau^2} E_y = \sigma_{yy} E_y \tag{3.14}$$

Finally a complete description of the conductivity tensor is achieved which reads

$$\sigma = \frac{\sigma_0}{1 + \omega_c^2 \tau^2} \begin{pmatrix} 1 & \omega_c \tau \\ -\omega_c \tau & 1 \end{pmatrix} \tag{3.15}$$

The Hall resistance ($R_{xy}$) is determined by measuring the voltage in $y$ direction and dividing through the applied current, which leads to the expression

$$R_{xy} = \frac{U_y}{I_x} = \frac{E_y}{J_x d} \tag{3.16}$$

For a system of two charge carriers the complete conductivity in $x$ direction will be determined by the sum of the single conductivities. Using equation 3.8 an expression for $J_x$ can be derived

$$J_x = \sum (J_{x,1} + J_{x,2}) = E_x(\sigma_{xx,1} + \sigma_{xx,2}) + E_y(\sigma_{xy,1} + \sigma_{xy,2}) \tag{3.17}$$

The current density in $y$ direction has to be zero, as the voltage is measured using a high internal resistance. Therefore, the analogue expression for the current density in the y-direction reads

$$J_y = \sum (J_{y,1} + J_{y,2}) = E_x(\sigma_{yx,1} + \sigma_{yx,2}) + E_y(\sigma_{yy,1} + \sigma_{yy,2}) = 0 \tag{3.18}$$

The Hall resistance is described by equation 3.16, which means that an expression is needed, where only $E_y$ and $J_x$ remain. This can be achieved by solving equation 3.18 for $E_x$ and inserting it into 3.17, which leads to a description of the Hall resistance for two carriers for all applied magnetic fields. To link it to the carrier density and mobility of the respective charge carriers, the expressions $\omega_{c,i} = \mu_i B / \tau_i$ and $\sigma_{0,i} = n_i e \mu_i$ are used. In the last step, sheet carrier densities are inserted using $n_{i,s} = n_i d$ to cancel out $d$. The final expression of the Hall resistance for a two carrier model reads

$$R_{xy}^{2e} = -\frac{B}{e} \frac{\frac{n_{1,s}\mu_1^2}{1+\mu_1^2 B^2} + \frac{n_{2,s}\mu_2^2}{1+\mu_2^2 B^2}}{\left( \frac{n_{1,s}\mu_1}{1+\mu_1^2 B^2} + \frac{n_{2,s}\mu_2}{1+\mu_2^2 B^2} \right)^2 + \left( \frac{n_{1,s}\mu_1^2}{1+\mu_1^2 B^2} + \frac{n_{2,s}\mu_2^2}{1+\mu_2^2 B^2} \right)^2 B^2} \tag{3.19}$$

Therefore, in a two carrier model the Hall resistance shows a non-linear field dependence for all applied magnetic fields. To reduce the amount of free parameters, the resistance at zero field is inserted by using the relation

$$\frac{1}{R_{xx}(B = 0)} = e(n_1\mu_1 + n_2\mu_2) \tag{3.20}$$

With these equations the Hall resistance at low temperatures can be described in absence of any magnetic moments in the sample which induce an anomalous Hall effect on top of the described two carrier model.

**Anomalous Hall effect**

In addition to the non-linearity caused by the multiple bands present in LAO/STO, the system can also become magnetic. The magnetic behavior of LAO/STO interfaces can facilitate in different ways such as e.g. Kondo-like resistance behavior to low temperatures. [17] In Hall measurements the magnetization can manifest in the presence of an anomalous Hall effect. In the Hall resistance, the magnetization of the sample leads to an additional resistance which scales which the magnetization of the sample. [76] Due to the anisotropic shape of magnetization in LAO/STO, [151–153] it is reasonable to assume that magnetic moments are oriented in plane. Therefore, the magnetic field would be oriented along the "easy" axis of magnetization in Hall measurements of LAO/STO. The behavior can then be described according to Ref. [95] as

$$R_{xy} = R_{xy}^{2e} + R_{xy}^{\text{AHE}} = R_{xy}^{2e} + R_0^{\text{AHE}} \tanh\left(\frac{B}{B_{\text{c}}}\right) \tag{3.21}$$

Here $R_0^{\text{AHE}}$ describes describes the magnitude of the anomalous Hall contribution and is proportional to the magnetization. $B_{\text{c}}$ is the critical field from which on the magnetization saturates.

## 3.5   Electrical conductivity relaxation

Electrical conductivity relaxation (ECR) is a method to determine the dynamics of electrical conductance changes, when the system transitions into a new thermodynamic equilibrium. To trigger a thermodynamic relaxation, elevated temperatures have to be applied. The exact values highly depend on the used material and are roughly in the range from 300 to over 1000 °C. The electrical properties of oxides highly depend on their defect chemical constitution, which depend on the surrounding $p\text{O}_2$ (see section A). Therefore, such changes in electrical conductance usually originate from a changed atomic constitution of the material, by e.g. the incorporation of oxygen vacancies. Therefore, carefully conducted ECR measurements can reveal the amount and dynamics of electrically active defects inside a sample. In contrast to high temperature equilibrium conductance (HTEC) measurements where an electrical conductance is plotted in equilibrium over different pressures and temperatures, in ECR measurements the transient conductance is monitored upon relaxation from one equilibrium state to another.
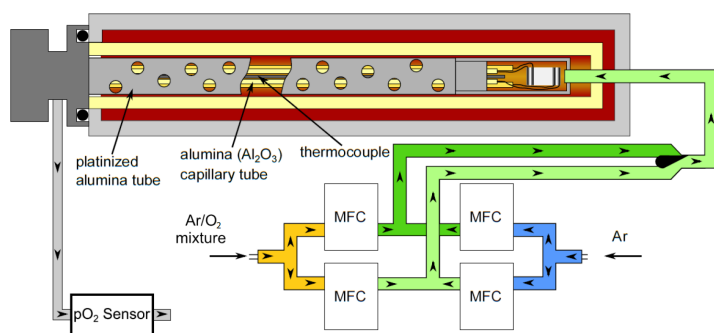
**Figure 3.4:** A sketch of the used ECR system is shown. Two gases are mixed by the use of mass flow controllers (example of Ar and and Ar/$O_2$ mixture shown here) and let to a four point valve. The valve lets either one or the other gas into the heated furnace. Inside the furnace the electrically contacted sample (achieved by four platinum wires) is set. A thermocouple is placed close to the sample to measure the temperature inside the chamber. The exhaust gas is collected into a $pO_2$ sensor. By courtesy of Ref.: [154]and [90]

For this purpose samples are electrically contacted and inserted into a furnace to apply a defined temperature. Ideally the atmosphere surrounding the sample is exchanged instantaneously to avoid a superposition of sample reaction and changing atmosphere. This makes the use of gas mixtures most suitable for this application. In the used system sketched in Figure 3.4, the inlet gas can be switched by a four-point-valve, which enables a rapid switching from one gas flow to another. Furthermore different compositions of the gas atmosphere can be achieved by the use of mass flow controllers (MFC). This enables the mixture of gases to atmospheres with a defined $pO_2$ without the need to acquire each gas composition in a designated bottle. From the four point valve the gas mixture flows into the chamber, where the sample under investigation is held in place by four platinum wires that also serve as electrical contacts. Sample preparation is carried out by cutting $5 \times 10$ mm$^2$ pieces, on which platinum contacts are sputtered in four stripes. Two stripes are placed at each end of the sample and two stripes are placed further to the center. The distances are set in a way that leaves an uncovered area in the middle of $5 \times 5$ mm$^2$ (see Figure 3.4). Current is driven through the sample by the outer two contacts while the resulting voltage is measured by the inner two contacts leading to a four point measurement. A thermocouple is placed close to the sample to measure the temperature inside the chamber. All of the electrical wiring is guided to the outside through alumina tubes that can withstand the elevated temperatures for insulation.

## 3.6   X-Ray photoelectron spectroscopy

X-Ray photoelectron spectroscopy (XPS) is an analytical method to determine the chemical states of a sample close to its surface. The working principle is visualized in a sketch of a band diagram in Figure 3.5 a. Here $E_{Vac}$ denotes the vacuum energy $E_{CB}$ the conduction band, $E_F$ the Fermi level, $E_{VB}$ the valence band and $E_{CL}$ a core level.
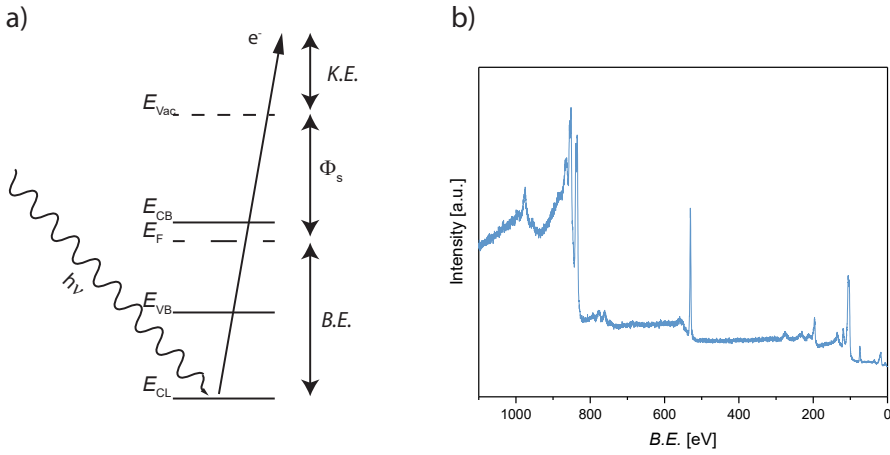
**Figure 3.5:** a) Sketch of a photoelectron emission process is shown. b) An example for a XPS spectra of an LAO/STO heterostructure is shown

The sample is illuminated by a monochromatic X-ray source inside a vacuum chamber. Core-level electrons absorb the incident light and convert the gained energy into kinetic energy. The used x-rays contain a high amount of energy, as usually Al $K_\alpha$ (1486.6 eV) or Mg $K_\alpha$ (1253.6 eV) are used. [155] Therefore, excited electrons can overcome their binding energy, emitting them from the illuminated metal. This so called photoelectric effect is the basic principle of XPS. For the analysis, the kinetic energy of emitted electrons has to be maintained, which is why ultra high vacuum conditions are needed. The emitted electrons are collected into an electron spectrometer that sorts them with respect to their kinetic energy. As the used X-ray source is monochromatic with an energy of $h\nu$ and the total energy has to be conserved, the kinetic energy ($K.E.$) will depend on the binding energy ($B.E.$) that holds the electron in its orbital, the work function of the analyzer ($\Phi_{XPS}$) leading to the photoemission equation which reads

$$h \cdot \nu = K.E. + B.E. + \Phi_{XPS} \tag{3.22}$$

The intensity of emitted electrons is plotted as a function of the recorded kinetic energy. Using equation 3.22, the kinetic energy can be converted into the binding energy of the respective orbitals. An example for a LAO/STO sample is shown in Figure 3.5 b. Each core-level electron of an atom has a characteristic $B.E.$, which depends most importantly but not exclusively on: The amount of protons of the atom, the core level it resides in, the chemical bond to the surrounding atoms and the general potential of the sample. A detailed elaboration of the technique and influencing factors can be found in Ref. [155]. Therefore, XPS is a chemically sensitive technique that allows to identify elements by their characteristic $B.E.$. Furthermore, the dependence of the $B.E.$ on the chemical bond of the element allows to identify the elements chemical state such as e.g. the ionization state of a transition metal ion. [156] Aside from the ability to identify elements and their chemical state, XPS holds a high surface sensitivity, analyzing only the first few nanometers of a given sample. This comes from the fact

that the emitted photoelectrons need to leave the sample first. In this context, inelastic scattering with the sample material is the main cause of intensity dampening. The loss of signal intensity by a certain material can be described by using the inelastic mean free path (IMFP or $\lambda$). It is defined as the mean distance between two scattering events inside a certain material. The attenuation behavior is exponential and described by the Lambert-Beer law

$$I(x) = I_0 \exp\left(-\frac{\Delta x}{\lambda}\right) \tag{3.23}$$

Here, $I$ denotes the signal intensity, $I_0$ the signal before attenuation and $\Delta x$ the traveled distance in the given material. The IMFP is therefore determined by the thickness needed to attenuate the intensity of emitted electrons to the 1/e part of its original value. In solids the IMFP is in the order of a few nanometers making XPS only able to extract electrons from the first few nanometers of any solid material. This limitation is also one of the biggest advantages, as by use of the attenuation behavior a depth profiling of the analyzed elements becomes possible. Therefore, XPS becomes more surface sensitive when the effective thickness photoelectrons have to penetrate is increased by e.g. measuring at different emission angles. Another way is to decrease $\lambda$, which can be achieved through the use of X-rays of lower energy, decreasing the kinetic energy of photoelectrons consequently their IMFP. When thin films of a known thickness are used (as is the case in LAO/STO), the expected attenuation by the overlayer can be furthermore determined by using the Lambert-Beer-law.

**Near-ambient pressure XPS**

Near-ambient pressure XPS (NAP-XPS) uses the same basic principle as regular XPS with the difference that a differential pumping system is installed to enable the spectroscopic characterization in higher pressures than the usually needed $1 \times 10^{-8}$ mbar. [157] A sketch of such a system is shown in Figure 3.6. The detection in close to ambient pressures is made possible by a differentially pumped nozzle, which is brought close to the sample surface. In this way, photoelectrons generated from the sample only have to travel a short distance in high pressure to reach lower pressures inside the nozzle. This reduces the loss of electrons by scattering in the gas atmosphere tremendously and pressures aside from UHV of a 0.001 - 10 mbar are made possible. [158] Additionally, samples can be heated by a resistive heater stage to enable thermodynamic equilibration. In this thesis a SPECS™ NAX-XPS system was used which is located at the Department of Surface and Plasma Science at the Charles University in Prague. The measurements there were enabled by the CERIC-ERIC consortium. Furthermore, a synchrotron-based NAP-XPS was used at Beamline 11.0.2 of the Advanced Light Source, Berkeley, USA. For the analysis of spectra the CasaXPS as well as KolXPD software was used.

The *B.E.* of emitted photoelectrons from a material in an XPS experiment depends on multiple factors. The most influential one being the element and core-level spectra they occupied. This makes it possible to identify the stoichiometry of a sample but also their chemical bonding. As each chemical configuration of an element leads to a very specific electron density that surrounds the core-level shells, the *B.E.* will also change due to Coulomb repulsion. A practical example would be to compare a phase pure
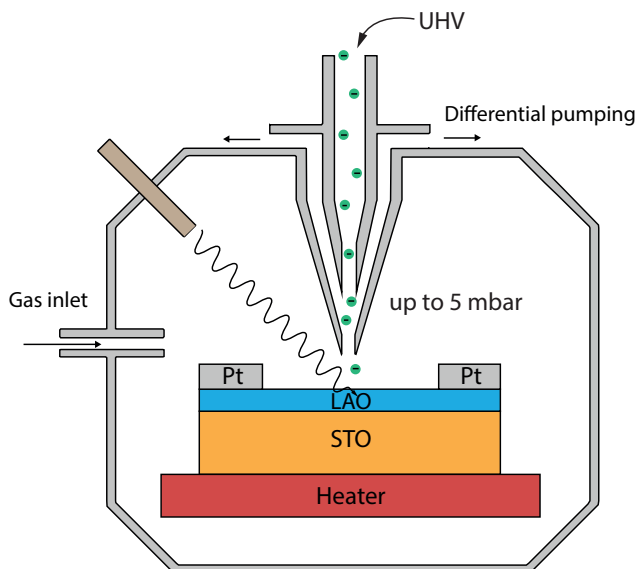
**Figure 3.6:** A sketch of a NAP-XPS system is shown, where an LAO/STO sample is analyzed.

material with one that reacted e.g. with oxygen in XPS. This leads to the appearance of a convolution of two or more spectra. One being the residual, un-reacted material and the others being the oxides it reacted to. Such spectra usually contain shoulders or even a completely separated core-level spectrum. This means that unless the chemical configurations are very similar, the chemical bonding of an element can be identified by comparison of their XPS spectrum to a known reference. In the case of NAP-XPS the state before and after oxygen exposure can be directly compared over the applied $pO_2$ and temperature. This aspect is one of the biggest advantages of NAP-XPS. It allows to follow changes of chemical states and band structure of a system, while applying different temperatures and $pO_2$ to trigger a controlled reaction of the material.

# Chapter 4

# Thin film growth using PLD

In this thesis, thin films were grown using pulsed laser deposition (PLD). For a complete description of the technique see chapter 3.1. Using this method, LAO thin films were grown, as well as sub-monolayer SrO for the growth of LAO/SrO/STO samples. The growth of both processes is addressed in this chapter, comparing the properties of resulting thin films. These were characterized using RHEED, AFM, XPS, XRD and Hall measurements. As is the case for any thin film grown via PLD, the exact deposition parameters heavily influence the properties of fabricated samples. The parameter variation and their effects will be the topic of this chapter. All samples used in this thesis where grown in the same PLD chamber that was built by Surface systems and Technology GmbH & Co. KG.

## 4.1   Growth of LAO thin films

To show the typical growth behavior of LAO/STO, the thin film deposition and characterization is elaborated at the example of a 16 unit cell (uc) thick LAO/STO sample. For ablation, an excimer laser (Compex 205F from Coherent) of 248 nm wavelength was used with a repetition rate of 1 Hz. The ablated area was set to 2 mm$^2$ on a single crystalline LAO target. The substrate was placed at a distance of 44 mm opposite to the LAO target and heated up to a temperature of 800 °C. These parameters were fixed for all samples grown and only the pressure and laser fluence were varied. As starting parameters an oxygen partial pressure of $1 \times 10^{-4}$ mbar and a laser fluence of 0.80 J/cm$^2$ were used. This parameter set was first taken as a starting point from Ref. [159], where the same PLD chamber was used. Later adjustments were applied, depending on the application. Prior to each deposition, a preablation step was carried out, where material was ablated from the target in deposition conditions using at least 1000 laser pulses. During this step a shutter prevents deposition and the frequency was increased to 5 Hz to accelerate the process.

The LAO deposition was monitored using a high-pressure RHEED system to monitor the growth mode and to determine the thin films thickness. For a description of the RHEED working principle see chapter 3.2. The RHEED intensity of the specular spot during the deposition of a 16 uc LAO thin film with the aforementioned parameters is shown in Figure 4.1a. Clear oscillations are visible indicating a layer-by-layer growth mode. The intensity oscillations are observed to the very end of the deposition process,
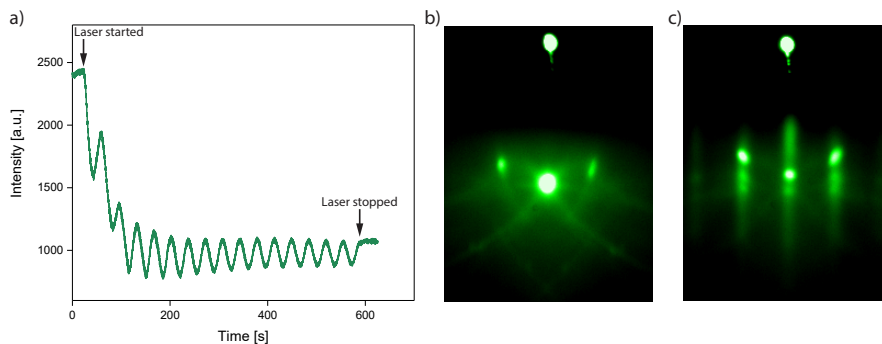
**Figure 4.1:** a) Shows the intensity of the specular RHEED spot during growth of an 16 uc LAO/STO sample. b) Shows the RHEED pattern before growth and c) after growth.

indicating a high quality thin film growth. In Figure 4.1b, the typical RHEED pattern of a $TiO_2$-terminated STO single crystal is shown. The specular spot is clearly visible in the center with the two first order diffracted spots at the sides. Faintly visible lines can be seen between the spots (called Kikuchi lines), which are a resonance pattern of inelastically scattered electrons and is best visible for nearly perfect surfaces on well ordered crystals (see chapter 7 in Ref. [140]). In general, the pattern observed in Figure 4.1b resembles the usually observed RHEED pattern for a $TiO_2$-terminated STO surface. After LAO growth, the pattern changed to the one shown in Figure 4.1c. The overall intensity of the spots is lowered in comparison to the initial STO substrate intensity, because the electron beam was aligned on STO to have maximum intensity. Furthermore, the electron reflectivity of LAO is lower compared to STO. The shape of the pattern is qualitatively conserved, which is typically observed for the growth of LAO on STO for films of this thickness. [141] No additional spot patterns indicating islands or strong loss of intensity indicating a surface roughening are observed.

The fabricated thin film were characterized using XPS, AFM, XRD and Hall measurements. The Hall measurement for the 16 uc LAO/STO sample reveals a conductive behavior with a sheet carrier density of $9.31 \times 10^{-13}$ cm$^{-2}$ and a mobility of 2.96 cm$^2$/Vs, which are typical values for the 2DEG of LAO/STO. [57] A comparison of core-level spectra area ratios recorded by XPS, reveal that the thin film grew almost completely stoichiometric with a La/Al ratio of roughly 0.97. A more detailed description of this analysis can be found in chapter 4.4. The surface topography determined from AFM and crystal structure observed by XRD are shown in Figure 4.2. The surface topography of the substrate (Figure 4.2a) is qualitatively copied by the LAO thin film (Figure 4.2b). The two corresponding AFM images show the same terrace lengths and smooth surfaces in both cases. Thin film and substrate are essentially not discernible by the AFM measurements. The crystallographic structure was determined via XRD. A (2θ-ω) scan from 44 to 54° is shown in Figure 4.2c. The expected angular positions for STO, LAO and a strained LAO thin film using a poison ratio of 0.24 [33] are depicted as dashed lines. The measurement was referenced to the STO substrate and therefore shows a perfect alignment between the expected and measured STO position. The LAO peak can be observed at higher angles and is a separated but broadened peak, due
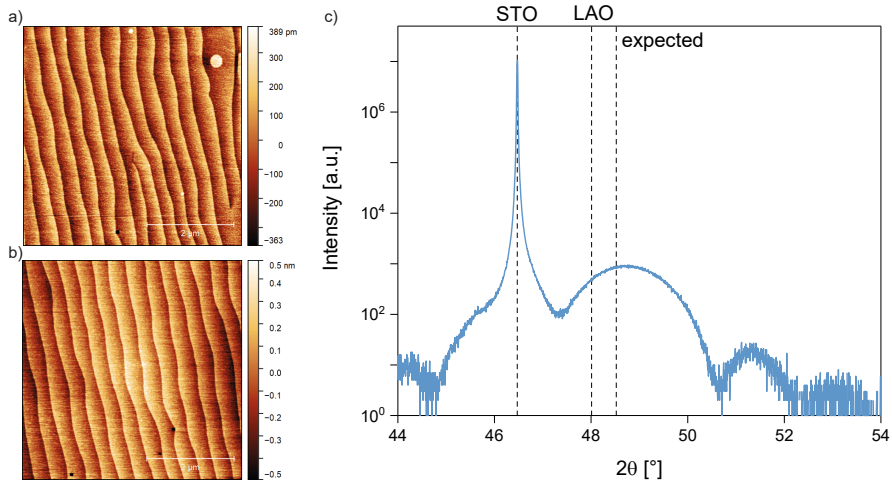
**Figure 4.2:** a) Shows the surface topography of a TiO$_2$-terminated STO substrate. b) Shows the surface topography of a 16 uc LAO thin film grown on the substrate shown in a). c) Shows a 2θ XRD scan of the sample shown in b). The AFM images are 5 μm × 5 μm in size.

to the very thin overlayer. [160] Additionally, a thickness oscillation pattern is visible over the whole measurement, showing a high interface and surface smoothness of the thin film. [161] Comparing the expected position of a pure LAO crystal to the thin film peak, it is clear that the thin film has a smaller *c*-lattice parameter than a LAO crystal, as is expected from a strained overlayer. The thin film peak is found close to the expected position of a completely strained LAO thin film with a slight deviation to higher angles. However, this also might be influenced by the strongly pronounced thickness oscillations or the accuracy of the used Poisson ratio. In summary, high quality thin films are achieved using the given parameter set.

When samples are kept in deposition conditions for a sufficient time (see chapter 4.3 below for details), electrical properties can be attributed to the interfacial 2DEG down to the low-temperature range. The typical behavior of an 8 uc LAO/STO sample in low-temperature Hall measurements is shown in Figure 4.3. The samples were grown using the same conditions as discussed above. A metallic conductivity down to low-temperatures can be observed (Figure 4.3a). When magnetic fields are applied, the Hall resistance ($R_{xy}$) shows a linear behavior at room temperature (deep blue curve in Figure 4.3b). At lower temperatures, the field dependence becomes increasingly non-linear, which is most pronounced for measurements below 10 K (light blue curves in Figure 4.3b). This deviation from a linear Hall resistance can be well described by a two carrier model, [149] which is derived in chapter 3.4.

Between 10 and 2 K, the data deviates from the two carrier model, due to an emergent anomalous Hall effect, which is best visible in the Hall coefficient ($R_H = R_{xy}/B$) shown in Figure 4.3c. Comparing the two lowest temperatures shown (2 and 10 K), a deviation from the bell-like shape of $R_H$ is observable at low fields. The anomalous Hall effect is attributed to emergent magnetic moments at the interface, leading to an upturn of $R_H$ around zero fields. This contribution can be accounted for,
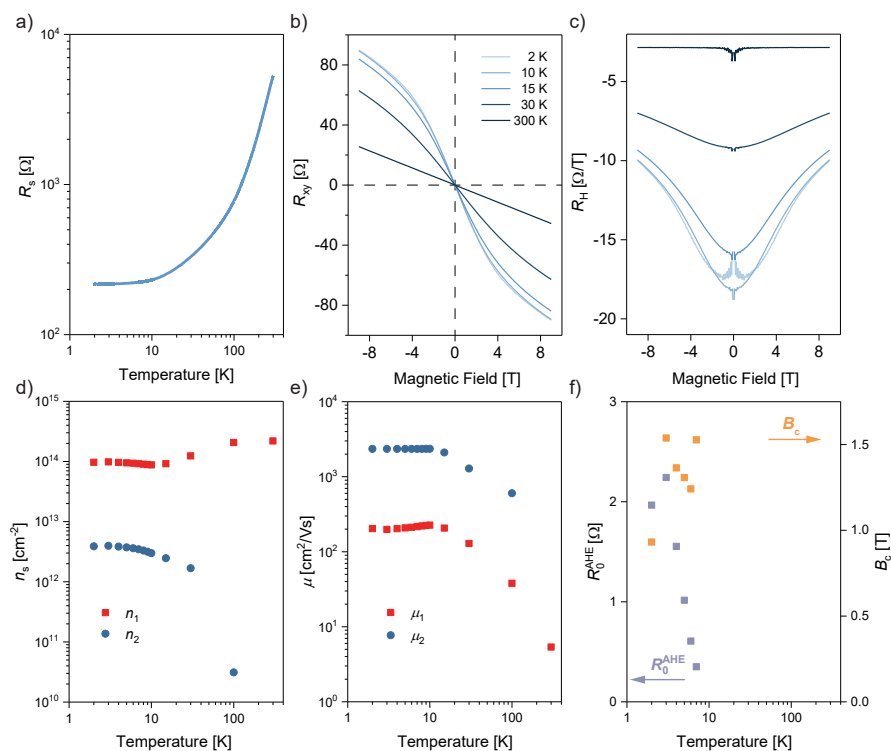
**Figure 4.3:** The electrical low-temperature behavior of a typical 8 uc LAO/STO sample with no STO bulk conduction (see chapter 4.3) is shown. a) Shows the sheet resistance from 300 to 2 K. b) Shows the Hall resistance ($R_{xy}$) at temperatures from 300 K (deep blue) to 2 K (light blue) under a magnetic field of up to 9 T. c) Shows the Hall coefficient ($R_H$) of the data shown in b). d) Shows the carrier densities obtained from a 2 carrier model fit. e) Shows the mobilities of the corresponding carrier densities shown in d). f) Shows the contribution of the anomalous Hall effect to $R_H$.

by the introduction of an additional term in the two carrier model, which characterizes the anomalous Hall effect through by two additional fitting parameters. These are $R_0^{\mathrm{AHE}}$, which corresponds to the saturation magnetization, and $B_c$, which corresponds to the coercive field of the magnetization.

The fitting parameters obtained from applying the two carrier model to the data shown in Figure 4.3b and c are the carrier densities of each population ($n_1$, $n_2$) and their corresponding mobilities ($\mu_1$, $\mu_2$). These are shown in Figure 4.3d and e respectively. The 2DEG holds a high density, low mobility population of carriers ($n_1$, $\mu_1$) and a low density, high mobility population ($n_2$, $\mu_2$). These two populations are frequently observed in LAO/STO and correspond to two possible conduction bands, that are not distinguishable at room temperature. [95, 96, 149]

The anomalous Hall contribution is increasingly present for lower temperatures, as can be seen by their signature values ($R_0^{\mathrm{AHE}}$, $B_c$) shown in Figure 4.3f. Both parameters increase with decreasing temperature, hinting at an increasingly pronounced magnetism in the analyzed sample. It turns out, that the exact magnitude of the anomalous Hall effect in LAO/STO depends highly on the LAO thin film stoichiometry and thermodynamic annealing applied to the heterostructure. These aspects are going to be discussed in chapter 8.

Through the characterization it could be shown that crystalline and stoichiometric LAO thin films are grown, using the given parameter set. The thin films show an overall high quality, with a smooth surface. Also the electrical propertiesof the LAO/STO heterostructure are compatible to literature values down to low-temperatures, showing that a typical 2DEG is achieved.

## 4.2   STO substrate treatment

LAO/STO heterostructures are especially sensitive to the termination of the STO single crystal they are grown on, as it determines the stacking order and therefore the direction of polarity present inside the thin film (see section 2.3). Because of this behavior, the used STO single crystals were terminated by an etching procedure to achieve a surface consisting exclusively of $TiO_2$. The used STO single crystals are oriented in (001) direction and were supplied by Shinkosha Co., Ltd., Japan and Crystec GmbH, Germany. An AFM topography image of a typical as-received substrate is shown in Figure 4.4a. Without any treatment, atomic terraces of the single crystal can already be seen, where the terrace edges form a disordered structure. The used etching process was first discovered by Kawasaki et al. [162] and was further refined by different groups. [102, 163] For this thesis, the following process was applied:

- A cleaning of the as-received substrates in acetone and isopropanol.

- A dip of the cleaned substrates in deionized water.

- The etching step for 2:30 min in buffered hydrofluoric acid.

- A second cleaning step to stop the etching.

An example of an etched STO substrate is shown in Figure 4.4b. In comparison with the untreated STO substrate it is discernible that parts of the terraces were removed
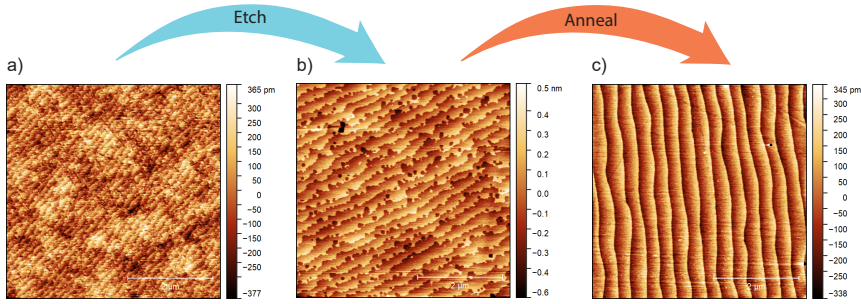
**Figure 4.4:** AFM topography images are shown for: a) as received STO, b) etched STO, c) etched and annealed STO. The AFM images are 5 μm × 5 μm in size.

and edge pits (rectangular holes) are formed due to the etching process. To form evenly distributed terraces and remove defects that may be introduced by the etching procedure, the STO substrates are annealed at 950 °C in air. An example for the resulting topography is shown in Figure 4.4c. The distinctly ordered and smooth topography enables a controlled nucleation for thin film growth. Furthermore, it enables the identification of discrepancies from imperfect growth of the epitaxial thin films that often form topographic features which are later distinguishable by AFM.

## 4.3   Influence of substrate reduction

In general the interest of this thesis lies in resolving the influences of the interface chemistry on the interfacial 2DEG of LAO/STO. During the deposition of LAO thin films on STO, oxygen vacancies are created, [89] which extend into the STO crystal [62]. Oxygen vacancies in STO act as donor dopants [41] (see section 2.4) and in the case of LAO/STO heterostructures lead to an extended 3D conduction behavior beneath the 2DEG, overshadowing the 2D behavior [164]. Therefore, to attribute changes of electrical properties to 2DEG behavior, the bulk conduction of the underlying substrate had to be minimized. To optimize the growth recipe in this regard, pressure and annealing time should be set in a way that ensures the absence of bulk STO conductivity. To achieve this goal, a post deposition annealing can be either implemented at high oxygen pressures and lowered temperature [164] or in growth conditions. [88] As a further goal of the thesis is to analyze the influence of thermodynamic annealing on the defect structure of the system, high annealing pressures are also undesired. These would make the distinction between growth induced properties and changes through later annealing impossible. Therefore, an annealing treatment in growth conditions was chosen. To analyze the contribution of the STO substrate to overall conductance, LAO/STO samples of subcritical thickness (3 uc) can be used since no 2DEG conductivity should be present in these samples. [63] Measured conductances can be completely attributed to the reduction of the STO substrate in this way.

   The following experiment was conducted. A series of samples consisting of 3 uc LAO on STO were grown in different oxygen partial pressures of $1 \times 10^{-4}$, $1 \times 10^{-3}$ and $1 \times 10^{-2}$ mbar. The other parameters were kept constant in this experimental series.
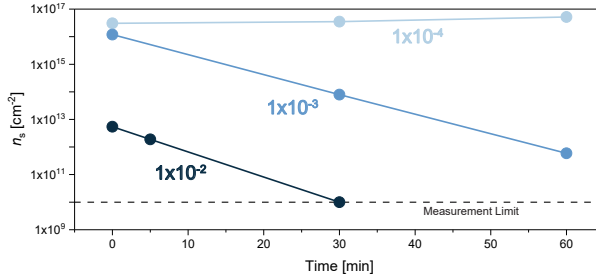
**Figure 4.5:** The sheet carrier densities of samples consisting of 3 uc LAO on STO in dependence of growth $pO_2$ (light to deep blue insets in mbar) and consecutive annealing time in growth conditions are shown.

After growth, samples were held in deposition conditions for systematically varied time frames of 0, 30 and 60 min. The used PLD chamber applies a laser heater system (see section 3.1) to heat the substrate up to the desired temperature. This enables a rapid cooling rate of 10 s which effectively "freezes in" the state at high temperatures by turning off the laser heater. Subsequently, Hall measurements (see section 3.4) at room temperature were conducted on all samples to determine their carrier density.

The results are shown in Figure 4.5, where the carrier density is plotted over annealing time. Samples grown in pressures of $1 \times 10^{-4}$ mbar show a carrier density of roughly $1 \times 10^{16}$ cm$^{-2}$ regardless of the time they were annealed in growth temperature (800 °C). For a pressure of $1 \times 10^{-3}$ mbar, a decrease over time can be seen, reaching a carrier density of $5.9 \times 10^{-11}$ after 60 min. A further increase to $1 \times 10^{-2}$ mbar leads to an acceleration of the reoxidation process, reaching the measurement limit of the Hall measurement ($1 \times 10^{10}$ cm$^{-2}$) in 30 min. The high carrier density ($1 \times 10^{16}$ cm$^{-2}$) seen for $1 \times 10^{-4}$ mbar exceeds the typical carrier density values for LAO/STO (and also the theoretically achievable of $3.3 \times 10^{14}$ cm$^{-2}$) by two orders of magnitude. Any electrical characterization would not be able to detect changes of the 2DEG in these samples as they would be overshadowed by 3D conduction. After one hour of annealing in $1 \times 10^{-3}$ mbar the residual conductance is diminished to $1 \times 10^{12}$ cm$^{-2}$ which is two orders of magnitude below the typical carrier density of LAO/STO and therefore changes in electrical behavior from this point can be mainly attributed to the 2DEG. This also holds for the higher pressures of $1 \times 10^{-2}$ mbar where no conductivity could be found after 30 min of annealing. However, since $1 \times 10^{-3}$ mbar is already sufficient to minimize the carrier density of the STO bulk and the pressure should be kept as low as possible, the pressure of $1 \times 10^{-3}$ mbar was chosen for growth and post annealing. The annealing time was set to 1 hour as this decreases the bulk carrier density to a value that is low enough to attribute the conduction behavior to the 2DEG. Interestingly the reoxidation process is completely suppressed in $1 \times 10^{-4}$ mbar even though in these conditions the equilibrium of STO [41] and also LAO/STO [39] would suggest a tendency to more insulating behavior. An explanation would be that the reoxidation process is slowed down to very long times that lie beyond the scale of this experiment.

## 4.4    LAO stoichiometry control

As described in section 3.1, PLD is inherently not an equilibrium process and the exact
stoichiometry of a grown sample is determined by the combination of pressure, laser
fluence and target-to-substrate distance. To determine the stoichiometry of fabricated
thin films, a series of LAO/STO samples were grown, where only the used laser fluence
was varied between 0.64 and 1.28 J/cm$^2$ in steps of 0.16 J/cm$^2$. These correspond
to an incoming laser energy of 16 to 32 mJ in steps of 4 mJ in this particular setup.
Consecutively, the fluence and its influence on thin film deposition was analyzed using
XPS. The LAO thickness was set to 8 uc under a deposition pressure of $1 \times 10^{-3}$ mbar.
The STO substrates were held at a temperature of 800 °C.

The LAO growth was monitored by a high pressure RHEED system (see chap-
ter 3.2). The LAO thickness was set to 8 uc for all depositions, which was determined
from the number of intensity oscillations of the specular spot in the RHEED pattern
(see chapter 3.2). The RHEED pattern before and after deposition is shown for the
example of a used laser fluence of 1.12 J/cm$^2$ in Figure 4.6a and b respectively. The
RHEED pattern evolution is qualitatively the same as discussed in chapter 4.1 and
no discrepancies from the discussed behavior could be observed for all of the used
fluences. The intensity oscillations of the specular spots are shown in Figure 4.6c for
all of the 5 used fluences. As expected, the deposition time behaves inversely to the
used laser fluence, leading to the highest deposition rate for the highest fluence of
1.28 J/cm$^2$. The deposition rate determined from the number of pulses needed for one
RHEED oscillation, is plotted over used fluences in Figure 4.6d. A small dependence
for the higher fluences can be seen with a strong increase for lower fluences.

The grown samples of the fluence series were analyzed by XPS to determine the
LAO stoichiometry. For this purpose the La 4$d$ and Al 2$p$ core level spectra were
recorded and analyzed. These two were chosen because of their close binding energies
and because their areas can be reliably determined by applying a simple Shirley
background. The La 4$d$ spectra are shown in Figure 4.7a, where their maximum
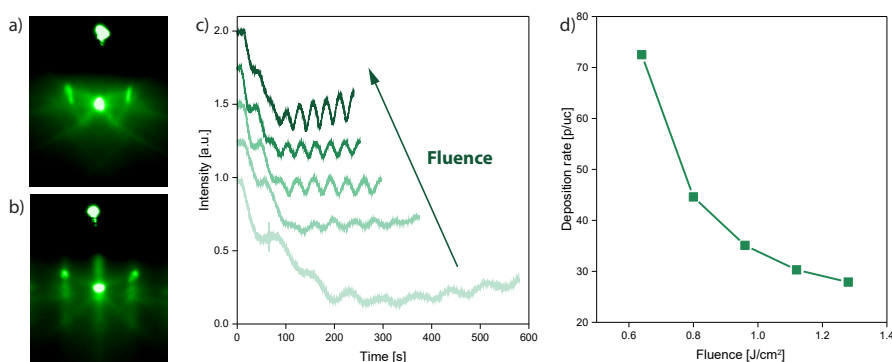


**Figure 4.6:** The RHEED patterns obtained before (a) and after (b) growth are shown. c) Shows
normalized and shifted intensities of the specular spot during the growth of LAO thin films
where increasing laser fluences were used. d) Shows the deposition rate over used the used
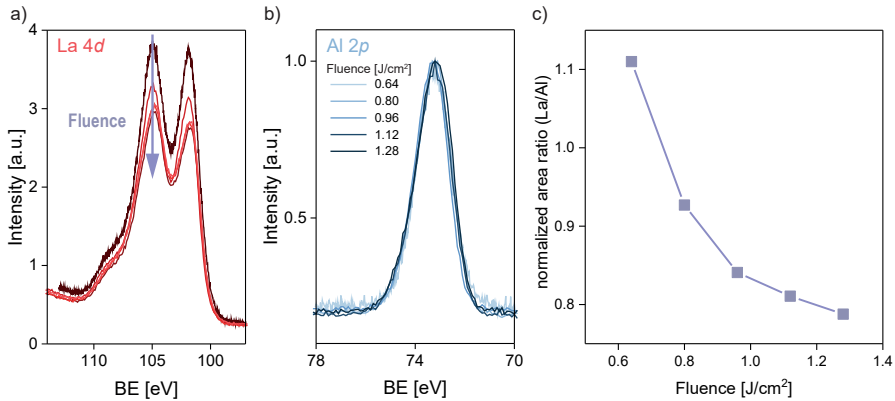Fluence, determined from c).

**Figure 4.7:** XPS core-level spectra are shown. They were recorded from LAO/STO samples where varied laser fluences were used for growth. a) Shows the La 4*d* spectra normalized to the Al 2*p* spectra. b) Shows the normalized Al 2*p* spectra. c) Shows the normalized La/Al area ratios. The normalization was achieved by referencing the areas obtained from a) and b) to a terminated LAO crystal.

intensity is normalized with respect to the maximum intensity of the respective Al 2*p* spectra. The corresponding Al 2*p* spectra are shown in Figure 4.7b with their maximum intensity normalized to one. From these two figures it is already obvious that the La/Al ratio in the LAO thin film is decreasing with increasing laser fluence. As these thin films are grown on a $TiO_2$-terminated STO substrate, the surface of the LAO thin films should be $AlO_2$ terminated. This conclusion stems from the stacking order inside the perovskite structure which is conserved in an epitaxial thin film, where the anion sublattice is continuous throughout the heterostructure and enforces an ABAB stacking of the perovskite planes (see also Figure 2.3). To achieve best comparable results of a stoichiometry analysis, a reference spectra was recorded from an $AlO_2$ terminated LAO (100) single crystal. The $AlO_2$ termination was achieved by a wet etching in diluted HCl after which the crystals were annealed at 1100 °C for 10 h in air. [165, 166] The La 4*d*/Al 2*p* ratio recorded from samples renormalized by the one of the reference yields the La/Al ratio inside the thin film, which is shown in Figure 4.7c. It can be seen that only for the lowest fluence used in this series the La content exceeds the one of Al. All other thin films of higher fluences turned out to be La-deficient with a trend to more La-deficient thin films for a higher fluences. The trend shows a less strongly pronounced dependence for higher fluences.

The $AlO_2$ surface termination of fabricated thin films could be verified by angle dependent XPS measurements. In these experiments, the angle between analyzer and surface is changed to achieve more surface sensitive measurements with lower emission angles. A sketch of the measurement principle is shown in Figure 4.8a. As emitted photoelectrons are traveling longer distances through the material in this way, they are more attenuated leading to a higher relative intensity from photoelectrons generated close to the surface. The area ratios of the La 4*d* to Al 2*p* core-level spectra are shown in Figure 4.8b. The LAO reference is shown in red and LAO thin films fabricated with increasing fluences are shown in light to deep purple. In all of the
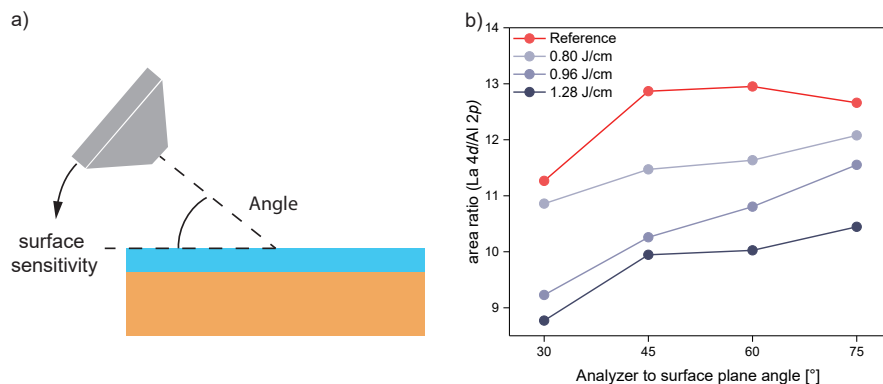
a)



b)

Figure 4.8: a) Shows a sketch of the angle dependent XPS measurement principle. b) Shows the La $4d$/Al $2p$ area ratios for LAO thin films of three different fluences (raising values for light to deep purple) over the analyzer to surface plane angle. A reference measurement, obtained from an AlO$_2$-terminated LAO crystal is shown in red.

analyzed samples, a clear trend to lower La $4d$ contributions for the more surface sensitive measurements is visible. This behavior is most pronounced for the most surface sensitive measurements at an angle of 30°. Through this analysis, the tendency of LAO thin films to form an AlO$_2$ surface termination can be confirmed. The behavior aligns well with the expected one for an epitaxial thin film.

The resulting thin films were furthermore analyzed by AFM to determine their surface topography. A comparison between the typically observed topography of an STO surface to the one of a grown LAO thin film is shown in Figure 4.9. The topography images were 3 dimensionally tilted in a way that aligns the terrace plane with the image plane. The STO substrate topography is shown in Figure 4.9a. A smooth surface, consisting of an evenly distributed terrace structure is observed, where the smooth terrace edges are visible as wavy lines. Edge pits are present as square holes in the surface and correspond to points where dislocations meet the surface leading to higher edge rates. A line scan is marked in dark blue in the topography image and shown in Figure 4.9b. The terrace heights are evenly distributed and are roughly at a value of 0.4 nm which corresponds well to the STO unit cell length of 0.3905 nm. An LAO thin film of 5 uc was grown on the STO substrate. The AFM topography is shown in Figure 4.9c. The topography of the LAO thin film resembles a qualitative copy of the STO topography. The etch pits appear to be larger, although their size can vary depending on the location. Also the terrace height is again around 0.4 nm. The LAO unit cell length is 0.3788 nm and for a strained thin film the expected $c$-lattice constant would be lower. Reported values of the $c$-lattice constants range from 0.3745 nm [33] to 0.378 nm, [167] the first being in well agreement with a Poisson ratio of 0.24. [168] Therefore, the expected difference from 0.4 nm is to small to be observable by the used AFM setup and the measurement agrees with literature observations. Differences in the stoichiometry of the thin film (see Figure 4.7) did not have any influence on the surface topography. Also the thin film thickness did not affect the thin film topography except for films thicker than 20 uc, where signs of relaxation occur, which will be
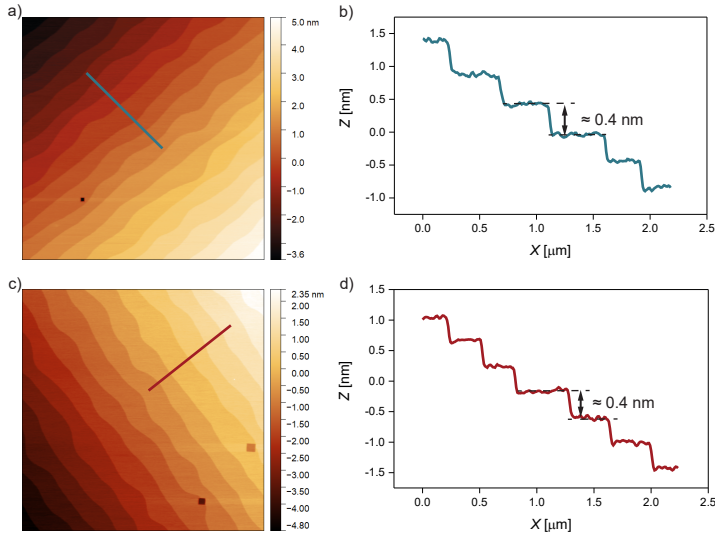
**Figure 4.9:** a) Shows the topography of a STO substrate. The inserted line corresponds to the linescan shown in b). c) Shows the topography of a LAO thin film, grown on the substrate shown in a). The inserted line corresponds to the linescan shown in c). The AFM images are 5 μm × 5 μm in size.

discussed below.

To ensure the crystallinity of grown thin films and confirm an epitaxially strained structure, XRD measurements were conducted, using the (2θ-ω)-geometry. A series of measurements for thin film thicknesses between 4 and 26 uc is shown in Figure 4.10a. For deposition, a fluence of 0.96 J/cm$^2$ was used, making these thin films slightly La-deficient. The expected STO (002) reflex at 46.47° is inserted as dashed line. For the LAO thin film, the reflex observed at 48.72° from 16 and 20 uc thick thin films is inserted as dashed line. For the lower thicknesses, the LAO thin film does not generate enough intensity to be observable as a separate peak, but as an elongated shoulder to the right side of the STO peak. With increasing thin film thickness, the recorded signal intensifies and leads to a broadened peak at roughly 48.72° which corresponds to a $c$-lattice constant of 3.735 Å ±0.008 Å. This is just slightly less than the reported literature values of 3.745 Å. [33] Using the Poisson ratio ($v$) according to $v = 1/(1 - 2(\epsilon_x/\epsilon_z))$ [169, 170], where $\epsilon_x$ is the in-plane strain and $\epsilon_z$ the out-of-plane strain, the XRD data leads to a Poisson ratio of 0.29, when the same reference values are used. This is just slightly more than reported values of 0.24. [168] In addition to the rising thin film peak, thickness oscillations are observable from thicknesses of 12 uc and higher, showing that high quality thin films were achieved. When the LAO thickness is increased to 26 uc, the thin film peak shifts to lower angles and becomes less broadened, which is a sign for relaxation of the thin film material. This can be confirmed by AFM topography images shown in Figure 4.10b. The surface of the LAO thin film shows a distribution of stripes which can be interpreted as small cracks, considering the XRD data. For smaller thicknesses, no such cracks are observable as is
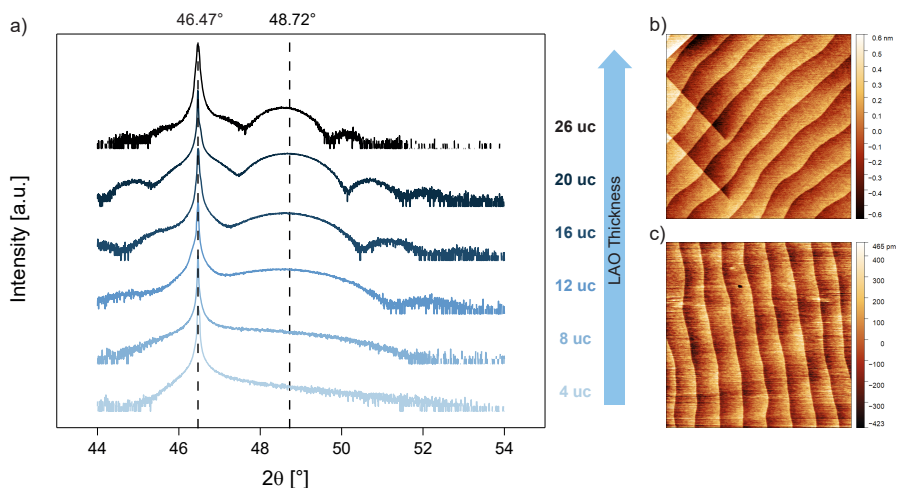
**Figure 4.10:** a) Shows XRD scans in 2-Theta/Omega geometry recorded at the (002) reflex at LAO/STO samples of thicknesses from 4 to 26 uc colored in light blue to dark blue respectively. b) Shows the topography of the 26 uc LAO/STO sample recorded by AFM. c) Shows the topography of the 20 uc LAO/STO sample recorded by AFM. The AFM images are 5 μm × 5 μm in size.

shown in typical topography image of a 20 uc LAO/STO sample shown in Figure 4.10c.

From XRD analysis it can be derived that relaxation of the LAO thin films occurs when at least 26 uc are deposited. However, to ensure that thin films of 20 uc are completely strained, reciprocal space maps (RSM) were recorded. The RSM of a La-deficient, 20 uc thick LAO/STO thin film is shown in Figure 4.11a. The recorded angles of the RSM were converted to the in-plane and out-of-plane lattice constants. For the in-plane lattice constant the LAO thin film is aligned with the STO substrate to a lattice parameter of 3.905 Å, showing that the thin film is almost perfectly strained. A slight shoulder to lower lattice parameters can be observed for the LAO thin film peak, showing a tendency to relax to its natural lattice parameter. However, if the LAO thin film is deposited stoichiometrically, signs of relaxation behavior can be observed at the same thickness. The RSM of a stoichiometric, 20 uc thick LAO/STO sample is shown in Figure 4.11b. The shoulder to lower thicknesses is more pronounced in this case, showing first signs of relaxation. Still, the shoulder is weakly pronounced and the main peak is still strained to the STO lattice. Regarding the out-of-plane lattice constant, both measurements give similar values which are slightly higher for the La-deficient case. These are 3.736 Å for the La-deficient and 3.739 Å for the stoichiometric sample. On none of the two cases, cracks could be observed as was the case for thicker LAO/STO samples (see Figure 4.10). The relaxation of the LAO thin films can, therefore, be suppressed when the LAO thickness is kept at 20 uc for La-deficient samples and is influenced by the thin film stoichiometry. Therefore, more stoichiometric thin films show an earlier tendency to relaxation.
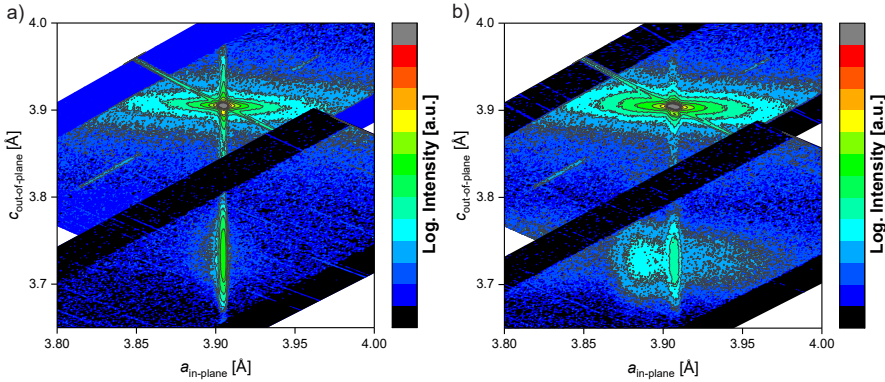
**Figure 4.11:** a) Shows the reciprocal space map, recorded from a La-deficient 20 uc LAO/STO sample. b) Shows the reciprocal space map recorded from a stoichiometric 20 uc LAO/STO sample.

## 4.5 Termination control by growth of SrO

To fabricate locally or completely insulating LAO/STO heterostructures, sub-monolayers to monolayers of SrO were grown on $TiO_2$-terminated STO. As will be shown in chapter 5, insulating local patches can occur in an otherwise conducting LAO/STO interface, since the 2DEG in LAO/STO heterostructures is only present on $TiO_2$-terminated STO. To fabricate a controlled mixed termination, SrO was deposited using a $SrO_2$ target. As the oxygen content in oxide thin film growth is not supplied by the target material but by the surrounding atmosphere, [130] the growth of SrO can be also achieved in this way. $SrO_2$ is more stable than SrO, which makes it easier to handle in practice. Still, in air the material tends to form $SrCO_3$ and $Sr(OH)_2$. Therefore, the target has to be heated above 100°C (150°C was used) to remove humidity. After insertion into UHV, it was kept in vacuum for at least 12 hours before deposition. For best results it is recommended to leave the material in vacuum as much as possible. Also this deposition process is based on previous works, using a fluence of 0.81 J/cm$^2$, a target-to-substrate distance of 44 mm and a deposition pressure of $2 \times 10^{-7}$ mbar. [43] The same PLD chamber was used as for LAO growth.

The growth of SrO starts by covering the substrate material with a monolayer and transitions quickly into a three dimensional island growth mode afterwards. Therefore, its growth is best described to be of the Stranski-Krastanov-type. This behavior is observable in the RHEED pattern, where the intensity of the specular spot first lowers to a plateau and continuously decreases afterwards (see Figure 4.12a). To follow the growth in practice, it is best to follow the behavior of the first order diffracted spot, which reaches its maximum when the substrate is covered with one monolayer. This leads to a crossover of the intensities of the diffracted and the specular spot, which is indicative of the termination conversion from $TiO_2$ to SrO. [44] The RHEED intensities for the growth of one monolayer SrO is shown in Figure 4.12b. The growth was stopped exactly where the diffracted spot reached its maximum in this case.

At the plateau, the coverage by a monolayer of SrO is reached and the continuous
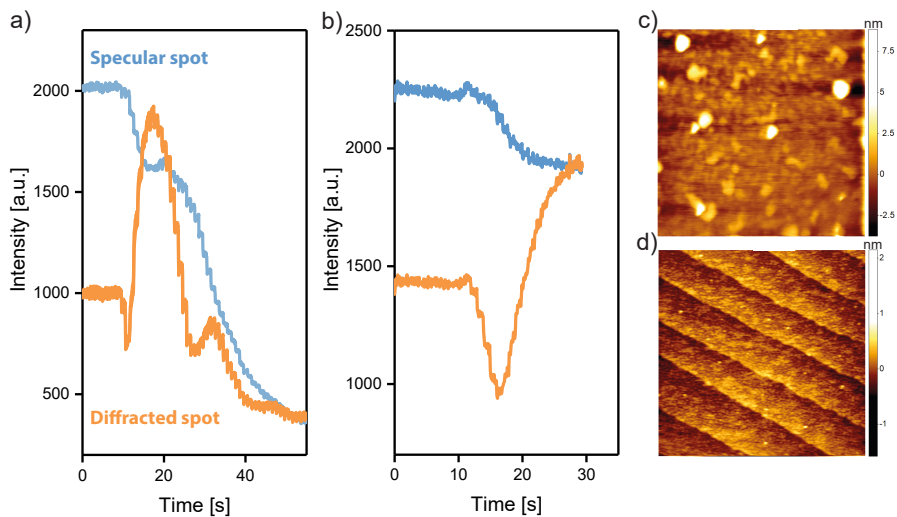
**Figure 4.12:** a) Shows the RHEED oscillations recorded during the growth process of SrO. The specular spot is colored in blue and the first order diffracted spot is colored orange. b) Shows the RHEED oscillations recorded on the growth of a single monolayer of SrO. The same coloring is used as in a. c) Shows an AFM image of the topography resulting from growth of more than 1 uc of SrO as shown in a). d) Shows an AFM image of the topography resulting from growth of 1 uc of SrO as shown in b). The AFM images are 1 μm × 1 μm in size.

decrease thereafter (Figure 4.12a) can be ascribed to three dimensional growth. This could be confirmed by AFM topography images, which show a smooth surface after growth of one monolayer (Figure 4.12d) and a roughened surface, consisting of agglomerated particles, after growth of thicker SrO layers (Figure 4.12c). Because the exact deposition rate varies depending on the exact condition of the target material due to its high sensitivity to humidity, the best way to achieve an exact monolayer is to conduct a test growth beforehand. From this, the number of pulses for one monolayer can be extracted and used for the monolayer growth. This was done for the deposition process shown in Figure 4.12b to achieve the exact point during growth, where one closed monolayer is achieved. When one closed monolayer is deposited, the material stays stable as long as it is not exposed to air. [43] Therefore, the material has to be capped by an LAO overlayer for well defined LAO/SrO/STO samples. However, the reconstruction of SrO poses a difficulty for the fabrication of sub-monolayer LAO/SrO/STO structures.

After the growth process is finished, the SrO monolayer is still restructuring. This process is made visible by a quenching experiment. Figure 4.13a shows the topography of a STO terminated substrate, where 1 pulse of SrO was deposited and quenched to room temperature by turning off the laser heater (see chapter 3.1). The data was recorded using an *in-situ* AFM setup, which is connected to the PLD chamber via a transfer tunnel system. This prevents the reaction of the deposited SrO with atmosphere, which would alter the surface morphology. [43] The SrO is evenly spread across the terrace planes, forming a flat structures of roughly 0.2 nm height without
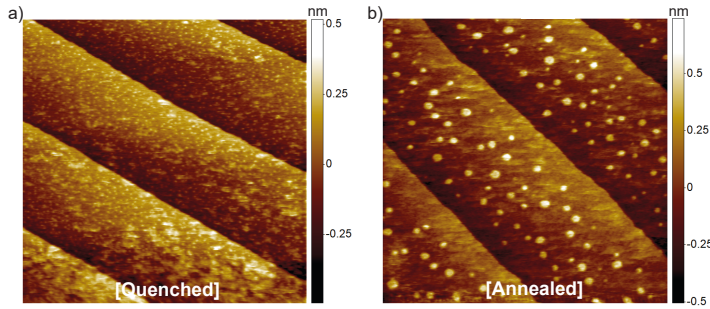
**Figure 4.13:** AFM images are shown which were recorded using *in-situ* in contact mode. a) Shows the topography a TiO$_2$-terminated STO crystal after deposition of 1 pulse of SrO. b) Shows the topography of the same sample after an anneal at 800 °C in $10^{-1}$ mbar oxygen. The AFM images are 1 μm × 1 μm in size.

any higher pillars. A subsequent anneal in oxygen atmosphere ($1 \times 10^{-1}$ mbar) at 800°C for 30 minutes leads to a change in topography as it is shown in Figure 4.13b. The SrO agglomerated into small, evenly spread particles which have a height of 0.4 nm. Therefore, the SrO is quickly changing from a termination of the STO to a secondary phase in the form of SrO which is most likely having a rock salt crystal structure regarding the particle height. This tendency to form rock salt particles makes the fabrication of true A-site terminations difficult and a quick capping with a another layer like LAO has to be conducted to preserve the termination of the STO crystal.

When the SrO layer is capped by LAO, the surface topography of the thin film effectively copies the one observed for SrO/STO surfaces. The growth process is shown in Figure 4.14 by means of RHEED and AFM. The RHEED intensity of the specular and diffracted spots, obtained during the deposition of four pulses of SrO on TiO$_2$-terminated STO, are shown in Figure 4.14a. As expected from growth of thicker SrO layers (see Figure 4.12a), the intensity of the specular spot lowered, while the diffracted spot is first lowered and then heightened. Therefore, the RHEED intensity qualitatively follows the typically observed behavior of SrO growth. When LAO is consecutively deposited on top, thin films are achieved that are comparable to the ones deposited on TiO$_2$-terminated STO. The RHEED intensity oscillations for the consecutive growth of 4 uc LAO are shown in Figure 4.14b. Clear intensity oscillations can be observed, showing that thin films are still grown in a layer-by-layer growth mode on SrO/STO samples.

The surface topography of the SrO layer was measured prior to LAO deposition using an *in-situ* AFM. The AFM image is shown in Figure 4.14c. Comparing this result to the topography of the consecutively grown LAO thin film (Figure 4.14d), it is visible that the two images are qualitatively the same. Therefore, it can be concluded that the SrO layer has little impact on LAO thin film growth, as neither RHEED nor AFM are able to detect any discrepancies from usual LAO growth.
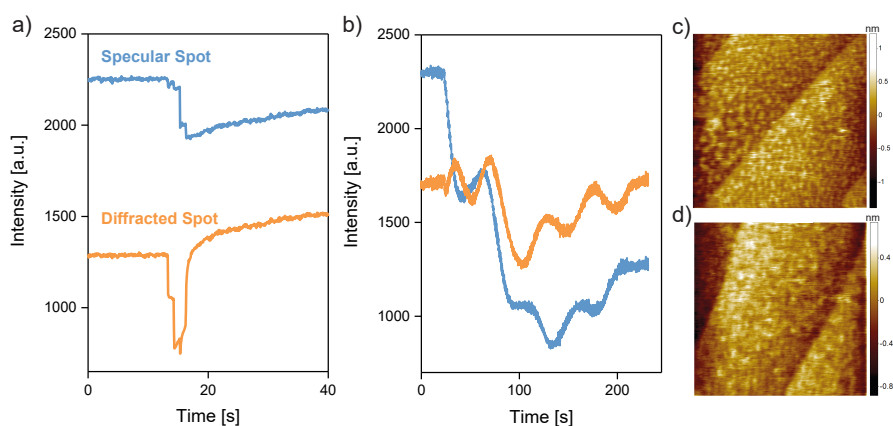
**Figure 4.14:** a) Shows the RHEED intensity of the specular and diffracted spot during deposition of four pulses SrO on $TiO_2$-terminated STO. b) Shows the same RHEED intensities as in a) during the consecutive growth of 4 uc LAO. c) Shows an *in-situ* AFM image of the sample surface after deposition of an SrO layer (corresponding to the RHEED data shown in a). d) Shows an *in-situ* AFM image of the sample surface after consecutive deposition of LAO (corresponding to the RHEED data shown in b). The AFM images are 1 μm × 1 μm in size.

# Chapter 5

# The local formation of the LAO/STO 2DEG

In this chapter it is shown how the scanning probe technique of conductive atomic force microscopy (c-AFM) can be applied to gain insightful information about the local 2DEG distribution. The 2DEG of the LAO/STO system is usually assumed to be completely homogeneous in the lateral dimension. However, inhomogeneities directly influence the electronic behavior of the heterostructure. To enable a deeper understanding of their origin and to check interfaces on their local behavior, various scanning probe techniques have been established to gain information about the LAO/STO 2DEG. These include: Kelvin probe microscopy which revealed how the band alignment of LAO/STO dependents on its amount of oxygen vacancies, [107] magnetic force microscopy which demonstrated magnetic moments to be depending on carrier density and LAO thickness, [108] and scanning superconducting quantum interference device measurements which at low temperatures showed magnetic patches, [171] conducting pathways [98] and strain-tunable magnetic ordering. [99] Furthermore, phase contrast in tapping AFM and lateral force in contact AFM can be used to distinguish surface terminations. [101, 102] The technique of scattering-type scanning near-field optical microscopy (s-SNOM) is able to detect free charge carriers of the 2DEG. [104–106]

The established techniques phase contrast AFM and s-SNOM are going to be used to corroborate that the current maps recorded by c-AFM are a signature of the interfacial 2DEG. This is not a given result, as the LAO/STO 2DEG is inherently a buried structure, which poses an experimental challenge for c-AFM analysis. It has been already shown that c-AFM is capable of writing conducting lines in LAO/STO heterostructures, [79, 109, 110] enabling nanopatterning the interface in this way. [111] Also it could be shown in cross-sectional c-AFM measurements, how the confinement of the LAO/STO 2DEG depends on the used PLD growth conditions. [62] To showcase how c-AFM can extract meaningful information from the LAO/STO system, the 2DEG is patterned in two approaches: 1. By using the variance of STO single crystals during the termination process. 2. By growth of SrO before LAO deposition. The changes of macroscopic electronic behavior can be directly linked to the nanoscopic origin in the interface chemistry of the LAO/STO heterostructure. This chapter was in part already published in Ref. [172].

## 5.1    Resolving the STO surface termination using phase contrast AFM

The 2DEG of the LAO/STO system is highly sensitive to the termination of the substrate surface. As it was discussed in chapter 2.3, the termination of the STO substrate determines the stacking order of the epitaxially grown LAO layer. This in turn leads to either conducting $n$-type interfaces for $TiO_2$-terminated STO ($TiO_2$/LaO stacking) or insulating $p$-type interfaces for SrO-terminated STO (SrO/$AlO_2$ stacking). [13] Even though, there have been reports of hole conduction in $p$-type interfaces [65, 173], the majority of $p$-type interfaces is observed to be insulating. [13, 43–45] To showcase that c-AFM is able to detect laterally occurring inhomogeneities, the inherent sensitivity of the LAO/STO 2DEG to the STO surface termination was used to incorporate insulating regions into the heterointerface.

In the first approach, STO single crystals were chemically etched and annealed as is described in chapter 4.1. The inherent sample-to-sample variation of STO single crystals can lead to different degrees of success of the termination process. Miscut angle between surface and lattice, [174–177] and the defect concentration of the crystal are known drivers for this behavior. [178] Therefore, crystals receiving the same treatment can have different surface termination degrees. [101, 179]

To identify the termination of STO surfaces, phase contrast in AFM measurements is used. The working principle is shown in Figure 5.1. When a cantilever is driven at a constant amplitude to its oscillation frequency, a phase difference between the measured frequency and driver is present. This phase difference depends on the tip-to-sample interaction force, which is determined by the surface chemistry of the analyzed material. [180] When two distinct surfaces are present, like the surface terminations of a STO single crystal, their distribution can be determined by measuring the phase in tapping AFM across the surface. However, care has to be taken when interpreting the phase of tapping AFM measurements. Roughness, tip shape and slow feedback loops also lead to artificially induced phase contrast. To exclude such artifacts, the recorded topography, amplitude and phase of the AFM measurement have to be compared. In this way, artifacts can be identified, as amplitude and phase are affected in such cases.
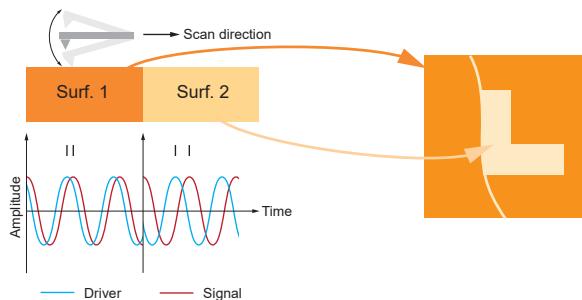


**Figure 5.1:** The working principle of phase contrast in AFM measurements is sketched to the left with an example structure to the right. The Figure was published in Ref. [172] (modified).
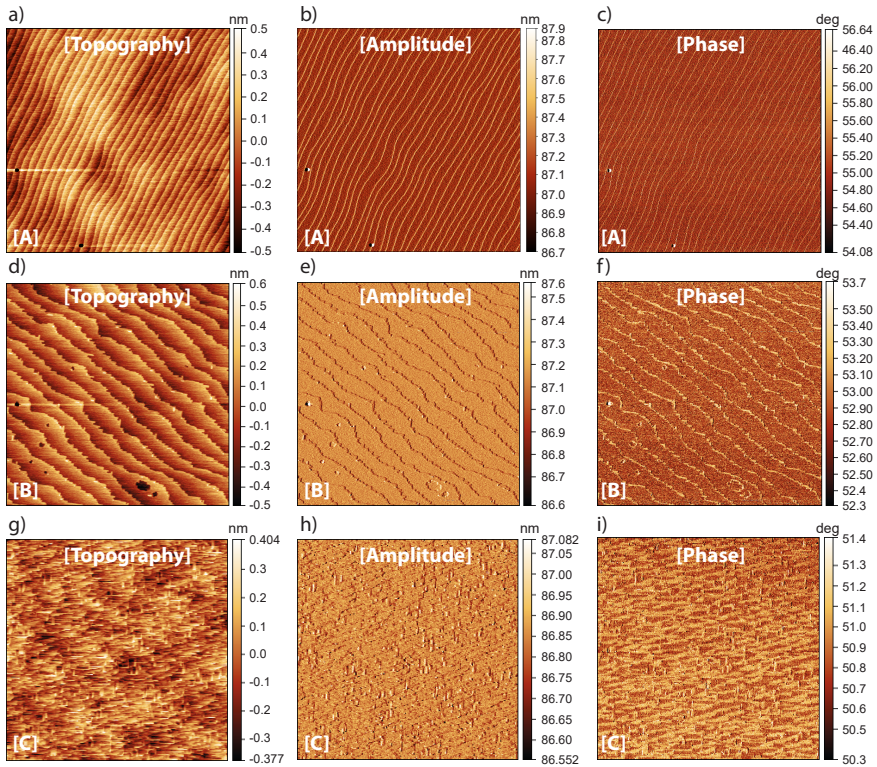
**Figure 5.2:** AFM measurements are shown for three STO single crystals. For a case [A] sample the topography, amplitude and phase are shown in a), b) and c) respectively. For a case [B] sample the topography, amplitude and phase are shown in d), e) and f) respectively. For a case [C] sample the topography, amplitude and phase are shown in g), h) and i) respectively. All AFM images are 5 μm × 5 μm in size.

Three distinct cases which will be named [A], [B] and [C] in the following are observed. Each case shows different termination ratios, even though all substrates were treated in the same manner. The identified surface terminations are shown in Figure 5.2 where the topography, amplitude and phase are shown for each case. Case [A] samples resemble a complete $TiO_2$-termination, discernible by a topography (Figure 5.2a) of smooth terrace planes which are separated by evenly distributed and smooth terrace edges without any kinks or other additional features. The amplitude (Figure 5.2b) shows sharp lines only where the terrace edges were reached due to the height regulation at these positions. The same behavior is observed in the phase signal (Figure 5.2c). As the phase shows no contrast except where height regulation took place, case [A] substrates are completely $TiO_2$-terminated as is expected for etched and annealed samples. [102, 162, 163] The topography of Case [B] substrates (Figure 5.2d) also consists of evenly distributed terrace planes, but the terrace edges are kinked along their complete length. The altered topography does not induce a significant influence on the amplitude signal (Figure 5.2e) compared to case [A] substrates. However, the phase signal (Figure 5.2f) is severely broader than expected from a height regulation. As discussed above, this effect is caused by two distinct tip-to-sample interaction forces which in the case of STO surface can be explained by a partial SrO-termination. [146] Finally, the case [C] substrates represent a more pronounced situation to the case [B] substrates. In addition to the kinked edges, rectangular features extend from the edge over the terrace plane reaching even to the next edge in some cases (Figure 5.2g). While the amplitude (Figure 5.2h) is not as sharply resolved as in case [A] and [B] the phase contrast shows a very distinct pattern over the substrate surface showing much broader features then the amplitude signal would suggest. Therefore, case [C] can be interpreted as more pronounced case [B] surfaces which hold a mixture of $TiO_2$- and SrO-termination.

## 5.2    The local distribution of the LAO/STO 2DEG resolved by c-AFM

On each of the discussed substrate cases ([A], [B] and [C]), LAO thin films were deposited and analyzed in *in-situ* c-AFM. The measurement system is located in a cluster tool where samples are transferred directly from the deposition chamber into the c-AFM chamber through a pumped tunnel section. In this way the influence of surface adsorbates which might influence the measurement, [129, 181–183] can be mostly excluded. The deposition parameters were set to: A fluence of 0.96 J/cm$^2$, a frequency of 1 Hz, a deposition pressure of $1 \times 10^{-3}$ mbar, a target-to-substrate distance of 44 mm and a temperature of 800 ℃. Samples were kept in deposition conditions for 1 hour after growth to ensure that the resistance is dominated by interfacial 2DEG. The insulating LAO top layer poses a significant experimental challenge, as it acts as barrier for electrical currents. To minimize current losses over the LAO layer, only four unit cells were deposited in all cases, which resembles the minimum thickness to achieve a 2DEG in LAO/STO heterostructures. [63]

Samples are glued on a metallic holder using silver paste which also serves as electrode in c-AFM experiments. To connect the 2DEG to the holder, the insulating
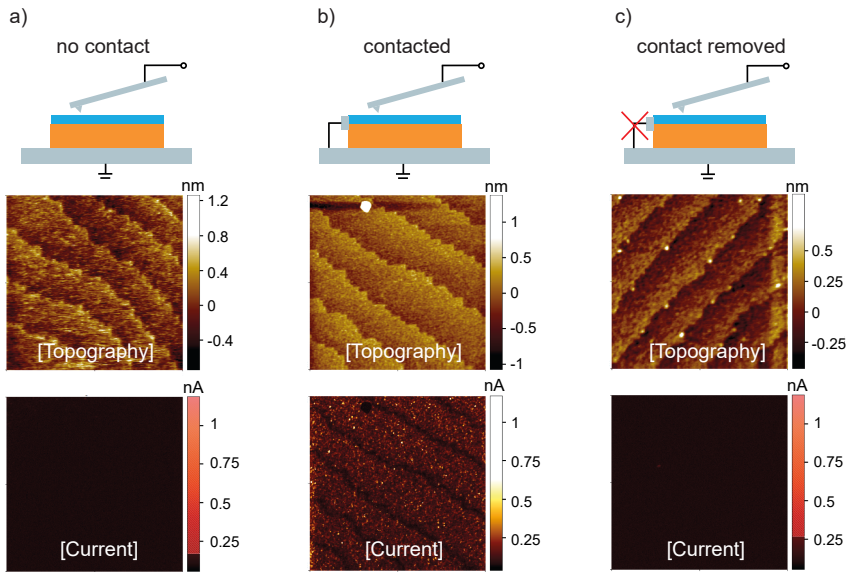
**Figure 5.3:** c-AFM measurements on a LAO/STO sample are shown where the sample was differently contacted. In a) the experiment without any side contact is shown. b) Shows the same experiment with a side contact applied. c) Shows the same experiment where the side contact was removed again. All AFM images are 1 μm × 1 μm in size. The Figure was published in the ESI of Ref. [172].

STO substrate has to be circumvented by applying a side contact. This contact was achieved by applying silver paste to one side of the sample. To proof that the side contact enables current through the 2DEG, a series of measurements is shown in Figure 5.3. c-AFM measurements on samples without an applied side contact show only noise in current maps in the order of the resolution limit of the setup (≈100 pA, as seen in Figure 5.3a). Applying the side contact, leads to significant currents as is shown in Figure 5.3b. Removing the side contact (Figure 5.3c) returns the same result as in the beginning, where no significant current could be detected. These experiments proof that current is transported through the interfacial 2DEG, passing the side electrode to the bottom electrode. Results of c-AFM measurements, conducted in this manner can therefore be related to the local electrical properties of the 2DEG.

The results shown here were recorded using a tip-to-sample voltage of 4 V. Higher voltages than 4 V lead to alterations of the surface topography and local conductance of the analyzed surface. An explanation for these morphology and conductance alterations could lie in a triggered oxygen exchange of the LAO thin film or substrate STO. [184–187] Lower voltages lead to currents which get to close to the resolution limit of the used setup leading first to noisy and ultimately to no currents above noise level. Due to LAO being a band-gap insulator, this behavior is expected, as the thin film poses a barrier for electron transport.

The topography and current maps for 4 uc LAO/STO samples grown on case

**Figure 5.4:** c-AFM measurements on 4 uc LAO/STO samples are shown with the topography in the top row and the current maps in t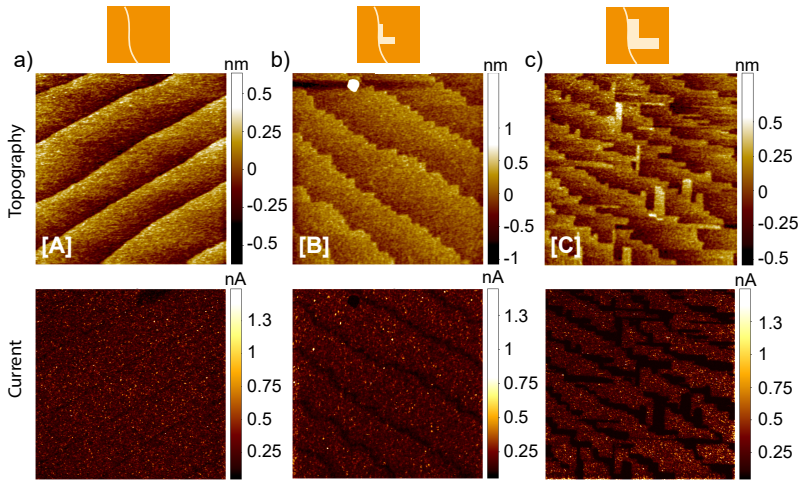he bottom row. a) Shows a measurement performed on a case [A] sample, b) on a case [B] sample and c) on a case [C] sample. All AFM images are 1 μm × 1 μm in size. The Figure was published in Ref. [172] (modified).

[A], [B] and [C] substrates are shown in Figure 5.4. In general, the topography of the underlying substrates is copied by the LAO thin film. For a case [A] sample (Figure 5.4a) a topography of smooth terrace edges and a homogeneous current map with sharp dark lines at the location of the terrace edges is observed. Case [B] samples (Figure 5.4b) show same the kinked features at the terraces edges as seen for the substrates. At these topographic features a broadening of the dark regions is present, extending similar to the phase contrast observed for the substrate (see Figure 5.2f). A similar but more pronounced behavior can be observed for the case [C] sample. Rectangular extended topographic features are present growing out of the terrace edges and reaching across the terrace planes. These features lead to extended dark regions in current maps in a similar way as the kinked ones of case [B] samples. Note that neither topography nor current maps are affected by multiple scans or by the scanning direction. The kinked topographic features (case [B]) as well as the extended rectangular topographic features (case [C]) could be identified by phase contrast AFM as SrO-terminated regions (see Figure 5.2). The dark regions in current maps of c-AFM measurements confirm this interpretation, as SrO-terminated regions lead to a *p*-type interface which are generally observed to be insulating. [13] Furthermore, the presence of both *p*- and *n*-type interface is visualized by the use of c-AFM. This highlights the ability of this method to analyze the local distribution of buried 2DEG resolved in the in-plane direction, which was not used before in this manner.

To provide a more quantitative evaluation of the current maps in Figure 5.4, the current histograms of all three cases are shown in Figure 5.5 where the percentage of a measured current value is shown over current. A histogram obtained from a sample without side contact is included in black to visualize the resolution limit of the system. The case [A] sample shown in light orange has the highest average currents and
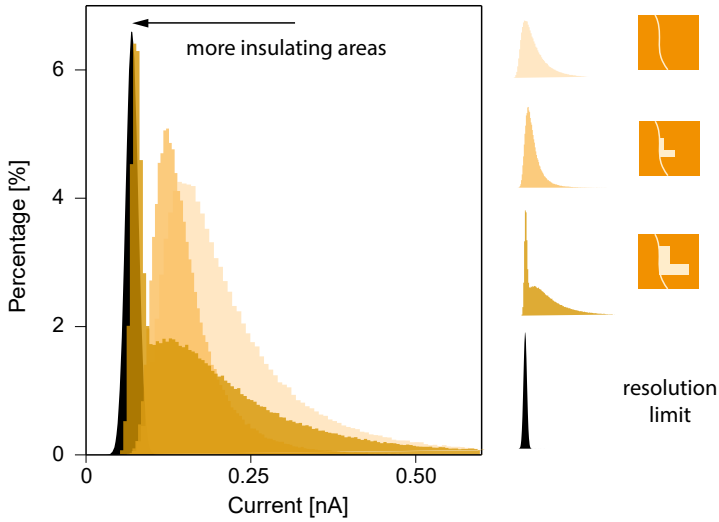
**Figure 5.5:** The current histograms obtained from the current maps in Figure 5.4 are shown for a case [A] (light orange), [B] (orange) and [C] (dark orange) sample. A measurement on a sample without side contact is inserted in black to show the resolution limit.The Figure was published in Ref. [172] (modified).

also the maximum of the current distribution is located at the highest current values. For a case [B] sample, the current distribution is shifted to overall lower currents, showing the same qualitative behavior as the case [A] sample. The case [C] sample shows a strikingly different behavior. A peak in the current distribution is visible which is located at current values of the resolution limit and to higher currents a similar distribution as in [A] and [B] samples is observed. The peak corresponds to the extended dark regions measured in case [C] samples that are effectively insulating. Thus, a clear distinction can be made between insulating and conducting and insulating regions of the sample, despite the overall low currents.

For the transport of current through the insulating LAO layer, a tunneling mechanism is the most likely explanation. $I(V)$ curves, which are shown in Figure 5.6, were recorded on the conducting regions of the heterostructure. These measurements were corrected by the current offset present in the used setup ($\approx 100$ pA). The curves behave fully symmetric over all of the applied voltage sweeps and behave similar to the ones recorded for metal-oxide-semiconductor structures. [188, 189] No degradation is observed as is in the case of scanning measurements. Therefore, significant current amounts can be induced without altering the electrical properties of the interface.

The symmetry of the $I(V)$ characteristic hints at a tunneling mechanism being responsible for electron transport. To further analyze this behavior, the ten recorded $I(V)$ curves were averaged and setup in the characteristic plots for potential tunneling mechanisms. The averaged curve is shown in Figure 5.7a on a linear scale and in Figure 5.7b on a logarithmic scale. For direct tunneling, the current ($I$) should be proportional to the applied voltage ($V$) in the lower voltage regime [190] and transition into an exponential behavior for higher voltages. [191] This behavior is not observed, in
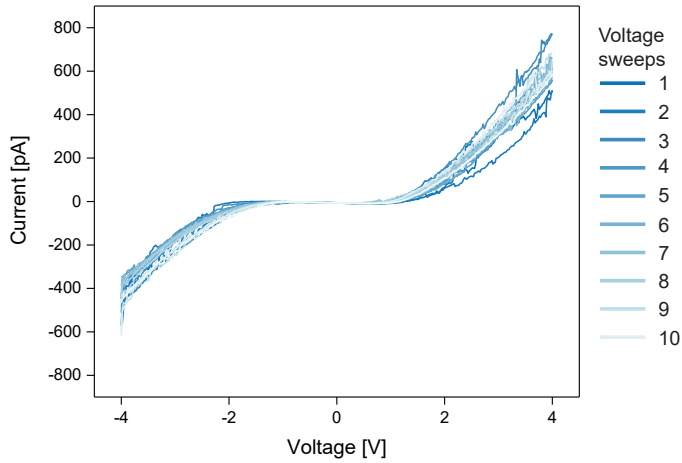
**Figure 5.6:** The $I(V)$ characteristic is shown for a conducting region of the LAO/STO samples analyzed by c-AFM. Ten voltage sweeps are shown in colors from dark to light blue. The Figure was published in the ESI of Ref. [172].

the $I(V)$ curve on the linear (Figure 5.7a) as well as on the logarithmic scale (Figure 5.7b), as the $I(V)$ characteristic is slightly curved. However, other tunneling mechanisms have been reported to contribute to the conduction across LAO. For one, Fowler Nordheim emission was reported in macroscopic tunnel junctions by Singh-Bhalla *et al.*. [192] Therein, a direct tunneling mechanism was observed at lower voltages which transitioned into Fowler Nordheim tunneling for higher voltages. In this case, $\ln(I/V^2)$ should behave linear over $1/V$ which is plotted in Figure 5.7c. No linearity can be seen over the recorded voltages, excluding this tunneling mechanism in the used voltage range for these particular samples. Other reports from Swartz *et al.* [193] show that trap-assisted tunneling (also called Poole-Frenkel tunneling) can impact the conduction across LAO. The corresponding behavior would be a linearity of $\ln(I/V)$ over $V^{1/2}$ which is plotted in Figure 5.7d. Indeed, a linearity can be observed in this case for the higher voltage regime. However, for lower voltages the Poole-Frenkel tunneling can not describe the observed behavior. Therefore, the tunneling current observed in the used heterostructures is most likely a convolution of direct tunneling and Poole-Frenkel tunneling. This makes the observed $I(V)$ curves consistent with comparable tunneling measurements in the literature. The characteristic $I(V)$ behavior, therefore, hints at defect states inside the LAO thin film which assist the tunneling to the analyzed 2DEG.
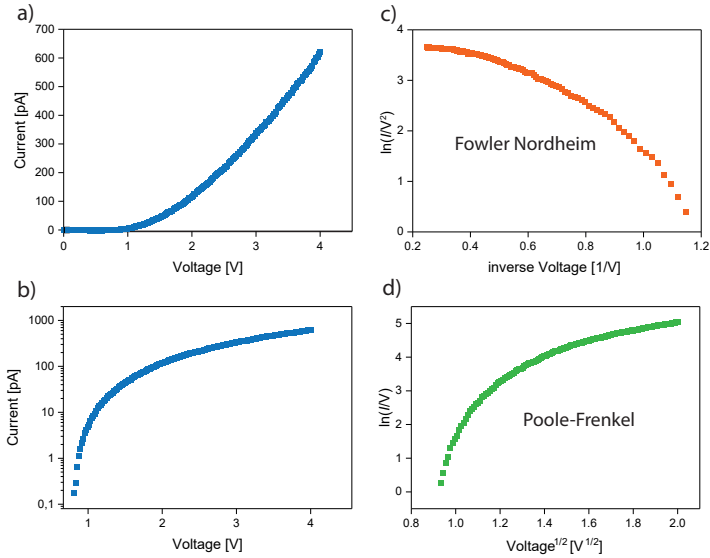
**Figure 5.7:** The characteristic plots for different tunneling mechanisms are shown. Each sub-Figure shows the same data obtained from the averaged plot in Figure 5.6. a) Shows the averaged $I(V)$. b) Shows $I(V)$ on a logarithmic scale. c) Shows $\ln(I/V^2)$ over $1/V$ . d) Shows $\ln(I/V)$ over $V^{1/2}$. The Figure was published in the ESI of Ref. [172].

## 5.3  Correlative scanning optical near-field microscopy measurements

This chapter is a collaborative study with the group of Prof. T. Taubner at the "I. Institute of Physics (IA)" at the RWTH Aachen University, making use of their expertise in scattering-type scanning near-field optical microscopy (s-SNOM). The sample preparation and characterization prior to the presented results were done by the author. Credit for the s-SNOM measurements go to Julian Barnett and Daniel Wendland. Further credit goes to Julian Barnett for providing model calculations for the interpretation of s-SNOM measurements.

Further analysis was conducted using s-SNOM, which allows to circumvent the otherwise limiting Abbé criterion for optical resolution by using the metal-coated cantilever tip of an AFM as optical probe. Through this approach, the technique enables the extraction of local optical properties on the nanoscale showing a high surface sensitivity. [194–196] A sketch of the s-SNOM setup is shown in Figure 5.8a. In the present case, infrared light is used, however, other light sources are also possible. The light is focused on the tip of the cantilever, which in a simplified model, induces a dipole that interacts with the sample as mirror dipole. The interaction is mitigated by strong optical near-fields that arise through the illumination. Due to the dipole-dipole coupling between tip and sample, the back-scattered light depends on the dielectric function of the material. [197] This information has to be extracted by demodulating the back-scattered light by the higher harmonics ($n\Omega$) of the cantilever
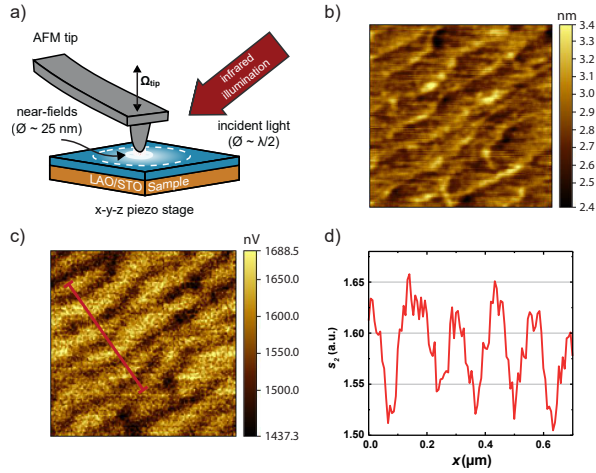
**Figure 5.8:** a) Shows a sketch of the s-SNOM working principle (created by J. Barnett) b) Shows the topography obtained in a s-SNOM measurement on a case [C] sample. c) Shows the second harmonic demodulation order of the optical signal recorded simultaneously with b). Both images are 1 μm × 1 μm in size. d) Shows a line scan of the optical signal as it is shown as red line in c). The Figure was published in Ref. [172].

tapping frequency ($\Omega$). Optical near-fields extend into the sample material up to a certain depth, which can extend up to 100 nm, depending on the dielectric function. This allows for the extraction of subsurface information, while the exponential decay of the near-fields results in a high surface sensitivity. [198–201] The method was chosen, as studies show that it can detect the buried LAO/STO 2DEG [105] and is also able to extract electronic properties like carrier density and mobility by spectroscopic investigation. [104, 106]

The measurements were conducted on a case [C] sample, where the most pronounced degree of inhomogeneity in the 2DEG is observable. The topography image is shown in Figure 5.8b and is qualitatively comparable to topographies recorded using c-AFM (see Figure 5.4c). Kinked features are present along the terrace edges, some extending out of the terrace edge onto the terrace planes. The resolution suffers from broadening, which is induced by the larger tip radii that are necessary to gain a sufficiently strong optical signal. The second demodulation order ($s_2$) of the optical signal is shown in Figure 5.8c. A clear contrast is visible at the location of the terrace edges, where dark regions of lower amplitude are observed. The observed features extending out of the terrace edges lead also to the extension of these dark regions. Therefore, the same behavior is observed as in the current maps recorded by c-AFM. To better quantify the result, a line scan of $s_2$ is shown in Figure 5.8d as marked in red in Figure 5.8c. The area of lower optical amplitude is clearly broader than the area of the topographic terrace edge. From this and the fact that a 0.4 nm high terrace edge is not expected to induce any optical contrast in s-SNOM measurements, it can be concluded that the observed optical contrast is caused by the sample properties rather than induced artifacts. The magnitude of the contrast is about about 25 % in $s_2$, which

fits well to reports for LAO/STO heterostructures with and without a 2DEG of the same spectral range. [104, 105] A further simulation of the optical amplitude could show that the contrast could be induced by either a locally lowered carrier density or a lowered mobility (see S9 in the ESI of Ref. [172] for details).

## 5.4  Influence on macroscopic transport

The low-temperature transport properties of the three distinct cases were analyzed in a mimicked Hall bar structure. The results are shown on a double logarithmic scale in Figure 5.9. For a case [A] sample a typical metallic behavior is observed where the resistance is lowered with lower temperatures and approaches a constant value to the lowest temperatures. For a case [B] sample, the entire curve is shifted to higher values, showing the same qualitative behavior. A strikingly different behavior is visible for the case [C] sample. Here, the resistance is first similar to the case [B] sample from room temperature to about 40 K. To lower temperatures it deviates from the metallic behavior, showing a resistance upturn. [17, 202] The observed resistance upturn could be an indication for Kondo-like behavior, which is related to the influence of magnetic scattering. However, in the present case the resistance upturn is more likely related to a freeze-out of percolation paths due to the temperature dependence of the dielectric function of STO. [54] The residual resistance at 5 K is increasing with the amount of insulating areas detected with c-AFM, showing about 200 $\Omega$ for the case [A] sample, about 400 $\Omega$ for the case [B] sample and about 2000 $\Omega$ for the case [C] sample. Therefore, a clear trend between residual resistance and insulating areas detected by c-AFM is observed, showing how the macroscopic behavior of the analyzed heterostructures depends on the nanoscopic structure of the interfacial 2DEG.
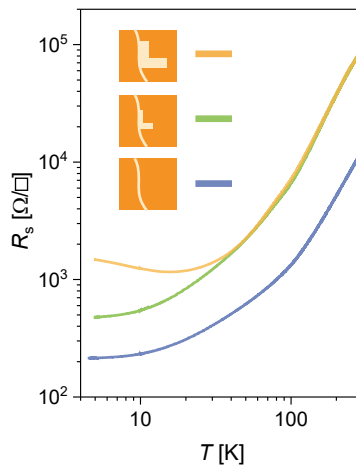


**Figure 5.9:** The low-temperature sheet resistances are shown for a case [A] sample colored in blue, a case [B] sample colored in green and a case [C] sample colored in orange. The figure was published in Ref.: [172].
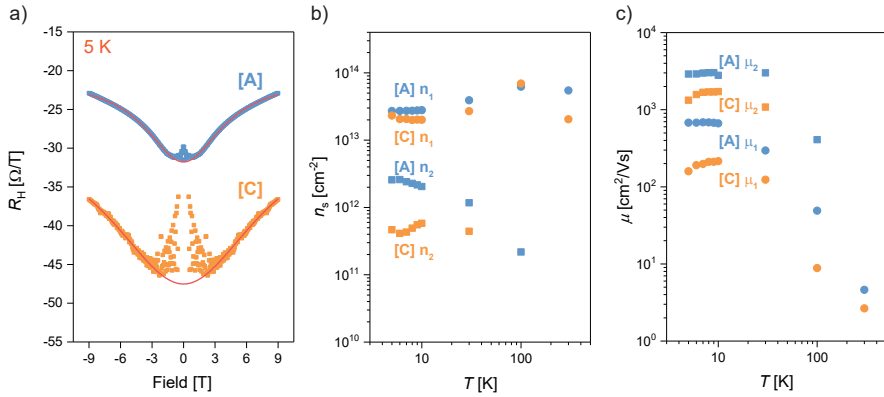
**Figure 5.10:** a) Shows the Hall coefficient measured at 5 K over the applied magnetic field for a case [A] sample in orange and [C] sample in blue. Two carrier model fits are included as red lines. b) Shows the extracted carrier densities from the two carrier model over temperature. c) Shows the extracted mobilities from the two carrier model over temperature. The Figure was published in the ESI of Ref.: [172].

To further distinguish the role of carrier density and mobility, Hall measurements were conducted at low temperatures. The Hall coefficients ($R_H = R_{xy}/B$) for a case [A] and case [C] sample are shown in Figure 5.10a at a temperature of 5 K over the applied magnetic field. For both cases a two carrier model (see chapter 3.4) is applied to extract carrier density and mobility. The determined carrier densities are shown in Figure 5.10b using the same color scheme as used in Figure 5.10a. The carrier density of both carrier types ($n_1$, $n_2$) is lowered for the case [C] sample compared to case [A]. This effect is more pronounced for $n_2$ which is lowered by almost one order of magnitude than for $n_1$. The mobility shown in Figure 5.10c behaves in a similar way. Both mobilities are lowered by roughly the same factor for the case [C] sample compared to case [A]. Due to the insulating areas that are observed in c-AFM and s-SNOM, the observed lowered carrier density and mobility in low-temperature Hall measurements can be explained. As conducting and insulating regions are present, the overall concentration of charge carriers is lowered. A lowered mobility can then be related to the additional scattering centers that are introduced by the insulating regions.

## 5.5   Induced insulating behavior of LAO/STO through SrO growth

To achieve a controlled degree of inhomogeneity in the 2DEG, an attempt was made to insert a defined amount of SrO at the interface of the LAO/STO heterostructure. For this purpose SrO was deposited on terminated STO substrates using PLD, to locally prevent the formation of the 2DEG. An experimental series was conducted where one, three and four pulses of SrO were deposited on TiO$_2$-terminated STO and analyzed *in-situ* using c-AFM. As eight pulses are required for a complete unit cell of SrO, it was

**Figure 5.11:** The topographies of STO samples covered with different degrees of partial SrO monolayers grown by PLD. The data was recorded using an *in-situ* AFM in contact mode. The result for one pulse SrO is shown in a), for three pulses in b) and for four pulses in c). All images are 1 μm × 1 μm in size.

decided to use just a few pulses to achieve minimal amounts of SrO at the interface.
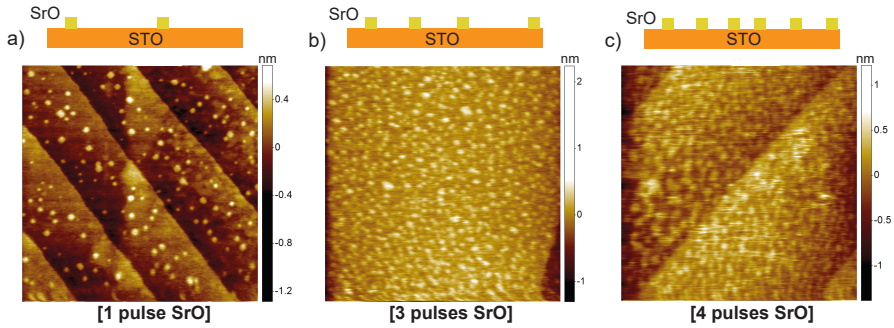
The corresponding topographies are shown in Figure 5.11. The same growth parameters were used as described in chapter 4.5. The material agglomerates into particles of 0.4 nm height. As described in chapter 4.5, this problem can be solved by rapid quenching of the sample temperature immediately after growth. However, as LAO layers are to be deposited on top, this approach is not applicable. The topography for 1 pulse of SrO is shown in Figure 5.11a. Separated particles form in this case, showing the typical height of 0.4 nm but larger particles are also observable. For three pulses of SrO shown in Figure 5.11b, still separated particles are observable, which start to connect in some places. In the case of four pulses of SrO, the particles start to form connected clusters. Note that the height distribution stays roughly the same with the majority of particles being 0.4 nm high. Using the obtained topography images, the coverage with SrO can be determined to be 5.5% for one pulse, 18.5% for three pulses and 30.6% for four pulses. Due to the small residual gaps in the case of four pulses of SrO, the resolution of the AFM setup leads to a high error for the last case of around 10%. The coverages fit to the same amount of SrO being deposited with each pulse. However, a higher coverage would be expected from eight pulses being needed for one unit cell. This can be explained by the agglomeration of the SrO which should have a height of 0.2 nm for the case of a termination layer (see chapter 4.5), leading to a lowered coverage by a factor of 2 if the material forms 0.4 nm particles.

On each of these samples 4 uc of LAO were grown to test if the same local conductivity behavior can be observed as for the STO termination variation. The results are shown in Figure 5.12. For the case of one pulse of SrO (Figure 5.12a), the LAO topography is changed more by the inserted SrO than expected. The complete surface is roughened instead of a few visible particles, as it is observed for SrO deposited on a STO surface (see Figure 5.11a). Under a voltage of 4 V, currents in the range of a few 100 pA are measured. However, the current distribution does not show a distinct pattern. For three pulses of SrO (Figure 5.12b), the topography is similar, but forms a finer surface structure. It is comparable to the one seen for three pulses of SrO on STO (Figure 5.11b). The current image shows similar behavior as for one pulse of SrO,
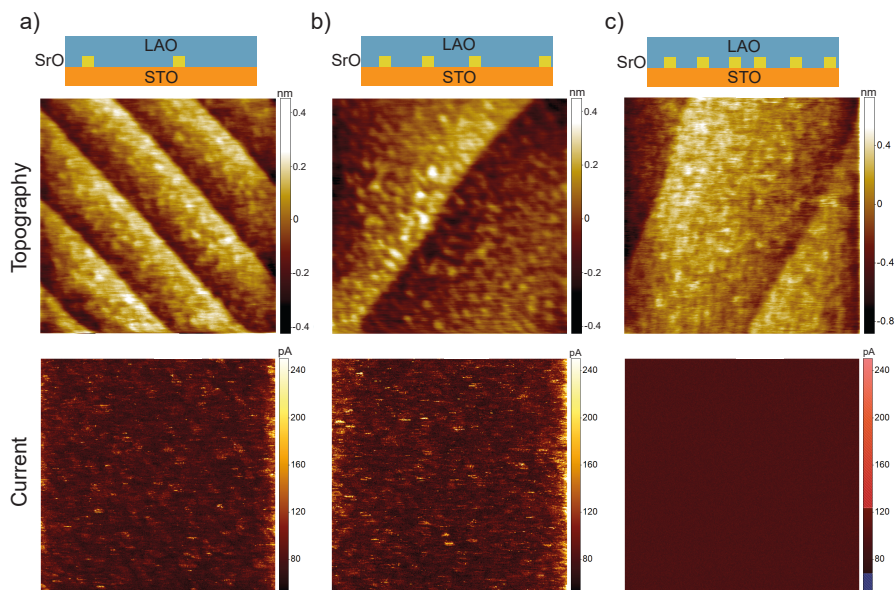
**Figure 5.12:** c-AFM measurements are shown of LAO/SrO/STO samples where the amount of SrO was varied by deposition of a view pulses of SrO. The resulting measurements for one pulse of SrO is shown in a), for three pulses of SrO in b) and for four pulses of SrO in c). All images are 1 μm × 1 μm in size.

showing no clear contrast but a distribution of current which cannot be directly linked to the topography. In the case of four pulses of SrO (Figure 5.12c) the topography shows an even finer structure. However, no current could be measured as can be seen in the current image in Figure 5.12c. Even tough no contrast could be seen in the current maps, the influence on the conductivity of samples is evident by the fully insulating behavior observed for four pulses of SrO.

The SrO content at the interface of the LAO/STO structure influences the resistance behavior as it is shown in Figure 5.13 from room temperature down to 5 K. Already at room temperature, a pronounced increase of the resistance by the interfacial SrO is observed. Going to lower temperatures, LAO/STO usually shows a metallic behavior as shown in light orange. Through the deposition of SrO at the interface, a metal-to-insulator transition is introduced as soon as an amount of one pulse of SrO is present. For one pulse of SrO, the resistance is shifted to higher values and at a temperature of around 10 K, the resistance increases abruptly outside the measurement limit of the setup. For three pulses the overall resistance is increased further and the metal-to-insulator transition shifts to temperature of around 30 K. The behavior for four pulses of SrO is completely altered, showing a semiconductor-like behavior with an increasing resistance to lower temperatures that quickly reaches the measurement limit of the setup.

Comparing the low-temperature behavior to the one obtained from mixed terminated substrates, distinct differences are observed. While the resistance also showed an increase with higher amounts of SrO at the interface, no metal-to-insulator behavior
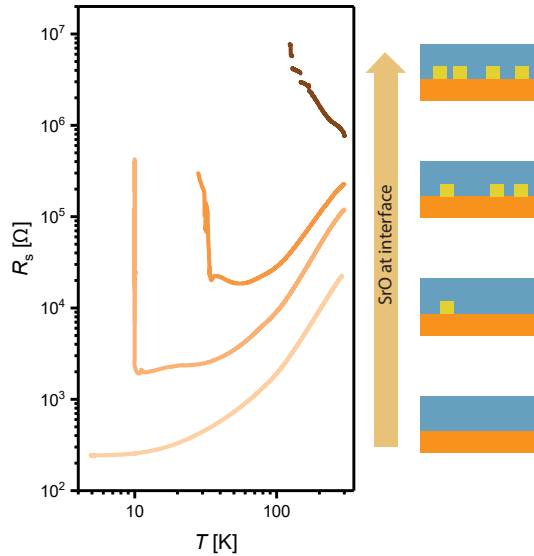
**Figure 5.13:** The low-temperature sheet resistances are shown on a double logarithmic scale for LAO/SrO/STO samples with different amounts of SrO deposited at the interface. In light orange a reference without SrO is shown. Going to dark orange the sheet resistances for samples are shown with 1, 3 and 4 pulses of SrO at the interface.

was observed. A reason for this difference might lie in the different phase the SrO inhabits on mixed terminated STO substrates. In the case of PLD grown SrO, the particles are of 0.4 nm size which corresponds to SrO in rock salt form. However, the low temperature data suggests an influence of the interfacial SrO on the consecutively grown LAO layer, that has to be taken into account. Because judging from the AFM images of the SrO distribution on STO substrates (Figure 5.11), the spacing between expected insulating areas (between SrO particles) should be enough to form a conducting 2DEG. Similarly large $TiO_2$-terminated areas were observed on pure substrates with a natural mixed termination (see Figure 5.4). Therefore, the interface should stay conducting to low temperatures, assuming that the surface structure is maintained during LAO deposition. However, an evenly distributed conductivity is observed in c-AFM on LAO/SrO/STO samples and the LAO surface shows an overall roughening, which hints at a redistribution of the SrO upon deposition of the LAO thin film. This might be caused by the SrO being less stable than the naturally mixed termination of STO substrates. In this scenario the evenly distributed conductivity as well as the low-temperature metal-to-insulator transition may be explained by a reordering of SrO across the interface, leading to "freeze-out" of percolation paths to low temperature. Such a finely distributed 2DEG would be below the resolution limit of the used c-AFM.

From the analysis of c-AFM data and low temperature behavior, the metal-to-insulator transition of LAO/SrO/STO samples seems to be induced by the ordering of the SrO layer. Therefore, the temperature of the SrO growth process was increased to enhance the mobility of the arriving Sr ions on the surface during deposition.
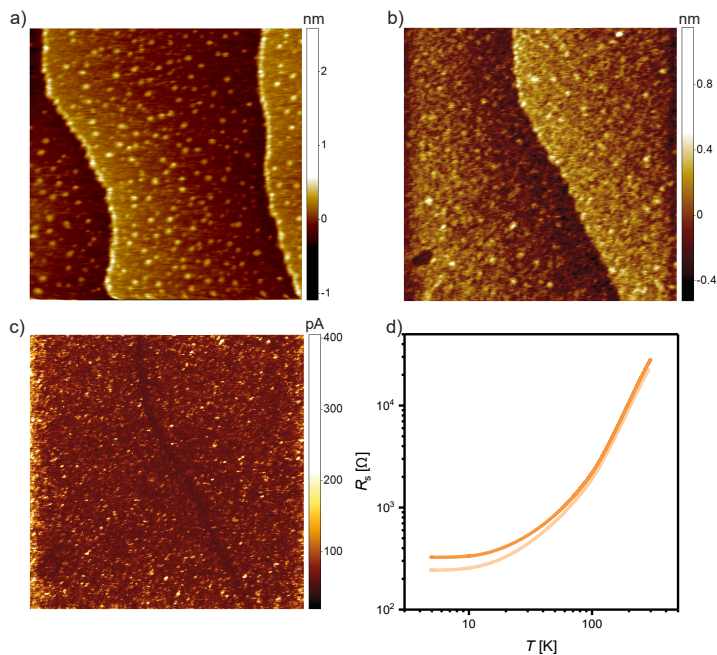
**Figure 5.14:**  a) Shows the topography of a STO surface where one pulse of SrO was deposited at higher temperatures (900°C). b) Shows the topography of a LAO thin film grown on the surface shown in a). c) Shows the current map recorded while scanning the surface shown in b). All images are 1 μm × 1 μm in size. d) Shows the resistance (dark orange) of the sample shown in b) and c) at low temperatures compared to a reference sample without SrO at the interface (light orange).

Under these circumstances the material might be able to order itself to the terrace structure. This hypothesis is based on the observation that at the surface of annealed STO substrates (annealing temperature of 950℃), SrO tends to agglomerate at the terrace edges (see Figure 5.2). Therefore the deposition temperature was increased to 900℃.

The resulting surface topography is shown in Figure 5.14a. The SrO forms a line on top of the terrace edge, confirming that SrO tends to agglomerate at terrace edges in a similar way as during annealing. In general the particles are much smaller than for lower deposition temperatures. Consecutively a LAO layer of 4 uc was grown and analyzed using c-AFM. The recorded topography is shown in Figure 5.14b and the recorded current map is shown in Figure 5.14c. While the ordered SrO at the terrace edges is not clearly discernible in the topography image, it shows a clear effect on the conductivity map, where a small insulating area is observable. Again the areas on the terrace planes which were covered with SrO cannot be resolved in the current map.

The difference between these two observations lies in the order of the SrO. The ordered areas at the terrace edges can be easier resolved as they form a coherent structure. The macroscopic resistance of the the sample turns out to experience no metal-to-insulator transition to low temperatures, in contrast to samples where SrO was deposited at 800℃ (see Figure 5.13). If the metal-to-insulator transition is indeed caused by the freeze out of percolation pathways, the more ordered structure of the SrO would leave larger areas of the 2DEG unaffected. Also this indicates that SrO grown at 900℃ is more stable to the consecutive deposition of LAO, as the reordering of SrO grown at 800℃ presumably lead to the metal-to-insulator transition observed in its LAO/SrO/STO samples.

## 5.6  Chapter summary

The local behavior of the LAO/STO 2DEG was analyzed using scanning probe techniques. Through the use of phase contrast AFM, the distribution of SrO- and $TiO_2$-terminated areas on STO substrates was determined. Distinct topographic features could be identified which show SrO-termination. Analysis employing *in-situ* c-AFM proofed the existence of insulating and conducting regions in LAO/STO samples using substrates that did show mixed terminations in phase contrast AFM. The interpretation could be corroborated by s-SNOM measurements that also showed a distinct contrast in the optical amplitude signal. Simulations of the optical amplitude signal furthermore showed that a locally diminished carrier concentration or mobility are the most likely explanation for the observed contrast. The influence of mixed termination could be seen in low-temperature transport measurements, where the presence of SrO-terminated features lead to an alteration of the low temperature behavior of the samples. The combined results show that the topographic features induce a local 2DEG distribution that can be mapped using c-AFM or s-SNOM. The comparison in low-temperature Hall measurements between samples with different degrees of inhomogeneity revealed that the resistance is not only increased but altered by the presence of increasing amounts of insulating areas. Therefore, macroscopic electronic properties can be linked to the nanoscopic 2DEG distribution. This shows how promising insights into the electronic behavior of 2-dimensional systems can be gained this

way.

The PLD growth of SrO was applied to artificially induce a mixed termination of the STO surface. However, SrO tends to agglomerate during the deposition process, leading to rock-salt particles on the surface of the STO crystal. The growth of LAO/SrO/STO interfaces with sub-monolayer coverage of SrO lead to the introduction of a metal-to-insulator transition of the system to low-temperatures. The transition temperature depends on the amount of SrO present at the interface. Altering the SrO deposition process was applied to influence the ordering of particles which lead to the agglomeration of SrO at the terrace edges of the STO surface. Altering the SrO growth in this manner leads to a suppression of the metal-to-insulator transition at low temperatures and to resolvable contrast in c-AFM measurements. It could be shown how the exact order of SrO is crucial for the understanding of mixed terminated LAO/STO heterointerfaces.

While in this chapter the analysis of the local (in)homogeneity of LAO/STO was the focus of attention, the following chapters are going to address the effects of thermodynamic annealing on the defect structure of the system. As shown in chapter 1, these change the analyzed dimension from the lateral to the vertical direction with respect to the interface, showing how elements distribute across the heterostructure when exposed to a new thermodynamic equilibrium. For this purpose, scanning probe techniques are less suitable and the methods are expanded to include electrical conductance relaxation and near-ambient pressure XPS.

# Chapter 6

# Dynamics of thermodynamic equilibration at the LAO/STO interface

In this chapter, the thermodynamic equilibration behavior of LAO/STO heterostructures is going to be analyzed. For this purpose, the conductance response of LAO/STO on different thermodynamic treatments such as annealing in defined temperatures and $pO_2$ is going to be monitored. For a meaningful interpretation, the equilibration behavior of the underlying STO substrate has to be first understood and discussed, to ensure that the following results on LAO/STO heterostructures can be attributed to the thermodynamic constitution of the interface.

It is known from donor doped STO that the carrier density depends highly on the thermodynamic conditions the system is exposed to. [41, 42] Comparing donor doped STO to LAO/STO, the main difference is that free electrons are not created by donor ions but through charge transfer from the LAO layer. Taking this into account, the two systems are comparable from a defect chemical point of view as the rules elaborated in chapter 2.4 and the Appendix can still be applied. In this case, the formed surface oxygen vacancies on the LAO side are handled as spatially separated donor ions.

The applicability of this concept was shown in previous works, which showed that the carrier density in LAO/STO/LSAT bilayers is reduced in oxidizing conditions by the power of -1/4 over the applied $pO_2$. [39, 40, 92] The $pO_2$ dependence fits to the decrease of conductivity in donor doped STO under oxidizing conditions caused by the incorporation of Sr vacancies. [41] In these experiments, bilayer structures were used to exclude the underlying STO substrate, which shows considerable $p$-type conduction under the used conditions. As these experiments only address states in thermodynamic equilibrium, the question is raised how LAO/STO heterostructures change dynamically.

To trigger the thermodynamic equilibration of oxides such as STO, high temperatures in the range of 950 to 1100 K are usually used over long time scales. Here, the conducting part of the analyzed system is a very thin layer in STO (2DEG) that only extends a few nanometers into the crystal and is capped by an even thinner layer of LAO. In contrast, equilibrium experiments of STO are usually conducted on bulk samples, where equilibration has to be achieved throughout their complete volume
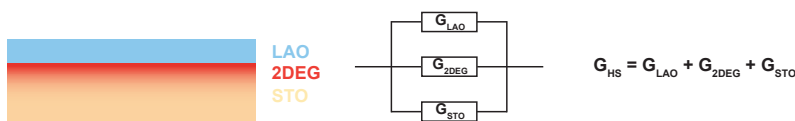
**Figure 6.1:** To the left a sketch of a LAO/STO heterostructure is shown with its equivalent circuit in the middle and the calculation of the conductance of the complete heterostructure to the right.

(usually a few millimeters). Because of this length scale difference of about six orders of magnitude, the equilibration of LAO/STO can be expected to be much faster. This in turn could lower the temperatures necessary for analysis in reasonable time frames. Therefore, the question is going to be approached, how low temperature can be set to trigger the equilibration on reasonable time scales.

ECR measurements (see section 3.5) were conducted as they allow to measure the electrical behavior of a sample while a thermodynamic condition is applied *in-situ*. In this way, information is gained on how fast ionic processes take place at the interface. The measured conductance consists of three parallel contributions which are assigned to the STO substrate, the 2DEG and the LAO thin film as shown in Figure 6.1. Due to the stacking of the system, the resulting equivalent circuit ultimately results in the conductance of the heterostructure ($G_{HS}$) being the sum of the LAO conductance ($G_{LAO}$), the 2DEG conductance ($G_{2DEG}$) and the STO conductance ($G_{STO}$). As the conductivity of LAO is about one order of magnitude lower than STO [38] and due to its low cross sectional area, its contribution to the overall conductance can be neglected. This simplifies the overall conductance to the sum of 2DEG and STO conductance. Therefore, to understand the conductance behavior of LAO/STO the behavior of STO has to be referenced first.

## 6.1   The thermodynamic equilibration behavior of the STO substrate

It is known that the STO conductance is highest in very reducing and in very oxidizing conditions. [38,39] (see also the Appendix). In reducing conditions, the system becomes an *n*-type conductor due to the incorporation of oxygen vacancies. In oxidizing conditions, oxygen vacancies are refilled. As they take part in the ionic compensation of acceptor dopants (impurities in undoped STO), this leads to a transition from *n*- to *p*-type conduction with a low conduction valley in intermediate pressures. To distinguish the conditions where STO conductance becomes dominant over the 2DEG conductance, reference measurements were conducted on a STO single crystal. In a first approach wet 4% $H_2$/Ar and wet Ar gases were used in temperatures of 300 to 600 °C in 50 °C steps. The wetting of the used gases was applied to shift the effective $pO_2$ in the respective gas mixtures to higher values. At each temperature, the atmosphere was changed from wet 4% $H_2$/Ar ($pO_2 \approx 1 \times 10^{-18}$ mbar) to wet Ar ($pO_2 \approx 0.3$ mbar)
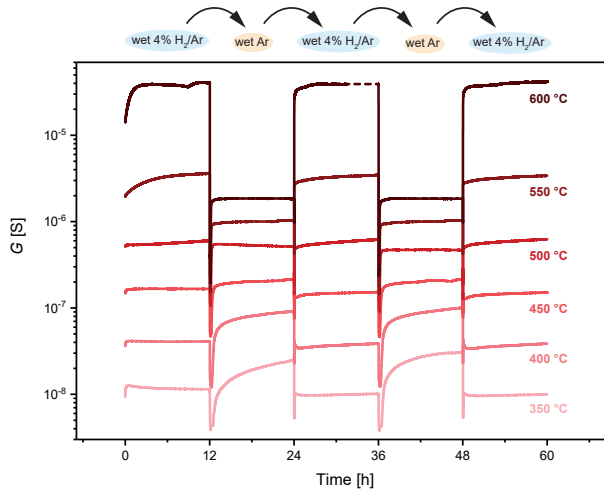
**Figure 6.2:** The conductance of a STO single crystal is plotted over time. The gas atmosphere was switched in intervals of 12 hours between wet 4% $H_2$/Ar and wet Ar in different temperatures.

and back two times. The given $pO_2$ values were obtained from the exhaust gas and measured at 750 °C in a λ-sensor.

All results of the measurement series are shown in Figure 6.2. The measured conductance during the applied process is fully reversible and reproducible, showing that indeed thermodynamic equilibrium reactions are monitored. At 300 °C, no current could be driven through the sample due to high resistances (last measurable value at ≈ 300 kΩ), making it the lower temperature limit for measurable conductance in STO in the used setup. Going from lower to higher temperatures the overall conductance of the STO single crystal increases. In this temperature regime, the mobility is dominated by phonon scattering and therefore lowered for higher temperatures. Consequently, the higher conductance has to be caused by a thermal activation of free charge carriers in the crystal.

At 350 °C the conductance in oxidizing conditions is higher than in reducing conditions. With increasing temperature (to 400 °C) the conductance in reducing conditions increases more rapidly than the one in oxidizing conditions. This continues until the conductance in reducing conditions becomes higher than in oxidizing ones (450 °C to 500 °C). For the highest temperatures (comparing 550 °C with 600 °C) the trend becomes more pronounced making the conductance in reducing conditions considerably higher than in oxidizing conditions.

After switching the atmosphere from reducing to oxidizing, the conductances are first decreasing and after passing a valley increase again. A more detailed view on this behavior is shown in Figure 6.3a. It is consistently observed for all temperatures, showing slower behavior for lower temperatures and faster behavior for higher ones. The complete process takes place in less than an hour at 600 °C and more than 12 hours at 350 °C, hinting at a temperature activated process. The reverse gas exchange from oxidizing to reducing conditions is shown in Figure 6.3b. In general, the conductance
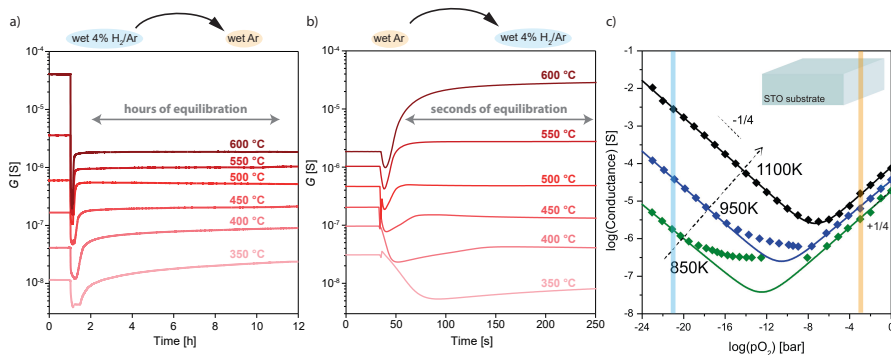
**Figure 6.3:**  a) The sheet conductance of an STO single crystal is shown over time for an atmosphere jump from wet 4% $H_2$/Ar to wet Ar in temperatures from 350 °C to 600 °C. b) Shows the same as a) but for a jump from wet Ar to 4% $H_2$/Ar atmosphere. c) The equilibrium sheet conductance of STO is shown over oxygen partial pressure in various temperatures (by courtesy of [121]). The used $pO_2$ are inserted as lines (blue and orange) in a simplified fashion (see text).

follows according to the previous finding of a decrease, followed by a valley and an increase. The behavior differs in the equilibration time, which is on the scale of seconds instead of hours (for temperatures above 350 °C). Also in this case, temperature accelerates the process. However, at a temperature of 600 °C an additional conductance increase is observed over longer time scales than the lower temperature processes. An explanation for this behavior could be the activation of oxygen vacancy diffusion in this temperature range.

The complete behavior is consistent with the well-known high temperature equilibrium behavior of STO which is shown in Figure 6.3c. The used oxygen partial pressures are inserted in light blue for wet 4% $H_2$/Ar and in light orange for wet Ar. Note here that this is a simplified view, as the real $pO_2$ will depend on temperature leading to higher $pO_2$ for higher temperatures. However, it is sufficient to evaluate the basic principle behind the STO reaction. The equilibrium conductance values in reducing conditions depend more strongly on applied temperature than in oxidizing conditions. This leads to the observed temperature dependent behavior of the equilibrium conductance as seen in Figure 6.3a-b.

The reason for this temperature dependence lies in the different formation enthalpies of oxygen vacancies in reducing and oxidizing conditions. Furthermore, the conductance in intermediate pressures is always lower than for the both extreme cases. In this region of minimal conductance, the STO crystal transitions from a *n*-type to a *p*-type conductor due to the refilling of oxygen vacancies which act as donors and compensate acceptor dopants. The system is not able to immediately jump from one state into the other, but has to slowly equilibrate itself towards the new state, causing the observed valley in ECR experiments. However, the different time scales observed for equilibration in oxidizing and reducing atmospheres (Figure 6.3a and b) cannot be explained by the equilibrium conditions.

One cause for this behavior could lie in an uncertainty of the real $pO_2$ surrounding
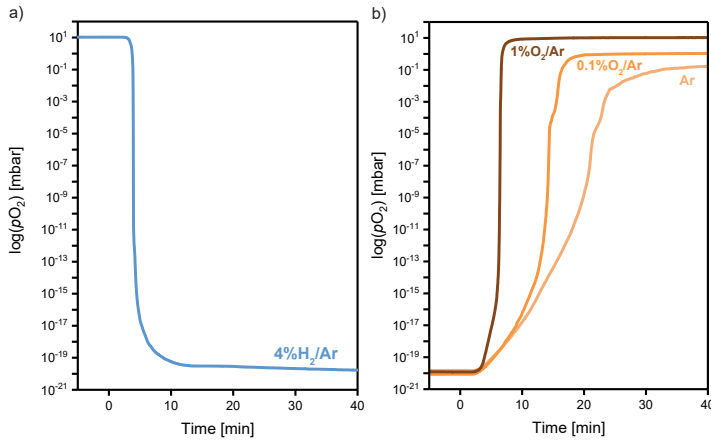
**Figure 6.4:** Oxygen partial pressures recorded from the ECR exhaust gas by a $ZrO_2$ oxygen sensor are shown over time. a) Shows the gas exchange from 1% $O_2$/Ar to 4% $H_2$/Ar (blue). b) Shows the gas exchanges from 4% $H_2$/Ar to Ar (light orange), from 4% $H_2$/Ar to 0.1% $O_2$/Ar (orange) and from 4% $H_2$/Ar to 1% $O_2$/Ar (deep orange).

the sample. While in both cases the atmosphere is changed by the inlet of gas mixtures, the $pO_2$ adjustment is determined in one case by a chemical reaction (4% $H_2$/Ar) and in the other case by convection (Ar). To achieve reducing conditions an $H_2$ mixture is used which reacts with oxygen in an exothermic reaction with a high energy gain. For this reason the $pO_2$ is expected to quickly drop when using a $H_2$ mixture. In contrast, the inlet of oxygen containing gas does not involve a chemical reaction, but purely relies on convection to raise the $pO_2$. A simple yet imperfect way to monitor the oxygen partial pressure evolution over time is to analyze the exhaust gas using a $ZrO_2$ oxygen sensor. Since a certain volume has to be filled between sample and the oxygen sensor, a minimal delay between the measured oxygen partial pressure and the actual pressure surrounding the sample is unavoidable.

A comparison between different gas exchanges is shown in Figure 6.4. Here, the gas exchange event is set to be 0 on the time axes. Compared are the exchanges from 1% $O_2$/Ar to 4% $H_2$/Ar shown in Figure 6.4a and the exchanges from 4% $H_2$/Ar to pure Ar, 0.1% $O_2$/Ar and 1% $O_2$/Ar shown in Figure 6.4b. In all cases certain delay time of roughly 3 minutes is observed between gas exchange event and reaction of the oxygen sensor. This minimal delay of reaction is unavoidable due to the volume between gas inlet and sensor that has to be filled. In the case of a gas exchange to reducing conditions using 4% $H_2$/Ar the complete process is finished in roughly 10 minutes with the majority of the $pO_2$ change being finished after roughly 5 minutes. The curve is characterized by a steep $pO_2$ change that slows down when close to the new equilibrium value. For gas exchanges to oxidizing conditions the necessary time to reach a new $pO_2$ depends on oxygen concentration of the used gas. For the lowest oxygen concentration present in the Ar gas, the equilibration time is around 25 minutes. For 0.1% $O_2$/Ar the equilibration time is roughly 17 minutes and for 1% $O_2$/Ar around 7 minutes.
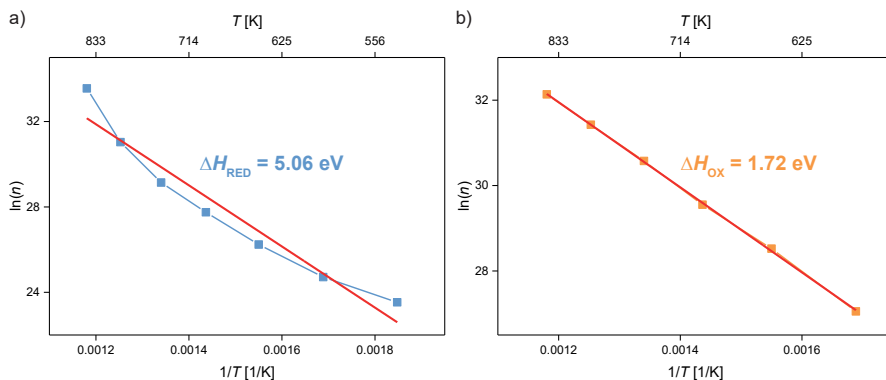
**Figure 6.5:** Arrhenius plots are shown for close to equilibrium values of the STO single crystal in reducing conditions (a) and oxidizing conditions (b).

These delay times have to be taken into consideration when the analyzed system equilibrates on similar or shorter time scales. This seems to be the case for the reducing step, as the conductance reaction of the STO crystal is on the time scale of seconds rather than minutes (see Figure 6.3b). Therefore, the equilibration might be faster, but as the sample reaction is finished before the gas sensor reacts, no certain conclusion can be drawn in this regard. For the step to oxidizing conditions, where an equilibration of the STO substrate is observed over hours (see Figure 6.3a), the $pO_2$ delay cannot explain the conductance behavior as the $pO_2$ is settled in minutes. Therefore, the influence of the gas exchange dynamic is not responsible for the observed behavior, meaning that the oxidation of STO is much slower than the reduction.

To understand why the two equilibration processes (oxidation and reduction) take place on such different time scales, the cause for conduction changes in STO has to be taken into account. In undoped and acceptor doped STO, only oxygen is actively contributing to conductance changes (see chapter A.1). The incorporation of oxygen vacancies leads to $n$-type conductance by intrinsic doping and their annihilation leads to $p$-type conductance as they compensate the small inherent acceptor dopant concentration of the crystal. Only to high temperatures, $p$-type conductance is observed, where a small amount of acceptors is compensated by holes. This means, that the measured conductance is governed by the incorporation and annihilation of oxygen vacancies. The diffusion of oxygen vacancies inside the crystal lattice should not be affected by the surrounding gas atmosphere. However, equilibration processes generally consist of surface exchange and diffusion contributions. [119, 203–205] As the diffusion coefficient of oxygen should not depend on the surrounding $pO_2$, the surface exchange reaction has to be the main difference between the two surrounding atmospheres. Therefore, the surface exchange coefficient is considerably higher in reducing than in oxidizing conditions.

The exact mechanisms of oxygen incorporation are complex and involve multiple reaction steps, [119] which makes it difficult to attribute an exact interpretation of this result. However, it is known that the surface exchange coefficient for the incorporation of oxygen into STO is $pO_2$ dependent. In contrast, the surface exchange coefficient

for the removal of oxygen is inversely depending on the square amount of oxygen vacancies inside STO. However, the $pO_2$ dependency is influenced by the magnitude of the pressure step and the rate limiting step of the surface exchange reaction might also change depending on the surrounding $pO_2$. [206] Therefore, a simple attribution is not possible without applying further investigation, which is refrained from in this reference measurement.

Besides the dynamical changes of conductivity, the equilibrium conductance of the STO single crystal in a given temperature and atmosphere hold additional information. Their temperature dependence corresponds to the thermally activated formation (in reducing conditions) and annihilation (in oxidizing conditions) of oxygen vacancies as discussed in Appendix A.1. The oxidation and reduction enthalpies respectively are extracted from the equilibrium conductance values of the measurements shown in Figure 6.2. For oxidizing conditions at lower temperatures, the equilibrium was not reached during the measurement time. In these cases the last recorded value in oxidizing conditions was taken. Even though some error is induced in this way, it is small as these conductance values are close to equilibrium as can be seen in Figure 6.3.

Using the electron mobility of STO (equation A.19) for reducing and the hole mobility of STO (equation A.20) for oxidizing conditions, the sheet carrier densities are extracted and plotted in an Arrhenius manner in Figure 6.5. The Arrhenius plot for reducing conditions is shown in Figure 6.5a with the calculated reduction enthalpy shown as inset. As the $H_2$ gas mixture was applied to reach the desired $pO_2$, the temperature dependence of the chemical reaction between $H_2$ and $O_2$ to water has to be taken into account. As the reaction directly influences the real $pO_2$ surrounding the sample, its temperature activated Boltzmann term will adulterate the determined reduction activation enthalpy. Taking an approach from Ref. [41], this factor can be corrected. Otherwise, a significant deviation from literature values, which account the real $pO_2$, is observed. Using the thermal activation energy of the reaction determined there ($E_{H_2} \approx 2.59$ eV), the slope of the Arrhenius plot ($m$) in Figure 6.5a relates to the reduction enthalpy as follows $m = (E_{H_2} - \Delta H_{RED})/2k_B$, where $k_B$ is the Boltzmann constant.

The curve does not show a linear behavior but a curvature, showing an increase to higher temperatures. However, applying a linear fit leads to a formation enthalpy of 5.06 eV being only slightly lower than expected from literature values, which show enthalpies from 5.18 eV [207] to 6.1 eV [41]. A reason for the observed non-linearity could be that the $pO_2$ itself is also depending on the real temperature surrounding the sample (aside from the chemical $H_2$ reaction). As the $pO_2$ was measured only at 750 °C from exhaust gas, the given $pO_2$ could be shifted, leading to the observed non-linearity in the Arrhenius plot.

The Arrhenius plot for oxidizing conditions is shown in Figure 6.5b with the extracted oxidation enthalpy from equation A.17 as inset. The obtained value of 1.72 eV is only slightly higher than literature values extracted for acceptor doped STO (1.4 eV). [208] As reduction and oxidation enthalpy are related by $\Delta H_{RED} + \Delta H_{OX} = 2E_g$ where $E_g$ is the band gap energy of STO, a simple mean to test the obtained values is to determine $E_g$. Doing this leads to a $E_g = 3.39$ eV, which is close to the observed literature values (3.2 eV) [55]. Therefore, the high temperature conductance behavior can be analyzed using the ECR setup to extract meaningful thermodynamic information.

## 6.2   The thermodynamic equilibration behavior of LAO/STO heterointerfaces

To distinguish the interfacial conductance of LAO/STO from the STO bulk conductance, the obtained conductances from a STO single crystal in chapter 6.1 are compared to a LAO/STO sample using the same ECR measurement protocol. For the LAO/STO sample, 8 uc LAO were grown close to the stoichiometric point (see chapter 4.1) on a $TiO_2$-terminated STO substrate. The same gas atmospheres as in experiments on STO single crystals were used, switching from wet 4% $H_2$/Ar to wet Ar and back at the same temperatures. The results are shown in Figure 6.6, where the temperature of 400 °C is shown in sub-Figure a), 500 °C in b), 550 °C in c) and 600 °C in d). The LAO/STO conductance shows a decrease for all temperatures when the atmosphere is switched from reducing to oxidizing conditions, which is completely reversed by the subsequent reducing atmosphere. Comparing 400 °C to 500 °C, a larger decrease is observed, which does not significantly change for higher temperatures. Examining the LAO/STO conductance in reducing condition and at 400 °C, the bulk STO conductance is found to be three orders of magnitude lower than the one of LAO/STO. Increasing the temperature to 500 °C leads to an increase of the STO conductance and decrease of LAO/STO conductance but still more than one order of magnitude lies between the two conductances in reducing conditions. At 550 °C the conductance difference diminishes to one order of magnitude and at 600 °C the STO substrate shows comparable conductances as the LAO/STO heterostructure.
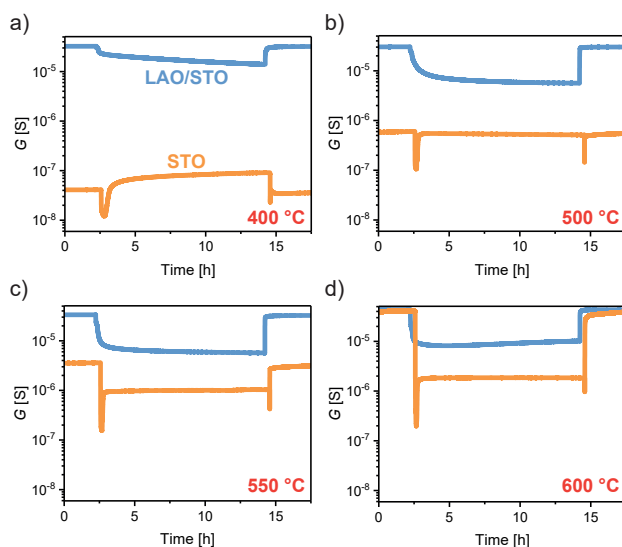


**Figure 6.6:** The conductances of an 8 uc LAO/STO heterostructure and a STO substrate are shown in an ECR experiment, where the atmosphere was switched between wet 4% $H_2$ and wet Ar gas at different temperatures. a) Shows the results for 400 °C, b) for 500 °C, c) for 550 °C and d) for 600 °C.
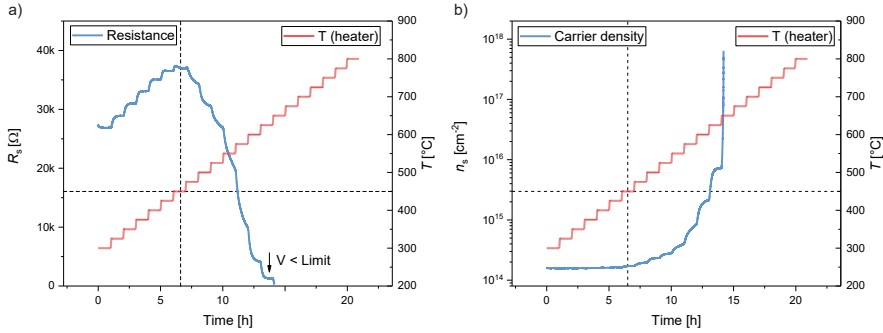
**Figure 6.7:** The resistance of a 8 uc LAO/STO sample is shown in a) while it is heated up in 4% $H_2$/Ar gas. The calculated sheet carrier densities are shown in b) for the same experiment.

Considering only the conductance comparison, the influence of the STO substrate seems to be negligible, if the temperature is not exceeding 500 °C. However, in practice STO substrates show considerable sample to sample variation caused e.g. by the exact impurity concentration. To entirely exclude STO substrate conductance a characterization of the LAO/STO conductance behavior is necessary.

To ensure a negligible contribution of the used STO substrate in conductance measurements the distinctly different temperature dependent conductance behavior of the LAO/STO 2DEG and the STO bulk is used here. While the 2DEG is metallic in moderately reducing conditions [38] and therefore should show an decrease of conductance with increasing temperature, STO is a thermally activated semiconductor at the used temperatures and should show a decreasing resistance with increasing temperature. Therefore, the conductance of LAO/STO was monitored during heating from 300 to 800 °C under 4% $H_2$/Ar gas flow. The result is shown in Figure 6.7a, where the resistance of the sample is plotted over time in blue and the applied temperature in red. The metallic 2DEG behavior is observed up until 450 °C, where the resistance is increased through lowered mobility caused by phonon scattering. For the steps to higher temperature of 475 °C and above, the resistance decreases continuously until the measured voltage falls below the resolution limit of the setup under the constant current used here.

The resistance drop is most likely caused by the thermally activated STO substrate conductance reaching similar values as the 2DEG forming a parallel conductor as shown in Figure 6.1. Using equation A.19, the measured sheet resistance is translated into the corresponding sheet carrier density and plotted in Figure 6.7b. Here it is assumed that the lowering of mobility due to temperature increase behaves similar to the one of pure STO. Reasonable values of sheet carrier densities of around $2 \times 10^{14}$ cm$^{-2}$ are obtained staying constant for temperatures below 450 °C. Above 450 °C the carrier density exponentially increases as expected from the observed resistance behavior. Consequently, the exact temperature above which the STO conductance dominates the measurements could be determined to be around 475 °C. Therefore, the result sets the upper limit of available temperatures to analyze interfacial conductance of the used LAO/STO sample.
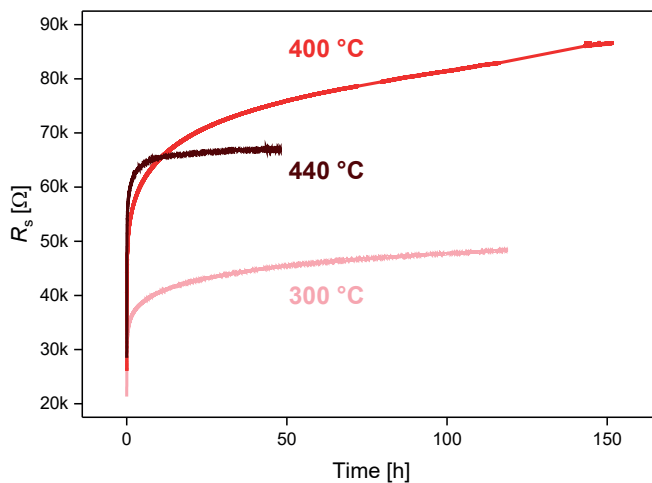
**Figure 6.8:** The resistance of a 8 uc LAO/STO sample is shown during a change of atmosphere from 4% $H_2$/Ar to 1% $O_2$ at temperatures of 300 ℃, 400 ℃ and 440 ℃.

Ionic equilibration processes take place on extremely long time scales when the used temperature is low. To ensure a reasonable investment of time for the experimental series, the equilibration process from 4% $H_2$/Ar to 1% $O_2$/Ar gas was monitored over temperatures of 300, 400 and 440 ℃ as shown in Figure 6.8. The equilibration process at 300 ℃ takes more than 120 hours where the experiment was aborted. Also at 400 ℃ the time to reach a new equilibrium state is longer than 150 hours, which still makes the experiment inconvenient. However, a slight increase to 440 ℃ is enough to bring the equilibration process of the sample to the time scale of roughly 48 hours. This leaves a tight temperature range for experiments from too high temperatures, where transport is dominated by the STO substrate and too low temperatures, where the investment of time becomes unreasonably high. The same sample of 8 uc LAO/STO was, therefore, systematically investigated in the temperature range from 430 ℃ to 460 ℃. At temperatures of 430 ℃, the time scales become already larger than desired but it was still included to increase the data pool. The upper temperature of 460 ℃, was determined by a fine tuning of the experiment shown in Figure 6.7 where an increasing resistance could still be observed when heating from 450 to 460 ℃. Steps of 10 ℃ were chosen and the atmosphere was switched between 4% $H_2$/Ar and 1% $O_2$/Ar to ensure a fast atmosphere change inside the chamber (see Figure 6.4).

The results are shown in Figure 6.9. Through the introduction of an oxidizing atmosphere (Figure 6.9a), the conductance is significantly lowered from values of roughly $3.5 \times 10^{-4}$ to $1.5 \times 10^{-4}$ S. The equilibration time increases with temperature as can be most profoundly seen when comparing 430 ℃ with higher temperatures. The reverse process, switching from oxidizing to reducing conditions (Figure 6.9b), takes place on much smaller time scales, which is similar to the observed behavior
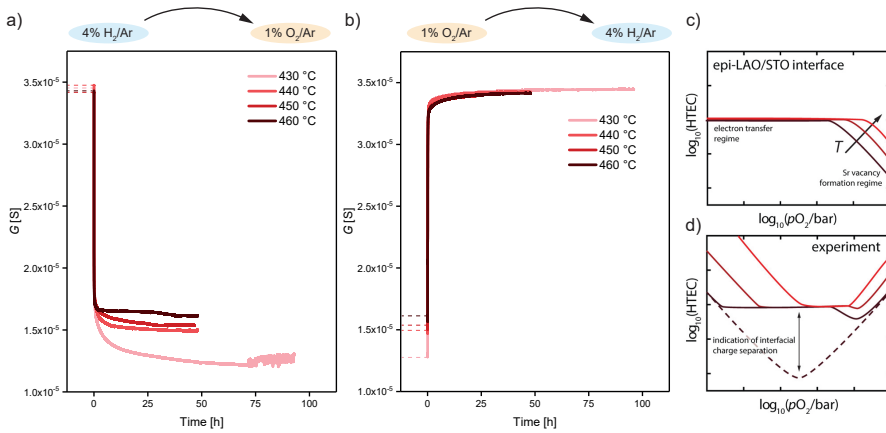
**Figure 6.9:** The conductivity of a 8 uc LAO/STO sample is shown at temperatures from 430 to 460 °C. a) Shows the conductivity of a gas exchange from 4% $H_2$/Ar to 1% $O_2$/Ar. b) Shows the conductivity of a gas exchange from 1% $O_2$/Ar to 4% $H_2$/Ar. c) Shows a schematic of the 2DEG conductivity contribution in thermodynamic equilibria under ionic charge transfer. d) Shows the combined conductance of bulk STO and interfacial 2DEG in thermodynamic equilibria under ionic charge transfer. Sub-figures c) and d) are by courtesy of Ref.: [92].

of STO. Furthermore, the equilibrium conductance states in oxidizing atmosphere depend on the the applied temperature while this behavior is only very weakly present for reducing conditions. The weak temperature dependence of the reduced state can be related to normal metallic temperature behavior. As the influence of the STO substrate was carefully considered for the chosen experimental parameters, the temperature dependence of the oxidized state has to be caused by thermodynamically activated defects related to the 2DEG. Further comparing the time scales of LAO/STO equilibration in oxidizing conditions (see Figure 6.9a) to the one of STO (see Figure 6.3a) shows that LAO/STO needs roughly ten times as long as STO to reach equilibrium. This could indicate, that the equilibration process of LAO/STO is not governed by the same defect species (oxygen vacancies) as STO. Alternatively, the surface exchange reaction coefficient could be also lowered by LAO layer.

With respect to defect chemistry, LAO/STO is comparable to donor doped STO leading to two possible defect scenarios causing the lowered conductivity. Either oxygen vacancies are refilled or Sr vacancies are introduced (see chapter A.2). A source of oxygen vacancies in LAO/STO might be their incorporation during thin film growth, but as the shown equilibration process is fully reversible, this possibility can be ruled out. A contribution of thermodynamically induced oxygen vacancies in the STO substrate, caused by the reducing atmosphere should have led to a visible increase of conductance during the heat-up experiment in 4% $H_2$/Ar (Figure 6.7), which was not observed. Additionally a high contribution from oxygen vacancies is not expected from thermodynamic equilibrium at the used $pO_2$, as can be directly derived from STO reference measurements (see Figure 6.3c). Therefore, a refill of oxygen vacancies can be mostly excluded to be the cause for the observed conductivity drop.

However, an incorporation of Sr vacancies could explain the lowered conductivity consistently as their formation is an electron depleting effect. Experiments on Nb-doped STO showed that Sr vacancies can form in similar $pO_2$ and temperatures. [42, 90] For LAO/STO, results from high temperature equilibrium conductance indicate the important role of Sr vacancies. [39] An excerpt from Ref. [92] sketches the theoretically observed $pO_2$ dependence of the expected equilibrium conductance of LAO/STO when considering Sr vacancies in a defect chemical model at different temperatures and is shown in Figure 6.9c. In oxidizing conditions, where the formation of Sr vacancies is expected, the LAO/STO 2DEG is depleted by their formation. The conductivity should remain constant for reducing and moderate $pO_2$. In more oxidizing atmospheres, a drop of the conductivity with a slope of -1/4 is expected as this corresponds to the $pO_2$ dependence predicted for Sr vacancy formation. [41] With increasing temperature the conductivity recovers closer to its original value, which is dominated by the electronic charge transfer of the LAO/STO interface. A similar temperature dependence is typically observed for donor doped STO [41] and is caused by the exothermic nature of the defect chemical reaction leading to Sr vacancy formation. The formation of the partial Schottky defect (equation A.8) can in this context be formulated as a reaction with the surrounding gaseous oxygen [39]

$$V''_{Sr} + (SrO)_{s.p.} \rightleftharpoons Sr^x_{Sr} + \frac{1}{2}O_2 + 2e' \tag{6.1}$$
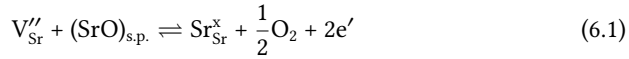
which leads to the mass action law of

$$\frac{pO_2 n^2}{[V''_{Sr}]} = K^S_0 \exp\left(-\frac{\Delta H_S}{k_B T}\right) \tag{6.2}$$

Using these equations, the activation energy of the Sr vacancy formation can be determined by analyzing the systems carrier density. In experiment, the conductance of the heterostructure normally consists of STO bulk and 2DEG conductance, leading to a convoluted conductance as sketched in Figure 6.9d. However, through the application of careful referencing, as discussed above, the contribution of the STO substrate to the overall conductance can be neglected. Therefore, the conductance behavior of the analyzed LAO/STO sample can be attributed to the 2DEG which corresponds to the behavior sketched in Figure 6.9c.

The equilibrium carrier density of the oxidized state are plotted in an Arrhenius manner to verify the presence of a temperature activated process by extracting the activation energy $\Delta H_S$. The resulting Arrhenius plot is shown in Figure 6.10 where the calculated $\Delta H_S$ is shown as inset. The obtained value of 0.81 eV is lower than the value obtained by high temperature equilibrium measurements, where roughly 2 eV were determined [39]. Also compared to values determined for bulk STO (2.5 eV) the activation energy is much lower. [41] Therefore, the observed temperature dependence appears to be much weaker than expected. Consequently, the energy needed to form Sr vacancies in the used LAO/STO heterostructures would be considerably lower than in bulk STO, making the defects "easier" to form. Various reasons could be responsible, such as the very small temperature window which could induce a larger error. Furthermore, in high temperature equilibrium experiments, LAO/STO/LSAT samples were used which leads to a different strain in the system, which can influence
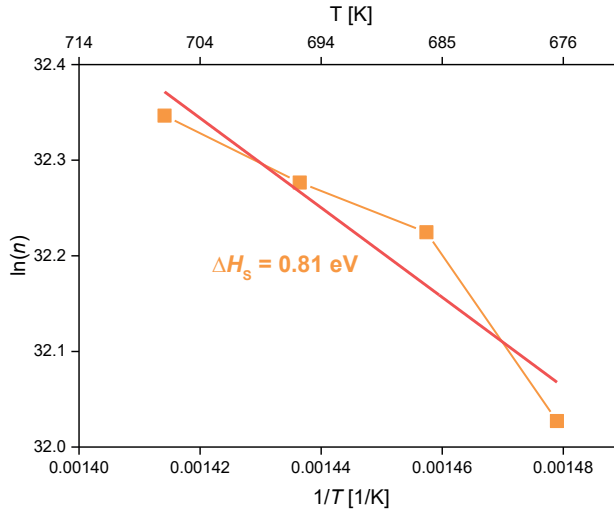
**Figure 6.10:** An Arrhenius plot of the equilibrium carrier density obtained from a stoichiometric 8 uc LAO/STO sample in 1% $O_2$ atmosphere is shown. The determined activation energy as derived from equation 6.2 is shown as inset.

the formation enthalpy of defects in STO. [209] Also it is unknown how the exact composition of the LAO thin film influences the chemical potential at its interface to STO. The defect formation can be highly influenced by the overlayer, as could be seen in experiments, where STO was capped with different materials. [210] However, even though the activation energy is low, a temperature dependent defect concentration can be related to lowered conductivity of the LAO/STO interface in ECR experiments.

After the presence of thermodynamically activated defect formation could be shown, the dynamics of the oxidation and reduction process are further analyzed. For this purpose, a normalization of the conductances has to be carried out in the form of

$$\bar{G} = \frac{G_{S,t} - G_{S,0}}{G_{S,\infty} - G_{S,0}} \qquad (6.3)$$

Here, the sheet conductance at a specific time $t$ is $G_{S,t}$, the sheet conductance at $t = 0$ is $G_{S,0}$ and the sheet conductance at $t = \infty$ is $G_{S,\infty}$. $t = 0$ denotes the gas exchange event and $xt\infty$ denotes the point where enough time has passed to reach a new equilibrium state. As the conductance equilibration of the analyzed system corresponds to a changed chemical defect state, the dynamics of defect equilibration can be compared through the normalized conductances. Defect formation involves the movement of ions out of the material over one of the crystal surfaces. The process involves for one, the diffusion of elements in the bulk of the material and second, an exchange reaction of the material with the surrounding atmosphere. [203] This surface exchange reaction is well understood for the oxygen exchange in STO, where multiple reaction steps are involved. [119] It could be shown that for acceptor- and undoped STO the surface exchange is the rate limiting step for lower temperatures (shown up to 730 ℃). [211]

The oxygen exchange behavior could then be described by the use of two surface exchange coefficients. [205] However, as was indicated in this chapter for the
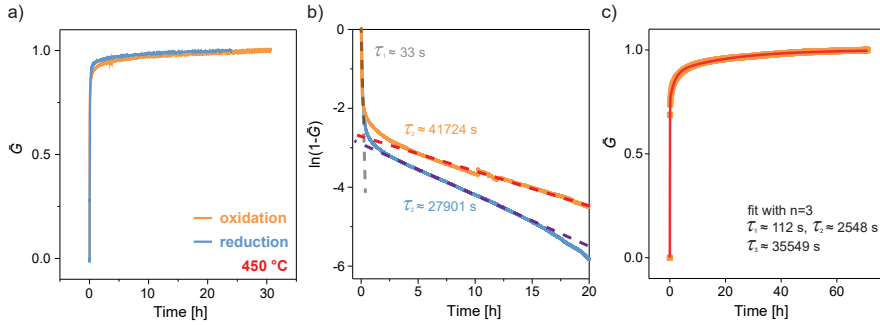
**Figure 6.11:** a) Shows the normalized conductances $\bar{G}$ of a 8 uc LAO/STO sample at 450 °C from reducing to oxidizing atmosphere (orange) and from oxidizing to reducing atmosphere (blue). b) Shows the ln(1-$\bar{G}$) of the conductances shown in a) with linear behavior inserted as dashed lines. c) Shows the normalized conductance shown in a) for the oxidizing step with a surface exchange fit of n=3 included as red line.

LAO/STO interface, the cause for the lowered conductivity are not oxygen but strontium vacancies. Therefore, the dynamics of the process are expected to be different, as e.g. the surface reaction product of strontium is a solid precipitate instead of a gaseous molecule. The conductance determining region, where defects are expected to form, is highly confined. It consists of the few-nanometer-wide 2DEG and the LAO thin film. Due to this confinement, the defect formation and dynamics might be different. As the length scales for diffusing ions are much smaller than compared to bulk samples, the process should be more dominated by the surface exchange reaction. Consequently, it is reasonable to assume a mostly surface dominated process instead of a bulk dominated process. As Sr cations are supposedly precipitating into the LAO layer in this hypothetical scenario, it is more precise to use the term interface exchange reaction. As done by Kerman et al., [205] a conductance change facilitated only by surface/interface exchange reactions can be described in the following manner

$$\bar{G} = 1 - \sum_{i=1}^{n} A_i \exp\left(-\frac{t}{\tau_i}\right) \tag{6.4}$$

Here, $A_i$ denotes the participating surface area with $\tau_i$ being the corresponding surface exchange coefficient. The complete conductance change is described by the sum of all parallel surface exchange processes to a total of $n$ processes.

The normalized conductances are shown in Figure 6.11a for the example of a 8 uc LAO/STO sample at 450 °C. It is visible that the oxidation process takes longer than the reduction process, which is the case for all analyzed temperatures. In both cases a fast initial conductance change is observed, which slows to a longer equilibration taking hours to complete. To test if the process can be described by a single or multiple surface/interface exchange processes, the ln(1-$\bar{G}$) is plotted in Figure 6.11b. According to equation 6.4 a linear behavior would be observed when only one surface exchange process is active.

For both processes it is clearly visible that at least two coefficients have to be applied. Additionally it can be seen that the equilibration of the reducing step shows

a steeper slope corresponding to a lower $\tau$ than the oxidizing step. This behavior is expected, considering that the reducing step needs less time to equilibrate. However, a fit of the data with only two surface exchange coefficients leads to an insufficient fitting result, where the intermediate region between short and long term equilibration is not adequately described. This behavior could be explained by the presence of either a third exchange coefficient or by a dependency of the two coefficients on each other. Using a purely surface exchange model, only the use of three exchange coefficients gives an adequate representation of the equilibration behavior as is shown in Figure 6.11c.

However, this model would suggest three active surface areas, where Sr moves on vastly different time scales. This does not resemble the reality of the process, which likely also involves a diffusive component inside the LAO layer. Still, information about the nature of the dynamics is gained by this analysis, as it shows that the equilibrium settles in first in a fast, short term and later on in a slow, long term process. Therefore, the equilibration is highly different than the behavior observed for single crystalline STO, where a description by surface exchange is sufficient. [205] The complex structure of the LAO/STO interface is clearly involved and additional systematic studies of the process need to be applied to gain further insights into the dynamic response. Examples of such studies would be systematic LAO thickness variations or the thorough application complex diffusion models to test for a correct description of conductance relaxation.

## 6.3   Chapter summary

ECR studies were conducted on single crystalline STO as well as on LAO/STO. For STO, the defect chemical response could be deduced which is in good agreement with the literature. Through the characterization of the substrate material, the experimental parameter window for a meaningful analysis of LAO/STO in ECR was determined. This laid the foundation for the determination of properties that can be solely attributed to the distinct behavior of the heterostructure. This included the determination of the temperature and $p$O$_2$ dependent conductance of substrate and the determination of the gas exchange dynamics using different gas mixtures. Furthermore, the reaction enthalpies for oxidation and reduction were determined for STO which are comparable with literature, showing that meaningful data can be obtained using the ECR setup.

For LAO/STO, the presence of a temperature activated defect formation process could be shown to be responsible for lowered conductances in oxidizing atmosphere. This process is most likely the precipitation of Sr, leaving behind electron depleting vacancies. The dynamics of this process were analyzed, showing a complex behavior, which deserves a more detailed approach in future research. The proposed Sr precipitation is consistent, however due to the indirect nature of the method, a decisive conclusion cannot be drawn. Approaching the LAO/STO system by the more direct means of *in-situ* spectroscopy to further clarify the ionic process at the LAO/STO interface, including an investigation of the models validity will be discussed in the next chapter.

# Chapter 7

# *In-situ* Characterization of ionic motion in LAO/STO by NAP-XPS

In this chapter the interplay of electronic and ionic charge transfer across the LAO/STO interface is going to be analyzed by the use of near-ambient pressure X-ray photoelectron spectroscopy NAP-XPS (for details on XPS method, see chapter 3.6). Through this analysis, the question is going to be addressed which changes in the interface chemistry are responsible for the electronic conductivity and magnetic signature changes observed in LAO/STO through oxidizing treatment. Furthermore, the interpretation of Sr migration being the responsible mechanism, as was achieved through indirect ECR analysis, is going to be spectroscopically corroborated.

As was explored in the previous chapter, it is evident that the electronic conductivity of the LAO/STO interface is strongly depending on the thermodynamic conditions it is exposed to. This behavior can be explained in context of the defect chemical models that where elaborated in chapter 2.4. The concept behind these interpretations is the balance between the electronic charge transfer induced by the LAO overlayer and ionic charge transfer induced by the defect equilibrium of STO. Electrons occupying the 2DEG can be compensated by cationic defects when oxidizing conditions are introduced and released again in reducing conditions as the system strives towards its respective equilibrium state. An example of an ECR measurement showcasing this behavior is shown in Figure 7.1a. The carrier density was extracted from the measured conductivity by using equation A.19, as the mobility is dominated by phonon scattering in these temperatures. At a temperature of 500 °C, oxidizing conditions (achieved by wet Ar gas) lead to a depletion of the carrier density by one order of magnitude while reducing conditions (achieved by a 4% $H_2$/Ar gas mixture) lead to a complete recovery of the initial state. The reversibility and prolonged time scales of this process lead to the interpretation of Sr migration being responsible for the changed conductivity (for a detailed discussion see chapter 6).

Furthermore this oxidized state can be "frozen in" by rapid cooling, which is achieved in quenching experiments. Consecutively conducted low-temperature conductance measurements are shown in Figure 7.1b. Here, one and the same sample of 4 uc LAO/STO was analyzed as-grown, quenched from oxidizing conditions(1 Torr $O_2$) and quenched from UHV conditions ($1 \times 10^{-8}$ mbar). The resistance at low temperatures is significantly lowered by the quenching procedure in oxidizing conditions and
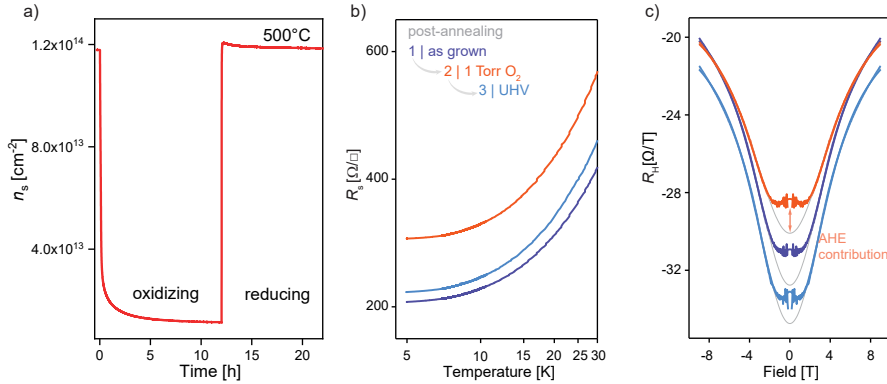
**Figure 7.1:** a) Shows an example of the extracted carrier density from an ECR experiment on a sample of 8 uc LAO/STO over time. The atmosphere was changed between oxidizing (wet 4% $H_2$) to reducing conditions (wet Ar). b) Shows the low temperature resistivity for a sample of 4 uc LAO/STO quenched from similar conditions as in a). c) Shows the Hall coefficient of the sample shown in b) at a temperature of 5 K under an applied magnetic field. The Figure was partly published in Ref.: [212].

recovers back close to its initial state by the reducing treatment. Therefore, the effect visible in ECR (Figure 7.1a) can be conserved down to the low-temperature regime. Further applied Hall measurements at low temperatures are shown in Figure 7.1c. Here it is visible that not only the resistance can be altered to higher values but also that the magnetic signature is enhanced, as is visible by the more strongly pronounced anomalous Hall effect in the oxidized sample. All of the observed changes can be turned back close to their original values by the reducing treatment, which indicates that a thermodynamic equilibrium reaction is taking place. A detailed discussion about the influence of annealing on low-temperature behavior can be found chapter 8. For the current discussion, it is most important to note that the observed changes in thermodynamic equilibrium facilitate a significant change of the electronic properties down to low temperatures and affect the strength of sample's magnetic signature.

The results from electrical analysis could be consistently explained by a cation lattice being active at much lower temperature than would be expected from bulk measurements. As in donor-doped STO (see chapter 2.4), the incorporation of Sr vacancies leads to a depletion of free charge carriers and to additional scattering centers. The dimensions of the heterointerfaces are by orders of magnitude smaller as compared to the relevant dimensions of a complete single crystal and therefore, the length-scales to overcome are in turn also much smaller. Still, the diffusion coefficient of Sr in STO at 500 °C ($D_{V_{Sr}''} = 3 \times 10^{-23} \mathrm{cm^2 s^{-1}}$) [126] would still not allow for significant movement of Sr ions. However, model calculations showed that the carrier density would still be significantly lowered even if Sr precipitation would only occur from the first unit cell of the interfacial STO. [40] Furthermore, Sr was found to be rather mobile at surfaces of *n*-doped STO. [42] This raises the scientific question if a similar effect is taking place in LAO/STO even though the STO is capped by an LAO layer. Results from ECR would suggest so, but their indirect nature hinders a

final conclusion. Results from low temperature Hall measurements show the striking reversible changes in resistivity and magnetic signature. The explanation for their appearance and disappearance would be of high interest for the deeper understanding of the LAO/STO 2DEG in general. Therefore, an *in-situ* spectroscopy approach is applied to reveal if Sr migration is indeed the cause of these phenomena.

Two series of NAP-XPS experiments were conducted, one at the Advanced Light Source facility using Synchrotron radiation (located in Berkeley, USA) and one at the Charles University (located at the Prague University, Czech Republic) using a conventional lab X-ray source. In the first series, the variability of synchrotron radiation energy was used to achieve a depth profiling of the recorded core-level spectra. In the second series, samples with varied LAO thicknesses were used to achieve additional separation between interface and surface. In both series, the core-level spectra of the La 4$d$, Al 2$p$, O 1$s$, Sr 3$d$ and Ti 2$p$ orbitals were recorded. For further experimental details see chapter 3.6. A consistent behavior could be observed throughout all experiments, when samples were exposed to oxygen while being spectroscopically characterized. It can be summarized in the following points:

1. Disappearance of the Ti$^{3+}$ core level spectrum

2. Appearance of a secondary Sr 3$d$ core level spectrum

3. Shifts to lower binding energy (BE) for all core-level spectra

4. Higher magnitude of the BE shift for overlayer elements (La, Al) compared to substrate elements (Sr, Ti)

In the following the different aspects of $p$O$_2$ dependent changes of the core-level spectra will be analyzed in the context of: 1. Spectral shape to identify their composition, 2. Incident photon energy and LAO thickness dependence to identify the component distribution, 3. Their apparent binding energy (BE) to identify implications for the LAO/STO band alignment. In a last step the results will be combined into one coherent model explaining the entirety of the recorded core level spectra.

## 7.1 Identification of active core level spectra and their $p$O$_2$ dependence

As explained in chapter 3.6, NAP-XPS allows the identification of secondary phases upon oxidation by comparing the core-level spectra shapes before and after inlet of oxygen. A shift of all core level spectra of a material to lower BE with increasing $p$O$_2$, like observed for the overlayer materials (La, Al), cannot be explained by an altered chemical bonding. Rather, such shifts of the complete core level spectrum hint at the presence of generally experienced potentials which will be analyzed in chapter 7.3.

To analyze if the elements at LAO/STO heterointerfaces changed their chemical bonding upon oxidation, the recorded core-level spectra were shifted by different amounts to align their maximum peak positions on each other. Qualitatively, the same behavior could be observed for all samples which is shown for the example of a 6 uc LAO/STO in Figure 7.2. In these measurements, the oxygen partial pressure
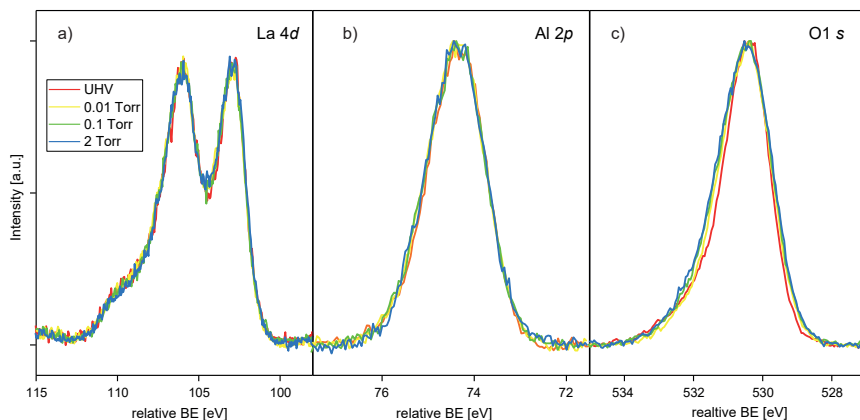
**Figure 7.2:** XPS core-level spectra of the LAO layer from a 6 uc LAO/STO sample are shown. a) Shows the La 4*d* spectra b) shows the Al 2*p* spectra and c) shows the O 1*s* spectra. All spectra were shifted to maximize overlap and facilitate a direct line-shape comparison. The temperature during recording was set to 470 ℃. The Figure was published in the SI of Ref.: [212] (modified)

was set to UHV ($pO_2 \approx 1 \times 10^{-8}$ Torr), 0.01 Torr, 0.1 Torr and 2 Torr, while maintaining a temperature of 470 ℃. For the La 4*d* (shown in Figure 7.2a) and the Al 2*p* spectra (shown in Figure 7.2b) the same observation can be made. They do not show any significant changes in peak shape when exposed to different amounts of oxygen partial pressure. Therefore, it can be concluded that these elements do not participate in the reaction driving the depletion of the 2DEG. The O 1*s* spectra shown in Figure 7.2c is significantly altered by the exposure to oxygen. However, the interpretation of the O 1*s* spectrum is rather difficult in this particular case. Contributions can be expected from the STO substrate, the LAO overlayer and eventual surface phases which are expected to form. As will be seen later, the band alignment of the LAO/STO interface (see chapter 7.3) further complicates the situation. Because of these reasons it is refrained from drawing conclusive decisions from this particular core-level spectrum. Note that this effect cannot be due to an overlapping oxygen gas peak, as it appears energetically well separated at 539 eV. [213]

However, a striking and systematic change could be observed when comparing the Sr 3*d* and Ti 2*p* spectra in this manner. The normalized data, including an applied fitting is shown in Figure 7.3a and b for the Ti 2*p* and Sr 3*d* spectrum respectively in UHV and 2 Torr oxygen. The Ti 2*p* spectrum consists of two overlapping spectra, one stemming from $Ti^{4+}$ ions (green area in Figure 7.3a) and one from $Ti^{3+}$ ions which are shifted to lower BE due to the additional electron occupying its Ti 3*d* orbital (red area in Figure 7.3a). [156, 214] The electrons generated by charge transfer in the LAO/STO 2DEG occupy this orbital, making it a signature of the free charge carrier density. [215, 216] Therefore, the electronic response that was shown in ECR can be monitored spectroscopically by the areal contribution of $Ti^{3+}$ to the Ti 2*p* spectrum. When oxidizing atmosphere is introduced the $Ti^{3+}$ component is considerably decreased,
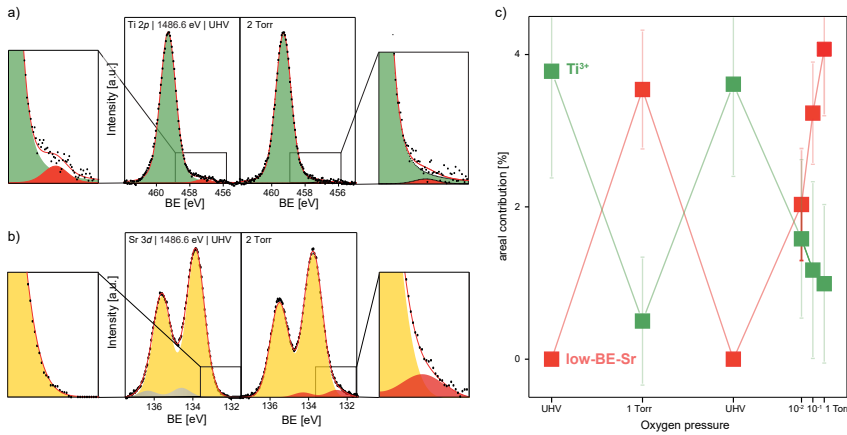
**Figure 7.3:** NAP-XPS results are shown for the Ti 2$p$ and Sr 3$d$ spectra, recorded from a sample of 6 uc LAO/STO using a lab source. A data fit was applied to both core-level spectra. a) Shows the Ti 2$p$ spectra in UHV and in 2 Torr oxygen atmosphere and b) shows the Sr 3$d$ spectra in UHV and 2 Torr oxygen atmosphere. The insets in a) and b) show a zoom in on the shoulders where the secondary components appear. c) Shows the contributions of the secondary components obtained from the data fits over cycles of oxygen pressure between UHV and different $p$O$_2$. The Figure was published in Ref.: [212] (modified)

showing an analogue behavior to the electrical characterization (Figure 7.1). At the same time the Sr 3$d$ spectra shows the appearance of a secondary component that is also shifted to lower BE (low-BE-Sr, red area in Figure 7.3b). The two secondary components show an inverse and reversible behavior to each other when the atmosphere is varied (see Figure 7.3c). In UHV the Ti$^{3+}$ component is strong while the low-BE-Sr component is weak and in 2 Torr oxygen the low-BE-Sr component is strong while the the Ti$^{3+}$ component is weak. This process could be observed for all of the three cycles that were conducted during this experimental series and for all of the tested samples, showing little to no sign of degradation. Moreover, smaller appearances of the low-BE-Sr component and disappearances of the Ti$^{3+}$ component could be observed by applying intermediate pressures of $1 \times 10^{-2}$ Torr, $1 \times 10^{-1}$ Torr and 1 Torr. These results show that the depletion of the 2DEG correlates with the formation of a secondary Sr containing phase, hinting at an ionic charge transfer process being active.

## 7.2 Identification of low-BE-Sr depth distribution

To elucidate the nature of the observed secondary Sr 3$d$ component, a detailed depth profiling of the chemical structure of the system is necessary. Two ways were used in this thesis to gain information about the depth distribution of the low-BE-Sr. One being the use of tunable synchrotron radiation and one being the use of a thickness series under Al-K$_\alpha$ lab source radiation. Both methods use the Lambert-Beer-law ($I = I_0 \exp(-d/\lambda)$) that describes the loss of photoelectron intensity by a material of a certain thickness ($d$). In the first approach of using synchrotron radiation, the used
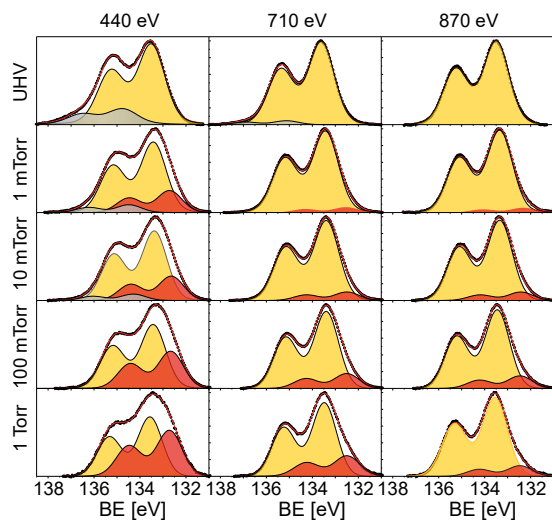
**Figure 7.4:** Sr 3*d* spectra from a 4 uc LAO/STO sample are shown, recorded by a NAP-XPS using synchrotron radiations of 440, 710 and 810 eV and pressures from UHV to 1 Torr. In all measurements a temperature of 470 °C was applied. The Figure was published in Ref.: [212]

X-ray beam can be tuned to a desired wavelength by the use of a double crystal monochromator [217]. As the inelastic mean free path of an electron depends on its kinetic energy and the kinetic energy again depends on the incident photon energy (see equation 3.22) a depth profiling can be achieved by tuning the incident photon energy. In this case, a lower photon-energy (PE) leads to more surface sensitive measurements.

In Figure 7.4, the recorded Sr 3*d* spectra are shown for a sample of 4 uc LAO/STO measured by NAP-XPS, using PE of 440, 710 and 870 eV. The pressure was varied from UHV to 0.001, 0.01, 0.1 and 1 Torr oxygen. To describe the recorded spectra for the entire range of this experimental matrix, it is necessary to apply a fitting including three doublets. These are a main Sr 3*d* component, a high-BE-Sr component and a low-BE-Sr component. The main component can be ascribed to the Sr occupying the STO lattice since it is strongest in intensity and is not diminished like the secondary components. As Sr occupying the STO lattice can in practice be regarded as constant, this behavior is to be expected also from its Sr 3*d* component. The low-BE-Sr component appears also in this experimental series and takes up large areal contributions in the most surface sensitive measurements. Its areal contribution is systematically increasing with increasing surface sensitivity of the measurement and with increasing $pO_2$. These results show that the low-BE-Sr component is linked to the surrounding oxygen and that it resides close to or even at the very surface of the heterostructure. The high-BE-Sr component is present in UHV conditions and begins to decrease in intensity as soon as the $pO_2$ is increased. As soon as a $pO_2$ of 0.1 Torr is reached, the component vanishes completely. Also this component appears to be strongest in intensity for the most surface sensitive measurements, although it never reaches the same amount as the low-BE-Sr component in the most oxidizing conditions.
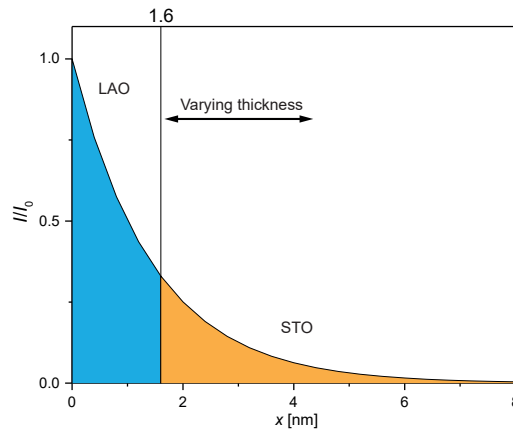
**Figure 7.5:** Illustration of the intensity attenuated at an escape depth $x$, as described by the Lambert-Beer-law using a $\lambda_{\text{eff}}$ of 2.787 nm, which corresponds to the IMFP of a Sr $3d$ photoelectron in LAO. The Figure was published in the SI of Ref.: [212]

It can be concluded from the synchrotron measurements that the low-BE-Sr component is definitely present (large areal contribution), is linked to the oxidation process ($p$O$_2$ dependence) and is close to or at the surface of the LAO/STO heterostructure (PE dependence). However, a final conclusion about the location of the low-BE-Sr component cannot be drawn in this way as it could reside at the surface of the heterostructure or at its interface, showing the same PE dependence.

To determine where low- and high-BE-Sr components reside, a series of LAO/STO samples was analyzed where the thickness of the LAO overlayer was systematically varied. Thicknesses of 4, 6, 8, 10 and 12 uc were investigated and the three Sr $3d$ components were fitted to the recorded data. In such a case of an increasing capping layer thickness, a phase that resides at the interface of the heterostructure should be attenuated exponentially, while a phase that resides inside the capping layer or at its surface should be independent of the capping layer thickness. Difficulties in applying this procedure to NAP-XPS experiments are the intensity attenuation by the applied gas pressure and intensity variations due to the alignment. To circumvent this effect, areal contributions have to be normalized when data from separate measurements are compared. Furthermore, the orbital used for normalization should have a rather similar BE. This is necessary, because the attenuation of the signal intensity follows the Lambert-Beer-law, which leads lower intensities for orbitals of higher BE. For these reasons, the areal contributions of the Sr $3d$ components were normalized to the La $4d$ spectrum and plotted over the LAO thickness. However, to accurately describe the attenuation behavior of these components an additional fit has to be implemented as the Sr $3d$ area is now divided by an increasing La $4d$ area. A method to describe such a attenuation behavior was published by Treske et al. [218] and the one used here follows the same principle, although slightly adjusted to correctly describe this particular case.

The approach is based on applying the Lambert-Beer-law ($I=I_0\exp(-x/\lambda_{\text{eff}})$) on a particular attenuation scenario. The intensity attenuation according to the Lambert-Beer- law is plotted in Figure 7.5 for the example of an effective inelastic mean free path ($\lambda_{\text{eff}}$) of 2.787 nm, which corresponds to a photoelectron from the Sr 3$d$ orbital traveling through an LAO layer. Because $\lambda$ is almost identical for LAO and STO, only one effective IMFP was used in this case. The used $\lambda_{\text{eff}}$ was calculated using the TPP2M formula [219], which allows to theoretically determine the IMFP of an electron depending on its kinetic energy in a specific material. For this purpose also the material properties of density, band-gap, atomic mass and number of valence electrons have to be known.

Photoelectrons are generated in the entire sample when illuminated by X-rays and attenuated by the material afterwards. Therefore, the recorded intensity is described by the integral of the Lambert-Beer terms over the sample depth. As measurements were conducted with the analyzer set perpendicular to the sample surface, no take-off angle correction had to be applied. Energetically close core-level spectra are used leading to only slightly varied IMFPs, due to its dependence on the photoelectron's kinetic energy. This means that one effective IMFP can be used for both core-level spectra to simplify the model. It will be assumed that the sample is laterally homogeneous, so variations in these directions are neglected for this model. Two cases are going to be described here: 1. An LAO/STO sample containing an additional Sr phase, which resides at the interface, 2. An LAO/STO sample containing an additional Sr phase, which resides on the surface. These two scenarios are shown in Figure 7.6, where the interface fitting model is shown in sub-figure 7.6a and the surface fitting model in sub-figure 7.6c. The integrals describing the intensity from La 4$d$ of the LAO layer ($I_{\text{La }4d}$), Sr 3$d$ from bulk STO ($I_{\text{Sr }3d\text{ (STO)}}$), Sr 3$d$ from an interface phase ($I_{\text{Interf.}}$) and Sr 3$d$ from a surface phase ($I_{\text{Surf.}}$) are

$$I_{\text{La }4d} = \int_0^{d_{\text{LAO}}} I_{\text{La }4d}^0 \exp\left(-\frac{x}{\lambda_{\text{eff}}}\right) dx \exp\left(-\frac{d_{\text{Surf.}}}{\lambda_{\text{eff}}}\right) \tag{7.1}$$

$$I_{\text{Sr }3d\text{ (STO)}} = \int_{d_{\text{LAO}}}^{\infty} I_{\text{Sr }3d}^0 \exp\left(-\frac{x}{\lambda_{\text{eff}}}\right) dx \exp\left(-\frac{d_{\text{Surf.}} + d_{\text{Interf.}}}{\lambda_{\text{eff}}}\right) \tag{7.2}$$

$$I_{\text{Surf.}} = \int_0^{d_{\text{Surf.}}} I_{\text{Sr }3d}^0 \exp\left(-\frac{x}{\lambda_{\text{eff}}}\right) dx \tag{7.3}$$

$$I_{\text{Interf.}} = \int_0^{d_{\text{Interf.}}} I_{\text{Sr }3d}^0 \exp\left(-\frac{x}{\lambda_{\text{eff}}}\right) dx \exp\left(-\frac{d_{\text{LAO}}}{\lambda_{\text{eff}}}\right) \tag{7.4}$$

Here, $d_{\text{LAO}}$ describes the LAO thickness, $d_{\text{Surf.}}$ the thickness of the surface phase, $d_{\text{Interf.}}$ the thickness of the interface phase. The intensity is further described be the un-attenuated original intensities ($I^0$) which are specific for the orbital they originate from and are proportional to the present amount of their element. These are $I_{\text{La }4d}^0$ for the La 4$d$ and $I_{\text{Sr }3d}^0$ for the Sr 3$d$ orbital. To simplify the model and to reduce the amount of fitting parameters, it is assumed that $I_{\text{La }4d}^0$ and $I_{\text{Sr }3d}^0$ are constant and do not depend on their specific location or configuration. Each integral is written in a general form which assumes both phases to be present (interface and surface) and is attenuated by the term $\exp(-d/\lambda_{\text{eff}})$ representing the attenuation by overlayers of total thickness ($d_{\text{total}} = d_{\text{LAO}} + d_{\text{Surf.}} + d_{\text{Interf.}}$).

The behavior of the Sr $3d$/La $4d$ ratios for a Sr containing surface phase can now be determined by building the ratios of equations 7.3 and 7.1. The behavior for bulk STO follows the ratio of equations 7.2 and 7.1. Without any interface phase being present ($d_{\text{Interf.}} = 0$) this leads to

$$\frac{I_{\text{Surf.}}}{I_{\text{La }4d}} = A\frac{\exp\left(\frac{d_{\text{Surf.}}}{\lambda_{\text{eff}}}\right) - 1}{1 - \exp\left(-\frac{d_{\text{LAO}}}{\lambda_{\text{eff}}}\right)} \tag{7.5}$$

$$\frac{I_{\text{Sr }3d\text{ (STO)}}}{I_{\text{La }4d}} = A\frac{1}{\exp\left(\frac{d_{\text{LAO}}}{\lambda_{\text{eff}}}\right) - 1} \tag{7.6}$$

where the constant $A = I^0_{\text{Sr }3d}/I^0_{\text{La }4d}$ serves as single fitting parameter, which is set to be equal for both equations. Here equation 7.5 describes the scaling behavior of a surface phase which approaches a constant value when $d_{\text{LAO}} \rightarrow \infty$. This is to be expected for a phase residing on the surface regardless of LAO thickness. The bulk phase scales down to 0 when $d_{\text{LAO}} \rightarrow \infty$ as expected for a signal passing through an infinitely thick layer. In the same manner, the model for an interface phase (ratio of equation 7.4 and 7.1) and the bulk component (ratio of equation 7.4 and 7.1) without any present surface phase ($d_{\text{Surf.}} = 0$) can be determined as

$$\frac{I_{\text{Interf.}}}{I_{\text{La }4d}} = A\frac{1 - \exp\left(-\frac{d_{\text{Interf.}}}{\lambda_{\text{eff}}}\right)}{\exp\left(\frac{d_{\text{LAO}}}{\lambda_{\text{eff}}}\right) - 1} \tag{7.7}$$

$$\frac{I_{\text{Sr }3d\text{ (STO)}}}{I_{\text{La }4d}} = A\frac{\exp\left(-\frac{d_{\text{Interf.}}}{\lambda_{\text{eff}}}\right)}{\exp\left(\frac{d_{\text{LAO}}}{\lambda_{\text{eff}}}\right) - 1} \tag{7.8}$$

In this case both equations 7.7 and 7.8 approach 0 when $d_{\text{LAO}} \rightarrow \infty$ which is again expected for phases that become more and more buried with increasing $d_{\text{LAO}}$.

Using these models, the positions occupied by the two secondary phases (high-BE-Sr and low-BE-Sr) can be determined. The areal weights for the combination of high-BE-Sr and bulk STO component where determined in UHV and for the combination of low-BE-Sr and bulk STO doublet in 1 Torr oxygen. Each area of the determined Sr $3d$ components was normalized to the total one of the La $4d$ spectrum of the same measurement for all measured LAO thicknesses. The thicknesses were determined via RHEED during the fabrication process. Subsequently, both fitting models (equation combinations 7.5, 7.6 and 7.7, 7.8) were applied to each of the two resulting data-sets. For the high-BE-Sr component, the interface model as sketched in 7.6a returned the best results. The data including the applied fit is shown in 7.6b on a logarithmic scale, where the data is displayed as points and the fits as lines. From the data points alone, a similar behavior between the high-BE-Sr component and the bulk STO component is already observable, showing an exponential attenuation behavior with increasing the LAO thickness. The data fit is in good agreement with the attenuation behavior, showing slightly higher deviations for higher LAO thicknesses. These discrepancies might stem from the simplifications that were made to apply analytical equations, such as using one single calculated $\lambda$. Best results were achieved by using a $d_{\text{Interf.}}$ of roughly
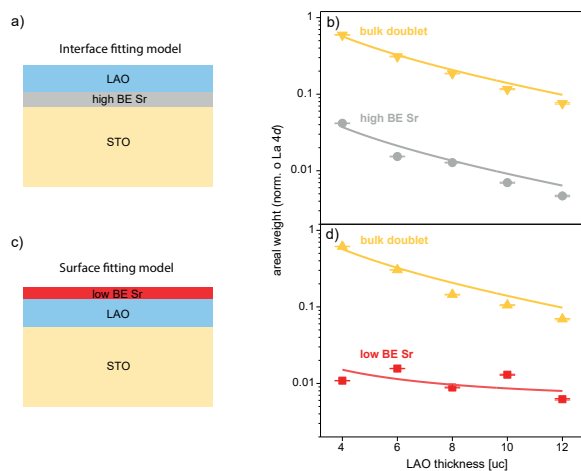
**Figure 7.6:** a) Shows a sketch of the high-BE-Sr component placed at the interface. b) Shows the areal weights of the STO and high-BE-Sr components (normalized to La 4$d$) as dots. The data fits for the interface model are inserted as lines in the same color. c) Shows a sketch of the low-BE-Sr component placed at the surface. d) Shows the areal weights of the STO and low-BE-Sr Sr 3$d$ components (normalized to La 4$d$) as dots. The data fits for the surface model are inserted as lines in the same color. The Figure was published in the SI of Ref. [212].

0.2 nm which coincides to effectively half a unit cell of STO. This indicates that this component is residing inside the very first unit cell of the interfacial STO. Therefore, its BE might be the result of a nearest neighbor effect, stemming from a changed Madelung potential as the chemical environment differs from bulk STO [118, 220]. Note that the presence of the potential well alone cannot cause the observed shifts although it might play an additional role. The experimentally determined bend bending is usually in the range of around 0.3-0.4 eV [68, 83, 221] and theoretical calculations show e.g. 0.5 eV [222]. The high-BE-Sr component differs from the bulk STO by about 1 eV, therefore chemical shifts have to present in addition to general potential shifts.

For the low-BE-Sr component, the surface fitting model as sketched in Figure 7.6c achieved best results. Data and applied fits are shown in Figure 7.6d on a logarithmic scale, where the data is displayed as points and the fits as lines. The bulk components show a very similar scaling compared to the interface fitting model, as is to be expected. The low-BE-Sr shows a very slight increase to smaller LAO thicknesses which stems from the normalization procedure. Otherwise, it shows almost no dependence on the LAO thickness, which is in good agreement with the surface fitting model. Best results could be accomplished by using a surface phase thickness $d_{\text{Surf.}}$ of 0.04 nm which is considerably smaller than any real unit cell. As was discussed by Treske et al. [218] the $d_{\text{Surf.}}$ is not to be seen as a real value for a surface phase thickness. A complete and evenly distributed layer of a surface phase is assumed in this way, while in reality the material will most likely agglomerate into clusters to minimize its energy. Coverage factors can be implemented to achieve more reasonable $d_{\text{Surf.}}$ but are arbitrary in nature, as a range of possible solutions is opened this way. For

example one could assume 0.2 nm layer of SrO and achieve a coverage of roughly 20 %. Therefore $d_{\text{Surf.}}$ has to be seen as an indication of the amount of material, residing at the LAO surface.

From analysis of the Sr $3d$ peak shapes under synchrotron radiation experiments (see Figure 7.4) the need of three distinct doublets to describe its $p\text{O}_2$ and PE dependent behavior was extracted. This leads to the conclusion that Sr is reacting into a secondary phase when oxygen atmosphere and temperature is applied to the LAO/STO heterointerface. From analysis of LAO thickness attenuation of these Sr $3d$ components in lab-source experiments (see Figure 7.6), the positions throughout the heterostructure could be determined. This leads to the conclusion that the low-BE-Sr resides on the LAO surface or (considering the experimental error) at least inside the LAO thin film, while the high-BE-Sr resides at the interface. The Sr ions are therefore diffusing out of the STO substrate upon oxidation, leaving behind Sr vacancies. This in turn can trap itinerant electrons from the 2DEG which is consistent with the diminished signature of $Ti^{3+}$ in the Ti $2p$ spectra. This ionic charge transfer leads to the observed inverse behavior of low-BE-Sr and $Ti^{3+}$ signature (see Figure 7.3) under $p\text{O}_2$ cycles. Therefore, the combined results discussed above lead to the consistent conclusion that Sr is precipitating out of the STO substrate into the LAO layer, eventually all the way to the surface.

## 7.3 Band alignment

A Sr $3d$ doublet on the lower BE side of bulk STO Sr $3d$ is a rather unusual observation as throughout the literature, secondary components in the Sr $3d$ spectrum reside almost exclusively on the high BE side. [42, 118, 220] Only few studies have observed components at similarly low BE, such as exotic defect states in the form of Sr/Ti anti-site defects in STO itself, observed in resistive switching experiments. [223] However, high current densities are applied in such experiments, making the formation of anti-site defects unlikely in the light thermodynamic treatments applied here. Since the position of the Sr containing phase could be determined to be in or on top of the LAO overlayer, the band alignment at the interface of the heterostructure might cause the unusual BE of the observed Sr $3d$ doublet. Similar shifts could be observed in STO/LAO/STO structures (see Figure 5.7 in Ref.: [224]) or in lanthanum strontium ferrite thin films [225]. In both cases, uncompensated potentials lead to a shift of the general potential surrounding the analyzed orbitals, which in turn shifts the apparent BE of overlayer materials. To test this hypothesis also for the case of the observed low-BE component, a detailed analysis of the LAO/STO band alignment has to be conducted. Note that for charging effects, shifts to higher BE would be expected, opposed to the observed shift to lower BE. Therefore, they can be excluded.

As was mentioned in the beginning of the chapter, all core-level spectra shift to lower BE with rising $p\text{O}_2$. As this behavior is opposite to a charging effect of the analyzed system and no charge compensation was applied, these shifts are an indication for a change of the materials Fermi-level. In combination with the observed difference of shift magnitude between overlayer and substrate core-level spectra, it can be concluded that the band alignment at the interface of the heterostructure is altered. The peak shifts in recorded core-level spectra are summarized in Figure 7.7 for the
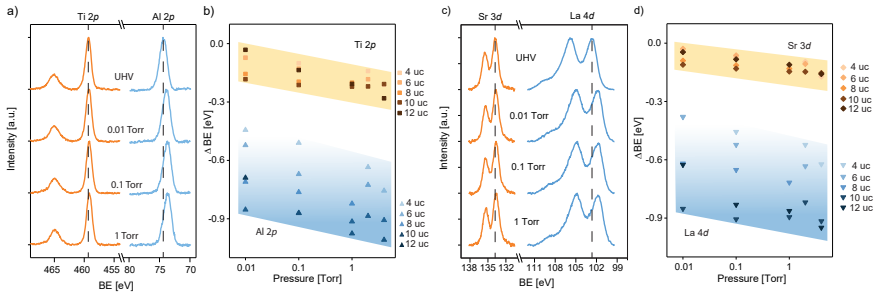
**Figure 7.7:** a) Shows the Ti 2*p* and Al 2*p* spectra of a 6 uc LAO/STO sample in oxygen partial pressures from UHV to 1 Torr. b) Shows the shifts of the maximum peak positions for Ti 2*p* and Al 2*p* spectra over the applied oxygen partial pressures for 4 to 12 uc LAO/STO samples. c) Shows the Sr 3*d* and La 4*d* spectra of a 6 uc LAO/STO sample in oxygen partial pressures from UHV to 1 Torr. d) Shows the shifts of the maximum peak positions for Sr 3*d* and La 4*d* spectra over the applied oxygen partial pressures for 4 to 12 uc LAO/STO samples. The ΔBE of the respective core-level spectra are defined as the BE in a set pressure subtracted by the BE in UHV. The Figure was published in the SI of Ref. [212].

example of a 6 uc LAO/STO sample. Figure 7.7a shows the behavior of the Ti 2*p* and Al 2*p* spectra in a $p$O$_2$ from UHV to 1 Torr. Lines are inserted at the maximum peak positions of the UHV spectra as guide-to-the-eye. To higher $p$O$_2$, the Al 2*p* spectra shift by considerably higher amounts than the Ti 2*p* spectra. This behavior is observed for all of the analyzed samples as is shown in Figure 7.7b. While the Ti 2*p* spectra only shift by about 0.1 to 0.2 eV the Al 2*p* spectra shift by about 0.6 to 1 eV to lower BE as oxygen is applied. Furthermore, the magnitude of the observed shift of the Al 2*p* spectra increases with thicker LAO overlayers.

The same behavior can be observed when comparing the Sr 3*d* and La 4*d* spectra which are shown in Figure 7.7c for the example of a 6 uc LAO/STO sample. Again the La 4*d* spectra shift by higher amounts than the Sr 3*d* spectra. The shifts of the Sr 3*d* and La 4*d* spectra over $p$O$_2$ for all the measured LAO thicknesses are shown in Figure 7.7d. The same behavior can be observed as for the Ti 2*p* and Al 2*p* spectra. The Sr 3*d* shifts by only 0.05 to 0.15 eV while the La 4*d* shifts by about 0.4 to 0.9 eV. Also in this case, the magnitude of the La 4*d* shift depends on the LAO thickness. The spectra where only small shifts, independent of the LAO thickness are observed belong to the substrate material. In contrary, the spectra where large shifts with a dependency on the LAO thickness are observed, belong to the overlayer material.

From the lowered apparent BE, it can be concluded that the Fermi-level of the analyzed material is moved deeper into the band gap, because the measured BE corresponds to the distance of Fermi-level to measured core level [42, 90](see also Figure 4.3 in Ref. [155]). The potential shift of the substrate material as observed by the shifted core-level spectra aligns well with the interpretation of a partially depleted 2DEG. The observed shift difference between substrate and overlayer material can be explained by two scenarios of a changing band alignment. One being an uncompensated potential across the LAO layer and the other being an increasing valence band offset at the interface. The first would result in a considerable, asymmetric peak broadening be-
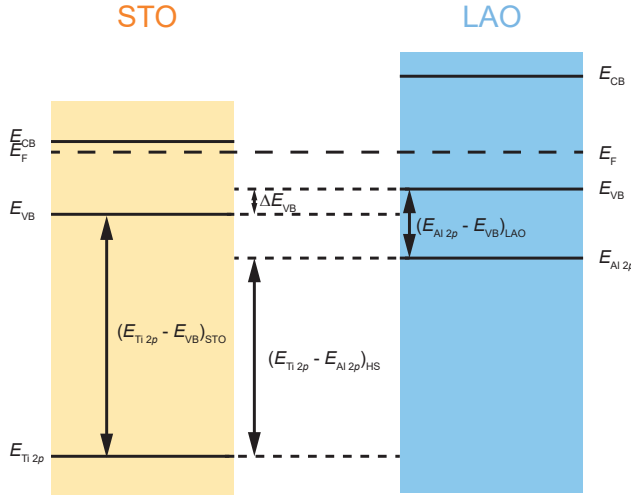
**Figure 7.8:** A sketch describing the route to determine the valence band offsets in a LAO/STO heterostructures is shown at the example of Sr 3$d$ and Al 2$p$. The Figure was published in the SI of Ref. [212].

cause a rising potential would induce multiple shifted peaks throughout the LAO layer which are exponentially attenuated [83, 226]. As was shown in Figure 7.2, no such broadening could be observed for the overlayer material. Therefore, a valence band offset (VBO) has to be involved to explain the observed behavior under increasing $p$O$_2$. In the literature, the determined VBOs for LAO/STO interfaces are usually close to zero [83, 227]. This is attributed to the similarity between the two valence bands in both materials, which consist of O 2$p$ orbitals in both cases. [83, 228] To determine the VBOs of the measured heterostructures as a function of $p$O$_2$, the same systematic as in Ref. [83] was used, using the same reference values.

A sketch describing the principle of VBO determination is shown in Figure 7.8. Here the principle is explained using the example of the Ti 2$p$ and Al 2$p$ spectra. As an epitaxial heterostructure is analyzed, the Fermi-level can be assumed to be constant throughout the interface. To determine the present energy difference between the valence bands of the two materials, the distances between valence band and core level spectra in the bulk material have to be known. The VBO is then determined by following the path along the arrows in Figure 7.8. In the shown example, the energy between the Ti 2$p$ core level and valance band ($E_{\text{Ti }2p} - E_{\text{VB}}$) plus the VBO ($\Delta E_{\text{VB}}$) has to be equal to the energy between the Al 2$p$ core level and the valence band ($E_{\text{Al }2p} - E_{\text{VB}}$) plus the energetic distance between the two core levels in the heterostructure ($E_{\text{Ti }2p} - E_{\text{Al }2p}$). Using this approach the valence band offset is determined by

$$\Delta E_{\text{VB}} = (E_{\text{Al }2p} - E_{\text{VB}})_{\text{LAO, bulk}} - (E_{\text{Ti }2p} - E_{\text{VB}})_{\text{STO, bulk}} + (E_{\text{Ti }2p} - E_{\text{Al }2p})_{\text{HS}} \qquad (7.9)$$
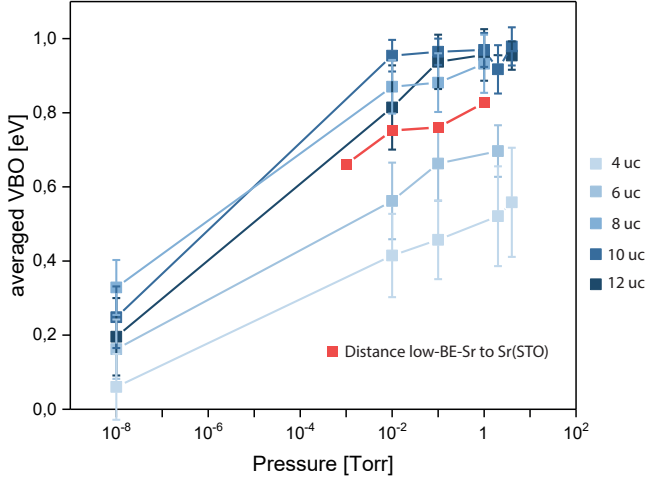
**Figure 7.9:** The average VBO, determined from equations 7.9-7.12, is shown with the standard deviation as error bars. The distance between the low-BE-Sr and the Sr(STO) doublet is inserted in red. The Figure was published in the SI of Ref. [212] (modified).

Using the same approach on other possible core-level spectra combinations between substrate and thin film, three additional ways to calculate the VBO open up which read

$$\Delta E_{\text{VB}} = (E_{\text{Al }2p} - E_{\text{VB}})_{\text{LAO, bulk}} - (E_{\text{Sr }3d} - E_{\text{VB}})_{\text{STO, bulk}} + (E_{\text{Sr }3d} - E_{\text{Al }2p})_{\text{HS}} \qquad (7.10)$$

$$\Delta E_{\text{VB}} = (E_{\text{La }4d} - E_{\text{VB}})_{\text{LAO, bulk}} - (E_{\text{Sr }3d} - E_{\text{VB}})_{\text{STO, bulk}} + (E_{\text{Sr }3d} - E_{\text{La }4d})_{\text{HS}} \qquad (7.11)$$

$$\Delta E_{\text{VB}} = (E_{\text{La }4d} - E_{\text{VB}})_{\text{LAO, bulk}} - (E_{\text{Ti }2p} - E_{\text{VB}})_{\text{STO, bulk}} + (E_{\text{Ti }2p} - E_{\text{La }4d})_{\text{HS}} \qquad (7.12)$$

The valence band offset is defined as positive when the valence band of LAO lies above the one of STO, creating the case of a staggered gap (type II heterojunction). [229] For a negative VBO the heterojunction would have a straddling gap (type I heterojunction). [229] The results of the determined VBOs from equations 7.9, 7.10, 7.11 and 7.12 are shown in Figure 7.9. While the VBO is close to zero when determined from UHV measurements, a clear trend to higher VBOs ($\approx 0.6$ eV) is observable to higher $p$O$_2$. Furthermore, the VBO increases for thicker LAO overlayers, saturating at around 1 eV the thickest LAO thin films. Therefore, the observed shifts in NAP-XPS experiments can be explained by the increase of a VBO at the heterointerface, leading to an increase of the overall experienced potential of the LAO core-level spectra. The distance between the low-BE-Sr and the Sr(STO) doublet is inserted in Figure 7.9, showing a similar dependence on $p$O$_2$. Therefore, the data is in good agreement with the low-BE-Sr component being a surface phase, as it is subject to the same general potential as the LAO layer.

However, the tendency of higher VBO values due to the increasing LAO thickness cannot be easily understood by this approach. The increase of the VBO can be
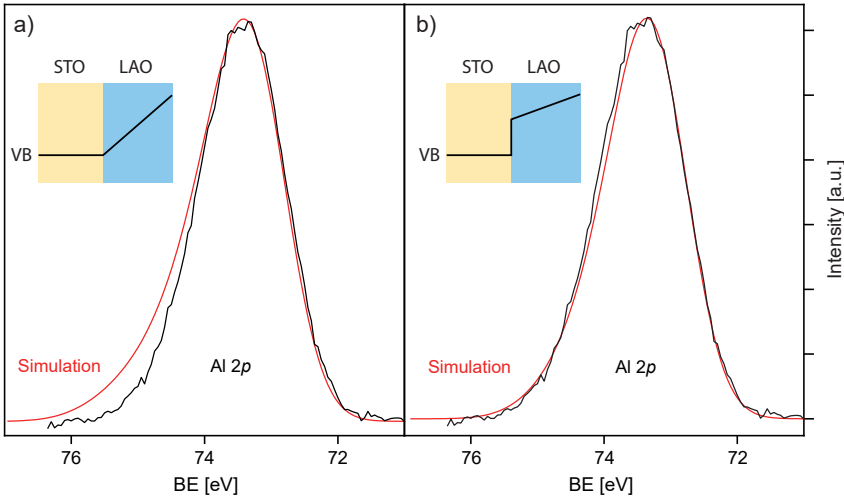
**Figure 7.10:** The results of an attenuation simulation for the Al 2$p$ spectra are shown. a) Shows the result for a linear potential across the LAO layer. b) Shows the results for the combination of a VBO and a linear potential across the LAO layer. The Figure was published in the SI of Ref. [212].

understood as an increase of the interface dipole and is therefore influenced by the local defect concentration. However, calculations of the precipitated Sr concentrations return roughly the same values regardless of the LAO thickness. Therefore, there is no reason for the VBO to increase due to thicker LAO thin films, as the Sr vacancy concentration at the interface stays comparable. Another factor has to be included to consistently explain the observed behavior. The calculation of the VBOs assumes completely flat bands across the LAO layer for all the applied $pO_2$ which in turn can result in artificially increased values when the situation differs from a flat band scenario.

The formation of the 2DEG is driven by the rising potential across the LAO overlayer during thin film growth, which is compensated by electronic charge transfer from the LAO surface towards the interface. The resulting positive charge at the LAO surface is in turn ionically compensated by surface oxygen vacancies. Refilling these oxygen vacancies at the LAO surface would require electrons and would, therefore, deplete the 2DEG. This in turn would lead to an uncompensated field across the LAO overlayer, as the starting point of the polar discontinuity model would be reestablished. As was mentioned before this process would lead to a severe broadening of the core-level spectra recorded from the LAO elements. However, if both effects take place a VBO and a linear potential across the LAO layer, the required linear potential would be much smaller to explain the observed behavior. In turn, the broadening of core-level spectra could be much less severe and even below the detection limit of the XPS method.

To analyze if a small linear potential in combination with a VBO could explain the

observed behavior, an attenuation simulation was conducted. The peak shape of the Al 2$p$ core-level spectra was chosen due to its simplicity. The principle consists of a layered structure where each layer contributes a signal of Voigt peak shape. The BE positions are shifted by set amounts which are defined by the resulting band structure of the two discussed scenarios, which are a linear potential or a combination of VBO and consequent smaller linear potential. Finally the signal intensity is attenuated using the Lambert-Beer-law and added up to the final peak shape. The used intensity is arbitrary and was normalized to the compared experimental result. The required potential was determined by the difference between the apparent Al 2$p$ position measured in UHV and in 1 Torr oxgen. The used Al 2$p$ spectra stems from a 12 uc LAO/STO sample as the effect of an increased shift to lower BE was most pronounced in this case. The result for the simulated peak shape of an Al 2$p$ spectrum affected by the required linear potential of 0.21 eV/nm compared to the Al 2$p$ recorded from a 12 uc LAO/STO sample in 1 Torr oxygen is shown in Figure 7.10a. As expected, a severe broadening of the peak shape is observable in the simulation which is not present in the recorded spectra. This confirms the statement that the shift to lower BE cannot be explained by a linear potential alone. Furthermore, it shows that the results cannot be explained solely by a refilling of LAO surface oxygen vacancies.

The results for the simulated peak shape of the Al 2$p$ spectrum affected by the combination of a VBO and a linear potential, compared to the Al 2$p$ spectrum recorded from a 12 uc LAO/STO sample in 1 Torr oxygen is shown in Figure 7.10b. Here a VBO of roughly 0.5 eV was used in combination with a linear potential of 0.1 eV/nm. This combination was extracted from plotting the BE shift of the Al 2$p$ spectra over the used LAO thickness. The comparison to the experimental data is in good agreement. Therefore, it can be concluded that a linear potential of about 0.1 eV/nm would not be detectable by the XPS method as it would only lead to a very small broadening. Therefore, the entirety of the observed shifts can be explained by the increase of the VBO due to a changed interface chemistry and the rise of a linear potential across the LAO overlayer due to compensated surface charges in the form of refilled surface oxygen vacancies.

Finally the analysis of core-level spectra shifts will be summarized. It could be observed that all core-level spectra shift to lower BE when an oxidizing environment is introduced. As can be seen in Figure 7.11a the overlayer material is shifted by higher amounts than the substrate material. This can be interpreted as an increase of the VBO between the two materials as is shown in Figure 7.11b. There, it can also be seen that the unusual BE of the low-BE-Sr component can be consistently explained by its location inside the heterostructure. It shifts by comparable amounts as the overlayer elements, therefore, further proving that Sr is precipitating into the LAO thin film.

The complete results from peak shift analysis can be summarized into a changed band alignment of the LAO/STO interface that is sketched in 7.12. In UHV conditions, the established scenario from literature is shown. In bulk STO the Fermi-level ($E_\mathrm{F}$) resides inside the band gap. At the interface the conduction band ($E_\mathrm{CB}$) is shifted to energies below the Fermi-level due to the insertion of electrons from the LAO layer. The LAO shows the typically observed band alignment with the valence band ($E_\mathrm{VB}$) close to the one of STO. When the atmosphere is changed to 1 Torr O$_2$, an oxidation process takes place. This results in the precipitation of Sr ions into the LAO layer
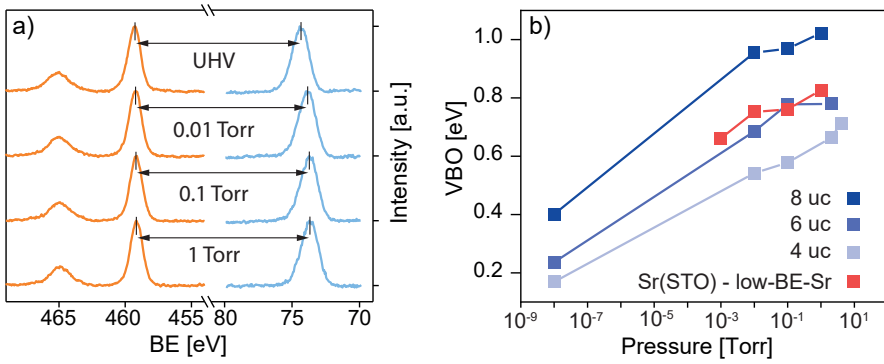
**Figure 7.11:** The deduction of the band alignment is summarized. a) Shows the increasing BE difference between substrate (Ti 2*p*, orange) and thin film (Al 2*p*, blue) with increasing $pO_2$. b) Shows the calculated VBOs for a LAO thickness of 4, 6 and 8 uc over $pO_2$ with the distance between the Sr(STO) and low-BE-Sr doublets inserted in red. The Figure was published in Ref. [212] (modified).
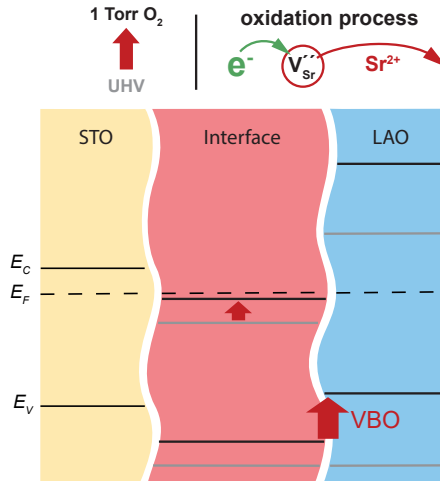


**Figure 7.12:** The deduced band alignment changes of LAO/STO heterostructures under oxidation are shown. The Figure was published in Ref. [212] (modified).

towards the surface, leaving Sr vacancies behind. As Sr vacancies require electrons to form, an ionic charge transfer from the 2DEG to the precipitating Sr ions is triggered. This depletes the 2DEG and results in a shift of interfacial bands to higher potentials. In NAP-XPS this process is visible as a small shift of the substrate core-level peaks to lower BE (see Figure 7.11a) and in the appearance of the low-BE-Sr component in the Sr 3$d$ spectra (see chapter 7.1). Due to the changed interface chemistry, the VBO at the interface is increased as was shown in Figure 7.11b which leads to the observed shifts of the overlayer elements and the unusual BE of the low-BE-Sr component.

## 7.4    Chapter summary

Using NAP-XPS, the precipitation of Sr ions from the STO substrate into the LAO layer could be revealed. This was achieved by the analysis of core-level spectra shapes, which show the disappearance of free electrons under the formation of a secondary Sr-containing phase. The results corroborate the interpretation gained from ECR experiments. The incorporation of Sr vacancies in the interfacial region leads to the depletion of the 2DEG in oxidizing atmosphere. Through the application of depth profiling approaches, for one by the use of synchrotron radiation and second by using LAO/STO heterostructures with varying overlayer thicknesses, it could be demonstrated that Sr is residing on top of the heterostructure or (considering experimental error) inside the LAO layer. Furthermore, it could be shown that the band alignment is significantly altered through this process, leading to an enhanced valence band offset between STO substrate and LAO thin film. This was achieved by an analysis of the core-level spectra shifts in combination with peak shape simulations. The analysis showed that a more pronounced spectral broadening than observed has to be present in overlayer core-level spectra if no VBO is included. Therefore, the increased VBO is a necessary part to explain the entirety of the observed behavior.

Ionic motion and the induced ionic charge transfer significantly affects the electronic structure of analyzed interfaces. The depletion of the 2DEG by Sr precipitation is observed at temperatures as low as 470 °C. This is much lower than the necessary temperatures for electron compensation by Sr vacancy formation in bulk STO. This makes the discussed results, the first direct proof of active ionic charge transfer across LAO/STO at such low temperatures. The ionic motion is considerably enhanced compared to bulk experiments due to the highly confined interface, where high electrical fields are involved. The small dimensions of the highly confined LAO/STO interface and its high electron density are the driving forces behind the enhanced ionic mobility. This concept is further explored in chapter 9.3.

As was shown in the beginning of this chapter, the low-temperature behavior of LAO/STO is significantly altered by oxidizing annealing, leading to lower higher resistances and a larger magnetic signature. Putting these results in context of the observed Sr precipitation in NAP-XPS experiments and exploring on the consequent possibilities to manipulate low-temperature behavior will be topic of the next chapter. This chapter was in part already published in Ref.: [212].

# Chapter 8

# Controlling transport and magnetism in LAO/STO by defect engineering

The emergent magnetism at LAO/STO heterointerfaces and its origin is a highly debated topic, although some understanding of its complex behavior was achieved. [57] The discovery of magnetism between the two non-magnetic material in itself was a surprising result. [17] It turned out that the presence of magnetic moments in LAO/STO heterostructures depends highly on the exact constitution of the interface. One important factor is the oxygen partial pressure during the PLD growth of the samples, as a more strongly pronounced magnetism could be shown for higher $pO_2$. [17] However, other works show opposite behavior, where an enhanced magnetism is observed for growth in lower $pO_2$. [230] In any case, the important role of the $pO_2$ on magnetism is evident and therefore oxygen vacancies are most likely involved. But since oxygen vacancies heavily impact the electronic structure because of their intrinsic doping effect, the disentanglement of intrinsic and extrinsic effects prove difficult. Considering the $pO_2$ dependency of Sr precipitation and the correlating magnetic signature presented in chapter 7, it is likely that the cation sub-lattice is also involved in shaping the magnetic constitution of the interface.

Consistent theories can explain the cause of magnetism to be an intrinsic property due to the STO band structure and high carrier density of the system. [215, 231] Other theories attribute magnetism to be a local phenomenon as the clustering of oxygen vacancies around the Ti ions can induce magnetic moments. [232, 233] This localization in magnetic patches could also explain the observed coexisting superconductivity. [234] Spectroscopically, the localization of electrons in oxygen deficient LAO/STO structures could be shown, strengthening this model of electronic phase separation. [27] However, this model is not able to explain the stronger magnetism in samples grown in high $pO_2$, hinting at a more complex behavior. In this context, the role of cation defects in the form of $Ti_{Al}$ A-site defects was recently proposed to be able to enhance the magnetism of LAO/STO. [235] The importance of these defects could be verified in La-rich LAO/STO structures. [96] As such interfaces do not show conduction in high $pO_2$, they correspond more to the behavior of amorphous LAO/STO controlled by the oxygen off-stoichiometry of the underlying STO substrate.

It raises the interesting prospect to involve the cation lattice into the magnetic ordering of the LAO/STO system. It could be proven in chapter 7 that strontium migrates out of the STO lattice into the LAO thin film in high $p$O$_2$ and that an enhanced magnetic signature is observed for oxidized samples. The used LAO/STO heterostructures were slightly La-deficient as was revealed by XPS analysis (see chapter 4.1). This is consistent with the literature, which suggests that PLD grown LAO is commonly La-deficient and that this property promotes 2DEG formation. [69, 236] Precipitating Sr ions must travel along present defect sites inside the LAO thin film and therefore, them occupying the empty A-sites is the most obvious and simple conclusion. The resulting defect structure could play a role for the emergent magnetism in La-deficient LAO/STO. The enhanced magnetism upon oxidation could be facilitated by one of the consequential defects of Sr precipitation, like Sr$_{La}$ A-site defects, Sr vacancies or precipitated surface phases (SrO). To answer the question, if magnetism can be consistently controlled by favoring or prohibiting Sr precipitation, the effect of oxygen annealing on LAO/STO with different thin film stoichiometry and thickness will be analyzed in this chapter.

## 8.1 Thermodynamic response of the LAO/STO low-temperature behavior

From NAP-XPS results in chapter 7, the Sr migration triggered by oxidizing atmospheres was spectroscopically identified. Therein, the inverse behavior between electrons and Sr precipitation could be seen. As the ionic and electronic properties in oxide heterostructures are strongly intertwined, the question arises, how the electronic properties of the heterostructure are changed by thermodynamic annealing. Furthermore, magnetism in LAO/STO evolves at very low temperatures. Therefore, it was attempted to "freeze in" the thermodynamic states observed at high temperatures, and to analyze them at a few Kelvin to investigate the property changes.

To achieve "frozen in" oxidized and reduced states of the heterostructure, sample pieces were annealed in a quenching oven, where they can be rapidly moved from the heated area into an area cooled by a constant gas flow. A sample of 4 uc close to the stoichiometric point was characterized by a low-temperature Hall measurement in its as-grown state. Subsequently the sample was annealed in a 0.1% O$_2$/Ar gas mixture to achieve an oxidized state and measured again. Afterwards, the sample was subjected to a reducing anneal in UHV conditions ($p$O$_2$=1 × 10$^{-8}$ mbar) to imitate the thermodynamic conditions in NAP-XPS experiments. Each annealing step was carried out in the corresponding atmosphere for 1 hour at 500 °C before quenching. For the reducing atmosphere the PLD deposition chamber was used, where the laser heating system enables a quenching of the sample.

To analyze the influence of thermodynamic annealing on the electronic and magnetic properties to low temperatures, the sample was cut into 1.25 × 5 mm pieces and bonded in a mimicked Hall bar geometry. Low-temperature Hall measurements were conducted in a Physical Property Measurement System (PPMS) from Quantum Design. The sample was cooled down to low temperatures while measuring the sheet resistance. Under magnetic fields of ±9 T at temperatures of 5, 6, 7, 8, 9 10, 15, 30, 100
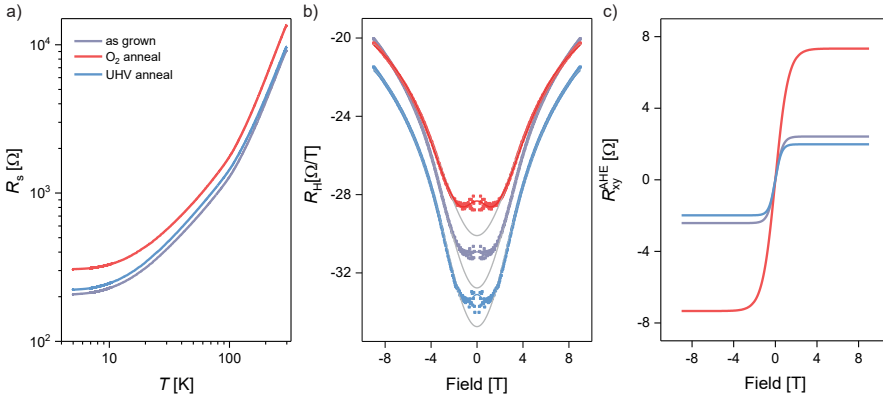
**Figure 8.1:** a) Shows the sheet resistance over temperature of a close to stoichiometric 4 uc LAO/STO sample in three states: as-grown state colored in purple, after an anneal in 0.1% oxygen atmosphere colored in red and after an anneal in 4% hydrogen atmosphere colored in blue. b) Shows the Hall coefficient of the same states as in a) at 5 K under an applied magnetic field. The same color scheme is used as in a). Data points are shown as squares and applied fits as lines of the same color. The grey lines show the applied fits without an anomalous Hall contribution. c) Shows the anomalous Hall component over magnetic field extracted from the Hall coefficient shown in b).

and 300 K the Hall resistance and magnetoresistance were recorded. The data was symmetrized to compensate offset voltages. This measurement protocol was used to characterize the as-grown, oxidized and reducing state.

The measured resistances of the three states upon cooling on a double logarithmic plot is shown in Figure 8.1a. A metallic behavior is observed for all three states. After the sample received an oxidizing anneal, the complete resistance curve is shifted to higher values by roughly a factor of two. The consecutive reducing anneal leads to a recovery of the resistance close to the as-grown state. An altered low-temperature resistance corresponds either to a change of charge carrier concentration or mobility. Furthermore, the mobility is determined by the effective mass caused by the band structure and/or a changed number of scattering centers due to a changed number of defects. To evaluate the observed behavior, a detailed analysis of the Hall effect at low temperatures is necessary.

The Hall coefficients ($R_H$) in dependence of the magnetic field for the three measured states are shown in Figure 8.1b. At high fields, a strong dependency of $R_H$ on the applied magnetic fields is observed which is caused by two electron populations occupying different bands. [149] At low fields, an anomalous Hall effect (AHE) is present, visible as an upturn of the Hall coefficient around zero. The magnitude of the AHE can be visually identified by the area between the pure two carrier model (grey lines in Figure 8.1) and the actual $R_H$ curve. A fit is necessary to understand the complex behavior of the low-temperature Hall coefficient. The details of the formalism are described in chapter 3.4. A two carrier model is applied to describe the non-linearity (equation 3.19) including an anomalous Hall component (equation 3.21). Applying this formalism, the carrier densities of the two conducting bands ($n_1$, $n_2$) and their
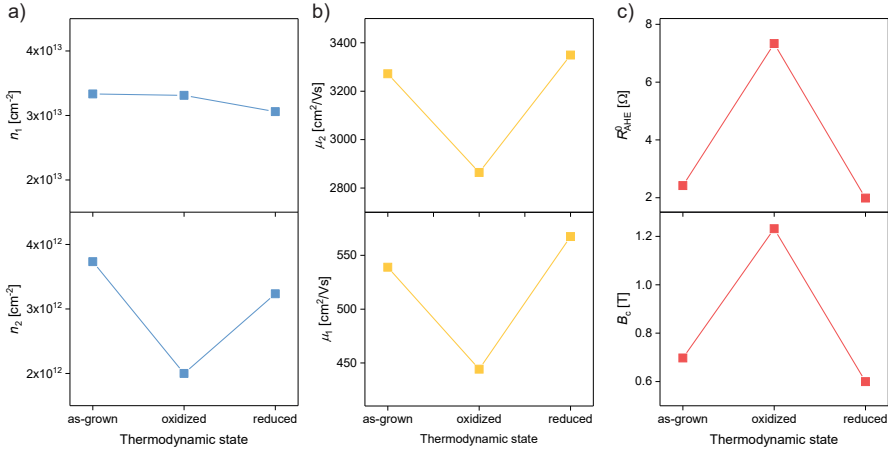
**Figure 8.2:** The extracted fitting parameters obtained from $R_H$ in Figure 8.1b of the as-grown, oxidized and reduced state at a temperature of 5 K are shown. a) Shows the carrier density, b) shows the mobility and c) shows the anomalous Hall coefficient and critical field.

mobilities ($\mu_1$, $\mu_2$) are obtained. The anomalous Hall effect is described by $R_0^{AHE}$ and $B_c$. To reduce the amount of fitting parameters, equation 3.20 is applied, using the resistance at zero field. The resulting anomalous Hall component ($R_{xy}^{AHE}$) is plotted over the magnetic field in Figure 8.1c. It is described by the relation $R_{xy}^{AHE} = R_{AHE}^0 \tanh(B/B_c)$, using the anomalous Hall coefficient ($R_{AHE}^0$) and the critical field ($B_c$). An increase of the anomalous Hall contribution is observed for the oxidized state, while the as-grown and reduced state are similar at lower values.

The changes of the low-temperature behavior due to thermodynamic annealing are summarized by plotting the fitting parameters obtained from Figure 8.1b over the thermodynamic states as shown in Figure 8.2. The two carriers consist of a high density, low mobility ($n_1$, $\mu_1$) and a low density, high mobility ($n_2$, $\mu_2$) population. By oxidizing the sample, the carrier density is altered. While $n_1$ is not significantly changed, the $n_2$ value is roughly half of its initial value. The reducing treatment leads to a recovery of $n_2$ close to its original value, while $n_1$ is slightly lowered. Therefore, the 2DEG is reversibly depleted and refilled by oxidizing and reducing treatments. The mobility (Figure 8.2b) is lowered for both carriers types ($\mu_1$ and $\mu_2$) when the sample is oxidized and both values recover close to their original values by the reducing anneal. Therefore, the mobility is reversibly lowered and recovered by the applied annealing steps.

It could be shown in NAP-XPS experiments (see chapter 7) that the LAO/STO system reacts on an oxidizing atmosphere by Sr precipitation. This mechanism can explain the observed data by invoking the presence of Sr vacancies at the interface. Sr vacancies take up two electrons upon formation and lead to the observed lowered carrier density (Figure 8.2a). At the same time the increase of point defects in the interfacial region would induce more scattering centers for electron transport. Therefore, also the observed lowered mobility (Figure 8.2b), is consistent with Sr vacancy formation.

The anomalous Hall coefficient shows an increase through the oxidizing treatment, which is reversible by the reducing treatment. The same behavior is observed for the critical field. Consequently, the AHE is reversibly increased by oxidizing the sample. The anomalous Hall effect is related to the spin polarization of charge carriers due to magnetic moments in the system and therefore an indication of magnetism in the heterostructure. [237–239] Therefore, it is frequently used in oxide heterostructures to identify the small magnetic moments of these systems. [76, 95, 240, 241] The increased magnetic signature is linked to Sr vacancy formation, as both phenomena concomitantly appear. However, at the current point of research it is unclear if this is a direct effect. The exact causation could also be indirect in nature, caused e.g. through altered strain fields or a the lowered mobility of the sample. In summary, upon an oxidizing anneal, the electron density and mobility are lowered while a the magnetic signature is increased. The whole process is reversible by an anneal in reducing atmosphere.

## 8.2 Defect engineering of low-temperature magnetism

From NAP-XPS results in chapter 7, the Sr migration triggered by oxidizing atmosphere was spectroscopically identified. Since Sr has to move via defect states inside the LAO layer it is most likely to occupy La-sites, as they own the same crystallography as Sr-sites in STO. Consequently, the defective structure of the LAO thin film should have a high impact the ionic mobility and, therefore, on the electronic properties changes under oxidizing atmosphere.

To control the stoichiometry of the LAO thin film, as well as the thermodynamic state of the heterostructure, different $p$O$_2$ are only applied after PLD growth, opposed to changing the growth pressure. As the deposition pressure influences the propagation of ablated ions in the plasma plume, which in turn changes the stoichiometry of the deposited thin film, [130] the deposition pressure is unsuitable to purely control the thermodynamic state of the sample. The LAO thin films were fabricated using the standard parameters established in chapter 4.1, from which the most important ones are a substrate temperature of 800 °C, a deposition pressure of $1 \times 10^{-3}$ mbar, a laser repetition rate of 1 Hz. The laser fluence was set to 0.8 J/cm$^2$ for close to stoichiometric growth and to 0.96 J/cm$^2$ for La-deficient growth.

As the changes of low-temperature behavior can be consistently explained by Sr precipitation, the LAO defectiveness and thickness should influence the process. Therefore, a set of samples was investigated, where the LAO stoichiometry was varied between La-deficient and close-to-stoichiometric LAO thin films. Furthermore, LAO thicknesses of 4, 8 and 12 uc were used. The temperatures 2, 3 and 4 K were added to the measurement protocol, enabling a more strongly pronounced AHE. For better processing, these samples were reduced using a 4% H$_2$/Ar gas mixture in the quenching oven. The close-to-stoichiometric 4 uc sample of this experimental series returned qualitatively same results as discussed above, showing that the process is not influenced by the lower $p$O$_2$. All other experimental parameters were kept the same.

The Hall coefficients of a La-deficient 4 uc LAO/STO sample for the three thermodynamic states are shown in Figure 8.3. Already in the as-grown state (Figure 8.3a), the AHE is much more pronounced than for the stoichiometrically grown sample. Through the oxidizing anneal (Figure 8.3b), the anomalous Hall contribution becomes
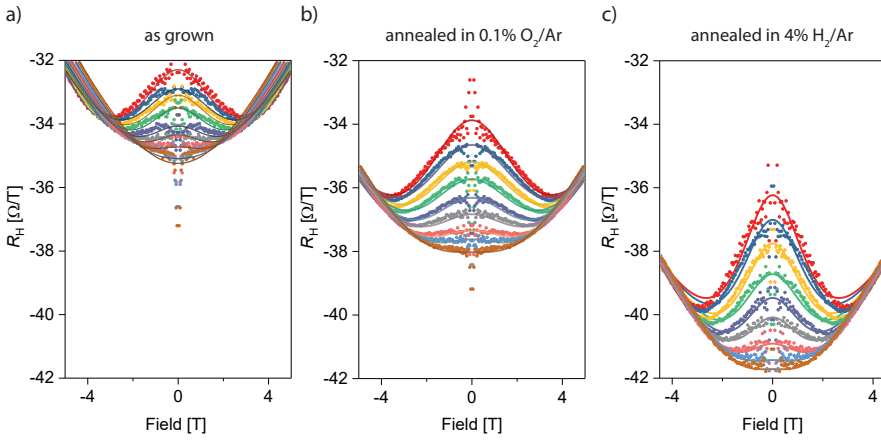
**Figure 8.3:** The Hall coefficient of a La-deficient 4 uc LAO/STO sample is shown for temperatures of 2 K (red), 3 K (blue), 4 K (yellow), 5 K (green), 6 K (purple), 7 K (grey), 8 K (light red), 9 K (light blue), 10 K (brown). The measured data is depicted as points and the applied fit as lines in the same color. a) Shows the as-grown state. b) Shows the state after an anneal in 0.1% $O_2$/Ar. c) Shows the state after a consecutive anneal in 4% $H_2$/Ar.

even more strongly pronounced. The reducing anneal alters the $R_H$ shape again, where the exact identification requires a fitting analysis. For such strongly pronounced AHE, the applied fit becomes increasingly unstable. These instabilities result from the high number of free parameters (5 in total), which are needed to describe the complete behavior of $R_H$ at low temperatures. Therefore, the fit has to be stabilized at lower temperatures, as otherwise unrealistically high values of $R_0^{AHE}$ and $B_c$ are computed. The stabilization is achieved by fixing $\mu_2$ at a value obtained from a slightly higher temperature, where the anomalous Hall component is not present. Note here that the anomalous Hall coefficient was not fitted, if the data could be described by a two carrier model alone. The results of the fit are shown as lines in Figure 8.3a-c for the temperature range between 2 and 10 K. The $\mu_2$ value was obtained from the 10 K data, as it could be sufficiently described by the two carrier model alone. The fit is in good agreement with the Hall coefficients for the complete temperature range for all of three of the measured states. The Hall coefficient at 10 K shows a typical behavior for a purely two carrier system (brown curves in Figure 8.3), which is distinguishable by the bell like shape with rising values to high fields.

To give better insight into the property changes through oxidizing and reducing treatment of the sample, low-temperature resistance and fit parameters are shown in Figure 8.4. The as-grown resistance at low temperatures (purple in Figure 8.4a) can be reversibly switched to higher resistances by the oxidizing treatment (red) and back close to the as-grown state by the reducing treatment (blue). This shows the qualitatively same result as for the stoichiometrically grown sample, except that the resistance stays at higher values for higher temperatures.

The carrier densities are shown in Figure 8.4b in the same color scheme and show that the carrier densities are lowered for both carrier types at all temperatures by the

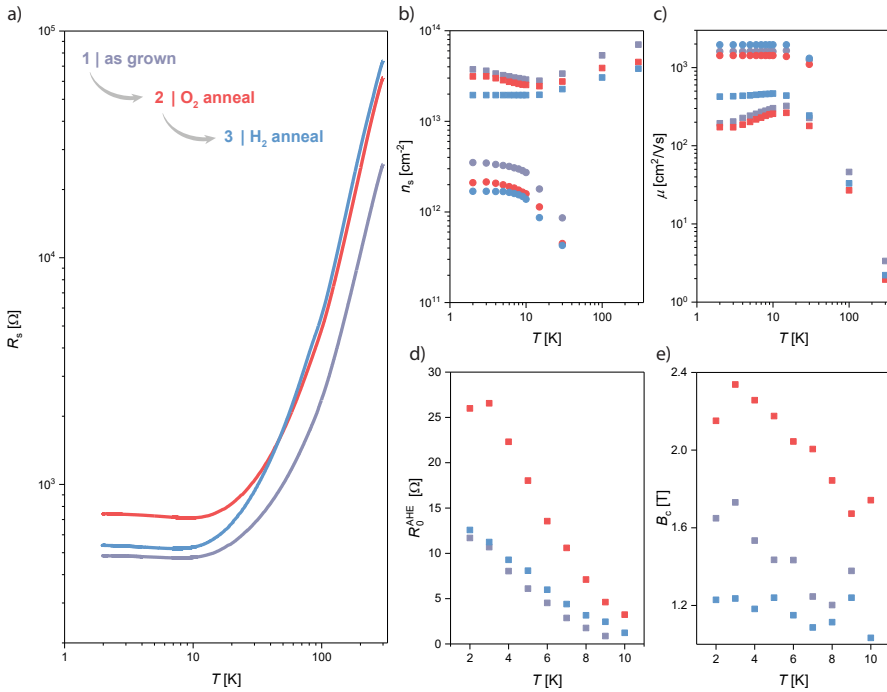**Figure 8.4:** The fitting parameters obtained from low temperature Hall coefficients for a La-deficient, 4 uc LAO/STO sample are shown. The as-grown state is colored in purple, the oxidized state in red and the reduced state in blue. The first carrier population is shown as squares and the second as circles. The carrier densities are shown in a), the mobilities in b), the anomalous Hall coefficient in c) and the critical field in d)

oxidizing treatment. This effect is more pronounced for the second carrier population ($n_2$, shown as dots) than for the first carrier population ($n_1$, shown as squares). The reducing treatment leads to a further lowering of both carrier densities in this particular case. However, for most samples measured, the carrier density shows a tendency to recover back to its pristine state.

The mobilities of the carrier populations are shown in Figure 8.4c. Both mobilities $\mu_1$ (shown as squares) and $\mu_2$ (shown as dots) are lowered by the oxidizing treatment and the reducing treatment leads to even higher mobilities than observed in the as-grown state. Comparing carrier density and mobility an inverse behavior is observed for $n_1$ and $\mu_1$, showing increasing values for $n_1$ in the range of 2-10 K and decreasing values for $\mu_1$. This behavior is a fitting artifact, stemming from the product of the two parameters in equation 3.21.

Regarding the magnetic signature of samples, the anomalous Hall coefficient ($R_0^{\mathrm{AHE}}$) shown in Figure 8.4d is reversibly switched from low values (12 $\Omega$ at 2 K) in the as-grown state to high values by the oxidizing treatment (26 $\Omega$ at 2 K) and back close to its original value by the reducing treatment. The qualitatively same behavior is observed for the critical field ($B_c$) shown in Figure 8.4e. Here the data is more scattered, but showing the same qualitative result.

Due to the generally high AHE contribution in these samples, the determination of carrier density and mobility suffers an increased amount of error. The aforementioned products of carrier density and mobility in the used two-carrier model, lead to multiple possible solutions of these values. While without AHE contributions, stable results can be frequently obtained, a high AHE contribution can lead the values of carrier density and mobility to drift apart. This behavior can explain the observed difference between stoichiometric and La-deficient samples.

The magnetism of the analyzed sample is reversibly switched between a high magnetic (high $R_{\mathrm{AHE}}^0$ and $B_c$) and a low magnetic state (low $R_{\mathrm{AHE}}^0$ and $B_c$), by the respective oxidizing and reducing treatments. Even though the fitting becomes more unstable, a similar behavior to the one of stoichiometric samples is observed, indicating that the underlying mechanism is related. Most importantly, the defectiveness of the LAO thin film has a strong influence on the generally observed magnitude of the $R_{\mathrm{AHE}}^0$ and $B_c$. Through the application of oxidizing annealing, their values can be increased more significantly than observed in the stoichiometric sample.

The complete experimental series of 4, 8 and 12 uc grown stoichiometrically and La-deficient was analyzed as discussed above. In these experiments some sample to sample variation of the resistance and the exact magnitude of charge carriers and mobilities upon thermodynamic annealing is observed. However, regarding the AHE contribution, a robust and reproducible behavior is visible. The $R_0^{\mathrm{AHE}}$ extracted from $R_{\mathrm{H}}$ fits over temperature are shown in Figure 8.5 for all samples in the as-grown, oxidized and reduced state. In each of these measurements the anomalous Hall contribution is increased when an oxidizing treatment was applied. A reducing treatment leads to a less pronounced anomalous Hall contribution close to the value of the as-grown state. Going from thinner to thicker thin films the AHE is most pronounced in the thinnest sample of 4 uc and is strongly suppressed for the 8 uc sample until it is almost not present at 12 uc. A suppression of the AHE is also observed for stoichiometrically grown samples, which show generally lower contributions of the
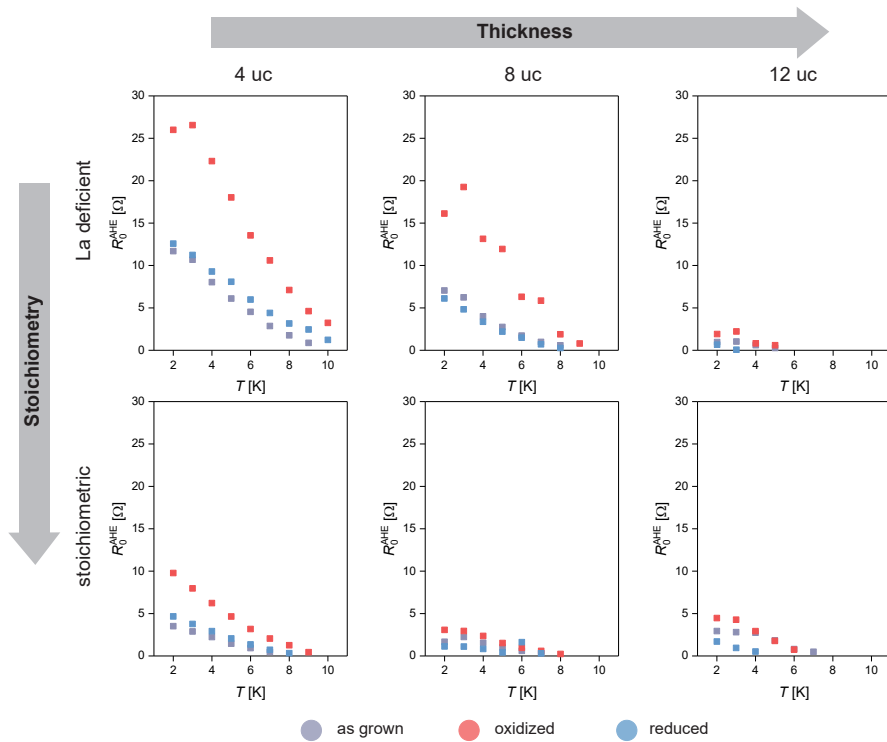
**Figure 8.5:** The $R_0^{\mathrm{AHE}}$ for a series LAO/STO samples are shown in three states: as-grown (purple), oxidized (red) and reduced (blue). The top row shows La deficient samples while the bottom row shows stoichiometric samples. The thickness is increased from left to right showing 4, 8 and 12 uc thick LAO/STO samples.

AHE at each thickness. The critical field behaves similar to the $R_0^{AHE}$ as shown in Figure 8.3e, in each case.

## 8.3   Chapter summary

It was shown in this chapter how the thermodynamic annealing of LAO/STO heterostructures leads to a reversible behavior of the magnetic signature (AHE). Oxidizing treatments increase the magnetic signature while reducing treatments lead to a reversal of the effect. At the same time, oxidizing treatments lead to a drop of carrier density as well as the mobility. These could be recovered back close to their original values by reducing treatments. However, for samples showing very high AHE contributions, the fitting procedure becomes unstable, making the determination of carrier density and mobility difficult. Furthermore, the distinct influence of LAO stoichiometry and thickness on the magnetic signature changes ($R_{AHE}^0$ and $B_c$) due to the thermodynamic annealing process was demonstrated. Most pronounced magnetism was achieved for the thinnest (4 uc), La-deficient sample, while the other samples show a clear trend to lower magnetism for thicker, more stoichiometric samples.

Putting these results in context with the ones obtained in chapter 7 can explain the observed behavior. It was shown that Sr ions precipitate out of the the STO substrate into the LAO thin film and migrate towards the LAO surface. The magnetic signature (defined by the magnitude of $R_{AHE}^0$ and $B_c$) is most pronounced in samples, which received a thermodynamic annealing that triggers Sr precipitation. Both effects (increase of magnetic signature and Sr precipitation) are reversible, further underlining the observed correlation. While the magnetic signature is increased, the carrier density and mobility is lowered for all analyzed heterostructures. Also this effect can be explained by Sr precipitation as the formation of Sr vacancies consumes two electrons and their presence poses scattering centers for electron transport.

A strong increase in the magnitude of the magnetic signature is observed for samples, that are La-deficient and as thin as possible for 2DEG formation (4 uc). Assuming Sr precipitation to be responsible, the higher defectiveness should promote Sr diffusion, as more closely spaced locations for ionic motion exist in the crystal lattice. Thinner LAO overlayers lead to smaller pathways for Sr ions to reach the LAO surface, which should promote the amount of surface precipitates. As it was shown that magnetic moments inside the LAO caused by cation intermixing can induce an increased magnetism in La-rich LAO/STO, [96] these results show that a similar effect might be responsible for La-deficient LAO/STO. Therefore, the presence of $Sr_{La}$ A-site defects or also SrO precipitates are likely causes for the observed behavior. These kinds of defects are neglected in current literature. However, the results presented here show that further investigation would be highly beneficial for the understanding of the magnetic behavior of LAO/STO. Based on the shown experiments, a tuning of magnetism in LAO/STO can be achieved by activating the thermodynamic defect structure of the interface. The magnitude of magnetism of the interface can be controlled by the La-content and the thickness of the LAO thin film. By the fabrication of thin and La-deficient LAO/STO heterostructures, magnetism emerges through oxidizing annealing treatment in a reversible manner.

# Chapter 9

# Discussion

During the course of this thesis, the interface chemistry of the LAO/STO system and its influence on electronic and magnetic properties was analyzed. The distribution of Strontium was identified to play a major role for the interface chemistry in the lateral direction as well as across the interface. For this purpose, the properties of LAO thin films fabricated under various deposition conditions were analyzed by XRD, XPS and AFM to improve the understanding of the interfacial constitution. By exploiting the sensitivity of the LAO/STO interface on the STO termination, a locally distributed 2DEG was achieved showing distinctly different behaviors in dependence of the areal fractions of SrO- and $TiO_2$-terminated regions, but also depending on the exact SrO morphology. This was achieved by the use of two approaches, one being the use of the inherent mixed termination of STO crystals and one being the controlled deposition of SrO on $TiO_2$-terminated STO. To link the local conductivity behavior to macroscopic sample properties, c-AFM was applied to map the local conductivity of the 2DEG in combination with corroborative experiments using s-SNOM. The suitability of this technique for this application was demonstrated and used to gain information in a destruction-free manner.

In the second part of this thesis, the interface chemistry was manipulated by annealing in defined atmospheres to trigger a reordering of Sr ions into thermodynamic equilibrium. The interfacial mechanism involves ionic and electronic charge transfer processes across the interface. Strontium distribution and reordering during annealing procedures proofed to be a key point to understand the electronic property changes of the interface upon oxidation. Applying NAP-XPS gave direct proof of cation movement at temperatures below 500 °C, much lower than expected from Sr bulk diffusion. The resulting changes of electronic and magnetic properties of the LAO/STO interface could be linked to the interplay between LAO properties and Sr precipitation. Using the model, a an engineering route was developed to control the magnetic state of LAO/STO heterointerfaces. By combining defective LAO thin films with thermodynamic annealing, the interface can be driven to favor the formation of Sr vacancies, which leads to a strongly pronounced magnetic signature.

# 9.1 Lateral distribution of local interface chemistry regions

In chapter 5, the local formation of the LAO/STO 2DEG was analyzed by the means of scanning probe techniques using phase contrast AFM, c-AFM and s-SNOM. From the results of phase contrast AFM, the distinct topographic features of STO substrates which received the same etching treatment could be identified as areas of different surface terminations (either SrO- or TiO$_2$-terminated). For surfaces showing smooth terrace edges, a single TiO$_2$-termination could be verified while surfaces which showed deviations in the form of kinked terrace features could be shown to have a mixed termination. The kinked features have an SrO-terminated surface and more extreme cases visible in the STO topography equally showed higher amounts of SrO-terminated areas (see Figure 5.2).

Through deposition of LAO on these STO substrates with different degrees of termination, the formation of a locally distributed 2DEG could be achieved. Its existence could be verified by applying c-AFM to measure the local resistance across the sample surface. Through application of a side contact, the local resistance of the 2DEG could be accessed. Therefore, the local electrical properties of LAO/STO samples could be mapped with lateral resolution in the nanometer range. The result for the most pronounced sample is shown in Figure 9.1a. The LAO thin film copied the distinct topographic features that were determined to be SrO-terminated by phase contrast AFM (Figure 5.2). At these local positions, the current maps show sharply resolved dark regions, where no current could be detected. These dark regions, therefore, correspond to locally insulating LAO/STO interfaces due to their $p$-type character with a SrO/AlO$_2$ stacking that is known to be insulating. [13, 43–45] The c-AFM results could be corroborated by the application of s-SNOM which is also able to detect the local



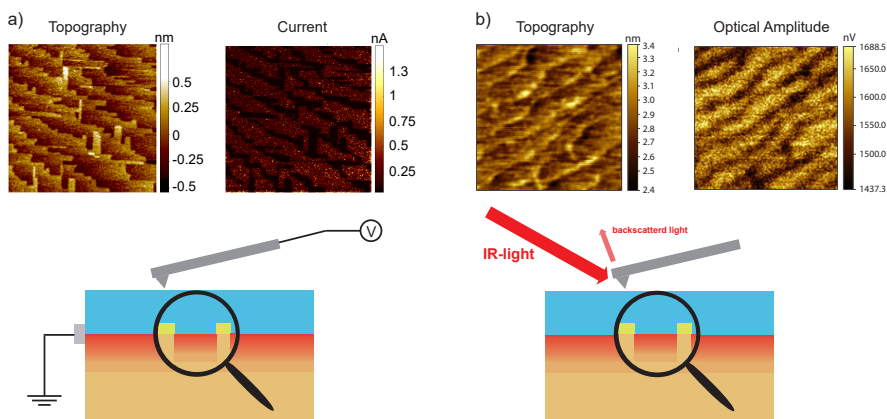**Figure 9.1:** a) Shows the topography and current map on a LAO/STO sample with local 2DEG due to mixed termination analyzed by c-AFM. An illustration of the principle is shown at the bottom. b) Shows the topography and optical amplitude of a LAO/STO sample with local 2DEG due to a mixed termination. An illustration of the principle is shown at the bottom. All scanning probe images are 1 μm × 1 μm.
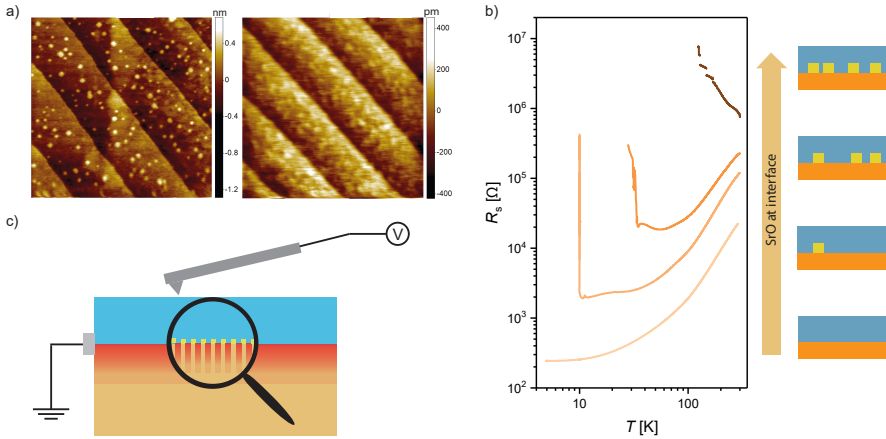
**Figure 9.2:** a) Shows topography of a STO substrate with 1 pulse of SrO deposited (left) and with a consecutively grown 4 uc LAO layer (right) of a LAO/SrO/STO sample. The images are 1 μm × 1 μm in size. b) Shows the low-temperature resistance of LAO/SrO/STO samples with increasing amount of SrO at the interface. c) Shows a sketch of the c-AFM measurement, where the finely grained SrO is depicted at the interface.

electronic properties of LAO/STO interfaces. [104–106] The result is shown in Figure 9.1b, showing the topography and optical amplitude of the s-SNOM measurement. The working principle is shown in a sketch at the bottom. It is based on illuminating a cantilever tip with a light source (IR light here) and analyzing the backscattered light, which amplitude depends (among other influences) on the local electrical properties of LAO/STO. [106] In the optical amplitude the s-SNOM measurements show the same pattern as observed in c-AFM. While c-AFM measurements are unable to differentiate between a local 2DEG and other sources for a locally increased resistance (like a local thickness variation of the thin film), the s-SNOM showing the same contrast corroborates the deduced interpretation.

Furthermore, the influences of the nanoscopic local features resolved by c-AFM and s-SNOM on macroscopic transport could be shown in low-temperature measurements (see Figure 5.9). Not only a trend to higher resistances at low temperatures for higher amounts of SrO related features is observable. Also the low-temperature resistance deviated from metallic behavior, showing a resistance upturn, which could be an indication of Kondo-like behavior. However, in this particular case, the resistance upturn can be well explained by a freeze out of percolation paths between conducting regions of the 2DEG and, therefore, is more likely an effect of the systems inhomogeneity rather than Kondo-scattering. Applied Hall measurements and modeling by a two carrier model revealed that macroscopically, the locally increased resistance shows influence from carrier density as well as mobility (see Figure 5.10). This result indicates that the observed inhomogeneities, therefore, also act as scattering centers for electron transport at low temperatures.

The study of the local inhomogeneity using scanning probe techniques at LAO/STO, revealed how the macroscopic transport is influenced by the nanoscopic structure of the system. The technique of c-AFM (not used before in this manner), could be

used to create a mapping of the 2DEG distribution. These results form the baseline for further studies to analyze the local 2DEG distribution and its influence on the electrical properties of LAO/STO. Applying c-AFM in the proposed way, enables the study of local interface phenomena in a destruction free manner even though it is a buried structure. The role of homogeneity at such charge transfer interfaces could hold important insights into the details of 2DEG formation and elucidate how and when the electrical properties of samples differ due to natural variations of the STO substrate. Furthermore, the local mapping of the 2DEG at room temperature could reveal inherently insulating and conducting LAO/STO for the first time in the same sample without any previous patterning applied.

In a further approach the interface chemistry was manipulated in a controlled manner by the deposition of SrO at the interface of the system. The results show that the interfacial properties show distinctly different behavior compared to the use of substrates with mixed termination. Instead of forming localized insulating patches, the SrO redistributes upon LAO deposition. This is evident for one by the inability to resolve insulating regions in c-AFM. Second, the surface topography (Figure 9.2a) is changed from a surface where the SrO is distributed as particles of 0.4 nm height to a surface where a finely grained structure is present where only height differences in the range of 0.2 nm are observed. To low temperatures (Figure 9.2b), the system undergoes a metal-to-insulator transition, occurring at increasingly high temperatures with increasing amount of SrO at the interface. As c-AFM shows an evenly distributed 2DEG and the LAO topography does not represent the observed structure of the SrO/STO sample, a redistribution must have taken place. In this case, finely distributed SrO at the interface can explain the observed behavior as sketched in Figure 9.2c. In c-AFM studies, where the termination was ordered in nanoscopic patches, a resistance upturn to low temperatures was observed. The observed metal-to-insulator transition could be an effect of the freeze out of percolation pathways, where the increasing amount of insulating pathways shifts the transition temperature to higher values.

The manipulation of the interface chemistry via SrO growth reveals the high importance of exact distribution of the 2DEG on the macroscopic behavior. The same amount of SrO-termination distributed in a different way can make the difference between metallic and insulating behavior. Only via the applied *in-situ* studies, the different constitutions of the interface could be identified, highlighting the important role of these techniques for research of complex material systems.

The lateral inhomogeneities, caused by differences in the local interface chemistry of the LAO/STO heterostructure show how the manipulation of the local interface structure affects macroscopic transport. The observed effects of the SrO-termination go beyond tuning the resistance of the interface by increasing amounts of locally insulating regions. The effective termination distribution depends on the constitution of SrO on STO, which can lead to ordered or finely spread SrO-terminated regions. Distinctly different macroscopic electrical behavior emerges, depending on the resulting distribution of conducting and insulating areas.

## 9.2   Interface chemistry manipulation via thermodynamic equilibria

In the work discussed in chapter 9.1, the interface chemistry of the LAO/STO system was analyzed in the lateral direction, analyzing the variations between heterostructures with different interface chemistry distributions. This approach was facilitated through the fabrication of samples that hold different amounts of local inhomogeneity. However, previous works have shown that the ionic constitution and thereby the interface chemistry of LAO/STO interfaces might be manipulable after growth. The behavior of LAO/STO when transitioning from one thermodynamic equilibrium to another was addressed by the ECR analysis in chapter 6. The ECR principle of measuring the conductance *in-situ* under applied temperature and $pO_2$ is sketched in Figure 9.3a. It could be observed that the conductance of the LAO/STO 2DEG is lowered under oxidizing atmospheres as shown in Figure 9.3b. The lowered conductance can be mainly attributed to a change in the carrier density of the system. The process is completely reversible, showing that a defect chemical equilibrium process is taking place. From the equilibrium conductance values, it could be furthermore shown that the process is temperature activated.

The lowered carrier density of the 2DEG, the reversibility of the process and the fact that it is temperature activated, all fit into the defect chemical model, where the 2DEG charge carriers are ionically compensated by Sr vacancies. The proposed behavior of epitaxial LAO/STO interfaces is sketched in Figure 9.3c. According to this model, the conductance in oxidizing conditions is lowered because the system incorporates Sr vacancies. This behavior is frequently observed in context of donor
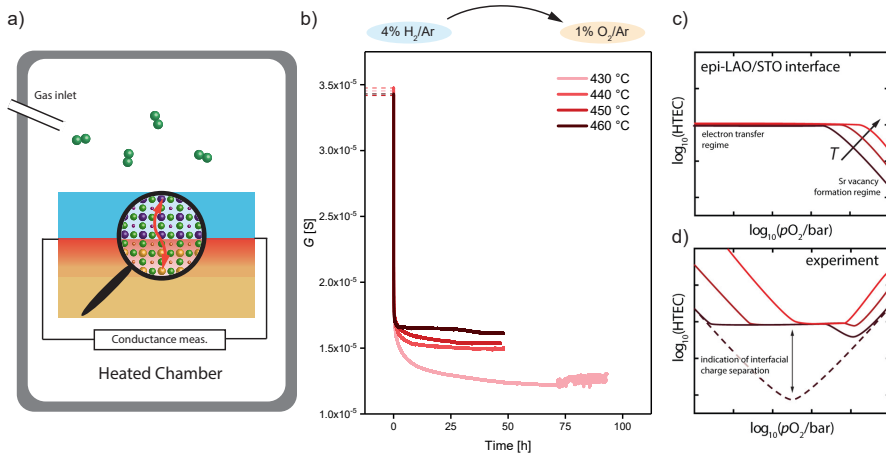


**Figure 9.3:** a) Shows the measurement principle of *in-situ* conductance measurements in ECR. b) Shows the conductance behavior of LAO/STO under oxidation. The conductance behavior proposed in the literature of an epitaxial LAO/STO interface in thermodynamic equilibrium is shown in c) without substrate conductance and in d) with substrate conductance as seen in experiment.
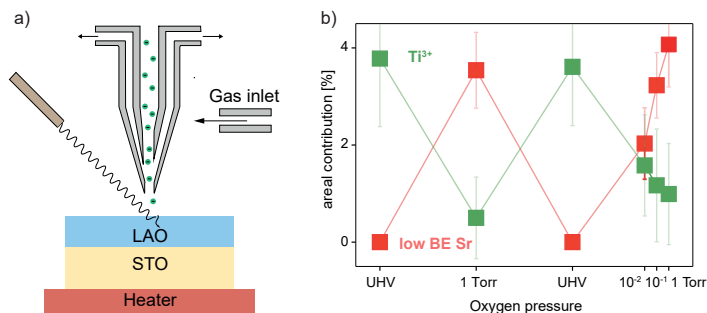
**Figure 9.4:** A sketch of the NAP-XPS measurement principle is shown in a). The inverse behavior of electrons (Ti$^{3+}$) and secondary Sr phase (low BE Sr) is shown in b). The Figure was published in Ref. [212] (modified).

doped STO ceramics. Sr vacancy formation requires temperature, as the process is otherwise kinetically limited through the lack of ionic motion. However, it is also an exothermic process, which makes the equilibrium Sr vacancy concentration lower with increasing temperature, showing the same temperature dependence as observed in ECR (Figure 9.3b). Through experimental referencing, the STO substrate could be excluded from the conductance of the heterostructure, as otherwise the behavior sketched in Figure 9.3d would be expected. Furthermore, the results reveal a decrease of the equilibration time with decreasing temperature, showing that the process is facilitated faster for higher temperatures. For details of this analysis, see chapter 6.

The dynamic changes of conductance at the LAO/STO heterointerface reveal that the defect chemical model of Sr precipitation is a valid explanation. However, the measurement is indirect in nature and cannot contribute direct proof. Furthermore, the reaction raises questions about the exact nature of the process, as the LAO/STO interface is rather complex in nature, involving five elements and a complex band alignment. Could other models explain the observed behavior? Does Sr form SrO or similar secondary phases right at the interface or is it moving across the LAO thin film? To give answer to these questions, a detailed analysis of the interface chemistry using NAP-XPS was conducted. The method enables the identification of chemical phases, while applying thermodynamic conditions. Further, depth profiling techniques such as synchrotron radiation or variation of the LAO thickness are applied to elucidate the location of Sr ions upon oxidation.

In NAP-XPS, samples are analyzed like in conventional XPS, however, a differential pumping system allows to apply thermodynamic conditions to the sample. This allows to spectroscopically investigate the observed conductance changes in ECR. A sketch of the working principle is shown in Figure 9.4a. Through careful analysis of core-level spectra from all elements (Sr 3$d$, Ti 2$p$, O 1$s$, La 4$d$ and Al 2$p$) a consistently reversible behavior between two elements could be observed, which is shown in Figure 9.4b. Through application of a peak fitting, the contribution of Ti$^{3+}$ ions, which correspond to the amount of free electrons in the 2DEG, to the Ti 2$p$ core-level spectra could be identified (green squares in Figure 9.4b). The amount of free electrons is diminished by exposing LAO/STO to oxygen in a reversible manner, essentially reproducing the effect
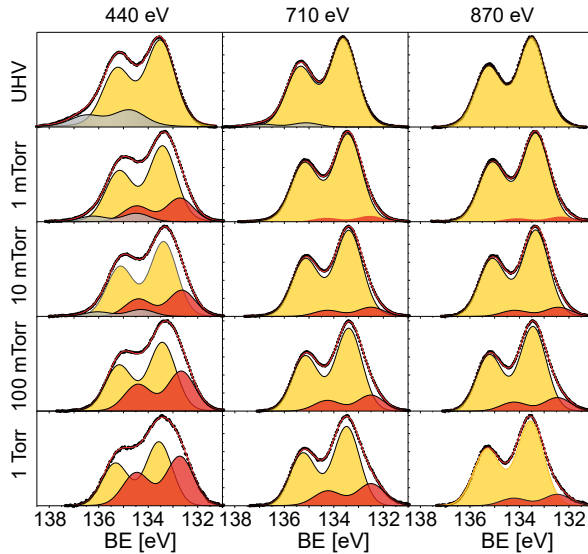
**Figure 9.5:** Sr 3*d* spectra from a 4 uc LAO/STO sample are shown, recorded by a NAP-XPS using synchrotron radiation of 440, 710 and 810 eV and pressures from UHV to 1 Torr. The Figure was published in Ref.: [212] (modified)

seen in ECR. At the same time, a secondary phase appears upon inlet of oxygen in the Sr 3*d* spectra (red squares in Figure 9.4b). Also in this case, the process is completely reversible and intermediate pressure steps lead to intermediate contributions from electrons (in the form of $Ti^{3+}$) and secondary Sr phase (in the form of a low BE Sr component). During this process, the shape of the La 4*d* and Al 2*p* spectra is not changing, showing that they are not participating in the formation of the Sr containing compound.

From the NAP-XPS results it is shown that indeed Sr precipitates out of the STO crystal lattice, while the 2DEG is depleted. The location of the precipitated Sr ions could be further elucidated by the application of depth profiling methods. In this experimental series it is observed, that the low-BE-Sr component is most pronounced in the most oxidizing and surface sensitive measurements (see Figure 9.5). Therein, the component shows a large areal contribution to the overall signal. In another experimental series, the LAO thickness was varied, showing that the low-BE-Sr component is attenuated like a surface phase and not like a phase residing at the interface of the heterostructure (see Figure 7.6). Through the application of these depth profiling methods, the location of precipitating Sr ions could be identified to be on the LAO surface or at least being distributed inside the LAO thin film.

It could be shown that the band alignment of the heterostructure changes upon exposure to oxygen (see Figure 7.12). This could be deduced from an observed higher positive valence band offset between substrate and thin film (see Figure 7.11). Therefore, the position of all overlayer materials is shifted to lower BE. Considering the location of the Sr containing compound, its low BE is expected as it is affected by the same

general potential difference as other overlayer elements. This explains why the Sr containing phase is found to have such an unusual BE value (low in respect to STO) opposed to the commonly observed BE for SrO precipitates (high in respect to STO). The higher valence band offset could be an effect of the changed dipole moment at the interface, which might be related to the presence of additional defects.

Sr cation movement across the interface could hence be proven to be present at temperatures as low as 470 °C. This is much lower than the usually observed temperatures, where cation movement is present in bulk STO. Through the high confinement of the interface, where high electrical fields are present, a strong driving force for Sr vacancy formation is given. This promotes the process as will be summarized below in a defect chemical model.

## 9.3   The derived defect chemical model of Sr precipitation

The ionic motion and electronic structure changes of the LAO/STO system through the influence of thermodynamic treatments were analyzed. At the used temperature of 470 °C and $p$O$_2$ between UHV and 4 Torr it is evident that ionic motion is significantly influencing the electronic properties of the system. The spectroscopic interface analysis proofs that Sr ions are precipitating out of the STO substrate while their vacancy formation depletes the 2DEG (see Figure 7.3). This result is further corroborated by the distinct behavior of the precipitating Sr ion's spectroscopic signature (low-BE-Sr). This behavior was analyzed in the applied depth profiling where surface phase like behavior was observed under varied PE (see Figure 7.4) and in samples of varied LAO thicknesses (See Figure 7.6). Furthermore, the lowered BE behaves accordingly to the changed band alignment of the heterointerface, showing the same BE shifts as other overlayer elements (see Figure 7.11). Therefore, it can be concluded that Sr is precipitating into the LAO layer towards the LAO surface when higher $p$O$_2$ is introduced. The formation of Sr vacancies depletes the 2DEG and the introduced defects act as scattering centers for electrical transport. In this context the lowered carrier density and mobility extracted from low temperature Hall measurements can be easily understood (see chapter 8). The observed enhanced magnetic signature, however, cannot by directly linked and remains phenomenological to this point. The influence of Sr vacancies on magnetism could also be indirect by local strain or through a stronger localization by the lowered mobility.

The role of an active Schottky equilibrium and resulting Sr precipitation was already discussed in the literature to be a possible explanation for the observed behavior at elevated temperatures [39, 40]. At complex oxide interfaces, however, an intricate interplay of the two materials LAO and STO is present and it has to be carefully evaluated if the observed behavior cannot be explained by other defect scenarios as well. The most prominent one that has to be taken into consideration is the presence of oxygen vacancies, which are known to play a vital role for properties of the LAO/STO system. [62, 234, 242] Therefore, it has to be elaborated if the incorporation and annihilation of oxygen vacancies in STO as well as at the LAO surface is able to consistently explain the results just as well as the proposed mechanism. On the STO

side, oxygen vacancies are mainly growth induced and do not appear in significant concentrations through the thermodynamic conditions applied here. As could be seen in chapter 4.1, growth induced oxygen vacancies can be removed by oxidizing treatments at elevated temperatures. However, it is not possible to reincorporate them by reducing treatments as they are not caused by the surrounding thermodynamic condition but by the PLD plasma plume. [88] For this reason the reversibility of Ti$^{3+}$ signature in the Ti 2$p$ core level spectra, as observed in NAP-XPS in this thesis, cannot be explained by growth induced oxygen vacancies in the STO substrate.

Inside the LAO thin film, the concentration of oxygen vacancies is partially fixed by its cation stoichiometry. Nonstoichiometry leads to the formation of cation vacancies which have to be ionically compensated by the incorporation of oxygen vacancies [72]. However, at the surface of the LAO thin film, oxygen vacancies are formed to compensate for the electrons which were transferred to the interface during 2DEG formation. [67, 68] These may be refilled when $p$O$_2$ is increased and thereby deplete the 2DEG, as additional electrons are required for this process. Essentially, this would lead to a reversal the 2DEG formation process, as the LAO polarity is not compensated anymore by interfacial electrons. However, there are three reasons against this scenario. First, a depletion of the charge carrier density of the 2DEG by one order of magnitude (as was seen in ECR and in NAP-XPS) would lead to a large potential across the LAO layer, as the LAO polarity would be mostly uncompensated (see above). It is known, that this scenario is not favored by LAO/STO, as the 2DEG is formation takes place to avoid this very state in the first place. Second, the resulting fields would be detectable in the NAP-XPS experiments as was discussed in chapter 7.3. Only a small field of 0.1 eV/nm is deduced to be present after oxidation, which indicates that indeed some oxygen vacancies might be refilled. However, a complete compensation can be ruled out as the observed potential should be comparable to the one of an uncompensated LAO thin film (0.6-0.9 V/nm), [79, 243, 244] if a complete surface oxygen vacancy compensation is assumed. Third, the distinct and reversible behavior of the Sr 3$d$ core-level spectra is ignored by the above mentioned scenario. The proven precipitation of Sr ions has to be compensated inside the STO, where the depletion of free carriers is the most likely scenario. Therefore, to explain the entirety of the observed behavior the Schottky equilibrium of the Sr lattice in the STO crystal has to be taken into account.

As a reversible dynamic response of the Sr 3$d$ spectrum was observed, the mobility of Sr ions is sufficient for them to move through the heterostructure. Two mechanisms of the evolving defect chemistry that describe this particular defect formation process are listed in Figure 9.6. In the case of a STO crystal, the release of Sr ions occupying the STO lattice (Sr$_{Sr}^{x}$) results in the formation of SrO surface precipitates (SrO$_{s.p.}$) due to the reaction with gaseous oxygen (O$_2$(g)) (right mechanism in Figure 9.6). To fulfill the charge neutrality the reaction consumes electrons or in other words, the Sr takes up its valence electrons upon leaving from the crystal. The same reaction can be written for the LAO/STO system if it is assumed that Sr is precipitating directly to the LAO surface. The defect reaction equation of this process is reads

$$\mathrm{Sr}_{\mathrm{Sr}}^{x} + \frac{1}{2}\mathrm{O}_2(\mathrm{g}) + 2e' \rightleftharpoons V_{\mathrm{Sr}}'' + \mathrm{SrO}_{\mathrm{s.p.}} \tag{9.1}$$
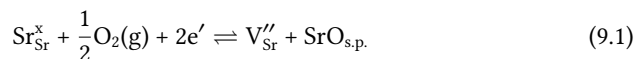
The driving forces behind this reaction are the concentration of available oxygen
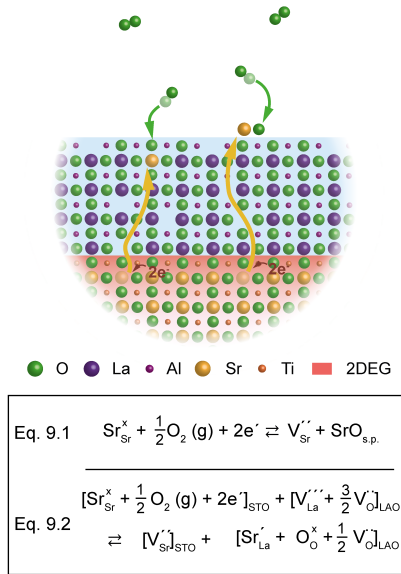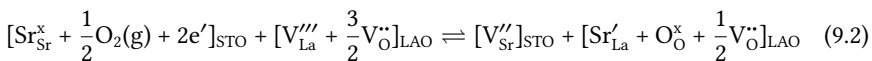
**Figure 9.6:** An Illustration of the possible Sr configurations are shown in an atomic model. Beneath the two resulting Schottky equilibria are shown for the precipitation of Sr to the LAO surface (Equation 9.1) and for the precipitation into the LAO thin film occupying La vacancy sites (Equation 9.2). The Figure was published in Ref. [212] (modified).

(giving by the $p\mathrm{O}_2$) and the available electron concentration. In LAO/STO, a highly dense electron gas is present at the interface which drives the reaction towards the formation of surface precipitates and consequently to the incorporation of Sr vacancies.

While this equation illustrates well the general behavior, in reality Sr ions have to pass through the LAO layer when they leave the STO crystal. Therefore, an intermediate reaction step is required which involves the defect states inside the LAO layer, as Sr ions are too big for interstitial diffusion. The LAO layer deposited by PLD is known to be not perfectly stoichiometric. La vacancies were found to be typically present in LAO thin films [69, 92, 245] and even promote the formation of the 2DEG [69, 236]. Further defects known to be present are the aforementioned oxygen vacancies which compensate cation non-stoichiometry [40, 69, 236] and surface oxygen vacancies compensating the interface dipole [67]. When Sr is diffusing into the LAO layer under the uptake of oxygen, this mechanism is facilitated through the present La and O vacancy complexes (left mechanism in Figure 9.6). In accordance to literature, an analysis of the XPS data determined that the LAO stoichiometry of the used thin films is indeed slightly La-deficient. [69, 236] Therefore, La vacancies will be present inside the used LAO overlayers. The defect reaction, where an Sr ion is moving from its STO lattice site on the empty La-site in the LAO lattice under concomitant refill of the oxygen vacancy reads

$$[\mathrm{Sr}_{\mathrm{Sr}}^{\mathrm{x}} + \tfrac{1}{2}\mathrm{O}_2(\mathrm{g}) + 2\mathrm{e}']_{\mathrm{STO}} + [\mathrm{V}_{\mathrm{La}}''' + \tfrac{3}{2}\mathrm{V}_{\mathrm{O}}^{\cdot\cdot}]_{\mathrm{LAO}} \rightleftharpoons [\mathrm{V}_{\mathrm{Sr}}'']_{\mathrm{STO}} + [\mathrm{Sr}_{\mathrm{La}}' + \mathrm{O}_{\mathrm{O}}^{\mathrm{x}} + \tfrac{1}{2}\mathrm{V}_{\mathrm{O}}^{\cdot\cdot}]_{\mathrm{LAO}} \quad (9.2)$$

The total charge inside the LAO is unaffected by this process, so the polarization of the LAO layer remains. When Sr is diffusing further through the LAO thin film, Equation 9.2 will ultimately transform into Equation 9.1, when Sr agglomerates and forms a surface precipitate. The driving parameters are the same for both equations. Therefore, higher $pO_2$ and electron density drive both reactions more to right hand side, leading to the formation of Sr vacancies and Sr precipitation. As they describe a route towards thermodynamic equilibrium, lower $pO_2$ and electron density will reverse the process and drive the reaction to the left hand side. Therefore, the behavior seen in NAP-XPS can be consistently explained by this defect chemistry model.

## 9.4  Supporting density functional theory calculations

The stability of the proposed Sr precipitation in the LAO/STO heterostructure was further corroborated by electronic density functional theory (DFT) calculations. These calculations were done by Ivetta Slipukhina of the Peter Grünberg Institute 1 and Institute for Advanced Simulation in the Jülich research center. The total energy of the heterostructure was calculated and compared in five distinct states which are shown in Figure 9.7a-e including the total energy of the respective case. First, the ideal heterostructure is simulated as shown in Figure 9.7a with an oxygen molecule in its vicinity. The oxygen molecule represents the gaseous oxygen in Equations 9.1 and 9.2, and has to be included to accurately account the total energy of the initial state. This is compared to two resulting possibilities: 1. The oxygen is adsorbed to the $AlO_2$ terminated LAO surface (Figure 9.7b). 2. An Sr ion is removed from the interface and placed on top of the LAO surface where it is bound to an oxygen atom (Figure 9.7c). The second configuration is imitating the defect reaction described in Equation 9.1 of Figure 9.6. Furthermore, the heterostructure including an La-O Schottky defect (Figure 9.7d) in vicinity to an oxygen molecule is compared to a heterointerface, where an Sr ion is removed from the interface and placed in the La vacancy site under refilling of the oxygen vacancy (Figure 9.7e). As can be seen by comparing the resulting energies (the lowest being referenced to zero), the most stable states are indeed achieved when Sr precipitates out of the STO crystal, either resulting in a surface phase or occupying the La vacancy site. The total energy of the system is lowered for both cases resulting in an exothermic reaction under the uptake of oxygen. The calculations, therefore, support the interpretations made from NAP-XPS experiments.

To further analyze the electronic structure changes of the system when the oxidation reaction through Sr precipitation takes place, the spin-polarized density of states (DOS) was calculated. The results are shown in Figure 9.7f for the ideal interface (situation in Figure 9.7a) and in Figure 9.7g for the oxidized interface, where an Sr ion was removed from the interface and placed on top of the heterointerface, bound to an oxygen atom (situation in Figure 9.7c). Overall the DOS changes drastically through the Sr precipitation. As can be seen by the dashed red lines which resemble the Fermi-level, the 2DEG is depleted by the presence of the Sr vacancy at the interface. This behavior fits well to the observed diminished $Ti^{3+}$ signature in the Ti $2p$ core level spectra (Figure 7.3). Furthermore the polarity of the LAO thin film can be compensated by the Sr vacancy which poses a localized negative counter-charge at the interface.
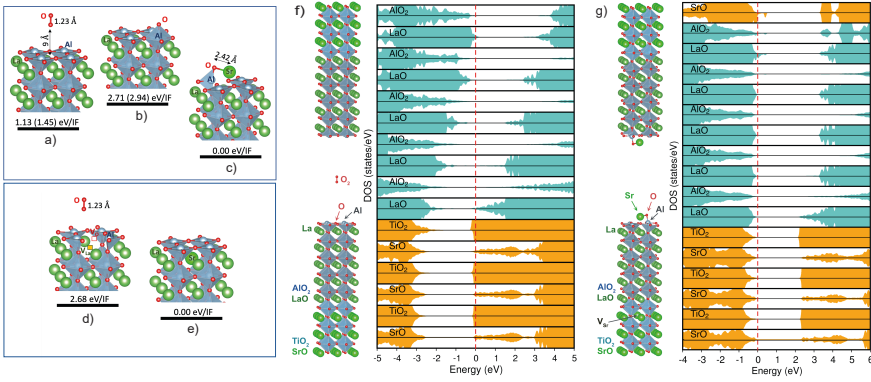
**Figure 9.7:** In a)-e) the relative energetic stability of a LAO/STO slab under oxidizing conditions is shown as obtained from DFT including the surface of the used simulation for: a) an ideal interface with an oxygen molecule in the vicinity, b) an ideal interface with an oxygen atom adsorbed to the $AlO_2$-terminated surface atop the Al site, c) an interface with a single Sr vacancy and SrO precipitate on an $AlO_2$-terminated surface, d) an ideal interface with La and O vacancies in the LaO overlayer upon oxidizing conditions, e)the interface with a Sr moved from the interface to a La vacancy site together with oxygen occupying the O vacancy site in the LaO overlayer. The values were obtained at $U_{Ti}$ = 4 eV. The numbers in parentheses were obtained at $U_{Ti}$ = 7.4 eV for comparison. In f) and g) the structural model and the layer-resolved spin-polarized DOS for a LAO/STO slab is shown under oxidizing conditions (obtained at $U_{Ti}$ = 4 eV). The case of an ideal interface (similar to (a)) is shown in f) and the case of a single Sr vacancy and SrO precipitate on an $AlO_2$-terminated surface (similar to (c)) is shown in g). Here the red dashed line represents the Fermi-level. The upper and lower parts of each graph correspond to the spin-up and spin-down DOS. The Figure was published in Ref. [212].

This behavior corroborates the interpretation made in chapter 7.4, that Sr vacancies are able to compensate the polarity in the same manner as the delocalized electrons of the 2DEG.

## 9.5 Influence of thermodynamic annealing and LAO stoichiometry on magnetism

Based on the above described defect chemical model, the precipitation of Sr ions should be kinetically promoted if the LAO thin film exhibits a more defective structure. In the proposed model, La vacancy sites are a key factor for the movement of Sr. Considering this model picture, samples should behave distinctly different upon thermodynamic annealing if the LAO thin film is fabricated non-stoichiometric. Furthermore, the LAO thin film thickness should also play a role for the diffusion of Sr, as longer length scales have to be overcome for thicker thin films. This was tested in a low-temperature experimental series, where La-deficiency and thin film thickness were systematically varied. The results show a pronounced increase of the magnetic signature in the form of an anomalous Hall effect, for thin and non-stoichiometric samples. The results show, that conditions which promote the Sr precipitation lead to the most pronounced

magnetism of samples. The changed defect structure of the system, therefore, plays a key role in understanding the emergent magnetism to low temperatures. The results corroborate that the role of $Sr_{La}$ A-site defects, as the proposed $Ti_{Al}$ for La-rich LAO/STO heterostructures, [96] could be a key point in understanding the magnetic signature in the analyzed La-poor counterpart. This conclusion stems from the fact, that the applied conditions should lead to an increased Sr precipitation from the STO substrate into the LAO thin film. However, at the current state of research the exact causation stands phenomenological and further research should be applied to identify the source of the highly increased magnetic signature of these samples.

# Chapter 10

# Conclusion and Outlook

In the course of this thesis, important aspects could be revealed for the understanding of the charge transfer process at interface of LAO and STO. The key results are summarized in Figure 10.1. The presence of local 2DEG formation (right side of Figure 10.1), based on substrate termination could be proven by the application of c-AFM in an unprecedented manner. Maps of the 2DEG distribution were achieved, even though it is a buried structure. The macroscopic electronic properties were highly influenced by the presence of the nanoscopic inhomogeneities down to the low-temperature range. The application of controlled SrO growth in the fabrication of the LAO/SrO/STO structures showed a strong variability of electrical behavior by local termination variation. The electronic LAO/STO properties highly depend on the exact constitution of the termination distribution. This principle of interface manipulation could be further explored. The analysis by c-AFM to create a mapping of the 2DEG distribution could be proven to be a valuable tool in this context. Further research regarding the multitude of possible termination distributions would open up another way to manipulate the interfacial properties of the system. For this purpose, further refinement of the SrO growth process would be beneficial. Also the control over naturally occurring termination variations on STO single crystals would be valuable for further study of possible emerging effects through this nanoscopic patterning.

The ability to manipulate the LAO/STO interface through local inhomogeneities in the form of SrO was already proposed in the literature, [101] but received little attention. Applying c-AFM to verify the resulting local distribution of the 2DEG, opens up a simple and destruction free way to link macroscopic electronic properties to its nanoscopic origin. This made it possible to identify distinctly different behavior, depending on 2DEG distribution. Further application of c-AFM and other scanning probe techniques (like s-SNOM) in this manner provide useful tools to refine the manipulation of the LAO/STO 2DEG by its local termination. In the practical context, this gives also a means of quality control and could help to identify and eliminate the origins of differing interfacial properties in nominally identical heterostructures, which currently hinders real-life application.

The essential role of Sr ions for the LAO/STO interface could be further highlighted in the *in-situ* spectroscopic analysis in thermodynamic equilibrium (left side of Figure 10.1). Upon exposure to oxidizing atmosphere, it could be shown that Sr precipitates into the LAO overlayer. The 2DEG is depleted by the resulting Sr va-
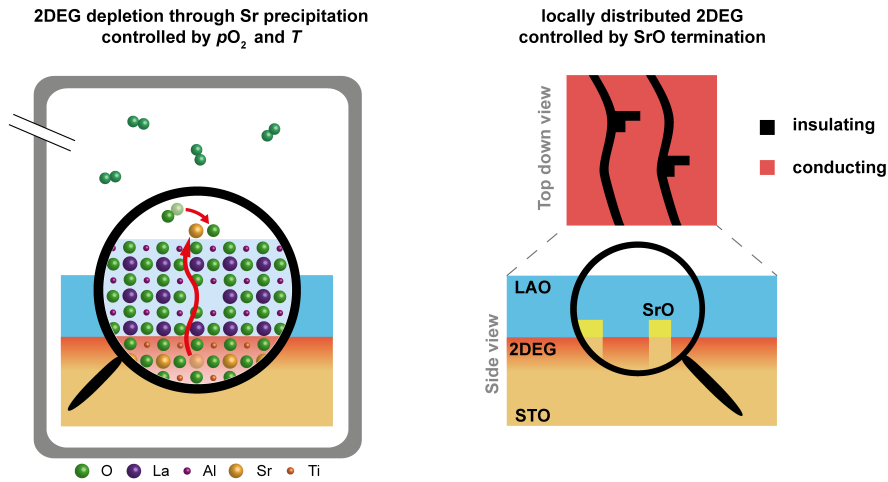
**Figure 10.1:** The twofold approach to use the interface chemistry to manipulate electrical LAO/STO properties is shown. To the left, the application of thermodynamic annealing to trigger Sr ion movement is shown. To the right, the induced locally distributed 2DEG by interfacial SrO is shown.

cancy formation, leading to lower carrier density and mobility of the system. Also enhanced magnetism could be observed. The process alters the band alignment of the heterointerface leading to an enhanced valence band offset between the STO substrate and LAO thin film. Sr precipitation could be embraced in a defect chemical model, where the reaction is facilitated by the defective nature of grown LAO thin films controlled by its stoichiometry. The importance of LAO stoichiometry for the process could be shown in low-temperature Hall series, where thickness and thin film defectiveness were systematically varied. The most pronounced magnetism is observed for heterostructures, which exhibit the highest concentration Sr vacancies according to the deduced model. Therefore, the model does not only provide insight into ionic charge transfer across LAO/STO interfaces, but also a means to control the complex properties of the system. Further research in the strongly pronounced magnetism emerging in this way could gain further insights about its exact source, clarifying if the incorporated defects are directly or indirectly contributing.

Applying the known literature on bulk experiments and well established defect chemical equilibria to the gained results, it could be shown that charge transfer at heterointerfaces is governed by the similar defect chemical principles, while, at the same time, showing much lower kinetic limitations. The principle of charge compensation by ionic defects, as known from the STO bulk, is extended to encompass the present charge transfer at the heterostructure. The resulting defect states at the interface lead to a significantly altered electronic behavior than expected from purely electrical models. Even though the ionic charge compensation is similar to the one observed in donor doped STO, due to the small length scales and highly confined charge carriers, the kinetic limitations are highly different. Therefore, they can be overcome by much lower temperatures than expected for a bulk process. The ionic

mobility at such confined interfaces is considerably enhanced due to the confined interface with strong electrical fields. Therefore, it could be shown that in nanoscaled systems, the possibilities of charge transfer are widened compared to the bulk, as small length scales and high confinement alter the kinetic limitations of defect formation.

Using the here established thermodynamic equilibrium states, the interfacial electronic properties can be systematically varied, by triggering Sr precipitation through the application of $p\mathrm{O}_2$ and temperature. This gives a means to manipulate the carrier density and mobility of free charge carriers in a reversible manner, which enables a tuning of electronic properties. Through this knowledge, thin film fabrication processes can be refined, making the result of general importance for all LAO/STO applications. Furthermore, the unexpected high mobility of cations in this oxide heterostructure is also an important factor to consider in other oxide systems as well, where cation motion might be overlooked due to their low mobility in the bulk. The Sr precipitation process does not only affect electronic, but also the magnetic properties of LAO/STO. A route was established, using the LAO stoichiometry and thermodynamic annealing to set the magnetic properties in a systematic manner. This control over the magnetism could be highly useful not only for scientific purposes, but also for spintronics applications, where the interaction of magnetic moments withelectron spin is of vital importance. Overall, the knowledge of using the ionic structure of LAO/STO to precisely tune its electronic and magnetic properties to their most pronounced extend could be significantly expanded through this work.

# Bibliography

[1] Gordon E. Moore. Cramming more components onto integrated circuits. *Electronics*, 38(8), April 1965.

[2] K. Sugibuchi, Y. Kurogi, and N. Endo. Ferroelectric field-effect memory device using $Bi_4Ti_3O_{12}$ film. *Journal of Applied Physics*, 46(7):2877–2881, 1975.

[3] Asif Islam Khan, Ali Keshavarzi, and Suman Datta. The future of ferroelectric field-effect transistor technology. *Nature Electronics*, 3(10):588–597, 2020.

[4] Tamalika Banerjee. *Oxide spintronics.* Jenny Stanford, Singapore, 2019.

[5] Manuel Bibes and Agns Barthelemy. Oxide spintronics. *IEEE Transactions on Electron Devices*, 54(5):1003–1023, May 2007.

[6] Geoffrey W. Burr, Abu Sebastian, Elisa Vianello, Rainer Waser, and Stuart Parkin. Emerging materials in neuromorphic computing: Guest editorial. *APL Materials*, 8(1):010401, 2020.

[7] Solomon Amsalu Chekol, Felix Cüppers, Rainer Waser, and Susanne Hoffmann-Eifert. An $Ag/HfO_2/Pt$ threshold switching device with an ultra-low leakage (< 10 fA), high on/offratio (> 1011), and low threshold voltage (< 0.2 V) for energy-efficient neuromorphic computing. In *2021 IEEE International Memory Workshop (IMW)*, pages 1–4, May 2021.

[8] Manuel Bibes, Javier E. Villegas, and Agnès Barthélémy. Ultrathin oxide films and interfaces for electronics and spintronics. *Advances in Physics*, 60(1):5–84, 2011.

[9] Darrell G. Schlom and Jochen Mannhart. Interface takes charge over Si. *Nature Materials*, 10(3):168–169, 2011.

[10] H. Y. Hwang, Y. Iwasa, M. Kawasaki, B. Keimer, N. Nagaosa, and Y. Tokura. Emergent phenomena at oxide interfaces. *Nature Materials*, 11(2):103–113, 2012.

[11] J. Mannhart and D. G. Schlom. Oxide interfaces—an opportunity for electronics. *Science*, 327(5973):1607–1611, 2010.

[12] L Bjaalie, B Himmetoglu, L Weston, A Janotti, and C G Van de Walle. Oxide interfaces for novel electronic applications. *New Journal of Physics*, 16(2):025005, feb 2014.

[13] A. Ohtomo and H. Y. Hwang. A high-mobility electron gas at the LaAlO$_3$/SrTiO$_3$ heterointerface. *Nature*, 427(6973):423–426, 2004.

[14] C. Woltmann, T. Harada, H. Boschker, V. Srot, P. A. van Aken, H. Klauk, and J. Mannhart. Field-effect transistors with submicrometer gate lengths fabricated from LaAlO$_3$/SrTiO$_3$-based heterostructures. *Phys. Rev. Applied*, 4:064003, Dec 2015.

[15] Srijit Goswami, Emre Mulazimoglu, Lieven M. K. Vandersypen, and Andrea D. Caviglia. Nanoscale electrostatic control of oxide interfaces. *Nano Lett.*, 15(4):2627–2632, April 2015.

[16] J.H. Ngai, F.J. Walker, and C.H. Ahn. Correlated oxide physics and electronics. *Annual Review of Materials Research*, 44(1):1–17, 2014.

[17] A. Brinkman, M. Huijben, M. van Zalk, J. Huijben, U. Zeitler, J. C. Maan, W. G. van der Wiel, G. Rijnders, D. H. A. Blank, and H. Hilgenkamp. Magnetic effects at the interface between non-magnetic oxides. *Nature Materials*, 6(7):493–496, 2007.

[18] N. Reyren, S. Thiel, A. D. Caviglia, L. Fitting Kourkoutis, G. Hammerl, C. Richter, C. W. Schneider, T. Kopp, A.-S. Rüetschi, D. Jaccard, M. Gabay, D. A. Muller, J.-M. Triscone, and J. Mannhart. Superconducting interfaces between insulating oxides. *Science*, 317(5842):1196–1199, 2007.

[19] Lu Li, C. Richter, J. Mannhart, and R. C. Ashoori. Coexistence of magnetic order and two-dimensional superconductivity at LaAlO$_3$/SrTiO$_3$ interfaces. *Nature Physics*, 7(10):762–766, 2011.

[20] D. A. Dikin, M. Mehta, C. W. Bark, C. M. Folkman, C. B. Eom, and V. Chandrasekhar. Coexistence of superconductivity and ferromagnetism in two dimensions. *Phys. Rev. Lett.*, 107:056802, Jul 2011.

[21] W. Liu, S. Gariglio, A. Fête, D. Li, M. Boselli, D. Stornaiuolo, and J.-M. Triscone. Magneto-transport study of top- and back-gated LaAlO$_3$/SrTiO$_3$ heterostructures. *APL Materials*, 3(6):062805, 2015.

[22] P. D. Eerkes, W. G. van der Wiel, and H. Hilgenkamp. Modulation of conductance and superconductivity by top-gating in LaAlO$_3$/SrTiO$_3$ 2-dimensional electron systems. *Applied Physics Letters*, 103(20):201603, 2013.

[23] Fabio Pulizzi. Oxidized spintronics. *Nature Materials*, 11(7):564–564, 2012.

[24] M. Bibes, N. Reyren, E. Lesne, J.-M. George, C. Deranlot, S. Collin, A. Barthélémy, and H. Jaffrès. Towards electrical spin injection into LaAlO$_3$/SrTiO$_3$. *Philosophical Transactions of the Royal Society A: Mathematical, Physical and Engineering Sciences*, 370(1977):4958–4971, 2012.

[25] Wolter Siemons, Gertjan Koster, Hideki Yamamoto, Walter A. Harrison, Gerald Lucovsky, Theodore H. Geballe, Dave H. A. Blank, and Malcolm R. Beasley. Origin of charge density at $LaAlO_3/SrTiO_3$ heterointerfaces: Possibility of intrinsic doping. *Phys. Rev. Lett.*, 98:196802, May 2007.

[26] Chun-Lin Jia, Juri Barthel, Felix Gunkel, Regina Dittmann, Susanne Hoffmann-Eifert, Lothar Houben, Markus Lentzen, and Andreas Thust. Atomic-scale measurement of structure and chemistry of a single-unit-cell layer of $LaAlO_3$ embedded in $SrTiO_3$. *Microscopy and Microanalysis*, 19(2):310–318, 2013.

[27] Alla Chikina, Frank Lechermann, Marius-Adrian Husanu, Marco Caputo, Claudia Cancellieri, Xiaoqiang Wang, Thorsten Schmitt, Milan Radovic, and Vladimir N. Strocov. Orbital ordering of the mobile and localized electrons at oxygen-deficient $LaAlO_3/SrTiO_3$ interfaces. *ACS Nano*, 12(8):7927–7935, August 2018.

[28] F. Gunkel, D. V. Christensen, Y. Z. Chen, and N. Pryds. Oxygen vacancies: The (in)visible friend of oxide electronics. *Applied Physics Letters*, 116(12):120505, 2020.

[29] Scott A. Chambers. Understanding the mechanism of conductivity at the $LaAlO_3/SrTiO_3(001)$ interface. *Surface Science*, 605(13):1133 – 1140, 2011.

[30] L Qiao, T C Droubay, V Shutthanandan, Z Zhu, P V Sushko, and S A Chambers. Thermodynamic instability at the stoichiometric $LaAlO_3/SrTiO_3(001)$ interface. *Journal of Physics: Condensed Matter*, 22(31):312201, jul 2010.

[31] P. R. Willmott, S. A. Pauli, R. Herger, C. M. Schlepütz, D. Martoccia, B. D. Patterson, B. Delley, R. Clarke, D. Kumah, C. Cionca, and Y. Yacoby. Structural basis for the conducting interface between $LaAlO_3$ and $SrTiO_3$. *Phys. Rev. Lett.*, 99:155502, Oct 2007.

[32] T. T. Fister, H. Zhou, Z. Luo, S. S. A. Seo, S. O. Hruszkewycz, D. L. Proffit, J. A. Eastman, P. H. Fuoss, P. M. Baldo, H. N. Lee, and D. D. Fong. Octahedral rotations in strained $LaAlO_3/SrTiO_3$ (001) heterostructures. *APL Materials*, 2(2):021102, 2014.

[33] C. Cancellieri, D. Fontaine, S. Gariglio, N. Reyren, A. D. Caviglia, A. Fête, S. J. Leake, S. A. Pauli, P. R. Willmott, M. Stengel, Ph. Ghosez, and J.-M. Triscone. Electrostriction at the $LaAlO_3/SrTiO_3$ interface. *Phys. Rev. Lett.*, 107:056102, Jul 2011.

[34] Yanwu Xie, Christopher Bell, Yasuyuki Hikita, Satoshi Harashima, and Harold Y. Hwang. Enhancing electron mobility at the $LaAlO_3/SrTiO_3$ interface by surface control. *Advanced Materials*, 25(34):4735–4738, 2013.

[35] Weitao Dai, Sanjay Adhikari, Andrés Camilo Garcia-Castro, Aldo H. Romero, Hyungwoo Lee, Jung-Woo Lee, Sangwoo Ryu, Chang-Beom Eom, and Cheng Cen. Tailoring $LaAlO_3/SrTiO_3$ interface metallicity by oxygen surface adsorbates. *Nano Lett.*, 16(4):2739–2743, April 2016.

[36] Ngai Yui Chan, Meng Zhao, JianXing Huang, Kit Au, Man Hon Wong, Hei Man Yao, Wei Lu, Yan Chen, Chung Wo Ong, Helen Lai Wa Chan, and Jiyan Dai. Highly sensitive gas sensor by the $LaAlO_3/SrTiO_3$ heterostructure with pd nanoparticle surface modulation. *Advanced Materials*, 26(34):5962–5968, 2014.

[37] S Gariglio, A Fête, and J-M Triscone. Electron confinement at the $LaAlO_3/SrTiO_3$ interface. *Journal of Physics: Condensed Matter*, 27(28):283201, jun 2015.

[38] F. Gunkel, S. Hoffmann-Eifert, R. Dittmann, S. B. Mi, C. L. Jia, P. Meuffels, and R. Waser. High temperature conductance characteristics of $LaAlO_3/SrTiO_3$-heterostructures under equilibrium oxygen atmospheres. *Applied Physics Letters*, 97(1):012103, 2010.

[39] F. Gunkel, P. Brinks, S. Hoffmann-Eifert, R. Dittmann, M. Huijben, J. E. Kleibeuker, G. Koster, G. Rijnders, and R. Waser. Influence of charge compensation mechanisms on the sheet electron density at conducting $LaAlO_3/SrTiO_3$-interfaces. *Applied Physics Letters*, 100(5):052103, 2012.

[40] Felix Gunkel, Rainer Waser, Amr H. H. Ramadan, Roger A. De Souza, Susanne Hoffmann-Eifert, and Regina Dittmann. Space charges and defect concentration profiles at complex oxide interfaces. *Phys. Rev. B*, 93:245431, Jun 2016.

[41] Ralf Moos and Karl Heinz Hardtl. Defect chemistry of donor-doped and undoped strontium titanate ceramics between 1000° and 1400°C. *Journal of the American Ceramic Society*, 80(10):2549–2562, 1997.

[42] Michael Andrä, Filip Dvořák, Mykhailo Vorokhta, Slavomír Nemšák, Vladimír Matolín, Claus M. Schneider, Regina Dittmann, Felix Gunkel, David N. Mueller, and Rainer Waser. Oxygen partial pressure dependence of surface space charge formation in donor-doped $SrTiO_3$. *APL Materials*, 5(5):056106, 2017.

[43] Felix V. E. Hensling, Christoph Baeumer, Marc-André Rose, Felix Gunkel, and Regina Dittmann. $SrTiO_3$ termination control: a method to tailor the oxygen exchange kinetics. *Materials Research Letters*, 8(1):31–40, 2020.

[44] Hong Yan, Jacqueline Marie Börgers, Marc-André Rose, Christoph Baeumer, Bongju Kim, Lei Jin, Regina Dittmann, and Felix Gunkel. Stoichiometry and termination control of $LaAlO_3/SrTiO_3$ bilayer interfaces. *Advanced Materials Interfaces*, 8(3):2001477, 2021.

[45] Christoph Baeumer, Chencheng Xu, Felix Gunkel, Nicolas Raab, Ronja Anika Heinen, Annemarie Koehl, and Regina Dittmann. Surface termination conversion during $SrTiO_3$ thin film growth revealed by x-ray photoelectron spectroscopy. *Scientific Reports*, 5(1):11829, 2015.

[46] Richard J. D. Tilley. *The ABX3 Perovskite Structure*, chapter 1, pages 1–41. John Wiley and Sons, Ltd, Chichester, West Sussex, United Kingdom, 2016.

[47] R. D. Leapman, L. A. Grunes, and P. L. Fejes. Study of the $L_{23}$ edges in the 3$d$ transition metals and their oxides by electron-energy-loss spectroscopy with comparisons to theory. *Phys. Rev. B*, 26:614–635, Jul 1982.

[48] S Piskunov, E Heifets, R.I Eglitis, and G Borstel. Bulk properties and electronic structure of $SrTiO_3$, $BaTiO_3$, $PbTiO_3$ perovskites: an ab initio hf/dft study. *Computational Materials Science*, 29(2):165 – 178, 2004.

[49] Yun-Yi Pai, Anthony Tylan-Tyler, Patrick Irvin, and Jeremy Levy. Physics of $SrTiO_3$-based heterostructures and nanostructures: a review. *Reports on Progress in Physics*, 81(3):036503, feb 2018.

[50] K. A. Müller, W. Berlinger, and F. Waldner. Characteristic structural phase transition in perovskite-type compounds. *Phys. Rev. Lett.*, 21:814–817, Sep 1968.

[51] P. A. Fleury, J. F. Scott, and J. M. Worlock. Soft phonon modes and the 110°k phase transition in $SrTiO_3$. *Phys. Rev. Lett.*, 21:16–19, Jul 1968.

[52] Farrel W. Lytle. X-ray diffractometry of low-temperature phase transformations in strontium titanate. *Journal of Applied Physics*, 35(7):2212–2215, 1964.

[53] Ulrich Aschauer and Nicola A Spaldin. Competition and cooperation between antiferrodistortive and ferroelectric instabilities in the model perovskite $SrTiO_3$. *Journal of Physics: Condensed Matter*, 26(12):122203, mar 2014.

[54] H. E. Weaver. Dielectric properties of single crystals of $SrTiO_3$ at low temperatures. *Journal of Physics and Chemistry of Solids*, 11(3):274 – 277, 1959.

[55] Manuel Cardona. Optical properties and band structure of $SrTiO_3$ and $BaTiO_3$. *Phys. Rev.*, 140:A651–A655, Oct 1965.

[56] R. Moos, T. Bischoff, W. Menesklou, and K. H. Hardtl. Solubility of lanthanum in strontium titanate in oxygen-rich atmospheres. *Journal of Materials Science*, 32(16):4247–4252, 1997.

[57] Joseph A. Sulpizio, Shahal Ilani, Patrick Irvin, and Jeremy Levy. Nanoscale phenomena in oxide heterostructures. *Annual Review of Materials Research*, 44(1):117–149, 2014.

[58] Pavlo Zubko, Stefano Gariglio, Marc Gabay, Philippe Ghosez, and Jean-Marc Triscone. Interface physics in complex oxide heterostructures. *Annual Review of Condensed Matter Physics*, 2(1):141–165, 2011.

[59] Seung-Gu Lim, Stas Kriventsov, Thomas N. Jackson, J. H. Haeni, D. G. Schlom, A. M. Balbashov, R. Uecker, P. Reiche, J. L. Freeouf, and G. Lucovsky. Dielectric functions and optical bandgaps of high-k dielectrics for metal-oxide-semiconductor field-effect transistors by far ultraviolet spectroscopic ellipsometry. *Journal of Applied Physics*, 91(7):4500–4505, 2002.

[60] A. Fête, C. Cancellieri, D. Li, D. Stornaiuolo, A. D. Caviglia, S. Gariglio, and J.-M. Triscone. Growth-induced electron mobility enhancement at the $LaAlO_3$/$SrTiO_3$ interface. *Applied Physics Letters*, 106(5):051604, 2015.

[61] O. N. Tufte and P. W. Chapman. Electron mobility in semiconducting strontium titanate. *Phys. Rev.*, 155:796–802, Mar 1967.

[62] M. Basletic, J.-L. Maurice, C. Carrétéro, G. Herranz, O. Copie, M. Bibes, É. Jacquet, K. Bouzehouane, S. Fusil, and A. Barthélémy. Mapping the spatial distribution of charge carriers in $LaAlO_3/SrTiO_3$ heterostructures. *Nature Materials*, 7(8):621–625, 2008.

[63] S. Thiel, G. Hammerl, A. Schmehl, C. W. Schneider, and J. Mannhart. Tunable quasi-two-dimensional electron gases in oxide heterostructures. *Science*, 313(5795):1942–1945, 2006.

[64] Naoyuki Nakagawa, Harold Y. Hwang, and David A. Muller. Why some interfaces cannot be sharp. *Nature Materials*, 5(3):204–209, 2006.

[65] H. Lee, N. Campbell, J. Lee, T. J. Asel, T. R. Paudel, H. Zhou, J. W. Lee, B. Noesges, J. Seo, B. Park, L. J. Brillson, S. H. Oh, E. Y. Tsymbal, M. S. Rzchowski, and C. B. Eom. Direct observation of a two-dimensional hole gas at oxide interfaces. *Nature Materials*, 17(3):231–236, 2018.

[66] Lixin Zhang, Xiang-Feng Zhou, Hui-Tian Wang, Jing-Jun Xu, Jingbo Li, E. G. Wang, and Su-Huai Wei. Origin of insulating behavior of the *p*-type $LaAlO_3/SrTiO_3$ interface: Polarization-induced asymmetric distribution of oxygen vacancies. *Phys. Rev. B*, 82:125412, Sep 2010.

[67] Liping Yu and Alex Zunger. A polarity-induced defect mechanism for conductivity and magnetism at polar-nonpolar oxide interfaces. *Nature Communications*, 5(1):5118, 2014.

[68] Uwe Treske, Nadine Heming, Martin Knupfer, Bernd Büchner, Emiliano Di Gennaro, Amit Khare, Umberto Scotti Di Uccio, Fabio Miletto Granozio, Stefan Krause, and Andreas Koitzsch. Universal electronic structure of polar oxide hetero-interfaces. *Scientific Reports*, 5(1):14506, 2015.

[69] M. P. Warusawithana, C. Richter, J. A. Mundy, P. Roy, J. Ludwig, S. Paetel, T. Heeg, A. A. Pawlicki, L. F. Kourkoutis, M. Zheng, M. Lee, B. Mulcahy, W. Zander, Y. Zhu, J. Schubert, J. N. Eckstein, D. A. Muller, C. Stephen Hellberg, J. Mannhart, and D. G. Schlom. $LaAlO_3$ stoichiometry is key to electron liquid formation at $LaAlO_3/SrTiO_3$ interfaces. *Nature Communications*, 4(1):2351, 2013.

[70] F. Gunkel, C. Lenser, C. Baeumer, F. Borgatti, F. Offi, G. Panaccione, and R. Dittmann. Charge-transfer in b-site-depleted $NdGaO_3/SrTiO_3$ heterostructures. *APL Materials*, 6(7):076104, 2018.

[71] Yunzhong Chen and Nini Pryds. 2d hole gas seen. *Nature Materials*, 17(3):215–216, 2018.

[72] D.M. Smyth. *The Defect Chemistry of Metal Oxides*. Classic dielectric science book series. Oxford University Press, 2000.

[73] W. E. Pickett, R. Weht, and A. B. Shick. Superconductivity in ferromagnetic $rusr_2gdcu_2O_8$. *Phys. Rev. Lett.*, 83:3713–3716, Nov 1999.

[74] L. N. Cooper, R. L. Mills, and A. M. Sessler. Possible superfluidity of a system of strongly interacting fermions. *Phys. Rev.*, 114:1377–1382, Jun 1959.

[75] H. Ibach and H. Lüth. *Festkörperphysik: Einführung in die Grundlagen.* Springer-Lehrbuch. Springer Berlin Heidelberg, 2002.

[76] Arjun Joshua, S. Pecker, J. Ruhman, E. Altman, and S. Ilani. A universal critical density underlying the physics of electrons at the $LaAlO_3$/$SrTiO_3$ interface. *Nature Communications*, 3(1):1129, 2012.

[77] A. D. Caviglia, S. Gariglio, N. Reyren, D. Jaccard, T. Schneider, M. Gabay, S. Thiel, G. Hammerl, J. Mannhart, and J.-M. Triscone. Electric field control of the $LaAlO_3$/$SrTiO_3$ interface ground state. *Nature*, 456(7222):624–627, 2008.

[78] N. Banerjee, M. Huijben, G. Koster, and G. Rijnders. Direct patterning of functional interfaces in oxide heterostructures. *Applied Physics Letters*, 100(4):041601, 2012.

[79] C. Cen, S. Thiel, G. Hammerl, C. W. Schneider, K. E. Andersen, C. S. Hellberg, J. Mannhart, and J. Levy. Nanoscale control of an interfacial metal-insulator transition at room temperature. *Nature Materials*, 7(4):298–302, 2008.

[80] Cheng Cen, Stefan Thiel, Jochen Mannhart, and Jeremy Levy. Oxide nanoelectronics on demand. *Science*, 323(5917):1026–1030, 2009.

[81] Dengyu Yang, Shan Hao, Jun Chen, Qing Guo, Muqing Yu, Yang Hu, Kitae Eom, Jung-Woo Lee, Chang-Beom Eom, Patrick Irvin, and Jeremy Levy. Nanoscale control of $LaAlO_3$/$SrTiO_3$ metal–insulator transition using ultra-low-voltage electron-beam lithography. *Applied Physics Letters*, 117(25):253103, 2020.

[82] Sinu Mathew, Anil Annadi, Taw Kuei Chan, Teguh Citra Asmara, Da Zhan, Xiao Renshaw Wang, Sara Azimi, Zexiang Shen, Andrivo Rusydi, Ariando, Mark B. H. Breese, and T. Venkatesan. Tuning the interface conductivity of $LaAlO_3$/$SrTiO_3$ using ion beams: Implications for patterning. *ACS Nano*, 7(12):10572–10581, December 2013.

[83] S.A. Chambers, M.H. Engelhard, V. Shutthanandan, Z. Zhu, T.C. Droubay, L. Qiao, P.V. Sushko, T. Feng, H.D. Lee, T. Gustafsson, E. Garfunkel, A.B. Shah, J.-M. Zuo, and Q.M. Ramasse. Instability, intermixing and electronic structure at the epitaxial $LaAlO_3$/$SrTiO_3$(001) heterojunction. *Surface Science Reports*, 65(10):317 – 352, 2010.

[84] Z. Q. Liu, C. J. Li, W. M. Lü, X. H. Huang, Z. Huang, S. W. Zeng, X. P. Qiu, L. S. Huang, A. Annadi, J. S. Chen, J. M. D. Coey, T. Venkatesan, and Ariando. Origin of the two-dimensional electron gas at $LaAlO_3$/$SrTiO_3$ interfaces: The role of oxygen vacancies and electronic reconstruction. *Phys. Rev. X*, 3:021010, May 2013.

[85] Z. Q. Liu, L. Sun, Z. Huang, C. J. Li, S. W. Zeng, K. Han, W. M. Lü, T. Venkatesan, and Ariando. Dominant role of oxygen vacancies in electrical properties of

unannealed LaAlO$_3$/SrTiO$_3$ interfaces. *Journal of Applied Physics*, 115(5):054303, 2014.

[86] Yunzhong Chen, Nini Pryds, Josée E. Kleibeuker, Gertjan Koster, Jirong Sun, Eugen Stamate, Baogen Shen, Guus Rijnders, and Søren Linderoth. Metallic and insulating interfaces of amorphous SrTiO$_3$-based oxide heterostructures. *Nano Lett.*, 11(9):3774–3778, September 2011.

[87] Dennis V. Christensen, Merlin von Soosten, Felix Trier, Thomas S. Jespersen, Anders Smith, Yunzhong Chen, and Nini Pryds. Controlling the carrier density of SrTiO$_3$-based heterostructures with annealing. *Advanced Electronic Materials*, 3(8):1700026, 2017.

[88] Chencheng Xu, Christoph Bäumer, Ronja Anika Heinen, Susanne Hoffmann-Eifert, Felix Gunkel, and Regina Dittmann. Disentanglement of growth dynamic and thermodynamic effects in LaAlO$_3$/SrTiO$_3$ heterostructures. *Scientific Reports*, 6(1):22410, 2016.

[89] Alexey Kalabukhov, Robert Gunnarsson, Johan Börjesson, Eva Olsson, Tord Claeson, and Dag Winkler. Effect of oxygen vacancies in the SrTiO$_3$ substrate on the electrical properties of the LaAlO$_3$/SrTiO$_3$ interface. *Physical Review B*, 75(12):121404, mar 2007.

[90] Michael Tobias Andrä. *Chemical control of the electrical surface properties of n-doped transition metal oxides.* PhD thesis, RWTH Aachen University, 2019.

[91] Wei Zhang, Yiqun Gao, Limin Kang, Meiling Yuan, Qian Yang, Hongbo Cheng, Wei Pan, and Jun Ouyang. Space-charge dominated epitaxial BaTiO$_3$ heterostructures. *Acta Materialia*, 85:207–215, 2015.

[92] F. Gunkel, S. Hoffmann-Eifert, R. A. Heinen, D. V. Christensen, Y. Z. Chen, N. Pryds, R. Waser, and R. Dittmann. Thermodynamic ground states of complex oxide heterointerfaces. *ACS Appl. Mater. Interfaces*, 9(1):1086–1092, January 2017.

[93] R. Waser and R. Hagenbeck. Grain boundaries in dielectric and mixed-conducting ceramics. *Acta Materialia*, 48(4):797–825, 2000.

[94] Roger A. De Souza. The formation of equilibrium space-charge zones at grain boundaries in the perovskite oxide SrTiO$_3$. *Phys. Chem. Chem. Phys.*, 11:9939–9969, 2009.

[95] F. Gunkel, Chris Bell, Hisashi Inoue, Bongju Kim, Adrian G. Swartz, Tyler A. Merz, Yasuyuki Hikita, Satoshi Harashima, Hiroki K. Sato, Makoto Minohara, Susanne Hoffmann-Eifert, Regina Dittmann, and Harold Y. Hwang. Defect control of conventional and anomalous electron transport at complex oxide interfaces. *Phys. Rev. X*, 6:031035, Aug 2016.

[96] D.-S. Park, A. D. Rata, I. V. Maznichenko, S. Ostanin, Y. L. Gan, S. Agrestini, G. J. Rees, M. Walker, J. Li, J. Herrero-Martin, G. Singh, Z. Luo, A. Bhatnagar,

Y. Z. Chen, V. Tileli, P. Muralt, A. Kalaboukhov, I. Mertig, K. Dörr, A. Ernst, and N. Pryds. The emergence of magnetic ordering at complex oxide interfaces tuned by defects. *Nature Communications*, 11(1):3650, 2020.

[97] M. Honig, J. A. Sulpizio, J. Drori, A. Joshua, E. Zeldov, and S. Ilani. Local electrostatic imaging of striped domain order in LaAlO$_3$/SrTiO$_3$. *Nature Materials*, 12(12):1112–1118, 2013.

[98] Beena Kalisky, Eric M. Spanton, Hilary Noad, John R. Kirtley, Katja C. Nowack, Christopher Bell, Hiroki K. Sato, Masayuki Hosoda, Yanwu Xie, Yasuyuki Hikita, Carsten Woltmann, Georg Pfanzelt, Rainer Jany, Christoph Richter, Harold Y. Hwang, Jochen Mannhart, and Kathryn A. Moler. Locally enhanced conductivity due to the tetragonal domain structure in LaAlO$_3$/SrTiO$_3$ heterointerfaces. *Nature Materials*, 12(12):1091–1095, 2013.

[99] D. V. Christensen, Y. Frenkel, Y. Z. Chen, Y. W. Xie, Z. Y. Chen, Y. Hikita, A. Smith, L. Klein, H. Y. Hwang, N. Pryds, and B. Kalisky. Strain-tunable magnetism at oxide domain walls. *Nature Physics*, 15(3):269–274, 2019.

[100] M. Foerster, R. Bachelet, V. Laukhin, J. Fontcuberta, G. Herranz, and F. Sánchez. Laterally confined two-dimensional electron gases in self-patterned LaAlO$_3$/SrTiO$_3$ interfaces. *Applied Physics Letters*, 100(23):231607, 2012.

[101] Florencio Sánchez, Carmen Ocal, and Josep Fontcuberta. Tailored surfaces of perovskite oxide substrates for conducted growth of thin films. *Chem. Soc. Rev.*, 43:2272–2285, 2014.

[102] Gertjan Koster, Guus Rijnders, Dave H.A. Blank, and Horst Rogalla. Surface morphology determined by (001) single-crystal SrTiO$_3$ termination. *Physica C: Superconductivity*, 339(4):215 – 230, 2000.

[103] Martin Lewin, Christoph Baeumer, Felix Gunkel, Alexander Schwedt, Fabian Gaussmann, Jochen Wueppen, Paul Meuffels, Bernd Jungbluth, Joachim Mayer, Regina Dittmann, Rainer Waser, and Thomas Taubner. Nanospectroscopy of infrared phonon resonance enables local quantification of electronic properties in doped SrTiO$_3$ ceramics. *Advanced Functional Materials*, 28(42):1802834, 2018.

[104] Weiwei Luo, Margherita Boselli, Jean-Marie Poumirol, Ivan Ardizzone, Jérémie Teyssier, Dirk van der Marel, Stefano Gariglio, Jean-Marc Triscone, and Alexey B. Kuzmenko. High sensitivity variable-temperature infrared nanoscopy of conducting oxide interfaces. *Nature Communications*, 10(1):2774, 2019.

[105] L. Cheng, D. Wang, S. Dai, Y. Yan, X. Fan, L. Wei, and C. Zeng. Near-field imaging of the LaAlO$_3$/SrTiO$_3$ interfacial conductivity. *J. Infrared Millim. Waves*, 36(5), October 2017.

[106] Julian Barnett, Marc-André Rose, Georg Ulrich, Martin Lewin, Bernd Kästner, Arne Hoehl, Regina Dittmann, Felix Gunkel, and Thomas Taubner. Phonon-enhanced near-field spectroscopy to extract the local electronic properties of

buried 2d electron systems in oxide heterostructures. *Advanced Functional Materials*, 30(46):2004767, 2020.

[107] F. V. E. Hensling, D. J. Keeble, J. Zhu, S. Brose, C. Xu, F. Gunkel, S. Danylyuk, S. S. Nonnenmann, W. Egger, and R. Dittmann. Uv radiation enhanced oxygen vacancy formation caused by the pld plasma plume. *Scientific Reports*, 8(1):8846, 2018.

[108] Feng Bi, Mengchen Huang, Hyungwoo Lee, Chang-Beom Eom, Patrick Irvin, and Jeremy Levy. LaAlO$_3$ thickness window for electronically controlled magnetism at LaAlO$_3$/SrTiO$_3$ heterointerfaces. *Applied Physics Letters*, 107(8):082402, 2015.

[109] Yanwu Xie, Christopher Bell, Takeaki Yajima, Yasuyuki Hikita, and Harold Y. Hwang. Charge writing at the LaAlO$_3$/SrTiO$_3$ surface. *Nano Lett.*, 10(7):2588–2591, July 2010.

[110] M. Boselli, D. Li, W. Liu, A. Fête, S. Gariglio, and J.-M. Triscone. Characterization of atomic force microscopy written conducting nanowires at LaAlO$_3$/SrTiO$_3$ interfaces. *Applied Physics Letters*, 108(6):061604, 2016.

[111] Patrick Irvin, Joshua P. Veazey, Guanglei Cheng, Shicheng Lu, Chung-Wung Bark, Sangwoo Ryu, Chang-Beom Eom, and Jeremy Levy. Anomalous high mobility in LaAlO$_3$/SrTiO$_3$ nanowires. *Nano Lett.*, 13(2):364–368, February 2013.

[112] Megan Briggeman, Michelle Tomczyk, Binbin Tian, Hyungwoo Lee, Jung-Woo Lee, Yuchi He, Anthony Tylan-Tyler, Mengchen Huang, Chang-Beom Eom, David Pekker, Roger S. K. Mong, Patrick Irvin, and Jeremy Levy. Pascal conductance series in ballistic one-dimensional LaAlO$_3$/SrTiO$_3$ channels. *Science*, 367(6479):769–772, 2020.

[113] Hanghui Chen and Andrew Millis. Charge transfer driven emergent phenomena in oxide heterostructures. *Journal of Physics: Condensed Matter*, 29(24):243001, may 2017.

[114] Fangdi Wen, Yanwei Cao, Xiaoran Liu, B. Pal, S. Middey, M. Kareev, and J. Chakhalian. Evolution of ferromagnetism in two-dimensional electron gas of LaTiO$_3$/SrTiO$_3$. *Applied Physics Letters*, 112(12):122405, 2018.

[115] Roger A. De Souza, Veronika Metlenko, Daesung Park, and Thomas E. Weirich. Behavior of oxygen vacancies in single-crystal SrTiO$_3$: Equilibrium distribution and diffusion kinetics. *Phys. Rev. B*, 85:174109, May 2012.

[116] F.A. Kröger and H.J. Vink. Relations between the concentrations of imperfections in crystalline solids. In Frederick Seitz and David Turnbull, editors, *Relations between the Concentrations of Imperfections in Crystalline Solids*, volume 3 of *Solid State Physics*, pages 307 – 435. Academic Press, 1956.

[117] M. Javed Akhtar, Zeb-Un-Nisa Akhtar, Robert A. Jackson, and C. Richard A. Catlow. Computer simulation studies of strontium titanate. *Journal of the American Ceramic Society*, 78(2):421–428, 1995.

[118] K. Szot, W. Speier, U. Breuer, R. Meyer, J. Szade, and R. Waser. Formation of micro-crystals on the (100) surface of SrTiO$_3$ at elevated temperatures. *Surface Science*, 460(1):112 – 128, 2000.

[119] Rotraut Merkle and Joachim Maier. How is oxygen incorporated into oxides? a comprehensive kinetic study of a simple solid-state reaction with SrTiO$_3$ as a model material. *Angewandte Chemie International Edition*, 47(21):3874–3894, 2008.

[120] Zhufeng Hou and Kiyoyuki Terakura. Defect states induced by oxygen vacancies in cubic SrTiO$_3$: First-principles calculations. *Journal of the Physical Society of Japan*, 79(11):114704, 2010.

[121] Felix Gunkel. *The role of defects at functional interfaces between polar and non-polar perovskite oxides.* PhD thesis, RWTH Aachen University, 2013.

[122] René Meyer, Rainer Waser, Julia Helmbold, and Günter Borchardt. Observation of vacancy defect migration in the cation sublattice of complex oxides by $^{18}$O tracer experiments. *Phys. Rev. Lett.*, 90:105901, Mar 2003.

[123] R. A. De Souza, F. Gunkel, S. Hoffmann-Eifert, and R. Dittmann. Finite-size versus interface-proximity effects in thin-film epitaxial SrTiO$_3$. *Phys. Rev. B*, 89:241401, Jun 2014.

[124] Karsten Gömann, Günter Borchardt, Michał Schulz, Anissa Gömann, Wolfgang Maus-Friedrichs, Bernard Lesage, Odile Kaïtasov, Susanne Hoffmann-Eifert, and Theodor Schneller. Sr diffusion in undoped and La-doped SrTiO$_3$ single crystals under oxidizing conditions. *Phys. Chem. Chem. Phys.*, 7:2053–2060, 2005.

[125] H.U. Anderson, M.M. Nasrallah, B.K. Flandermeyer, and A.K. Agarwal. High-temperature redox behavior of doped SrTiO$_3$ and LaCrO$_3$. *Journal of Solid State Chemistry*, 56(3):325–334, 1985.

[126] René Meyer, Alexander F. Zurhelle, Roger A. De Souza, Rainer Waser, and Felix Gunkel. Dynamics of the metal-insulator transition of donor-doped SrTiO$_3$. *Phys. Rev. B*, 94:115408, Sep 2016.

[127] Michael Andrä, Carsten Funck, Nicolas Raab, Marc-André Rose, Mykhailo Vorokhta, Filip Dvořák, Břetislav Šmíd, Vladimír Matolín, David N. Mueller, Regina Dittmann, Rainer Waser, Stephan Menzel, and Felix Gunkel. Effect of cationic interface defects on band alignment and contact resistance in metal/oxide heterojunctions. *Advanced Electronic Materials*, 6(1):1900808, 2020.

[128] F. Baiutti, G. Logvenov, G. Gregori, G. Cristiani, Y. Wang, W. Sigle, P. A. van Aken, and J. Maier. High-temperature superconductivity in space-charge regions of lanthanum cuprate induced by two-dimensional doping. *Nature Communications*, 6(1):8586, 2015.

[129] Yanwu Xie, Yasuyuki Hikita, Christopher Bell, and Harold Y. Hwang. Control of electronic conduction at an oxide heterointerface using surface polar adsorbates. *Nature Communications*, 2(1):494, 2011.

[130] R. Dittmann. 9 - stoichiometry in epitaxial oxide thin films. In G. Koster, M. Huijben, and G. Rijnders, editors, *Epitaxial Growth of Complex Metal Oxides*, Woodhead Publishing Series in Electronic and Optical Materials, pages 231–261. Woodhead Publishing, 2015.

[131] J. Schou. Physical aspects of the pulsed laser deposition technique: The stoichiometric transfer of material from target to film. *Applied Surface Science*, 255(10):5191–5198, 2009. Laser and Plasma in Micro- and Nano-Scale Materials Processing and Diagnostics.

[132] Rik Groenen, Jasper Smit, Kasper Orsel, Arturas Vailionis, Bert Bastiaens, Mark Huijben, Klaus Boller, Guus Rijnders, and Gertjan Koster. Research update: Stoichiometry controlled oxide thin film growth by pulsed laser deposition. *APL Materials*, 3(7):070701, 2015.

[133] H M Christen and G Eres. Recent advances in pulsed-laser deposition of complex oxides. *Journal of Physics: Condensed Matter*, 20(26):264005, jun 2008.

[134] Dave H.A Blank, Gertjan Koster, Guus A.J.H.M Rijnders, Eelco van Setten, Per Slycke, and Horst Rogalla. Epitaxial growth of oxides with pulsed laser interval deposition. *Journal of Crystal Growth*, 211(1):98–105, 2000.

[135] C Xu, S Wicklein, A Sambri, S Amoruso, M Moors, and R Dittmann. Impact of the interplay between nonstoichiometry and kinetic energy of the plume species on the growth mode of $SrTiO_3$ thin films. *Journal of Physics D: Applied Physics*, 47(3):034009, dec 2013.

[136] G. Z. Liu, Q. Y. Lei, and X. X. Xi. Stoichiometry of $SrTiO_3$ films grown by pulsed laser deposition. *Applied Physics Letters*, 100(20):202902, 2012.

[137] Kasper Orsel, Rik Groenen, Bert Bastiaens, Gertjan Koster, Guus Rijnders, and Klaus-J. Boller. Influence of the oxidation state of $SrTiO_3$ plasmas for stoichiometric growth of pulsed laser deposition films identified by laser induced fluorescence. *APL Materials*, 3(10):106103, 2015.

[138] F. Gunkel, K. Skaja, A. Shkabko, R. Dittmann, S. Hoffmann-Eifert, and R. Waser. Stoichiometry dependence and thermal stability of conducting $NdGaO_3$/$SrTiO_3$ heterointerfaces. *Applied Physics Letters*, 102(7):071601, 2013.

[139] J.H Song and Y.H Jeong. $SrTiO_3$ homoepitaxy by the pulsed laser deposition method: island, layer-by-layer, and step-flow growth. *Solid State Communications*, 125(10):563–566, 2003.

[140] Ayahiko Ichimiya and Philip I. Cohen. *Reflection High-Energy Electron Diffraction*. Cambridge University Press, 2004.

[141] G. Koster, M. Huijben, A. Janssen, and G. Rijnders. 1 - growth studies of heteroepitaxial oxide thin films using reflection high-energy electron diffraction (rheed). In G. Koster, M. Huijben, and G. Rijnders, editors, *Epitaxial Growth of Complex Metal Oxides*, Woodhead Publishing Series in Electronic and Optical Materials, pages 3 – 29. Woodhead Publishing, 2015.

[142] Gertjan Koster, Guus J. H. M. Rijnders, Dave H. A. Blank, and Horst Rogalla. In situ initial growth studies of srtio3 on srtio3 by time resolved high pressure rheed. *MRS Online Proceedings Library*, 526(1):33–37, 1998.

[143] Gertjan Koster, Guus J. H. M. Rijnders, Dave H. A. Blank, and Horst Rogalla. Imposed layer-by-layer growth by pulsed laser interval deposition. *Applied Physics Letters*, 74(24):3729–3731, 1999.

[144] Gertjan Koster, Boike L. Kropman, Guus J.H.M. Rijnders, Dave H.A. Blank, and Horst Rogalla. Influence of the surface treatment on the homoepitaxial growth of SrTiO₃. *Materials Science and Engineering: B*, 56(2):209–212, 1998.

[145] J. Li, W. Peng, Ke Chen, Y. Zhang, L.M. Cui, Y.F. Chen, Y.R. Jin, Y.Z. Zhang, and D.N. Zheng. High pressure rheed study on the initial structure and growth dynamics of YBa₂Cu₃O₇₋δ thin films on SrTiO₃ (001). *Solid State Communications*, 152(6):478–482, 2012.

[146] Bert Voigtländer. *Atomic Force Microscopy*. Springer, Berlin, June 2019.

[147] E. Hall. On a new action of a magnet on electric currents. *American Jounal of Mathematics*, 2:287–292, 1879.

[148] L. J. van der Pauw. A method of measuring specific resistivity and hall effect of discs of arbitrary shape. *Philips Research Reports*, 13(1), 1958.

[149] Veerendra K. Guduru, A. McCollam, J. C. Maan, U. Zeitler, S. Wenderich, M. K. Kruize, A. Brinkman, M. Huijben, G. Koster, D. H. A. Blank, G. Rijnders, and H. Hilgenkamp. Multi-band conduction behaviour at the interface of LaAlO₃/SrTiO₃ heterostructures. *Journal of the Korean Physical Society*, 63(3):437–440, 2013.

[150] Neil Ashcroft. *Solid state physics*. Holt, Rinehart and Winston, New York, 1976.

[151] Feng Bi, Mengchen Huang, Sangwoo Ryu, Hyungwoo Lee, Chung-Wung Bark, Chang-Beom Eom, Patrick Irvin, and Jeremy Levy. Room-temperature electronically-controlled ferromagnetism at the LaAlO₃/SrTiO₃ interface. *Nature Communications*, 5(1):5019, 2014.

[152] Beena Kalisky, Julie A. Bert, Christopher Bell, Yanwu Xie, Hiroki K. Sato, Masayuki Hosoda, Yasuyuki Hikita, Harold Y. Hwang, and Kathryn A. Moler. Scanning probe manipulation of magnetism at the LaAlO₃/SrTiO₃ heterointerface. *Nano Lett.*, 12(8):4055–4059, August 2012.

[153] J.-S. Lee, Y. W. Xie, H. K. Sato, C. Bell, Y. Hikita, H. Y. Hwang, and C.-C. Kao. Titanium $d_{xy}$ ferromagnetism at the LaAlO₃/SrTiO₃ interface. *Nature Materials*, 12(8):703–706, 2013.

[154] Katharina Johanna Skaja. *Redox processes and ionictransport in resistive switchingbinary metal oxides*. phdthesis, RWTH Aachen, 2016.

[155] P. van der Heide. *X-ray Photoelectron Spectroscopy: An introduction to Principles and Practices*. Wiley, 2011.

[156] T. Le Mercier, J.-M. Mariot, P. Parent, M.-F. Fontaine, C.F. Hague, and M. Quarton. Formation of ti3+ ions at the surface of laser-irradiated rutile. *Applied Surface Science*, 86(1):382 − 386, 1995.

[157] D. Frank Ogletree, Hendrik Bluhm, Gennadi Lebedev, Charles S. Fadley, Zahid Hussain, and Miquel Salmeron. A differentially pumped electrostatic lens system for photoemission studies in the millibar range. *Review of Scientific Instruments*, 73(11):3872−3877, 2002.

[158] Michael E. Grass, Patrik G. Karlsson, Funda Aksoy, Måns Lundqvist, Björn Wannberg, Bongjin S. Mun, Zahid Hussain, and Zhi Liu. New ambient pressure photoemission endstation at advanced light source beamline 9.3.2. *Review of Scientific Instruments*, 81(5):053106, 2010.

[159] Felix V. E. Hensling. *Defect engineering in oxide thin films*. PhD thesis, RWTH Aachen University, 2019.

[160] Kiichi Nakashima. A novel analysis method for peak broadening due to thin structures in double crystal x-ray diffraction measurements. *Japanese Journal of Applied Physics*, 40(Part 1, No. 9A):5454−5463, sep 2001.

[161] Mario Birkholz. *Thin film analysis by X-ray scattering*. Wiley-VCH, Weinheim, 2006.

[162] Masashi Kawasaki, Kazuhiro Takahashi, Tatsuro Maeda, Ryuta Tsuchiya, Makoto Shinohara, Osamu Ishiyama, Takuzo Yonezawa, Mamoru Yoshimoto, and Hideomi Koinuma. Atomic control of the $SrTiO_3$ crystal surface. *Science*, 266(5190):1540−1542, 1994.

[163] T. Ohnishi, K. Shibuya, M. Lippmaa, D. Kobayashi, H. Kumigashira, M. Oshima, and H. Koinuma. Preparation of thermally stable $TiO_2$-terminated $SrTiO_3(100)$ substrate surfaces. *Applied Physics Letters*, 85(2):272−274, 2004.

[164] C. Cancellieri, N. Reyren, S. Gariglio, A. D. Caviglia, A. Fête, and J.-M. Triscone. Influence of the growth conditions on the $LaAlO_3/SrTiO_3$ interface electronic properties. *EPL (Europhysics Letters)*, 91(1):17004, jul 2010.

[165] Katrin Pingen. Pulsed laser deposition and characterisation of epitaxial hfo2 thin films, 2020.

[166] Abhijit Biswas, Chan-Ho Yang, Ramamoorthy Ramesh, and Yoon H. Jeong. Atomically flat single terminated oxide substrate surfaces. *Progress in Surface Science*, 92(2):117 − 141, 2017.

[167] J.-L. Maurice, C. Carrétéro, M.-J. Casanove, K. Bouzehouane, S. Guyard, É. Larquet, and J.-P. Contour. Electronic conductivity and structural distortion at the interface between insulators $SrTiO_3$ and $LaAlO_3$. *physica status solidi (a)*, 203(9):2209−2214, 2006.

[168] P. Bouvier and J. Kreisel. Pressure-induced phase transition in LaAlO$_3$. *Journal of Physics: Condensed Matter*, 14(15):3981–3991, apr 2002.

[169] M. Golalikhani, Q.Y. Lei, M.A. Wolak, B.A. Davidson, and X.X. Xi. Narrow growth window for stoichiometric, layer-by-layer growth of LaAlO$_3$ thin films using pulsed laser deposition. *Journal of Crystal Growth*, 443:50–53, 2016.

[170] J. F. Nye. *Physical Properties of Crystals*. (page 143). Oxford University Press, May 1985.

[171] Beena Kalisky, Julie A. Bert, Brannon B. Klopfer, Christopher Bell, Hiroki K. Sato, Masayuki Hosoda, Yasuyuki Hikita, Harold Y. Hwang, and Kathryn A. Moler. Critical thickness for ferromagnetism in LaAlO$_3$/SrTiO$_3$ heterostructures. *Nature Communications*, 3(1):922, 2012.

[172] M.-A. Rose, J. Barnett, D. Wendland, F. V. E. Hensling, J. M. Boergers, M. Moors, R. Dittmann, T. Taubner, and F. Gunkel. Local inhomogeneities resolved by scanning probe techniques and their impact on local 2deg formation in oxide heterostructures. *Nanoscale Adv.*, 3:4145–4155, 2021.

[173] R. Pentcheva, M. Huijben, K. Otte, W. E. Pickett, J. E. Kleibeuker, J. Huijben, H. Boschker, D. Kockmann, W. Siemons, G. Koster, H. J. W. Zandvliet, G. Rijnders, D. H. A. Blank, H. Hilgenkamp, and A. Brinkman. Parallel electron-hole bilayer conductivity from electronic interface reconstruction. *Phys. Rev. Lett.*, 104:166804, Apr 2010.

[174] R. Bachelet, F. Sánchez, F. J. Palomares, C. Ocal, and J. Fontcuberta. Atomically flat SrO-terminated SrTiO$_3$(001) substrate. *Applied Physics Letters*, 95(14):141915, 2009.

[175] Gyu Bong Cho, Yasuhiro Kamada, and Masahiko Yamamoto. Studies of self-organized steps and terraces in inclined SrTiO$_3$(001) substrate by atomic force microscopy. *Japanese Journal of Applied Physics*, 40(Part 1, No. 7):4666–4671, jul 2001.

[176] Gyu Bong Cho, Masahiko Yamamoto, and Yasushi Endo. Investigation of self-organized steps and terraces in SrTiO$_3$(001) substrate inclined in [110] direction by scanning tunneling microscopy. *Japanese Journal of Applied Physics*, 43(4A):1555–1560, apr 2004.

[177] R. Bachelet, F. Sánchez, J. Santiso, C. Munuera, C. Ocal, and J. Fontcuberta. Self-assembly of SrTiO$_3$(001) chemical-terminations: A route for oxide-nanostructure fabrication by selective growth. *Chem. Mater.*, 21(12):2494–2498, June 2009.

[178] Martin R Castell. Nanostructures on the SrTiO$_3$(001) surface studied by stm. *Surface Science*, 516(1):33–42, 2002.

[179] Florian Gellé, Roxana Chirita, Damien Mertz, Mircea V. Rastei, Aziz Dinia, and Silviu Colis. Guideline to atomically flat TiO$_2$-terminated SrTiO$_3$(001) surfaces. *Surface Science*, 677:39–45, 2018.

[180] Geoffrey K.H Pang, K.Z Baba-Kishi, and A Patel. Topographic and phase-contrast imaging in atomic force microscopy. *Ultramicroscopy*, 81(2):35–40, 2000.

[181] Sanjay Adhikari, Andrés C. Garcia-Castro, Aldo H. Romero, Hyungwoo Lee, Jung-Woo Lee, Sangwoo Ryu, Chang-Beom Eom, and Cheng Cen. Charge transfer to $LaAlO_3$/$SrTiO_3$ interfaces controlled by surface water adsorption and proton hopping. *Advanced Functional Materials*, 26(30):5453–5459, 2016.

[182] Feng Bi, Daniela F. Bogorin, Cheng Cen, Chung Wung Bark, Jae-Wan Park, Chang-Beom Eom, and Jeremy Levy. "water-cycle" mechanism for writing and erasing nanostructures at the $LaAlO_3$/$SrTiO_3$ interface. *Applied Physics Letters*, 97(17):173110, 2010.

[183] Aleksandar Staykov, Shun Fukumori, Kazunari Yoshizawa, Kenta Sato, Tatsumi Ishihara, and John Kilner. Interaction of SrO-terminated $SrTiO_3$ surface with oxygen, carbon dioxide, and water. *J. Mater. Chem. A*, 6:22662–22672, 2018.

[184] Michael Andrä, Felix Gunkel, Christoph Bäumer, Chencheng Xu, Regina Dittmann, and Rainer Waser. The influence of the local oxygen vacancy concentration on the piezoresponse of strontium titanate thin films. *Nanoscale*, 7:14351–14357, 2015.

[185] Amit Kumar, Thomas M. Arruda, Yunseok Kim, Ilia N. Ivanov, Stephen Jesse, Chung W. Bark, Nicholas C. Bristowe, Emilio Artacho, Peter B. Littlewood, Chang-Beom Eom, and Sergei V. Kalinin. Probing surface and bulk electrochemical processes on the $LaAlO_3$-$SrTiO_3$ interface. *ACS Nano*, 6(5):3841–3852, May 2012.

[186] T. Menke, R. Dittmann, P. Meuffels, K. Szot, and R. Waser. Impact of the electroforming process on the device stability of epitaxial fe-doped $SrTiO_3$ resistive switching cells. *Journal of Applied Physics*, 106(11):114507, 2009.

[187] C. Baeumer, N. Raab, T. Menke, C. Schmitz, R. Rosezin, P. Müller, M. Andrä, V. Feyer, R. Bruchhaus, F. Gunkel, C. M. Schneider, R. Waser, and R. Dittmann. Verification of redox-processes as switching and retention failure mechanisms in $Nb$:$SrTiO_3$/metal devices. *Nanoscale*, 8:13967–13975, 2016.

[188] Werner Frammelsberger, Guenther Benstetter, Richard Stamp, Janice Kiely, and Thomas Schweinboeck. Simplified tunnelling current calculation for mos structures with ultra-thin oxides for conductive atomic force microscopy investigations. *Materials Science and Engineering: B*, 116(2):168–174, 2005.

[189] Chun-Hsing Shih and Fu-Chien Chiu. A review on conduction mechanisms in dielectric films. *Advances in Materials Science and Engineering*, 2014:578168, 2014.

[190] G. Wang, T.-W. Kim, T. Lee, W. Wang, and M.A. Reed. 4.16 - electronic properties of alkanethiol molecular junctions: Conduction mechanisms, metal-molecule contacts, and inelastic transport. In David L. Andrews, Gregory D. Scholes, and

Gary P. Wiederrecht, editors, *Comprehensive Nanoscience and Technology*, pages 463–487. Academic Press, Amsterdam, 2011.

[191] Chang-Hoon Choi, Kwang-Hoon Oh, Jung-Suk Goo, Zhiping Yu, and R.W. Dutton. Direct tunneling current model for circuit simulation. In *International Electron Devices Meeting 1999. Technical Digest (Cat. No.99CH36318)*, pages 735–738, Dec 1999.

[192] Guneeta Singh-Bhalla, Christopher Bell, Jayakanth Ravichandran, Wolter Siemons, Yasuyuki Hikita, Sayeef Salahuddin, Arthur F. Hebard, Harold Y. Hwang, and Ramamoorthy Ramesh. Built-in and induced polarization across $LaAlO_3/SrTiO_3$ heterojunctions. *Nature Physics*, 7(1):80–86, 2011.

[193] Adrian G. Swartz, Satoshi Harashima, Yanwu Xie, Di Lu, Bongju Kim, Christopher Bell, Yasuyuki Hikita, and Harold Y. Hwang. Spin-dependent transport across $Co/LaAlO_3/SrTiO_3$ heterojunctions. *Applied Physics Letters*, 105(3):032406, 2014.

[194] T. Taubner, R. Hillenbrand, and F. Keilmann. Performance of visible and mid-infrared scattering-type near-field optical microscopes. *Journal of Microscopy*, 210(3):311–314, 2003.

[195] Fritz Keilmann and Rainer Hillenbrand. Near-field microscopy by elastic light scattering from a tip. *Philosophical Transactions of the Royal Society of London. Series A: Mathematical, Physical and Engineering Sciences*, 362(1817):787–805, 2004.

[196] A. Huber, N. Ocelic, T. Taubner, and R. Hillenbrand. Nanoscale resolved infrared probing of crystal structure and of plasmon-phonon coupling. *Nano Lett.*, 6(4):774–778, 2006.

[197] B. Knoll and F. Keilmann. Near-field probing of vibrational absorption for chemical microscopy. *Nature*, 399(6732):134–137, 1999.

[198] T. Taubner, F. Keilmann, and R. Hillenbrand. Nanoscale-resolved subsurface imaging by scattering-type near-field optical microscopy. *Opt. Express*, 13(22):8893–8899, October 2005.

[199] Rainer Jacob, Stephan Winnerl, Harald Schneider, Manfred Helm, Marc Tobias Wenzel, Hans-Georg von Ribbeck, Lukas M. Eng, and Susanne C. Kehr. Quantitative determination of the charge carrier concentration of ion implanted silicon by ir-near-field spectroscopy. *Opt. Express*, 18(25):26206–26213, Dec 2010.

[200] Kiwon Moon, Hongkyu Park, Jeonghoi Kim, Youngwoong Do, Soonsung Lee, Gyuseok Lee, Hyeona Kang, and Haewook Han. Subsurface nanoimaging by broadband terahertz pulse near-field microscopy. *Nano Lett.*, 15(1):549–552, January 2015.

[201] Lars Mester, Alexander A. Govyadinov, Shu Chen, Monika Goikoetxea, and Rainer Hillenbrand. Subsurface chemical nanoidentification by nano-ftir spectroscopy. *Nature Communications*, 11(1):3359, 2020.

[202] Jonathan Ruhman, Arjun Joshua, Shahal Ilani, and Ehud Altman. Competition between kondo screening and magnetism at the $LaAlO_3/SrTiO_3$ interface. *Phys. Rev. B*, 90:125123, Sep 2014.

[203] M.W. den Otter, L.M. van der Haar, and H.J.M. Bouwmeester. Numerical evaluation of eigenvalues of the sheet diffusion problem in the surface/diffusion mixed regime. *Solid State Ionics*, 134(3):259–264, 2000.

[204] Han-Ill Yoo and Chung-Eun Lee. Two-fold diffusion kinetics of oxygen re-equilibration in donor-doped $BaTiO_3$. *Journal of the American Ceramic Society*, 88(3):617–623, 2005.

[205] Kian Kerman, Changhyun Ko, and Shriram Ramanathan. Orientation dependent oxygen exchange kinetics on single crystal $SrTiO_3$ surfaces. *Phys. Chem. Chem. Phys.*, 14:11953–11960, 2012.

[206] Rotraut Merkle and Joachim Maier. Oxygen incorporation into Fe-doped $SrTiO_3$: Mechanistic interpretation of the surface reaction. *Phys. Chem. Chem. Phys.*, 4:4140–4148, 2002.

[207] G.M. Choi and H. l. Tuller. Defect structure and electrical properties of single-crystal $Ba_{0.03}Sr_{0.97}TiO_3$. *Journal of the American Ceramic Society*, 71(4):201–205, 1988.

[208] Maximilian Fleischer, Hans Meixner, and Christian Tragut. Hole mobility in acceptor-doped, monocrystalline $SrTiO_3$. *Journal of the American Ceramic Society*, 75(6):1666–1668, 1992.

[209] L. Iglesias, Alexandros Sarantopoulos, C. Magén, and F. Rivadulla. Oxygen vacancies in strained $SrTiO_3$ thin films: Formation enthalpy and manipulation. *Phys. Rev. B*, 95:165138, Apr 2017.

[210] M. Leonhardt, R. A. De Souza, J. Claus, and J. Maier. Surface kinetics of oxygen incorporation into $SrTiO_3$. *Journal of The Electrochemical Society*, 149(2):J19, 2002.

[211] R. Merkle, R. A. De Souza, and J. Maier. Optically tuning the rate of stoichiometry changes: Surface-controlled oxygen incorporation into oxides under UV irradiation. *Angew. Chem. Int. Ed.*, 40:2126–2129, 2001.

[212] Marc-André Rose, Břetislav Šmíd, Mykhailo Vorokhta, Ivetta Slipukhina, Michael Andrä, Hendrik Bluhm, Tomáš Duchoň, Marijana Ležaić, Scott A. Chambers, Regina Dittmann, David N. Mueller, and Felix Gunkel. Identifying ionic and electronic charge transfer at oxide heterointerfaces. *Advanced Materials*, 3/a33(n/a):2004132, dec 2021.

[213] Tahereh G. Avval, Shiladitya Chatterjee, Grant T. Hodges, Stephan Bahr, Paul Dietrich, Michael Meyer, Andreas Thißen, and Matthew R. Linford. Oxygen gas, o2(g), by near-ambient pressure xps. *Surface Science Spectra*, 26(1):014021, 2019.

[214] J.-M. Pan, B. L. Maschhoff, U. Diebold, and T. E. Madey. Interaction of water, oxygen, and hydrogen with tio2(110) surfaces having different defect densities. *Journal of Vacuum Science & Technology A*, 10(4):2470–2476, 1992.

[215] R. Pentcheva and W. E. Pickett. Charge localization or itineracy at $LaAlO_3$/$SrTiO_3$ interfaces: Hole polarons, oxygen vacancies, and mobile electrons. *Phys. Rev. B*, 74:035112, Jul 2006.

[216] M. Salluzzo, J. C. Cezar, N. B. Brookes, V. Bisogni, G. M. De Luca, C. Richter, S. Thiel, J. Mannhart, M. Huijben, A. Brinkman, G. Rijnders, and G. Ghiringhelli. Orbital reconstruction and the two-dimensional electron gas at the $LaAlO_3$/$SrTiO_3$ interface. *Phys. Rev. Lett.*, 102:166804, Apr 2009.

[217] Amardeep Bharti and Navdeep Goyal. Fundamental of synchrotron radiations. In Daisy Joseph, editor, *Synchrotron Radiation*, chapter 2. IntechOpen, Rijeka, 2019.

[218] Uwe Treske, Nadine Heming, Martin Knupfer, Bernd Büchner, Andreas Koitzsch, Emiliano Di Gennaro, Umberto Scotti di Uccio, Fabio Miletto Granozio, and Stefan Krause. Observation of strontium segregation in $LaAlO_3$/$SrTiO_3$ and $NdGaO_3$/$SrTiO_3$ oxide heterostructures by x-ray photoemission spectroscopy. *APL Materials*, 2(1):012108, 2014.

[219] S. Tanuma, C. J. Powell, and D. R. Penn. Calculations of electron inelastic mean free paths. v. data for 14 organic compounds over the 50–2000 ev range. *Surface and Interface Analysis*, 21(3):165–176, 1994.

[220] P.A.W van der Heide, Q.D Jiang, Y.S Kim, and J.W Rabalais. X-ray photoelectron spectroscopic and ion scattering study of the $SrTiO_3$(001) surface. *Surface Science*, 473(1):59 – 70, 2001.

[221] Bo-Chao Huang, Ya-Ping Chiu, Po-Cheng Huang, Wen-Ching Wang, Vu Thanh Tra, Jan-Chi Yang, Qing He, Jiunn-Yuan Lin, Chia-Seng Chang, and Ying-Hao Chu. Mapping band alignment across complex oxide heterointerfaces. *Phys. Rev. Lett.*, 109:246807, Dec 2012.

[222] Yun Li, Sutassana Na Phattalung, Sukit Limpijumnong, Jiyeon Kim, and Jaejun Yu. Formation of oxygen vacancies and charge carriers induced in the *n*-type interface of a $LaAlO_3$ overlayer on $SrTiO_3$(001). *Phys. Rev. B*, 84:245307, Dec 2011.

[223] Christian Lenser, Annemarie Koehl, Ivetta Slipukhina, Hongchu Du, Marten Patt, Vitaliy Feyer, Claus M. Schneider, Marjana Lezaic, Rainer Waser, and Regina Dittmann. Formation and movement of cationic defects during forming and resistive switching in $SrTiO_3$ thin film devices. *Advanced Functional Materials*, 25(40):6360–6368, 2015.

[224] Erik Slooten. *When X-rays and oxide heterointerfaces collide*. PhD thesis, University of Amsterdam, 2013.

[225] L. Wang, Y. Du, L. Chang, K. A. Stoerzinger, M. E. Bowden, J. Wang, and S. A. Chambers. Band alignment and electrocatalytic activity at the p-n $La_{0.88}Sr_{0.12}FeO_3/SrTiO_3(001)$ heterojunction. *Applied Physics Letters*, 112(26):261601, 2018.

[226] G. Berner, A. Müller, F. Pfaff, J. Walde, C. Richter, J. Mannhart, S. Thiess, A. Gloskovskii, W. Drube, M. Sing, and R. Claessen. Band alignment in $LaAlO_3/SrTiO_3$ oxide heterostructures inferred from hard x-ray photoelectron spectroscopy. *Phys. Rev. B*, 88:115111, Sep 2013.

[227] E. Slooten, Zhicheng Zhong, H. J. A. Molegraaf, P. D. Eerkes, S. de Jong, F. Massee, E. van Heumen, M. K. Kruize, S. Wenderich, J. E. Kleibeuker, M. Gorgoi, H. Hilgenkamp, A. Brinkman, M. Huijben, G. Rijnders, D. H. A. Blank, G. Koster, P. J. Kelly, and M. S. Golden. Hard x-ray photoemission and density functional theory study of the internal electric field in $SrTiO_3/LaAlO_3$ oxide heterostructures. *Phys. Rev. B*, 87:085128, Feb 2013.

[228] G. Drera, G. Salvinelli, A. Brinkman, M. Huijben, G. Koster, H. Hilgenkamp, G. Rijnders, D. Visentin, and L. Sangaletti. Band offsets and density of $Ti^{3+}$ states probed by x-ray photoemission on $LaAlO_3/SrTiO_3$ heterointerfaces and their $LaAlO_3$ and $SrTiO_3$ bulk precursors. *Phys. Rev. B*, 87:075435, Feb 2013.

[229] Giorgio Margaritondo, editor. *Electronic Structure of Semiconductor Heterojunctions*. Springer Netherlands, November 1988.

[230] Hai-Long Hu, Lei Ao, Anh Pham, Danyang Wang, Yu Wang, Zhigang Chen, Charlie Kong, Thiam Teck Tan, Xiaotao Zu, and Sean Li. Oxygen vacancy dependence of magnetic behavior in the $LaAlO_3/SrTiO_3$ heterostructures. *Advanced Materials Interfaces*, 3(20):1600547, 2016.

[231] Karen Michaeli, Andrew C. Potter, and Patrick A. Lee. Superconducting and ferromagnetic phases in $SrTiO_3/LaAlO_3$ oxide interface structures: Possibility of finite momentum pairing. *Phys. Rev. Lett.*, 108:117003, Mar 2012.

[232] N. Pavlenko, T. Kopp, E. Y. Tsymbal, G. A. Sawatzky, and J. Mannhart. Magnetic and superconducting phases at the $LaAlO_3/SrTiO_3$ interface: The role of interfacial Ti 3$d$ electrons. *Phys. Rev. B*, 85:020407, Jan 2012.

[233] Frank Lechermann, Lewin Boehnke, Daniel Grieger, and Christoph Piefke. Electron correlation and magnetism at the $LaAlO_3/SrTiO_3$ interface: A dft+dmft investigation. *Phys. Rev. B*, 90:085125, Aug 2014.

[234] N Mohanta and A Taraphder. Oxygen vacancy clustering and pseudogap behaviour at the LaAlO3/SrTiO3interface. *Journal of Physics: Condensed Matter*, 26(21):215703, may 2014.

[235] Ming Yang, Ariando, Jun Zhou, Teguh Citra Asmara, Peter Krüger, Xiao Jiang Yu, Xiao Wang, Cecilia Sanchez-Hanke, Yuan Ping Feng, T. Venkatesan, and Andrivo Rusydi. Direct observation of room-temperature stable magnetism in

$LaAlO_3/SrTiO_3$ heterostructures. *ACS Appl. Mater. Interfaces*, 10(11):9774–9781, March 2018.

[236] H. K. Sato, C. Bell, Y. Hikita, and H. Y. Hwang. Stoichiometry control of the electronic properties of the $LaAlO_3/SrTiO_3$ heterointerface. *Applied Physics Letters*, 102(25):251602, 2013.

[237] Wanjun Jiang, X. Z. Zhou, and Gwyn Williams. Scaling the anomalous hall effect: A connection between transport and magnetism. *Phys. Rev. B*, 82:144424, Oct 2010.

[238] S. X. Zhang, W. Yu, S. B. Ogale, S. R. Shinde, D. C. Kundaliya, Wang-Kong Tse, S. Y. Young, J. S. Higgins, L. G. Salamanca-Riba, M. Herrera, L. F. Fu, N. D. Browning, R. L. Greene, and T. Venkatesan. Magnetism and anomalous hall effect in Co-(La, Sr)$TiO_3$. *Phys. Rev. B*, 76:085323, Aug 2007.

[239] R. Mathieu, A. Asamitsu, H. Yamada, K. S. Takahashi, M. Kawasaki, Z. Fang, N. Nagaosa, and Y. Tokura. Scaling of the anomalous hall effect in $Sr_{1-x}Ca_xRuO_3$. *Phys. Rev. Lett.*, 93:016602, Jun 2004.

[240] D. Stornaiuolo, C. Cantoni, G. M. De Luca, R. Di Capua, E. Di Gennaro, G. Ghiringhelli, B. Jouault, D. Marrè, D. Massarotti, F. Miletto Granozio, I. Pallecchi, C. Piamonteze, S. Rusponi, F. Tafuri, and M. Salluzzo. Tunable spin polarization and superconductivity in engineered oxide interfaces. *Nature Materials*, 15(3):278–283, 2016.

[241] D. V. Christensen, Y. Frenkel, P. Schütz, F. Trier, S. Wissberg, R. Claessen, B. Kalisky, A. Smith, Y. Z. Chen, and N. Pryds. Electron mobility in $\gamma$-$Al_2O_3/SrTiO_3$. *Phys. Rev. Applied*, 9:054004, May 2018.

[242] V. N. Strocov, A. Chikina, M. Caputo, M.-A. Husanu, F. Bisti, D. Bracher, T. Schmitt, F. Miletto Granozio, C. A. F. Vaz, and F. Lechermann. Electronic phase separation at $LaAlO_3/SrTiO_3$ interfaces tunable by oxygen deficiency. *Phys. Rev. Materials*, 3:106001, Oct 2019.

[243] Y. Segal, J. H. Ngai, J. W. Reiner, F. J. Walker, and C. H. Ahn. X-ray photoemission studies of the metal-insulator transition in $LaAlO_3/SrTiO_3$ structures grown by molecular beam epitaxy. *Phys. Rev. B*, 80:241107, Dec 2009.

[244] Jaekwang Lee and Alexander A. Demkov. Charge origin and localization at the $n$-type $SrTiO_3/LaAlO_3$ interface. *Phys. Rev. B*, 78:193104, Nov 2008.

[245] D. J. Keeble, S. Wicklein, L. Jin, C. L. Jia, W. Egger, and R. Dittmann. Nonstoichiometry accommodation in $SrTiO_3$ thin films studied by positron annihilation and electron microscopy. *Phys. Rev. B*, 87:195409, May 2013.

[246] G. M. Choi, H. L. Tuller, and D. Goldschmidt. Electronic-transport behavior in single-crystalline $Ba_{0.03}Sr_{0.97}TiO_3$. *Phys. Rev. B*, 34:6972–6979, Nov 1986.

[247] Gabriele Balducci, M. Saiful Islam, Jan Kašpar, Paolo Fornasiero, and Mauro Graziani. Reduction process in $CeO_2$-MO and $CeO_2$-$M_2O_3$ mixed oxides: A computer simulation study. *Chem. Mater.*, 15(20):3781–3785, October 2003.

# Appendix A

# The defect chemistry of SrTiO₃

The electrons in the LAO/STO system reside on the STO side occupying the Ti ions. [64] These change their valence state from $Ti^{4+}$ to $Ti^{3+}$ and take up the additional electrons transferred due to the polarity mismatch (see above). However, in oxides in general and especially in STO the system can react to electrical (as in LAO/STO) or chemical potential changes (as at grain boundaries of STO) by electric as well as ionic charge transfer. To understand changes in electrical behavior of LAO/STO it is crucial to know the compensation mechanisms in STO itself. Ionic compensation is achieved by the incorporation of intrinsic defects, which are described in the defect chemistry model. This model is explained in great detail in Ref.: [72] in a general form for metal oxides. Regarding STO itself the complete derivation of the defect chemistry model was done in Ref.: [41] including experimentally determined reaction constants. With this model, it can be described in a simple manner where the systems equilibrium concentrations of point defects are settled. These include oxygen, strontium and titanium vacancies, as well as commonly observed defect compositions like Schottky defects to name the most important cases of STO.

Point defects are commonly described in Kröger Vink notation [116] where the elements are described by their symbols used in the periodic table and vacancies by a V. Negative charge is described by a dot in superscript (˙), positive charge by a ′ and no charge by a x in superscript (ˣ). At last, the element or vacancy site in the crystal lattice is set as subscript by symbol of the element that resides in this place in a perfect crystal lattice. Electrons are described by an e and holes by a h. In an ionic crystal, the charge neutrality condition that has to be fulfilled for any stable ionic crystal lattice (moreover for any material), as all electrical fields will be minimized by the system in equilibrium. This leads to the conclusion that every charge in the form of electrons or defects has to be compensated either electronically (by holes) or ionically by another charged defect (vacancies or dopants). The total net charge has to be zero leading to the charge neutrality condition in STO as follows

$$n + 2[V_{Sr}''] + 4[V_{Ti}''''] + [A'] = p + 2[V_O^{\bullet\bullet}] + [D^{\bullet}] \tag{A.1}$$

Here the denotations stand for the amount of their respective species and follow the aforementioned Kröger Vink notation: $n$ for electrons, $[V_{Sr}'']$ for Sr vacancies, $[V_{Ti}'''']$ for Ti vacancies, $[A']$ for acceptor dopants, $p$ for holes, $[V_O^{\bullet\bullet}]$ for oxygen vacancies and $[D^{\bullet}]$ for donor dopants. The description for defect concentration profiles are deduced

from statistical physics and can be described using a law of mass action, including a Boltzmann term. Based upon the charge neutrality under inclusion of the law of mass action of the regarded reaction, the defect equilibria of STO can be formulated. In this way it can be determined how the defect concentration evolves as a function of oxygen partial pressure. The temperature determines wherever an equilibrium state can be established, as ionic species move rather slowly, if not at all at room temperature and their mobility has to be activated. Another limiting factor to lower temperatures is the low surface exchange coefficient, which hinders the exchange with the surrounding atmosphere. [119] Furthermore, the defect concentration also highly depends on the majority concentration of charge carrier in the system, due to the charge neutrality condition. For this reason, acceptor and donor doped STO show distinctly different behavior.

Starting at room temperature in a stoichiometric crystal without any dopants, STO is a band gap insulator where the energetic height of the band gap (E$_g$) is at around 3.6 eV. By exciting an electron from the valence to the conduction band an electron hole pair can be formed following the law of mass action as follows

$$n \cdot p = N_e(T)N_p(T) \exp\left(-\frac{E_g(T)}{k_B T}\right) \tag{A.2}$$

Here $n$ denotes the concentration of electrons, $p$ the concentration of holes, $N_e$ the density of states (DOS) inside of the conduction band, $N_p$ the DOS inside of the valence band and $E_g$ the band gap. This formula describes the temperature excitation of electron-hole pairs and is valid for all temperatures.

When the temperature is increased above 750 K the oxygen sub lattice is activated. This means that above this temperature oxygen anions can move in and out of the crystal lattice, making the bulk crystal able to change its defect concentration according to the surrounding gas atmosphere. This process of lattice oxygen forming gaseous oxygen molecules is described by the reduction reaction

$$O_O^x \rightleftharpoons \frac{1}{2}O_2 + V_O^{\bullet\bullet} + 2e' \tag{A.3}$$

In this context an oxygen vacancy releases two electrons into the crystal lattice. This is due to their very low ionization energies. In principle also singly ionized or neutral oxygen vacancies can occur but due to their very small ionization energies, they are only relevant for low temperatures [120]. The change in concentration for oxygen occupying the oxygen lattice (O$_O^x$) will be small, so it can be assumed to stay constant. With this assumption, a corresponding law of mass action for equation A.3 can be written as

$$[p(O_2)]^{\frac{1}{2}}[V_O^{\bullet\bullet}]n^2 = K_0^{red}\exp\left(-\frac{\Delta H_{red}}{k_B T}\right) \tag{A.4}$$

Here, $p(O_2)$ describes the oxygen partial pressure, $K_0^{red}$ the reaction constant and $\Delta H_{red}$ the activation energy of the reduction reaction. Equation A.4 gives the means to describe how electron concentration and oxygen vacancy formation correlate under certain temperature and $p$O$_2$. The inverse process, namely law of mass action of the oxidation reaction, can be derived in the same way to describe the interplay of the hole

concentration with the oxygen vacancy concentration and oxygen partial pressure. The oxidation reaction reads

$$\frac{1}{2}O_2 + V_O^{\cdot\cdot} \rightleftharpoons 2h^\cdot + O_O^x \tag{A.5}$$

From this the law of mass action of the oxidation reaction can be derived

$$\frac{p^2}{(pO_2)^{\frac{1}{2}}[V_O^{\cdot\cdot}]} = K_0^{Ox} \exp\left(-\frac{\Delta H_{Ox}}{k_B T}\right) \tag{A.6}$$

In this context $K_0^{Ox}$ describes the reaction constant of the oxidation reaction and $\Delta H_{Ox}$ the corresponding reaction enthalpy. With the equations above the reaction of the STO anion lattice on the surrounding thermodynamic conditions is described. This leaves the reaction of the cation lattice to complete the picture. Above 1250 K this lattice becomes active, meaning that the formation of Schottky defect order has to be taken into consideration. The formation of a Schottky defect, which describes the complete removal of one elementary cell can be written as

$$Sr_{Sr}^x + Ti_{Ti}^x + 3O_O^x \rightleftharpoons V_{Sr}'' + V_{Ti}'''' + 3V_O^{\cdot\cdot} + SrTiO_3 \tag{A.7}$$
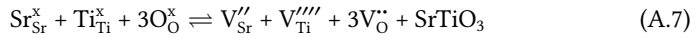
It has been shown that STO is more likely to incorporate Sr than Ti vacancies. This has been observed for donor doped STO, [56] as well as for undoped STO [118] and theoretical calculations show that the partial Schottky defect involving only Sr and O needs less energy to form than the one of Ti and O. [117] Therefore, to describe the reaction of the cation lattice, equation A.7 can be simplified into the partial Schottky defect
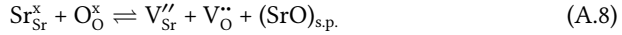
$$Sr_{Sr}^x + O_O^x \rightleftharpoons V_{Sr}'' + V_O^{\cdot\cdot} + (SrO)_{s.p.} \tag{A.8}$$

Assuming the amount of crystalline species, namely $Sr_{Sr}^x$, $O_O^x$ and SrO, to be constant the corresponding law of mass action reads

$$[V_{Sr}''][V_O^{\cdot\cdot}] = K_0^S \exp\left(-\frac{\Delta H_S}{k_B T}\right) \tag{A.9}$$

It will be seen in the following, that the complete defect chemistry of the STO system can be derived by using equations A.2, A.4, A.6 and A.9 in combination with the corresponding charge neutrality condition. As mentioned before each equation has a distinct temperature range where it is valid. Only equation A.2 is valid in all temperatures, while equation A.4 and A.6 will only be active above 750 K. At last, equation A.9 is only considered above 1250 K, as the diffusion coefficient of Sr has to be sufficiently high to move over the length scale of micrometers. This changes the reaction of the crystal conductivity on oxygen partial pressure, depending on the temperature. In the following the charge neutrality conditions, which are determined by the majority charge carriers, will be combined with the law of mass actions to describe the complete behavior of STO in thermodynamic equilibria. In the following it will be only distinguished between temperatures above or below 1250 K (active or inactive cation lattice) as below 750 K no oxygen partial pressure dependence is observed (see equation A.2).

## A.1　Undoped and acceptor doped STO

Undoped STO generally behaves like acceptor doped STO. This comes from the fact that only a finite purity of the material can be achieved in practice. Since most impurities (like e.g. iron) are acceptors for STO the behavior of undoped STO can described by the one of slightly acceptor doped STO. [41, 207, 246] Below 1250 K in very reducing conditions the amount of charge carriers will be determined by the amount of oxygen vacancies. Therefore, the charge neutrality condition (eq. A.1) can be approximated as

$$n \simeq 2V_O^{\bullet\bullet} \tag{A.10}$$

Inserting this simplified condition into equation A.4 and redistributing of the equation leads to a $p$O$_2$ dependent expression for the concentration of electrons

$$n = (p\text{O}_2)^{-\frac{1}{6}} (2K_0^{\text{red}})^{\frac{1}{3}} \exp\left(-\frac{\Delta H_{\text{red}}}{3\text{k}_\text{B}T}\right) \tag{A.11}$$

which means that

$$n \propto (p\text{O}_2)^{-\frac{1}{6}} \tag{A.12}$$

From this we can determine that in very reducing conditions the concentration of electrons will depend on the oxygen partial pressure to the power of -1/6. As equation A.2 does not show a dependence on $p$O$_2$ it can be simplified for a constant temperature to

$$n \cdot p = \text{const} \tag{A.13}$$

and can therefore be used with equation (12) to deduce the proportionality of holes on $p$O$_2$ in this regime

$$p \propto (p\text{O}_2)^{\frac{1}{6}} \tag{A.14}$$

Therefore, electrons and holes behave inversely to each other with electrons contributing the majority carrier concentration from oxygen vacancy incorporation and holes contributing the minority carrier concentration from band gap excitation. When the $p$O$_2$ is increased the concentration of oxygen vacancies will decrease until the point is reached where

$$2[V_O^{\bullet\bullet}] \simeq [A'] \tag{A.15}$$

From this point, the amount of oxygen vacancies is largely fixed by the acceptor dopant concentration to compensate their charge. An effect that is used in ion conductors like CeO$_2$ or YSZ to enhance the concentration of oxygen vacancies in the system. [247] Assuming the amount is exactly fixed and putting this equation again in equations A.4 and A.6 the amount of electrons and holes can be derived, leading to

$$n = (p\text{O}_2)^{-\frac{1}{4}} \left(\frac{2K_0^{\text{red}}}{[A']}\right)^{\frac{1}{2}} \exp\left(-\frac{\Delta H_{\text{red}}}{2\text{k}_\text{B}T}\right) \propto (p\text{O}_2)^{-\frac{1}{4}} \tag{A.16}$$

and

$$p = (p\text{O}_2)^{\frac{1}{4}} \left(\frac{[A']K_0^{\text{red}}}{2}\right)^{\frac{1}{2}} \exp\left(-\frac{\Delta H_{\text{Ox}}}{2\text{k}_\text{B}T}\right) \propto (p\text{O}_2)^{\frac{1}{4}} \tag{A.17}$$
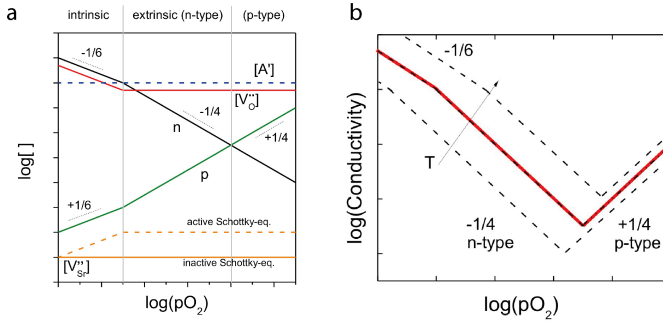
**Figure A.1:** a) The concentration of defects and charge carriers is plotted over oxygen partial pressure in acceptor doped STO b) The resulting conductivity dependence on oxygen partial pressure of STO through the changes in carrier densities is shown including an indication of the temperature dependence. By courtesy of Ref.: [121].

While electrons decrease to the power of -1/4, holes increase to the power of 1/4 when the oxygen partial pressure is increased. This leads to a crossover point when the majority of charge carriers switches and STO goes from a n-type to a p-type conductor.

When the temperature is increased above 1250 K the general behavior in acceptor doped STO is not changed. Sr vacancies will be generated according to equation A.9, leading to an increase in very reducing conditions inverse to the amount of oxygen vacancies$\propto (pO_2)^{\frac{1}{6}}$. When the $pO_2$ is increased the amount of oxygen vacancies is largely fixed and therefore also the amount of Sr vacancies. However, this does not significantly change the conductivity behavior as is the case for donor doped STO (see below). The complete results of this discussion can be summarized in a so called Brouwer-diagram which is shown in Figure A.1 a. There, the concentrations of charge carriers and defects are schematically sketched over the oxygen partial pressure on a double logarithmic scale. From the amount of charge carriers the conductivity behavior of STO can also be derived. As in metals the overall conductivity is given by

$$\sigma = n \cdot \mu_n + p \cdot \mu_p \tag{A.18}$$

The mobilities of electrons ($\mu_n$) and holes $\mu_p$ are temperature but not $pO_2$ dependent. Their temperature dependence can be written as [41]

$$\mu_n \approx 3.95 \cdot 10^4 \, T^{-1.62} \frac{cm^2}{Vs} \tag{A.19}$$

$$\mu_p \approx 1.1 \cdot 10^6 \, T^{-2.36} \frac{cm^2}{Vs} \tag{A.20}$$

Since the dependence of carrier concentration on temperature is exponential, the conductivity of STO increases with temperature. This leads to the $pO_2$ dependence of STO conductivity that is shown in Figure A.1 b. In the intrinsic regime it follows the -1/6 power law, decreasing the slope to -1/4 when the extrinsic regime is reached and oxygen vacancies are fixed by the acceptor dopant concentration. Further increase

leads to a valley where the crossover from n- to p-type conductivity leads to a minimum in the observed conductivity. Finally conductivity increases again to the power of 1/4 in further increasing $p$O$_2$ as holes become the majority charge carriers. An increase in temperature leads to a shift of the curve to higher values as charge carrier concentration shows an exponential dependence on temperature. The temperature dependence is less strongly pronounced for the p-type regime due to the different activation enthalpy for oxidizing and reducing conditions.

## A.2   Donor doped STO

Also in the case of donor doped STO three distinct regimes exist. Starting below 1250 K in an inactive Schottky equilibrium, the intrinsic regime in very reducing conditions behaves the same as in acceptor doped STO and both charge carrier concentrations (n and p) are determined by the formation of oxygen vacancies. However, at higher $p$O$_2$ the behavior is completely altered.  The electron density is first fixed by the concentration of donor dopants which can be written as

$$n \simeq [D^{\bullet}] \tag{A.21}$$

Therefore, it is fixed to a constant value. Inserting equation A.21 into equation A.4 leads to

$$(p\text{O}_2)^{\frac{1}{2}}[V_{\text{O}}^{\bullet\bullet}][D^{\bullet}]^2 = K_0^{\text{red}}\exp\left(-\frac{\Delta H_{\text{red}}}{\text{k}_\text{B}T}\right) \Rightarrow [V_{\text{O}}^{\bullet\bullet}] \propto (p\text{O}_2)^{-\frac{1}{2}} \tag{A.22}$$

This reveals that the concentration of oxygen vacancies is depleted to the power of -1/2.  Plugging this proportionality into equation A.6 shows that the hole density stays constant. This leads to a very simple behavior of conductivity over $p$O$_2$ staying constant over most pressures and only rising to very reducing conditions. However, when the Schottky equilibrium is activated at temperatures above 1250 K the formation of Sr vacancies changes the defect chemistry behavior. First in the intrinsic region an increase in Sr vacancy concentration to the power of 1/6 is present just as in acceptor doped STO. This comes from the inverse behavior to the oxygen vacancy concentration that can be deduced from equation A.9.  The slope of Sr vacancy formation then enhances to the power of 1/2 as oxygen vacancy depletion is present at a rate to the power of -1/2. However, this does not change the concentration of electrons thus far. The concentration of Sr vacancies continues to increase until it comes close to the concentration of donor dopants and electrons. Now the charge neutrality condition has to account for them and reads

$$n + 2[V_{\text{Sr}}''] = [D^{\bullet}] \tag{A.23}$$

When the concentration of Sr vacancies finally exceeds the half the electron concentration they dominate the left hand side of equation A.23 leading to

$$2[V_{\text{Sr}}''] = [D^{\bullet}] \tag{A.24}$$

Equation A.24 finally fixes the concentration of Sr vacancies. However, this also fixes the concentration of oxygen vacancies (eq. A.9). A fixed oxygen vacancy concentration
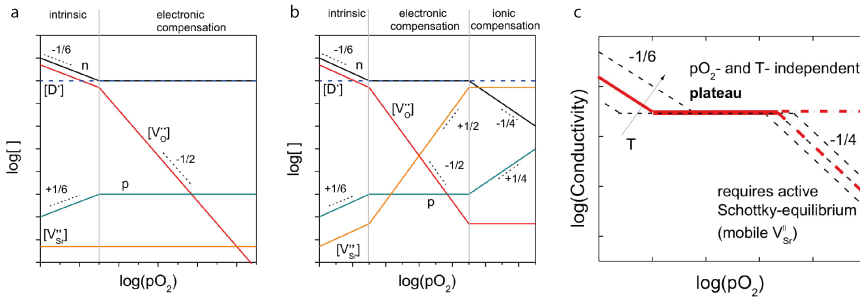
**Figure A.2:** a) The concentration of defects and charge carriers is plotted over oxygen partial pressure in donor doped STO b) The concentration of the species as in a) are shown but in an active Schottky equilibrium c) The resulting conductivity dependence on oxygen partial pressure of donor doped STO through the changes in carrier densities is shown including an indication of the temperature dependence with and without an active Schottky equilibrium. By courtesy of Ref.: [121].

put into equation A.4 and A.6 leads to a rise of holes to the power of 1/4 and a depletion of electrons to the power of -1/4. This leads to a similar behavior as observed in acceptor doped STO for lower $p\mathrm{O}_2$, however in this case the oxygen vacancy concentration is fixed by the Schottky equilibrium instead of charge neutrality with the acceptor dopants. Therefore, at this point the electron concentration is just depleted, a crossover as seen in acceptor doped STO lies at unreasonable high $p\mathrm{O}_2$ and is not relevant. For the conductivity this leads to a rise to very reducing conditions, a plateau region in intermediate pressures and a decrease to oxidizing conditions.

# Acknowledgments

This thesis would not have been possible without the help and support of many people. I would like to express my personal thanks to all people, who contributed professionally but also brightened my days during the countless hours of work that went into this project.

First of, I would like to express thanks to my supervisor Felix Gunkel. He provided me with the scientific knowledge, that I needed to succeed in the field of oxide electronics. However more importantly, he gave me the freedom to work independently, while taking the time for in depth discussions and challenging my interpretations. In this way, I could improve my scientific skills and grow as a person.

I want to thank Prof. Regina Dittmann, who agreed to give me the opportunity to work at the Institute. Her tremendous knowledge about oxide thin film growth was a great help for my thesis. Also her way of getting our group to discuss and exchange, but also to engage in social activities, helped us all scientifically and generated a very good working atmosphere.

Thanks go to Prof. Thomas Taubner, who agreed to officially supervise my thesis. The collaborative work with him and his group was an exciting part of this work, where both parties profited well from the expertise of the other.

In this context I also want to express my thanks to Julian Barnett, who was my counterpart in Prof. Taubners group, working on the LAO/STO system. He was a very good partner to work with. Planning and discussing experiments with him was always a pleasant and fun experience.

Regarding the spectroscopic part of this work, which included a detailed analysis, special thanks go to David N. Müller. Without his huge knowledge about the XPS method, I would not have been able to extract this amount of information from the data I collected. He was always happy to help me out with discussions and advice, and in general a great person to work with.

Regarding spectroscopic analysis, I also want to thank Prof. Scott A. Chambers, who helped me putting together the last but vital steps of the analysis. His different perspective on the data and background knowledge about the material system were a huge help.

I want to thank Prof. Marjana Ležaić and Ivetta Slipukhina, who supported this work by providing the density-functional theory calculations presented in this thesis and were great people to work with. It was a nice experience to see through their independent results, that the derived defect chemical model is indeed valid from a fundamental point of view.

Without the help of external collaborators, it would not have been possible to collect the high quality of NAP-XPS data, that was the basis of my analysis. For this, I

want to express my thanks to Hendrik Bluhm, who supported our measurements at the ALS in Berkeley. Thanks also go to Mykhailo Vorokhta and Břetislav Šmíd, who helped to conduct experiments at the Charles University in Prague. They were not only a huge help, but also great people in general and made the stay in Prague very enjoyable.

Of course, I also received a huge amount of support from my colleagues. Michael Andrä, who helped me in my first steps in XPS analysis. Felix Hensling, who introduced me to the PLD process and helped me grow my very first LAO thin films. Jaqueline Börgers, who also worked on the same material system and was a good person to discuss with and was a great help regarding low-temperature experiments. Thomas Heisig, who helped me out with the lithographic patterning of samples. Maria Glöß, who was a helped me regarding c-AFM experiments. In this regard, also special thanks go to Marco Moors, who introduced me to the c-AFM technique and helped me record my first map of a 2DEG.

I want to thank Alexandros Sarantopoulos, who helped me keep the PLD system running and took a lot of work of my hands, when I started the writing process of my thesis.

My days at the Institute were also brightened by all the great other colleagues, who did not directly contribute to this work, but shaped the nice working atmosphere. My thanks go to Venkata Raveendra Nallagatla, Alexander Gutsche, Lisa Heymann, Moritz Weber, Stephan Außen, Sebastian Siegel, Niclas Schmidt, Solomon Chekol, Nuno Casa Branca and Tim Kempen.

I want to thank Markus Wohlgemut, who shared my interest in music and books. I would have loved to go on more concerts, with him and would have done so, if the pandemic did not make such activities impossible for the time.

Especially I want to thank Sebastian Hambsch, Felix Cüppers, Tobias Ziegler and Jan Hempelmann with whom I spend many evenings, playing pen and paper role playing games. Even though I have played such games for a long time, this group has a very special dynamic, that gave me a entirely new view on how to play them.

I want to thank Paul Müller, Christian Pithan and Rana Vikas with whom I had exciting discussions about all kinds of topics, during my breaks from work.

Without working technical equipment and the constant efforts of the technicians that keep them running, nothing could be accomplished in any institute. For this, my thanks go to Georg Pickartz, who helped me keep the PLD running. René Borowski, who prepared the termination of countless STO single crystal surfaces for me. Stephan Maßberg, who supported the maintenance work at the c-AFM. Jochen Friedrichs, who build up and helped repair the ECR setup. At last but not least, I want to thank Marcel Gerst, who keeps all the computers of the Institute running and helped me in resolving multiple computer related issues.

Schriften des Forschungszentrums Jülich
Reihe Information

Band / Volume 75
**Development of Electrochemical Aptasensors for the Highly Sensitive,
Selective, and Discriminatory Detection of Malaria Biomarkers**
G. Figueroa Miranda (2021), XI, 135 pp
ISBN: 978-3-95806-589-5

Band / Volume 76
**Nanostraw- Nanocavity MEAs as a new tool for long-term
and high sensitive recording of neuronal signals**
P. Shokoohimehr (2021), xi, 136 pp
ISBN: 978-3-95806-593-2

Band / Volume 77
**Surface plasmon-enhanced molecular switching for optoelectronic
applications**
B. Lenyk (2021), x, 129 pp
ISBN: 978-3-95806-595-6

Band / Volume 78
**Engineering neuronal networks in vitro: From single cells to population
connectivity**
I. Tihaa (2021), viii, 242 pp
ISBN: 978-3-95806-597-0

Band / Volume 79
**Spectromicroscopic investigation of local redox processes in resistive
switching transition metal oxides**
T. Heisig (2022), vi, 186 pp
ISBN: 978-3-95806-609-0

Band / Volume 80
**Integrated Control Electronics for Qubits at Ultra Low Temperature**D.
Nielinger (2022), xviii, 94, xix-xxvi
ISBN: 978-3-95806-631-1

Band / Volume 81
**Higher-order correlation analysis in massively parallel recordings in
behaving monkey**
A. Stella (2022), xiv, 184 pp
ISBN: 978-3-95806-640-3

Band / Volume 82
**Denoising with Quantum Machine Learning**
J. Pazem (2022), 106 pp
ISBN: 978-3-95806-641-0

Schriften des Forschungszentrums Jülich
Reihe Information

Weitere *Schriften des Verlags im Forschungszentrum Jülich* unter
http://wwwzb1.fz-juelich.de/verlagextern1/index.asp

JÜLICH
Forschungszentrum